SEISMOLOGICAL FORWARD AND INVERSE MODELLING FOR UPPER MANTLE SEISMIC ANISOTROPY STUDIES

Coordinator: Prof. Claudia AGNINI

Supervisor: Prof. Manuele FACCENDA

Co-Supervisor: Dr. Brandon Paul VANDERBEEK

Ph.D. student: Francesco RAPPISI

"Essere colti non significa ricordare tutte le nozioni, ma sapere dove andare a cercarle"

U. Eco

Abstract

Seismic anisotropy is the dependence of seismic wave velocity on the propagation direction and, in the Earth's mantle, it is mainly generated by strain-induced lattice preferred orientation (LPO) of intrinsically anisotropic minerals. Despite previous studies have demonstrated that neglecting anisotropy introduces notable imaging artifacts, most tomographic methods rely on the assumption of isotropy, interpreting fast and slow velocity anomalies as related to seismically isotropic sources (e.g., temperature anomalies, presence of a liquid phase, etc). In this Thesis I carried out numerical simulations aiming at improving strain-induced fabric estimates and predicting realistic elastic properties in 2-D and 3-D synthetic domains. I generated synthetic datasets with forward waveform modelling and explored different inverse methodologies (e.g., P- and S-wave travel time tomography, automatic partitioned waveform inversion of surface waves) both with real and synthetic data. Among the results, I present ani-NEWTON21, the first 3D anisotropic teleseismic P-wave tomography revealing upper mantle structures and dynamics beneath the Central Mediterranean. By performing synthetic seismic data inversions I tested how ray density, data quality and regularization (i.e., damping and smoothing factors) influence the tomographic image. Finally, from the comparison of purely isotropic and anisotropic tests, I observed that the first-order effect of including anisotropy in the inversion is to reduce the magnitude of isotropic anomalies, more significantly for low-velocity zones relative to high-velocity zones. The research activities described in this Thesis altogether provide important insights for predicting and isolating seismic anisotropy, and for obtaining more reliable and physically consistent imaging of the Earth's internal structure.

Sommario

L'anisotropia sismica è la dipendenza della velocità di un'onda dalla direzione di propagazione ed è principalmente dovuta all'allineamento di minerali intrinsecamente anisotropi causato dalla deformazione indotta dai flussi mantellici. La maggior parte dei metodi tomografici si basa sul presupposto che la Terra sia isotropa, interpretando le anomalie di velocità come dovute a sorgenti di natura sismicamente isotropa (ad esempio, anomalie di temperatura, presenza di una fase liquida, ecc), nonostante diversi studi abbiano dimostrato che trascurare l'anisotropia introduce notevoli artefatti nei risultati. In questa Tesi abbiamo effettuato simulazioni numeriche con l'obiettivo di (i) migliorare le stime dei fabrics indotti dalla deformazione, (ii) ottenere predizioni sempre più realistiche delle proprietà elastiche di modelli sintetici 2-D e 3-D, (iii) generare datasets sintetici, ed infine (iv) esplorare diverse metodologie di inversione sia con dati reali che sintetici. Tra i risultati viene presentato ani-NEWTON21, il primo modello tomografico anisotropico ottenuto tramite l'inversione di delay times di onde P telesismiche che rivela le strutture e la dinamica del mantello superiore al di sotto del Mediterraneo centrale. Eseguendo inversioni di dati sismici sintetici, abbiamo testato come la densità dei raggi, la qualità dei dati e la regolarizzazione (cioè i fattori di damping e smoothing) influenzino l'immagine tomografica. Infine, dal confronto di test puramente isotropi e anisotropi, abbiamo osservato che l'effetto principale che si ha includendo l'anisotropia nell'inversione è quello di ridurre l'entità delle anomalie isotrope, specialmente quelle di bassa velocità. Nel complesso, le attività di ricerca descritte in questa Tesi forniscono importanti spunti per lo studio e la stima dell'anisotropia sismica nel mantello superiore, e dunque per ottenere immagini tomografiche più affidabili della struttura interna della Terra.

Contents

List of Figures

List of Tables

To my friend Gaetano

Chapter 1

INTRODUCTION

Studying the Earth's interior has always fascinated scientists around the world. The first exploratory approaches involved drilling the Earth's crust, but due to the technological limitations that still persist, drilling allows an exclusively superficial and punctual study that does not guarantee the reconstruction of a three-dimensional model from the crust to the core. The deepest well ever drilled reaches a depth of about 12 km, nothing compared to the 6371 km of the Earth's radius. What we know today of the Earth's interior mainly derives from indirect observations obtained through the analysis of geophysical data (e.g., seismic data) recorded at the surface.

Introduced in the late '70s, seismic tomography (Aki et al., 1977; Dziewonski et al., 1977; Sengupta & Toksöz, 1976) is the most common and powerful imaging method that uses seismic waves radiating from earthquakes or explosions to produce 3-D (or 2-D) images of the subsurface. A tomographic model is represented in colors that indicate how specific parameters (e.g., P-, S-wave velocity) vary inside the study volume. Although the mathematical solution of the seismic problem is quite complex and thus involves the use of strong computational resources, the theoretical approach is simple: given that lateral variations in seismic wave velocities depend on, for example, temperature, phase transitions and composition, using the travel time and distance of the wave from the hypocentre to the receiver, seismologists can calculate the average speed of the seismic waves, thus interpret

the resulting model in terms of 3-D distribution of thermal, petrological and compositional anomalies. There are several approaches to perform seismic tomography (e.g., travel time tomography, full waveform inversion, dispersion curves inversion, etc), but all of them involves the solution of direct and inverse problems (Figure 1.1). Any physical model can be described by a series of parameters which can be used to estimate specific measurements (e.g., P-wave travel times) through the volume we are analyzing. This is called forward (or direct) problem. The opposite procedure, the inverse problem, involves the estimation of the model parameters starting from the measurements. The mathematical expression for linear problems, where the relation between measurements and parameters is indeed linear, is:

$$Gm = d^{obs} \tag{1.1}$$

where d^{obs} is a vector of observed data, m is a vector containing the model parameters and G is a matrix called direct operator. G allows for the estimation of the predicted data d^{pre} associated with a set of model parameters m^{est}. The solution of an inverse problem is given by the model m^{est} for which the difference between d^{pre} and d^{obs} is as small as possible (Tarantola, 1986). For non-linear problems, where the direct operator G depends on the unknowns itself, the formulation becomes:

$$g(m) = d^{obs} \tag{1.2}$$

where g now is a function. In this case, inverting the matrix G is not sufficient to solve the inverse problem. Much more complex techniques are required to obtain a reliable estimation of the model parameters. The most used optimization methods involve the minimization of an error (or object function) that defines the discrepancy between the observed and the predicted data. However, as it is common in the case of travel-time tomography,

the non-linear problem is often "linearized" and solved iteratively assuming small steps than can be considered linear.

Considering the high number of model parameters (i.e. unknowns) and the low number of independent data and a priori information (i.e. constraints), the inverse problem in seismology is usually ill-posed, which means that multiple models satisfy the data. Several factors control the nonuniqueness of the solution, among them data coverage, noise, choice of parameterization, choice of forward and inverse methods used for data prediction and inversion. In this study I applied different methodologies to solve both direct and inverse problem that will be discussed in the following chapters.
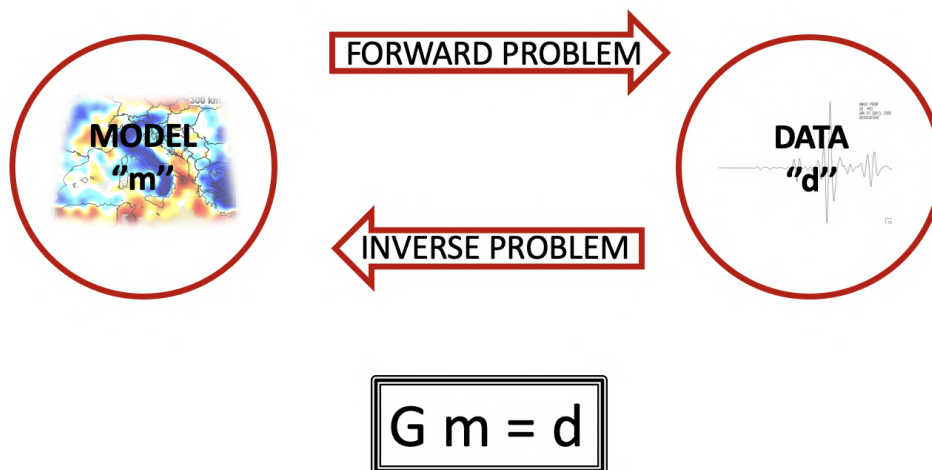
Figure 1.1: *Forward and inverse problems illustration. The forward problem predicts observations if the model parameters are known. The inverse problem infers the model parameters from the observations.*

In many cases, adding contributions from additional sources and receivers helps producing a better tomographic result (Rawlinson et al., 2014). The more and better a target region is sampled, the more reliable the tomography will be (Lai & Garnero, 2020), thus the better resolved. For this reason, in the last decades, the number of fixed and mobile stations has increased

and the advent of internet has made accessible seismic data through digital databases. Among these, the one of the International Seismologic Centre compiles and shares bulletins of seismic data (i.e. hypocentre locations, phase and amplitude measurements, focal mechanism, etc) collected from more than 130 agencies. For this work I have used both real and synthetic data, from the ISC-EHB bulletins or generated with specific software (e.g., SPECFEM3D_GLOBE, Komatitsch & Tromp, 2002). While real data allowed to apply our methodologies to real geological scenarios (e.g., the Mediterranean) and thus to produce accurate anisotropic images of specific regions, synthetic data tests allowed to evaluate the effect that using different data coverage and data noise has on the tomographic image. It is clear that, due to the inherent nature of seismic data, a certain amount of noise in the data is always present. This means that even with an overdetermined problem, i.e. a problem where the number of independent data is bigger than the unknowns, the uniqueness of the solution is never achieved. Therefore, the question still open is: how much does the noise influence the tomography? The increase in seismic noise causes an increase in tomography models that fit the data (Rawlinson et al., 2014), but to properly answer this and other questions, synthetic tests have been performed with different amounts of data noise and will be discussed in the next chapters (e.g., Chapter 5).

In linear least square inverse problems, to further constrain the space of tomographic solutions that satisfy the data, regularization factors, i.e. damping and smoothing, are frequently used and will be applied to both real and synthetic cases in Chapter 4 and 5, 6, 7, respectively.

On the basis of the scale of application, in the literature, we distinguish two classes of tomography: global and regional. Global scale P- (Figure 1.2) and S-wave (Figure 1.3) tomography investigates the entire volume of the Earth's mantle. Due to the uneven distribution of sources and stations and

the intrinsic characteristic of the wave phase, P-wave tomography (e.g., Bijwaard et al., 1998; Boschi & Dziewonski, 2000; Fukao et al., 2003; Kárason & van der Hilst, 2001; Lei & Zhao, 2006; Li et al., 2008; Obayashi & Fukao, 1997; Obayashi et al., 2013; Simmons et al., 2011; Su & Dziewonski, 1997; Van der Hilst et al., 1997; Young et al., 2013; Zhou, 1996) provides good resolution under subduction zones but less in oceanic settings. For this reason, P-wave tomography has been successfully used to image high velocity regions, clarifying the behaviour of the slabs in correspondence of the 670 km discontinuity (e.g., penetrating or stagnating slabs?). On the contrary, P-wave models do not well resolve low velocity zones, usually beneath the oceans (Romanowicz, 2003). On the other hand, global S-wave tomography that combines body S-waves and surface waves (e.g., Chang et al., 2014, 2015; French et al., 2013; Moulik & Ekström, 2014; Panning & Romanowicz, 2006; Ritsema et al., 2011; Ritsema et al., 1999; Schaeffer & Lebedev, 2013) provides good constraints on the longest wavelength features of mantle heterogeneity and, in particular, a better resolution in the oceans (Romanowicz, 2003).

In order to improve the resolution in both P- and S-wave tomography, it is necessary to add later-arriving phases (e.g., pP, pwP, PcP, PKPdf, PKP-bcS, SS, SSS, ScS, ScSn, SKS, etc), which unfortunately are not frequently reported in public databases. Based on this principle, a valid alternative to the most common travel time tomography comes from the world of exploration and is represented by full waveform inversion (e.g., Pratt, 1999; Virieux & Operto, 2009), in which not only the first arrivals of specific phases but entire waveforms are used as input data for the inversion. Making use of the full waveform produced by active and/or passive seismic events means including both body and surface wave modes and, given the higher content of information contained in the signal, this method should in principle be superior to others (e.g., travel times tomography) that are based on the use of

more discrete data (Nolet, 1990). For example, multimode waveform techniques (Cara & Lévêque, 1987; Nolet, 1990) can constrain both the structure in the upper 200–300 km of the mantle and the underlying structures down to the transition zone (Lebedev & Van Der Hilst, 2008), sampled by the fundamental mode surface waves and the S- and multiple S-waves (e.g., Lebedev et al., 2002), respectively. An example of this type will be addressed in Chapter 7 of this Thesis.
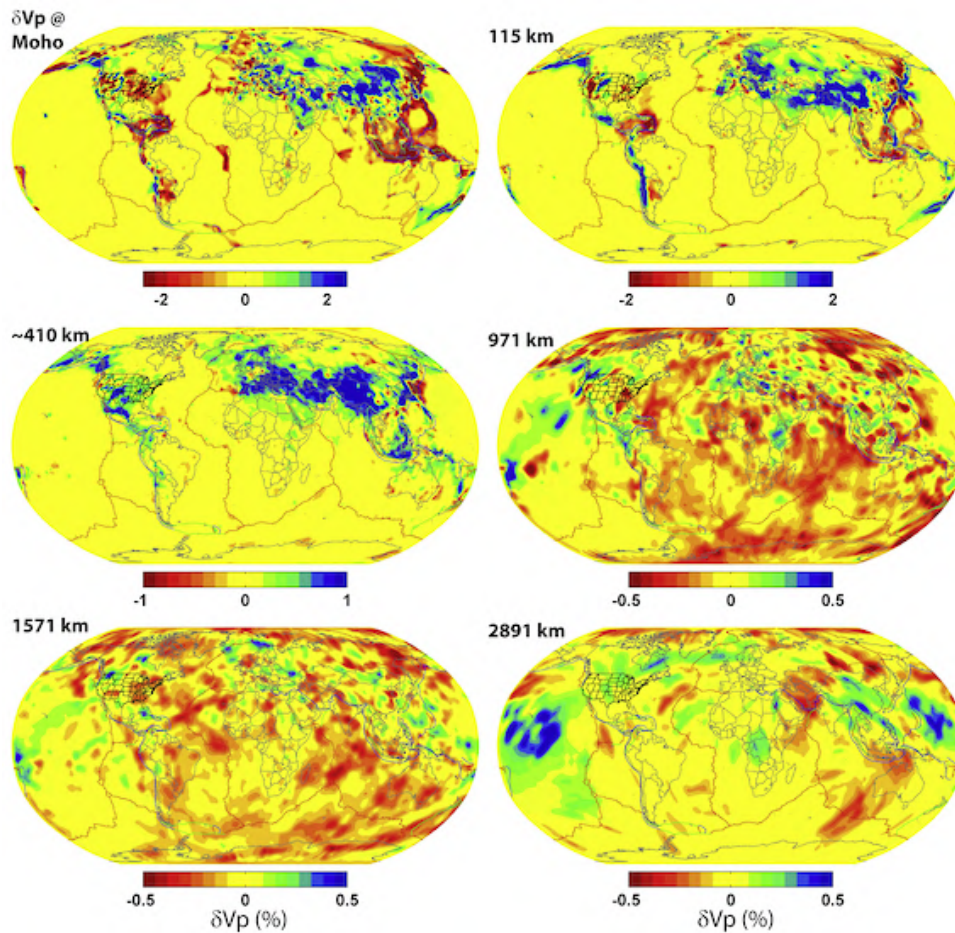
Figure 1.2: *Global P-wave tomography from Simmons et al. (2012). LLNL-G3Dv3 P-wave velocity is represented with respect to the 1D starting model at selected depths (LLNL-G3Dv3 minus the starting model).*

In the last decades, the increased seismic resolution allowed the study, and consequently the interpretation, of smaller scale (i.e. local and regional) features, such as subduction zones, volcanic arcs, mantle plumes and mid-ocean ridges (e.g., Asamori & Zhao, 2015; Bezada et al., 2013; Calò et al., 2012;
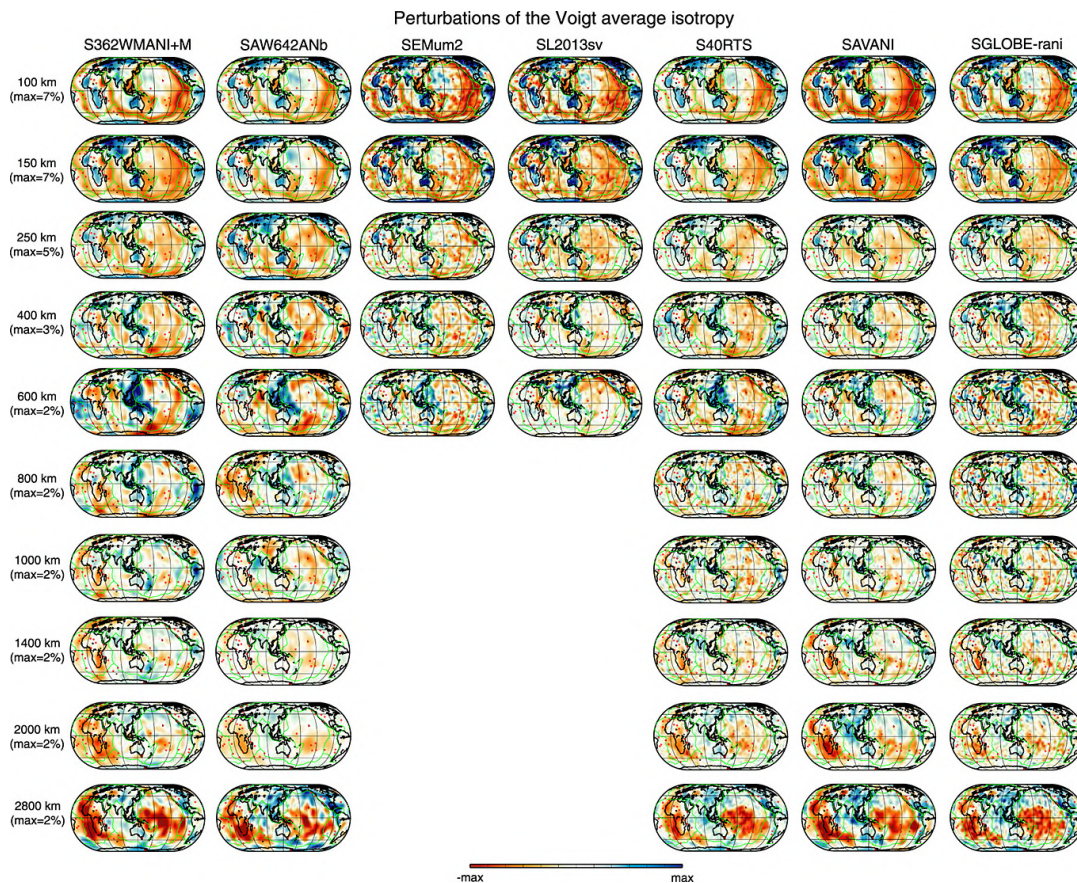
Figure 1.3: *Comparison of the isotropic V_S structure in SGLOBE-rani (Chang et al., 2015) and in the isotropic shear wave velocity models S362WMANI + M (Moulik & Ekström, 2014), SAW642ANb (Panning et al., 2010), S40RTS (Ritsema et al., 2011), SL2013sv (Schaeffer & Lebedev, 2013), SAVANI (Auer et al., 2014) and SEMum2 (French et al., 2013) at selected depths. The range of model amplitude variations is shown at the left of each row. Taken from Chang et al. (2015)*

Calò et al., 2013; Hua et al., 2017; Kästle et al., 2019; Lippitsch et al., 2003; Liu & Zhao, 2016a, 2016b; Paffrath et al., 2021; Piromallo & Morelli, 2003; Spakman, 1991; Spakman et al., 1993; Wang & Zhao, 2008; Witek et al., 2018; Zhao & Hua, 2021; Zhao et al., 2001; Zhu et al., 2012). Several regional tomography models have illuminated the areas of greatest interest on our planet, with particular focus on subduction settings such as the Mediterranean and the Alps (e.g., Bezada et al., 2013; Calò et al., 2012; Calò et al., 2013; Hua et al., 2017; Lippitsch et al., 2003; Paffrath et al., 2021; Piromallo & Morelli, 2003; Spakman, 1991; Spakman et al., 1993; Zhu et al., 2012), Cascadia (e.g., Zhao & Hua, 2021; Zhao et al., 2001), Japan (e.g., Liu & Zhao, 2016a, 2016b; Wang

& Zhao, 2008) where relatively dense seismic networks are present.

In seismic tomography, fast and slow velocity anomalies have been mainly interpreted in terms of temperature and compositional anomalies, and presence of fluids (Bijwaard & Spakman, 1999; Calò et al., 2012; Fuchs, 1997; Goes et al., 2000; Goes & van der Lee, 2002; Hammond & Toomey, 2003; Paulatto et al., 2012; Tommasi, 1998; Villagómez et al., 2014; Wiens et al., 2008). However, since seismic anisotropy has been mapped in the crust, mantle and core, it must be considered as well when interpreting velocity models as it can cause important velocity variations in the study volume. Seismic anisotropy is the dependence of the seismic wave velocity on the propagation direction and, as observed in natural and experimentally deformed samples (e.g., Hansen et al., 2016b; Hansen et al., 2014; Karato, 2008), it is mainly caused by the preferential alignment of intrinsically anisotropic minerals (Crystal/Lattice-Preferred-Orientation, CPO/LPO) due to mantle-flow-induced deformation, that results into macroscopically anisotropic rocks. Another mechanism that contributes to create seismically observable anisotropy involves the alignment of structural elements with contrasting isotropic elastic properties (Shape-Preferred Orientation, SPO; Wang et al., 2013) and it is called extrinsic anisotropy. However, although SPO due to the alignment of fluid- or melt-filled cracks/pores can be potentially strong (Kawakatsu & Yoshioka, 2011), Faccenda et al. (2019) demonstrated that compositional layering produces negligible seismic anisotropy in the upper mantle and as such it can be ignored. We distinguish two principal types of anisotropy: radial, that helps distinguishing between horizontal and vertical mantle flow, and azimuthal, that provides constraints on the direction of horizontal mantle flow (Chang et al., 2015).

The amount of anisotropy in a specific area is directly linked to the properties of the constituent minerals, their rheological behavior when subject to

tectonic stresses, temperature and water content (Blackman, 2007). The composition of the upper mantle can be approximated as made by the two most abundant minerals, olivine ($\sim$ 70%, $(Mg, Fe)_2SiO_4$) and enstatite ($\sim$ 30%, $(Mg, Fe)SiO_3$) (Ringwood, 1975) which are highly anisotropic. Depending on the stress conditions, crystal aggregates deform by diffusion (low stress and/or grain size) or dislocation creep (high stress and/or grain size). Dislocation creep is the most common mechanism to generate an LPO as it exploits the anisotropic mechanical properties of crystals. Since the '90s, numerical methods based on the geometric relationship between grain's slip systems and an external reference system have been developed to simulate strain-induced anisotropy in olivine (or olivine and enstatite) crystals aggregates. By averaging the elastic contribution of each grain, the seismic properties of a mineral aggregates are calculated (Kaminski & Ribe, 2001; Ribe & Yu, 1991). Then, these elastic properties, in the form of elastic tensors, can be validated through seismic modelling and comparisons with seismological observations (e.g., SKS splitting measurements, anisotropic P- and S-wave tomography).

Although previous studies conducted on synthetic data (e.g., Bezada et al., 2016; Blackman & Kendall, 1997; Lloyd & Van Der Lee, 2008; Sobolev et al., 1999; VanderBeek & Faccenda, 2021) have demonstrated that neglecting seismic anisotropy introduces abundant artifacts in the tomographic image, thus compromising its correct interpretation (Figure 1.4), most tomographic methods rely on the assumption of an isotropic Earth's interior. Figure 1.4(a-f), adapted from Bezada et al. (2016), shows the results of inverting anisotropic delays when considering (Figure 1.4b,e) the true anisotropy or (Figure 1.4c,f) in isotropic approximation, compared with (Figure 1.4a,d) the "true" model. Similarly, Figure 1.4(g-n), adapted from VanderBeek and Faccenda (2021), exhibits the results of purely isotropic inversion of (Figure 1.4g,h,k,l) isotropic and (Figure 1.4i,j,m,n) anisotropic delays. Bezada et al. (2016) show that some of these artifacts may subject to misinterpretations, and suggest

caution when interpreting isotropic velocity models when studying areas where seismic anisotropy is known to be strong (e.g., subduction zones). The authors demonstrate that imaging artifacts can be substantially damped even from coarse approximations of seismic anisotropy. VanderBeek and Faccenda (2021), using teleseismic P-wave delays, have demonstrated that both dip and azimuth of anisotropic fabrics are necessary to correctly image both isotropic structures and anisotropic patterns in the upper mantle. For example, isotropic or azimuthal assumptions result in low-velocity artifacts particularly behind the slab (Figure 1.4i,j,m,n) that are similar to those imaged in several real subduction areas (e.g., Bodmer et al., 2018; Hawley et al., 2016; Li & Van Der Hilst, 2010; Portner et al., 2017). Moreover, considering only the azimuthal component results in spurious anisotropic fabrics, where the true anisotropic patterns are inclined, that are eliminated when considering the dip of anisotropic structures.

To improve the interpretation of seismic signals and, from these, to obtain information on anisotropy and therefore on mantle flow patterns, we can use geodynamic numerical models. In the last decades, numerical methods had increasingly widespread applications and together with mineral physics and seismology, they represent an important tool to investigate upper mantle seismic anisotropy. The main advantage of numerical modelling is the possibility of simulating, and therefore observing, phenomena that occur in nature over millions of years (e.g., plate motion, orogeny, subduction, slab retreat, opening of new oceanic basins, etc).

Here, I use the recent methodology proposed by Faccenda (2014) and Faccenda and Capitanio (2012, 2013), which uses the 3-D and time-dependent mantle flow to compute strain-induced fabrics, as a function of the deformation mechanisms. In this way, I quantify mantle fabrics and seismic anisotropy due to LPO in 2-D and 3-D geological settings (i.e. primarily subduction zones). The elastic tensors obtained during the modelling phase are then

used for seismological simulations, such as anisotropic P- and S-wave travel time tomography, partitioned waveform inversion of S and surface waves, shear wave splitting, etc.

This Thesis is structured as the following: the methodologies used for geodynamic and seismological modelling are described in Chapter 2, with more details presented in the subsequent and more specific chapters. The geodynamic simulations aiming at improving strain-induced fabrics predictions through comparisons with laboratory experiments and seismological observations are described in Chapter 3. The different numerical approaches tested for solving forward and inverse problems and for more reliably recovering isotropic structures and anisotropic patterns, thus reducing tomographic artifacts are presented in the following chapters. These methods (e.g., P- and S-wave travel time tomography) were tested both with real and synthetic data. For example, in Chapter 4 I presented the first anisotropic tomographic image of the upper mantle in the Central Mediterranean, obtained by inverting P-wave delay times from teleseismic events reported by the International Seismological Centre. I observed that the primary effect of including anisotropic parameters in the inversion is to reduce the magnitude of low velocity anomaly artifacts present in purely isotropic images. In Chapter 5 I performed seismological forward and inverse simulations by testing different types of parameterization (e.g., isotropic or anisotropic), receiver distribution and data quality on a 3-D synthetic scenario that reproduces the Central-Western Mediterranean region. I observed that anisotropic P-wave tomography is a powerful tool to investigate upper mantle structures and flow, although the reliability of the solution strongly depends on data quality and coverage. Then, similarly to what VanderBeek and Faccenda (2021) have done with teleseismic P-wave time delays, in Chapter 6 I performed isotropic and anisotropic inversions using teleseismic S-wave time delays from a 3-D

synthetic subduction zone. In this way, I evaluated the effect that the iso-
tropic assumption has on S-wave tomography. Furthermore, I explored how
a specific coordinates system in which S-wave arrival times are measured
(e.g., radial, transverse or polarization) affects the imaging result. In Chapter
7 I used the spectral elements method to calculate synthetic shear and sur-
face wavefields and performed automatic partitioned waveform inversion to
recover S-wave velocity and radial anisotropy in a 3-D model resembling an
oceanic scenario with a ridge in the middle and two subduction zones on the
western and eastern sides, respectively. By comparing the results of the syn-
thetic inversions (e.g., Chapter 5, 6 and 7), with the target model (i.e. the ge-
odynamic model), I evaluated limits and capabilities of the many numerical
approaches employed. Finally, the results of this work have been discussed
in the concluding Chapter 8 that integrates the main deductions and findings
on seismic anisotropy in the upper mantle with possible future perspectives.
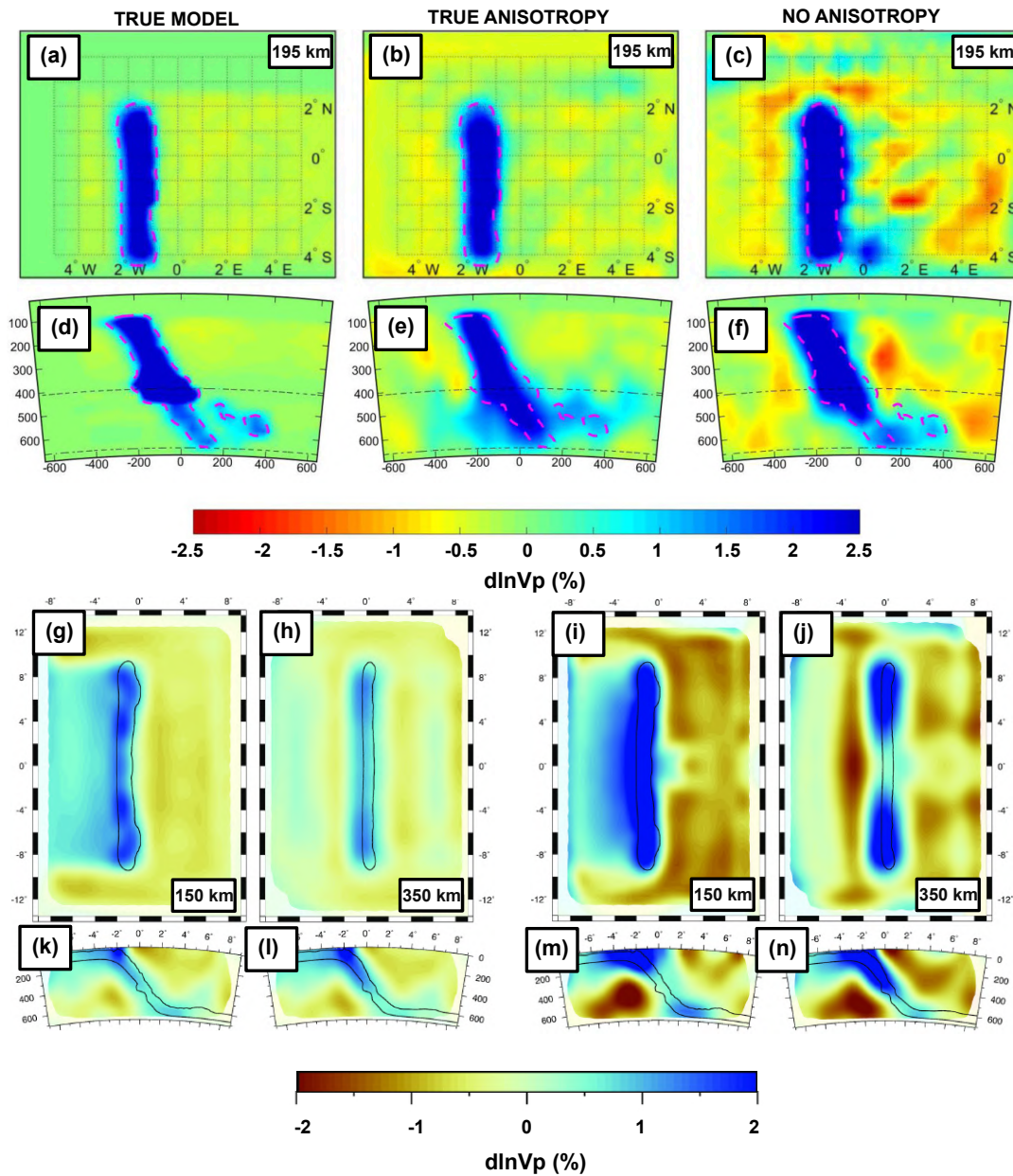
Figure 1.4: *Results of inverting anisotropic delays while using (b,e) the true anisotropy field or (c,f) no anisotropy as a priori constraints, and the "true" model for comparison (a,d). (a-c) represent depth slices at 195 km depth, (d-f) represent East-West cross-sections at 0.25°S from a 3-D subduction model. Adapted from Bezada et al. (2016). Isotropic inversion of isotropic data (g,h,k,l) and isotropic inversion of anisotropic data (i,j,m,n). Depth slices at (g,i) 150 km and (h,j) 350 km depth, cross sections at (k,m) 0°N and (l,n) 4°30S for a 3-D subduction model analogous to that of Bezada et al. (2016). The 1% isotropic velocity contours for the true models are drawn in (a-f) magenta and (g-n) black dashed lines for reference. Adapted from VanderBeek and Faccenda (2021)*

Chapter 2

METHODS

The present work involved the use of a combined numerical approach including geodynamic, seismic forward and inverse modelling. Initially I have explored parameter sensitivity on simulations of strain-induced LPO for a single crystal aggregate with a composition relevant for ultramafic lithologies. Then, by considering a geodynamic model resembling a tectonic setting extending from the ridge to the trench composed by thousands of these aggregates, I estimated mantle fabrics and seismic anisotropy in a larger context. I tested the mechanical response of the system (i.e. single aggregate or multi aggregate) when subject to the velocity field generated by the geodynamic modelling. Successively, the resulting elastic tensors were used for seismological tests such as seismic wave propagation (i.e. forward modelling) and inversion (i.e. tomography) using different numerical techniques, primarily to improve the retrieval of seismic anisotropy and to estimate the effect that neglecting seismic anisotropy has on the tomographic result.

Below a more detailed description of the principal methods and a list of the main software used for this Thesis.

2.1   2-D Geodynamic modelling - software I2VIS

In geodynamics, numerical modelling has become an essential tool for exploring processes in the Earth's mantle. Its greatest advantage is to allow the

simulation of events (e.g., plate movement, subduction, mantle dynamics, etc) that in nature occur over millions of years, in a few hours or days.

In the following paragraphs I describe the numerical method used for the 2-D numerical modelling. The 3-D geodynamic models that will be presented in the following chapters to discuss seismological synthetic tests are based on the same numerical methodology, although extended for the additional third dimension. Since the three-dimensional modelling has been performed by other co-authors, it will not be discussed in this section. The reader is invited to address to Gerya (2019) and Lo Bue et al. (2021) for a more detailed description.

I model oceanic plate formation, spreading and subsequent subduction with I2VIS (Gerya & Yuen, 2003) that is based on the finite difference method and the marker-in-cell technique. The finite difference method (Patankar, 2018) is a numerical approach used for solving partial differential equations within a certain degree of accuracy. Given a quantity ψ for which we want to compute the first partial derivative with respect to the x-coordinate, the finite difference approach suggests that:

$$\frac{\partial \psi}{\partial x} \approx \frac{\Delta \psi}{\Delta x} = \frac{\psi_2 - \psi_1}{x_2 - x_1} \tag{2.1}$$

where 1 and 2 indicate two points of the calculation grid whose mutual distance influence the accuracy of the solution. The finer is the mesh, i.e. the closer are the points, the more realistic the approximation $\partial \psi \approx \Delta \psi$ is and the more accurate the derivative will be. The same approach can be used for higher-order partial derivatives by computing their value at each point of the grid using lower-order derivatives.

For the present work, I used two different numerical meshes, one with fixed and not deformable points and one with moving and deformable points,

i.e., the *Eulerian* and *Lagrangian* grid, respectively. It is worth noting that using two grids means having two formulations for each phenomena we want to model, hence given a specific variable its derivative can be written in both the Eulerian and Lagrangian form. Therefore, which are the advantages of a double grid? The Eulerian grid is subjected to numerical problems when solving for advection of physical properties through the computational domain. The Eulerian form of the advection equation is (Gerya, 2019):

$$\frac{\partial A}{\partial t} = - \overrightarrow{v} \cdot grad(A) \tag{2.2}$$

where A is a scalar quantity and $\overrightarrow{v}$ is the velocity. Solving this equation causes numerical diffusion that smooths sharp gradients (Gerya, 2019). To minimize this artifact, the most common modelling approach is to use a combination of Lagrangian and Eulerian points and the mutual interpolation of the properties. The Lagrangian particles are in fact free to advect as a function of the velocity field interpolated from the Eulerian grid, and only after the advection the physical properties are interpolated to the Eulerian points. In literature, this is known as the marker-in-cell technique.

The main processes occurring in the Earth's mantle are well described and approximated by three fundamental equations of continuum mechanics that are the mass (eq. 2.3), momentum (eq. 2.4) and energy (eq. 2.5) conservation equations. The continuity equation (eq. 2.3) expresses the conservation of mass taking into account the fact that in numerical modelling the medium (i.e. the mantle) has to be considered *continuous*, that means that no voids are allowed to be present within the material. Derived from the second Newton's law of motion, the momentum equation (eq. 2.4) balances the internal and external forces to which a medium is subjected, and relates these forces to the resulting deformation. Lastly, considering that heat plays an important role in influencing mantle dynamics, temperature changes has to be considered

in such geodynamic studies, by solving the heat conservation equation (or simply conservation of energy, eq. 2.5). The original code has been modified to solve the conservation equations as needed in Cartesian or polar coordinates. In a Lagrangian reference frame, assuming incompressibility (Boussinesq approximation), and in Cartesian coordinates, these equations take the form:

$$\nabla \cdot \vec{v} = 0 \tag{2.3}$$

$$-\nabla P + \nabla \cdot \tau = -\rho \vec{g} \tag{2.4}$$

$$\rho C_p \frac{DT}{Dt} = -\nabla \cdot \vec{q} + H \tag{2.5}$$

where $\vec{v}$ is the velocity ($\vec{v} = (v_x, v_y)$), P pressure, τ deviatoric stress, ρ density, $\vec{g}$ gravitational acceleration, C_p specific heat capacity, T temperature, D/Dt time derivative, $\vec{q}$ heat flux and H is heat source term accounting for radiogenic, adiabatic and shear heating.

To model the mantle mechanical behaviour a visco-plastic rheology based on deformation invariants (Ranalli, 1995) is used. I use the Plagioclase An$_{75}$ flow law reported in Ranalli (1995) for the oceanic crust. The effective ductile viscosity for the mantle is given by the harmonic average of the combined dislocation, diffusion and Peierls creep mechanisms (parameters and physical meaning are defined in Table 2.1):

$$\eta_{ductile} = \left(\frac{1}{\eta_{disl}} + \frac{1}{\eta_{diff}} + \frac{1}{\eta_{peierls}} \right)^{-1} \tag{2.6}$$

where the dislocation and diffusion creep are given by Karato and Wu (1993):

$$\dot{\varepsilon}_{II} = A \left(\frac{\tau_{II}}{\mu} \right)^n \left(\frac{b}{d} \right)^m exp \left(-\frac{E + PV}{RT} \right) \tag{2.7}$$

$$\eta = \frac{\tau_{II}}{2\dot{\varepsilon}_{II}} \tag{2.8}$$

where τ_{II} and $\dot{\varepsilon}_{II}$ are the second invariant of the deviatoric stress and strain rate tensors.

At deviatoric stresses $> 0.1 GPa$ and low-T conditions, creep is accommodated via the Peierls mechanism as Katayama and Karato (2008):

$$\eta_{peierls} = 0.5 A \tau_{II}^{-1} exp \left\{ \frac{E + PV}{RT} \left[1 - \left(\frac{\tau'_{II}}{\sigma_{Peierls}} \right)^p \right]^q \right\}. \tag{2.9}$$

A pseudo-plastic viscosity is computed as:

$$\eta_{pl} = \frac{\tau_y}{2\dot{\varepsilon}_{II}} \tag{2.10}$$

where the plastic strength τ_y is determined with a plastic Drucker–Prager criterion:

$$\tau_y = C_{DP} + \mu P \tag{2.11}$$

with $C_{DP} = C \cos \phi = 1 MPa$ being the cohesion, $\mu = \sin \phi$ the friction coefficient and ϕ the friction angle.

Finally, the effective viscosity is given by:

$$\eta_{eff} = min(\eta_{ductile}, \eta_{pl}) \tag{2.12}$$

Table 2.1: *Reference physical parameters used in I2VIS simulations.*

Physical Meaning	Symbol	Unit
Pre-exponential factor	A	s^{-1}
Activation energy	E	$kJmol^{-1}$
Activation volume	V	cm^3mol^{-1}
Stress exponent	n	-
Grain-size exponent	m	-
Peierls stress*	$\sigma_{Peierls}$	GPa
Exponent	p,q	-,-
Gas constant	R	$Jmol^{-1}K^{-1}$
Shear modulus	μ	GPa
Burger vector	b	nm
Grain size	d	mm

2.2   Strain-induced LPO modelling - software D-Rex_S

To test the evolution of mantle fabrics and related elastic properties, our work started from studies on a single crystal aggregate of olivine or combinations of olivine and enstatite (olivine:enstatite = 70:30 in volume proportion, mimicking a harzburgitic composition) by imposing a gradually increasing shear-strain. Anisotropy as function of the flow field, amount of strain, crystal plasticity and P-T conditions is here computed with the D-Rex_S software included in the package ECOMAN, a modified version built from the original D-Rex by Kaminski et al. (2004). By performing microscale simulations I aimed at better calibrating the choice of the D-Rex_S parameters, i.e. efficiency of grain boundary migration (*M*), grain nucleation (λ), volume fraction threshold below which no dislocation creep occurs (χ) and normalized reference resolved shear stresses of the anisotropic phase slip systems (nRRSS). Before deformation, the orientation of the N aggregates forming grains is random and mechanically isotropic. By imposing a gradually increasing deformation, the grains undergo rotation, controlled

by intracrystalline slip, dynamic recrystallization and grain boundary sliding (GBS). Small grains are mainly deformed by GBS, instead of dislocation creep. If the volume fraction of a specific grain goes below that threshold (χ), the crystal does not deform by intracrystalline plasticity. The larger is the threshold, the bigger is the contribution of GBS in deforming the aggregate. χ equal to 0 means 100% dislocation creep, while χ equal to 1 means 100% grain boundary sliding which would lead to no LPO.

The deformation rate of each grain ν is described by the following formula (Kaminski et al., 2004)

$$d_{ij}^{\nu} = G_{ij}\gamma^{\nu} - \epsilon_{ijk}\omega_k^{\nu} \qquad (2.13)$$

where d_{ij}^{ν} is a local velocity gradient tensor, ω_k^{ν} the rotation rate of the crystallographic axes, used to quantify the change of orientations, γ^{ν} the rate of slip on the weakest slip system, used to estimate strain energy, and G_{ij} is (Ribe & Yu, 1991)

$$G_{ij}^{\nu} = 2\sum_{s=1}^{S}(\beta_{ij}^{sv}l_i^{sv}n_j^{sv}) \qquad (2.14)$$

where s is the slip system, l_i^{sv} and n_j^{sv} are unit vectors in the slip direction and normal to the slip plane, and β_{ij}^{sv} controls the activity of the slip systems of each phase. The imposed external velocity gradient tensor D_{ij} is accommodated by each crystal according to the orientation and RRSS of the different slip systems. The quantities γ^{ν}, ω_k^{ν}, are then analytically calculated by minimizing the difference between the local crystal velocity gradient tensor d^{ν} and the imposed global ij velocity gradient tensor D_{ij} (Kaminski & Ribe, 2001). It is worth noting that the RRSS values change not only among different mineral phases but also with the variation of physical and chemical conditions. For this reason, laboratory experiments (Bai et al., 1991; Durham & Goetze, 1977; Hanson & Spetzler, 1994; Jin et al., 1994; Kohlstedt & Goetze,

1974; Raleigh et al., 1971) have been often performed aiming at measuring these values for different phases, water content and P-T conditions (see Table 2.2).

Table 2.2: *Reference dimensionless resolved shear stress from laboratory experiments (e.g., Bai et al., 1991; Durham & Goetze, 1977; Hanson & Spetzler, 1994; Jin et al., 1994; Kohlstedt & Goetze, 1974; Raleigh et al., 1971). The symbol inf indicates an inactive shear plane.*

nRRSS from laboratory experiments (Kaminski et al., 2004)				
Mineral	(010)[100]	(001)[100]	(010)[001]	(100)[001]
Olivine A-type	1	2	3	inf
Olivine B-type	3	2	1	inf
Olivine C-type	3	2	inf	1
Enstatite	inf	inf	inf	1

The same numerical procedure was applied to a larger scale, by considering a geodynamic model ideally composed by thousands of aggregates arranged on a Lagrangian grid, from the surface down to 400 km depth. The system undergoes external deformation expressed by the velocity field output from the geodynamic simulations (see section 3.2.1). Strain-induced mantle fabrics develop and particles advection occurs at each strain increment. LPO fabrics are calculated down to 400 km depth, below which upper mantle particles enter the transition zone and LPO fabrics are reset, i.e., the aggregates are randomly oriented and their composition changes to spinel and majoritic garnet crystals. It is worth noting that strain-induced LPO is computed only for the fraction of deformation accommodated by dislocation creep $f_{disl} = \eta_{eff}/\eta_{disl}$. As will be discussed in the next chapters, when considering a 2-D geodynamic model resembling the Earth from the ridge to the trench, f_{disl} is high in hot mantle regions close to the oceanic plate and subjected to high deviatoric stresses. Finally, to obtain the elastic properties of the entire geodynamic model, I compute for each crystal aggregate the elastic tensor scaled by the local P-T conditions as a function of the grain size, orientation and modal composition, and of the local P-T conditions.

2.3 Seismology

2.3.1 Forward problem: The shortest path algorithm

For its simplicity and efficiency ray theory is one of the most popular methodologies for forward calculations in seismic tomography. This approach involves the use of a grid that discretizes the study volume, i.e. the Earth or a chunk of it. Following Fermat's principle, the shortest path algorithm (Moser, 1991) calculates raypaths and travel-times of first arrivals and, if needed, later arrivals at every point of the grid inside the main study area. Outside I applied the TauP method by Crotwell et al. (1999) described in section 2.3.2.

The shortest travel-time is calculated using Dijkstra's algorithm (Dijkstra et al., 1959), through Bellman's equation (Bellman, 1958):

$$tt(i) = min_{j \neq i}[tt(j) + d_{ij}] \tag{2.15}$$

with $i, j \in N$, where i and j are nodes, with j preceding i, $tt(i)$ is the shortest path from the source node s to i and d_{ij} is a matrix of weights for every single arc connecting neighboring nodes.

Starting from the source, where $tt(s) = 0$, the Dijkstra's algorithm gradually builds a shortest path tree. In agreement with equation 2.15 the travel-times of all nodes connected with s are calculated. Among them, the shortest path is found and the algorithm proceeds moving to the next neighboring nodes. The procedure continues until the number of known travel-times is equal to the number of nodes.

In this way, with a computational time linearly proportional to the number of nodes (Moser, 1991), we obtain the shortest path connecting the source to a point on the Earth's surface (i.e., usually where the receiver is placed).

2.3.2   Forward problem: The TauP method

To predict raypaths and travel-times through a 1-D velocity and density model
that well approximate the elastic properties of the Earth in the volume out-
side the main study area I used the TauP Toolkit (Crotwell et al., 1999).

Developed by Buland and Chapman (1983), the *TauP* method takes its
name from the domain in which it works. τ is the zero-distance intercept
and p the slope of the tangent to the travel-time curve at a specific distance.
The algorithm can be summarized in the following steps: (i) sampling the
velocity-depth model in slowness (i.e. the inverse of velocity); (ii) getting
distance and time increments for depth ranges by integrating the slowness;
the sum of these depth ranges along a particular path results in the corre-
sponding range of the travel-time curves; (iii) given a specific phase (e.g., P
or S), summing all the travel-time curves along the path; (iv) finally, the time
of the exact distance of interest is obtained through an interpolation between
time-distance samples.

The medium slowness is

$$u(z) = v^{-1}(z)d^{obs} \tag{2.16}$$

and the horizontal and vertical ray slowness are

$$p = \frac{sin((i)z)}{v(z)} \tag{2.17}$$

$$q(p,z) = (u^2(z) - p^2)^{1/2} \tag{2.18}$$

where $i(z)$ is the incident angle, the angle between the direction of ray
propagation and the vertical. Finally, the ray slowness vector is

$$\mathbf{p}(x,z) = p\widehat{x} \pm q\widehat{z} \tag{2.19}$$

with $+$ for un up-going and $-$ for a down-going segment. Hence, the integrated travel-time along the total raypath is

$$T(p) = \oint \frac{u^2(z)dz}{q(p,z)} \tag{2.20}$$

and the delay time function

$$\tau(p) = \oint q(p,z)dz \tag{2.21}$$

2.3.3 Forward problem: software SPECFEM3D GLOBE

To simulate three-dimensional seismic wave propagation through the geo-dynamic model domain I used the software package SPECFEM3D GLOBE. This code is largely used in seismology and is based on the spectral element method (SEM) to solve forward problems (Tromp et al., 2008). The first step of the forward calculation involves the subdivision of the 3-D domain Ω into n elements Ω_e where $e = 1, 2, 3, ..., n$. For this purpose I used the internal spectral-element mesher of SPECFEM3D that allows for regional or global simulations. The meshing methodology is based on the cubed-sphere approach (Ronchi et al., 1996; Sadourny, 1972) that breaks the globe in 6 chunks, further divided in mesh slices. Next, one can interpolate any Earth's velocity model to the grid. In our specific case I interpolated the one predicted by geodynamic models as described in section 3.2.1 and 2.2. SPECFEM3D GLOBE doesn't allow to use external models (i.e. non-built-in models), therefore I wrote a FORTRAN routine that makes user defined models (e.g., the output of D-Rex) readable by the SPECFEM3D mesher.

Given the large amount of computational work to be done and required memory, multiple computational units are necessary to calculate seismic waves that propagate in such large models and with the resolution required by our studies. For this reason, I implemented the method on parallel computers

and let each processor work on specific elements of a mesh slice. I used the High-Performance-Computing (HPC) resources of the CINECA Marconi 100 cluster.

Since the accuracy of the forward problem depends on the number of grid nodes, an important part of this step involves choosing of the number of spectral elements (i.e. the number of nodes) along each horizontal side of the Earth's chunk. For a regional simulation, the shortest period resolved (T_{min}) is in fact derived from the following formula:

$$T_{min} = \frac{256}{NEX_{XI}} \frac{XI}{90} \times 17 \tag{2.22}$$

where NEX_{XI} is the number of spectral element along the E-W axes and XI is the angular width in degrees. Through the input file the user also defines NEX_{ETA}, that is the number of elements along the N-S axes, while the vertical resolution is automatically derived by the mesher itself so that its size increases with depth and is doubled at the main discontinuities (i.e. Moho, 670 km and core-mantle-boundary, CMB).

Once the mesh has been generated, the solver computes the waveforms. Given an Earth's model volume Ω, the seismic wave equation is (Aki, 1980; Dahlen & Tromp, 2021)

$$\mathbf{f} = \rho \delta_t^2 \mathbf{s} - \nabla \cdot \mathbf{T} \tag{2.23}$$

where $\mathbf{s}(\mathbf{x},t)$ denotes the displacement, function of the material points $\mathbf{x}$ and time t, the force $\mathbf{f}$ represents the earthquake, ρ the mass density and T the stress, calculated from the linear constitutive low as

$$T_{ij} = c_{ijkl} \epsilon_{kl} \tag{2.24}$$

where c_{ijkl} is the forth order elastic tensor in index notation. It is worth

noting that in isotropic approximation the tensor **c** is given by only two elastic parameters (i.e. bulk and shear modulus). In this study I removed such approximation, considering the Earth as a fully anisotropic body defined by all the 21 elastic coefficients.

At the initial conditions, where $\mathbf{s}(\mathbf{x},0) = 0$ and $\delta_t\mathbf{s}(\mathbf{x},0)$, equation 2.23 can be written in terms of moment tensor **M** to represents the earthquake as follows (Aki, 1980; Dahlen & Tromp, 2021)

$$\mathbf{f} = -\mathbf{M} \cdot \nabla\delta(\mathbf{x} - \mathbf{x}_s)S(t) \tag{2.25}$$

where $\delta(\mathbf{x} - \mathbf{x}_s)$ is the Dirac Delta distribution at point $\mathbf{x}_s$ and $S(t)$ is the source-time function.

Our work only involved regional simulations and to avoid artifacts introduced by seismic effects produced at the model edges, I applied Perfectly Matched Layer (PML; Berenger, 1994) absorbing boundary conditions at the sides of the chunk.

2.3.4   Inverse problem: P- and S-wave anisotropic travel time tomography

P-wave travel time tomography is probably the most common method used to image the Earth's interior. Given their ability to constrain anisotropic patterns, P-wave delay times (i.e. the difference between observed travel time and predicted travel time through a reference model) are perfect input data for resolving large-scale features in anisotropic regions of the mantle. Here, I shortly describe the methodology proposed VanderBeek and Faccenda (2021). The authors present a new parametrization for imaging isotropic upper mantle structures and arbitrarily oriented hexagonal anisotropy.

For a hexagonally symmetric media the directional dependence of P-wave velocity can be approximated by a periodic function of 2α and 4α, given α

the angle between the symmetry axes and the wave propagation direction (Backus, 1965; Thomsen, 1986). Considering that in the mantle 4α is an order of magnitude smaller than 2α, P-wave velocity can be approximated as:

$$v = \overline{v}[1 \pm f\cos(2\alpha)] \tag{2.26}$$

where $\cos(2\alpha)$ is equal to the dot product of the ray directional vector and the anisotropic symmetry axis vector. Thus, we have:

$$v = \overline{v}[1 \pm f(2[\cos(\theta)\cos(\gamma)\cos(\phi - \psi) + \sin(\theta)\sin(\gamma)]^2 - 1)] \tag{2.27}$$

where $\overline{v}$ is the isotropic velocity, f the fractional magnitude of the velocity variations whose sign indicates whether the symmetry axis is the fast or the slow one, and it is decided by the user before starting the inverse process. θ and γ are elevation and ϕ and ψ are azimuth of the ray and symmetry axis, respectively.

VanderBeek and Faccenda (2021) propose a parametrization that, although non-linear, separately manages variables of the symmetry axis controlling azimuth and magnitude from that controlling elevation. The main advantage of this method is the possibility of using a purely isotropic starting model from which estimating in a first step azimuthal anisotropy, and subsequently dip anisotropy. Alternative methods exist for for azimuthal and dip anisotropy inversions, but require anisotropic starting models already close to the final solution (Munzarová et al., 2018).

By introducing three anisotropic terms,

$$A = (n_1^2 - n_2^2) \tag{2.28}$$

$$B = 2n_1 n_2 \tag{2.29}$$

$$C = n_3 \tag{2.30}$$

where n is the symmetry axis vector, VanderBeek and Faccenda (2021) rewrite equation 2.27 in terms of slowness u as follows

$$
\begin{aligned}
u = \overline{u}[1 \pm ([A\cos(2\phi) + B\sin(2\phi)]\cos^2(\theta) - G\sin^2(\theta) - C^2\cos(2\theta) \\
+\sqrt{2}C[s_1(G+A)^{1/2}\cos(\phi) + s_2(G-A)^{1/2}\sin(\phi)]\sin(2\theta))]^{-1}
\end{aligned}
\tag{2.31}
$$

where $G = \sqrt{A^2 + B^2}$ and $s_1 = sign(n_1)$, $s_2 = sign(n_2)$ to avoid sign ambiguity. One can recover the spherical anisotropic parameters of equation 2.27 as $f = G + C^2$, $\psi = \arctan[B/(G+A)]$ and $\gamma = \arctan[C/G^{1/2}]$.

The next step is calculating the partial derivatives of the travel time with respect to the slowness and the three anisotropic parameters from equation 2.31. The obtained system of equations is solved using the LSQR approach (Paige & Saunders, 1982) but given the high number of unknowns (i.e. $4 \times$ *#nodes*), regularization through damping and smoothing factors is required to solve the ill-posed problem. In the next chapters we will see several examples of ill-posed problems and how a proper regularization, subject to damping and smoothing factors, helps to solve them.

Unlike P-waves, S-waves travelling through an anisotropic medium split into two orthogonally polarised quasi-shear waves propagating at different velocities. Here I shortly describe a novel approach that, similarly to what VanderBeek and Faccenda (2021) have done with P-waves, inverts S-wave travel times to image upper mantle anisotropy. The method is addressed

more in detail in Chapter 6. In brief, ray theory is not valid for independently tracing the quasi-shear phases generated by splitting (Coates & Chapman, 1990), no simple strategy exists for modelling such travel-times in a ray-theoretical framework. Because of splitting the final waveform recorded at the receiver contains two arrivals within the frequency range of S-waves. It is not clear which of these two quasi-shear wave arrivals, thus which travel-time related to the anisotropic properties along the ray path, should be measured to allow for a linearesed inverse scheme. I propose to invert S-wave travel-times measured in the direction of the initial linear polarisation. This decision is based on the consideration that anisotropy does not significantly perturb the incoming wavelet for small splitting times relative to its period (Chevrot, 2000; Silver & Chan, 1988; Vinnik et al., 1989) and on the assumption that the polarisation of a shear wave is and remains approximately linear as it propagates through the imaging volume.

The isotropic velocity of the two orthogonal quasi-shear waves (v_1 and v_2) through an anisotropic layer can be approximated as periodic functions of 2α and 4α where, similarly to eq. 2.26, α is the angle between the hexagonal symmetry axis and the S-wave ray path.

$$v_1 = \overline{v_1}[1 \pm g \cos(2\alpha)] \tag{2.32}$$

$$v_2 = \overline{v_2}[1 \mp h \cos(4\alpha)] \tag{2.33}$$

where g and h are the fractional magnitude of the velocity variations associated with the 2α- and 4α-cosines, respectively. Noting that $\cos(2\alpha)$ is given by the dot product between the ray unit vector and the anisotropic symmetry axis unit vector, we can expand equations 2.32 and 2.32 as a function of the symmetry axis azimuth ψ and elevation γ as,

$$v_1 = \overline{v_1}[1 \pm g(2[\cos(\theta)\cos(\gamma)\cos(\phi - \psi) + \sin(\theta)\sin(\gamma)]^2 - 1)] \qquad (2.34)$$

$$v_2 = \overline{v_2}[1 \mp h(8[\cos(\theta)\cos(\gamma)\cos(\phi - \psi) + \sin(\theta)\sin(\gamma)]^4$$
$$-8[\cos(\theta)\cos(\gamma)\cos(\phi - \psi) + \sin(\theta)\sin(\gamma)]^2 + 1)] \qquad (2.35)$$

where ϕ and θ are the ray elevation and azimuth, respectively. In the direction of polarization the shear-wave velocity is

$$v = \frac{v_2 + v_1}{2}\left[1 + \frac{v_2 - v_1}{v_2 + v_1}\cos(2\omega - 2\psi')\right] \qquad (2.36)$$

where ω is the angle of shear wave polarisation and ψ' is the orientation of the symmetry axis projected into the ray-normal plane.

Equation 2.34 and 2.35 can be rewritten as

$$v_1 = \overline{v_1}[1 \pm (Q - G - C^2)] \qquad (2.37)$$

$$v_2 = \overline{v_1}\frac{1 \pm g}{1 \mp gr_{hg}}\left[1 \pm r_{hg}\left(\frac{2}{g}Q^2 - 4Q + G - C^2\right)\right] \qquad (2.38)$$

where Q is

$$Q = [A\cos(2\phi) + B\sin(2\phi) + G]\cos^2(\theta) + 2C^2\sin^2(\theta)+$$
$$\sqrt{2}C[s_1(G + A)^{1/2}\cos(\phi) + s_2(G - A)^{1/2}\sin(\phi)]\sin(2\theta)] \qquad (2.39)$$

and $G = \sqrt{A^2 + B^2}$ and A, B and C are the three anisotropic terms already described for the P-wave tomography (i.e., eq. 3.12, 2.29, 3.13).

Chapter 3

MICRO- AND MACRO-SCALE GEODYNAMIC AND SEISMOLOGICAL NUMERICAL MODELLING FOR SEISMIC ANISOTROPY STUDIES

Abstract

Through a comparison with laboratory experiments and seismological observations (i.e. SKS splitting measurements), I have constrained numerical simulations aiming at estimating strain-induced seismic anisotropy at the scale of single crystal aggregates and subduction zone models. Although it is considered the most representative fabric of the upper mantle, from our study it emerged that the A-type olivine fabric does not reproduce the expected trench-parallel anisotropic response in subduction zones when steeply dipping slabs are present. I observed that the A-type olivine fabric tends to overestimate seismic anisotropy of single aggregates of olivine crystals, resulting into trench-perpendicular SKS splitting azimuths along the oceanic plate and in correspondence of the trench. With respect to the A-type, the weaker AG-type olivine fabric better fit the multiphase aggregates laboratory experiments resulting into a trench-parallel SKS splitting where vertical flow is present, i.e. above the forearc. From our study the AG-type fabric seems to represent a good approximation to model upper mantle seismic anisotropy, especially in proximity of the slab and up-welling areas. Furthermore, I observed a strong correlation between SKS splitting azimuths and delay times and the D-Rex parameters (i.e. M, λ and χ). In particular, imposing a poorly efficient dynamic recrystallization mechanism (i.e. low M and high χ) together with a harzburgitic mantle compostion (olivine:enstatite = 70:30) produces results that are more consistent with seismological observations. Our study highlights that this new calibration of the D-Rex software parameters allows to reproduce more reliably subduction zones and the related seismic response in geodynamic models. Given that seismic anisotropy is widespread in the upper mantle, I expect that better estimating strain induced fabric by combining geodynamic and seismological modelling will

improve our understanding of the oceanic Earth's mantle isotropic and anisotropic structures.

3.1 Introduction

The Earth's upper mantle is seismically anisotropic mainly due to the non-random distribution of intrinsically anisotropic minerals (Karato et al., 2008; Silver & Chan, 1991), defined as lattice-preferred orientation (LPO) or crystal-preferred orientation (CPO) (Hu et al., 2017). Among these minerals the most abundant are olivine and pyroxene which approximate the composition of most upper mantle rocks (Ringwood, 1975). Another cause of seismic anisotropy is the shape preferred orientation (SPO) of bodies with contrasting isotropic seismic velocities (Faccenda et al., 2019). Despite water content and partial melting largely influence strain-induced anisotropy, they will not be considered in the present work (Kaminski & Ribe, 2002; Karato et al., 2008). Furthermore, this study focuses on the effects due to LPO on large-scale anisotropic patterns, while SPO effects will be neglected as it has been shown that compositional layering is not relevant on Earth (Faccenda et al., 2019).

Previous studies based on seismological observations (e.g., SKS splitting, Becker et al., 2012; Long & Silver, 2009a), on laboratory experiments (Kaminski & Ribe, 2002; Karato et al., 2008; Zhang & Karato, 1995) as well as on 3-D geodynamic simulations (Faccenda & Capitanio, 2013) revealed the close correlation between deformation and seismic anisotropy. Deformation, which is direct consequence of mantle flow gradients and patterns, can induce a preferential orientation (CPO) of anisotropic minerals, yielding macroscopically anisotropic rocks. These fabrics are recorded in the seismic data, such as SKS splitting measured around subduction areas. It has been observed that SKS fast azimuths align with the direction of plate motion in oceanic areas, with a trench-perpendicular orientation, while they rotate by 90° in fore-arc areas

where the subducting plate induces descending asthenospheric flows (Long & Silver, 2008). It follows that the study of seismic anisotropy can be used as a proxy to infer the Earth's mantle flows.

Strain-induced LPO is due to dislocation glide and recrystallization processes. Deformation by dislocation motion occurs along preferential directions defined as slip directions which together with the slip plane constitute the slip system. Every slip system is uniquely characterized by the Burgers vector and by the normal to the slip plane. The preferential slip system of a crystal will depend not only on the nature of the mineral itself, but also on the conditions of temperature, pressure and water content. Hence, it is worth considering that the preferential slip system can change over time if the boundary conditions change, generating different anisotropic fabrics. Recrystallization consists in the growth of low-energy crystals at the expenses of high-energy (highly-deformed) crystals, and it manifests with the migration of crystal boundaries. According to the von Mises criterion, 5 slip systems are needed to accommodate intra-crystalline deformation. However, most of strain is typically accomodated by a single slip system that controls the LPO development (Karato et al., 2008).

Given the inaccessible nature of the Earth's mantle, starting from the 1970s numerous laboratory experiments on plastic deformation of olivine aggregates have been performed. Carter and Ave'Lallemant (1970) revealed the principal relations between P-T conditions and dominant slip system in dunites and olivine single crystals. They observed that at high temperature and low strain rate olivine develops A-type fabric with a dominant slip system [100](010). At low temperature and high strain rate the dominant slip system has Burgers vector [100] and slip plane (010) and/or (100). At intermediate values of temperature and strain rate the Burgers vector is [100] but several slip planes are active (Karato et al., 2008). Hansen et al. (2014) conducted torsional deformation experiments to examine the evolution of olivine fabrics

at high shear strain (γ up to $\sim$20). According to their results a steady-state fabric is reached with strain higher than $\sim$10. More recently Tasaka et al. (2017) conducted similar laboratory experiments on multiphase crystal aggregates of 74% olivine and 26% orthopyroxene, reaching maximum strain $\gamma = 26$ at $T = 1200°$C and $P = 300$ MPa. The authors studied the effect of phase mixing on fabric weakening. They observe that at strain ~ 4.2 olivine and orthopyroxene grains tend to elongate at low angles with respect to the shear plane, while at $\gamma \geq 17.3$ the micro-samples exhibit smaller but equant grains. They also observe the fabric strength increasing until $\gamma < 4.2$ and then decreasing as the strain increases without any variation in the induced CPO as an effect of phase-mixing.

In parallel with more advanced laboratory experiments, in recent years, technology development allowed the generation of more accurate numerical simulations in the field of geodynamics and rock physics. New software and powerful computational resources nowadays allow to numerically recreate Earth's mantle conditions (e.g., of T and P) and the consequent formation of anisotropic patterns which otherwise are impossible to observe directly. Hence, together with the study of deformed rock samples, laboratory experiments and seismological observations (e.g., SK(K)S splitting measurements), in the last decades numerical simulation became a useful tool to investigate anisotropic structures and their relation to mantle flow patterns.

In this work, I study seismic anisotropy developing in 2-D models of oceanic plate tectonic evolution from the ridge to the subduction zone. I want to obtain a more complete description of mantle flow dynamics and the related strain-induced LPO. Although the 2-D case may seem a simplification of the three-dimensional one, it well reproduces the central portions of wide tectonic plates that are dominated by poloidal flow components.

3.2   Method

Below I describe the methodologies and list the main software used for this
work. Some of them have been partially modified to be adapted to the spe-
cific case study.

3.2.1   2-D Geodynamic modelling: I2VIS

The 2-D petrological-thermo-mechanical numerical simulations were con-
ducted using I2VIS (Gerya & Yuen, 2003) based on the finite difference method
and marker-in-cell technique to solve the equations of conservation of mass
(eq. 3.1), momentum (eq. 3.2) and energy (eq. 7.4). In a Lagrangian reference
frame and assuming incompressibility these equations take the form:

$$\nabla \cdot \overrightarrow{u} = 0 \tag{3.1}$$

$$-\nabla P + \nabla \cdot \tau = -\rho \overrightarrow{g} \tag{3.2}$$

$$\rho C_p \frac{DT}{Dt} = -\nabla \cdot \overrightarrow{q} + H \tag{3.3}$$

where $\overrightarrow{u}$ is the velocity, P pressure, τ deviatoric stress, ρ density, $\overrightarrow{g}$
gravitational acceleration, C_p specific heat capacity, T temperature, D/Dt La-
grangian time derivative, $\overrightarrow{q}$ heat flux and H is heat source term accounting
for radiogenic, adiabatic and shear heating.

The model domain extends from 0 to 4000 km along the horizontal direc-
tion and for 700 km along depth, and is discretized with 1001 by 351 nodes.
The initial setup (Figure 3.1a) is composed by a left plate defined by an age
increasing from 0 Myr at the oceanic ridge to 60 Myr, and a right plate with a
constant 20 Myr age. The two plates are characterized by a 7 km thick oceanic
crust and are separated by a $\sim 30°$ dipping weak zone. A 30 km thick sticky

air layer is placed at the top to model free surface. The thermal ages are defined with the half-space cooling model (Turcotte & Schubert, 2014) for a 90 km thick layer, while below a $0.5K/km$ adiabatic gradient is imposed. Free slip velocity boundary conditions are imposed everywhere, except for the lower permeable boundary where I apply external free slip (Gerya, 2019). A convergence speed of 4 cm/yr is applied to the left plate, while the right plate is fixed. The vertical boundaries are insulating, while I impose a constant T = 273 K for the sticky air layer and T = 1890 K at the bottom boundary. The model runs for $\sim$40 Myr (Figure 3.2d).
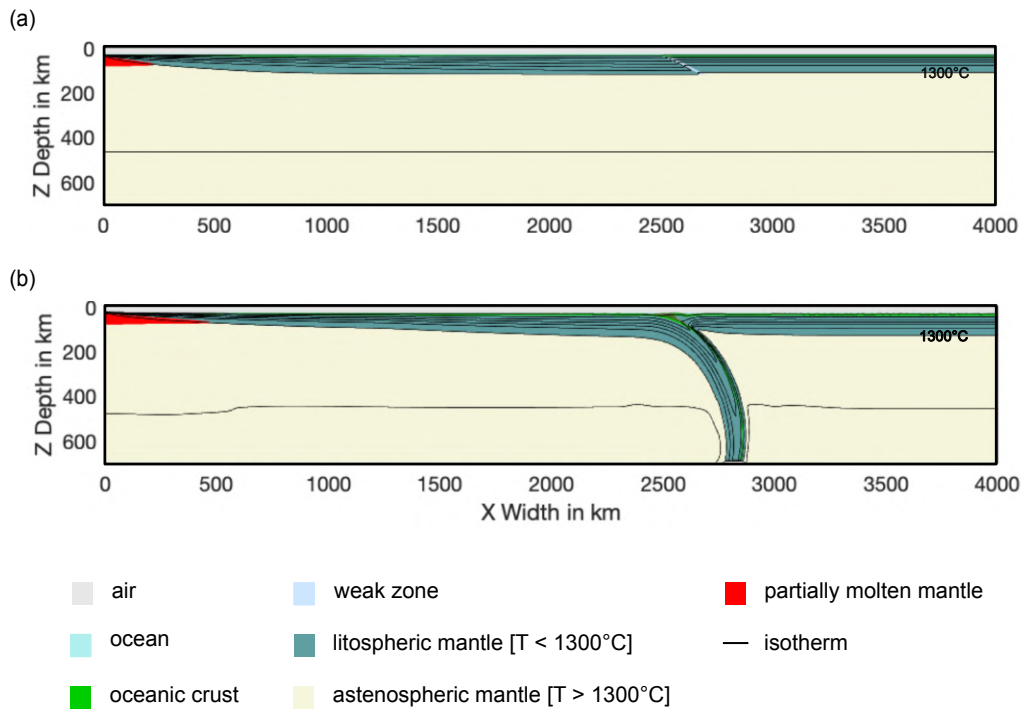
Figure 3.1: *(a) Initial model setup of 2-D oceanic plate formation at the ridge and subsequent subduction. (b) Snapshot at $\sim$29 Myr. The black lines are isotherms at every* $200°C$. *See legend*

The mechanical behaviour is defined by a visco-plastic rheological model based on deformation invariants (Ranalli, 1995). For the oceanic crust I use the Plagioclase An_{75} flow law reported in Ranalli (1995). The harmonic average of the combined dislocation, diffusion and Peierls creep mechanisms (parameters and physical meaning are defined in Table 3.1) gives the effective ductile viscosity for the mantle:

$$\eta_{ductile} = \left(\frac{1}{\eta_{disl}} + \frac{1}{\eta_{diff}} + \frac{1}{\eta_{peierls}} \right)^{-1} \tag{3.4}$$

where the dislocation and diffusion creep flow laws are given by Karato and Wu (1993):

$$\dot{\varepsilon}_{II} = A \left(\frac{\tau_{II}}{\mu} \right)^n \left(\frac{b}{d} \right)^m exp \left(-\frac{E + PV}{RT} \right) \tag{3.5}$$

$$\eta = \frac{\tau_{II}}{2\dot{\varepsilon}_{II}} \tag{3.6}$$

where τ_{II} and $\dot{\varepsilon}_{II}$ are the second invariant of the deviatoric stress and strain rate tensors.

At deviatoric stresses $> 0.1 GPa$ and low-T conditions, creep is accommodated via the Peierls mechanism as (Katayama & Karato, 2008):

$$\eta_{peierls} = 0.5 A \tau_{II}^{-1} exp \left\{ \frac{E + PV}{RT} \left[1 - \left(\frac{\tau_{II}}{\sigma_{Peierls}} \right)^p \right]^q \right\} \tag{3.7}$$

A pseudo-plastic viscosity is computed as:

$$\eta_{pl} = \frac{\tau_y}{2\dot{\varepsilon}_{II}} \tag{3.8}$$

The Drucker–Prager criterion is used to determine the plastic strength τ_y:

$$\tau_y = C_{DP} + \mu P \tag{3.9}$$

where $C_{DP} = C \cos \phi = 1$ MPa is the cohesion, $\mu = \sin \phi$ is the friction coefficient and ϕ is the friction angle. To model strain-induced brittle weakening, the initial friction 0.6 coefficient is linearly decreased to 0.4 in the $0.5 \leq \varepsilon_p \leq 1.5$ range, where ε_p is the accumulated brittle/plastic strain. For the crust I use a constant $\mu = 0.05$ to ensure lubrication at the plates contact.

Finally, the effective viscosity is given by:

$$\eta_{eff} = min(\eta_{ductile}, \eta_{pl}) \qquad (3.10)$$

The lower and upper cutoff of η_{eff} are set to 10^{18} and 10^{25} *Pa s*.

Table 3.1: *Creep parameters for mantle rocks.*

Property	Symbol	Value	Unit
Diffusion Creep (Karato & Wu, 1993)			
Pre-exponential factor	A	$8.7 \cdot 10^{15}$	s^{-1}
Activation energy	E	300	$kJmol^{-1}$
Activation volume	V	4.5	cm^3mol^{-1}
Stress exponent	n	1	-
Grain-size exponent	m	2.5	-
Dislocation Creep (Karato & Wu, 1993)			
Pre-exponential factor	A	$3.5 \cdot 10^{22}$	s^{-1}
Activation energy	E	540	$kJmol^{-1}$
Activation volume	V	17	cm^3mol^{-1}
Stress exponent	n	3.5	-
Grain-size exponent	m	0	-
Peierls Creep (Katayama & Karato, 2008)			
Pre-exponential factor	A	$10^{7.8}$	Pa^2s
Activation energy	E	532	$kJmol^{-1}$
Activation volume	V	12	cm^3mol^{-1}
Peierls stress*	$\sigma_{Peierls}$	9.1	GPa
Exponent	p,q	1, 2	-,-

$R = 8.313 \ Jmol^{-1}K^{-1}$ is the gas constant, $\mu = 80 \ GPa$ is the shear modulus, $b = 0.5nm$ is the Burger vector, $d = 1mm$ is the grain size. * (Evans & Goetze, 1979)

3.2.2   Strain-induced LPO

Strain-induced LPO development in the upper mantle is controlled by plastic deformation and recrystallization and it is here computed with the modified version of D-Rex (Kaminski et al., 2004) included in the software package ECOMAN which allows to estimate the induced LPO and the elastic properties of single-crystal aggregates as a function of the conditions of T, P, deformation mechanism, flow field and strain history.

The modelling was initially applied to a single crystal aggregate of either pure olivine or combinations of olivine and enstatite (olivine:enstatite = 70:30 in volume proportion, mimicking a harzburgitic composition) with shear-strain incremented from 0 to 25. Successively, it was applied to a larger scale on the subduction model where thousands of crystal aggregates are arranged down to 400 km. Deformation is expressed by the velocity field at $\sim$31 Myr (Figure 3.1b, Figure 3.2h) when a steady state mantle flow stage is reached and a well developed subduction is observed. With each strain increment we thus compute the strain-induced anisotropic fabrics and advection of the particles from the ridge toward the trench and beyond, down into the transition zone. LPO fabrics are reset when upper mantle particles enter the transition zone and the aggregates are composed by randomly oriented spinel and majoritic garnet crystals.

Strain-induced LPO is computed only for the fraction of deformation accommodated by dislocation creep $f_{disl} = \eta_{eff}/\eta_{disl}$ (Faccenda, 2014). As shown in Figure 3.2, f_{disl} is high in hot mantle regions close to the oceanic plate and subjected to high deviatoric stresses. The elastic properties of each crystal aggregate are finally computed as a function of the LPO and single crystal elastic tensor scaled by the local P-T conditions.

The modelling of these phenomena using the D-Rex code is regulated by three parameters which are respectively nucleation (λ), grain-boundary mobility (M) and volume threshold for activation of grain-boundary sliding (χ), and by the normalized reference dimensionless resolved shear stress (nRRSS). The choice of these parameters, decided on the basis of comparisons with laboratory experiments, is summerized in Table 3.2 and will be discussed later on.

Table 3.2: *Reference dimensionless resolved shear stress from laboratory experiments (e.g., Bai et al., 1991; Durham & Goetze, 1977; Hanson & Spetzler, 1994; Jin et al., 1994; Kohlstedt & Goetze, 1974; Raleigh et al., 1971) and D-Rex parameters used in this work. The symbol inf indicates an inactive shear plane.*

nRRSS

Mineral/fabric	(010)[100]	(001)[100]	(010)[001]	(100)[001]
Olivine A-type	1	2	3	inf
Olivine B-type	3	2	1	inf
Olivine C-type	3	2	inf	1
Olivine AG-type	1	5	1	inf
Enstatite	inf	inf	inf	1
D-Rex parameters				
test	M	λ	χ	nRRSS
Test 1	125	5	0.3	1 2 3 inf
Test 2	10	5	0.3	1 2 3 inf
Test 3	1	5	0.9	1 5 1 inf

3.2.3 SKS splitting measurements

SKS wave splitting is estimated as a function of the back-azimuth with the FSTRACK software package (Becker et al., 2006b), through the calculation of the harmonic response of an incident plane wave with an angle of 5 °, the subsequent filtering of the seismograms in the frequency band typical of SKS waves (0.1 - 0.3 Hz) and the cross-correlation method (by Menke & Levin, 2003). A virtual line of 40 equally-spaced receivers was placed on the model surface. The seismic response is calculated on a stack of horizontal layers whose number is proportional to the number of crystal aggregates found within a radius of 50 km from the vertical on the position of each individual receiver. In order to avoid the effects of too thin layers, the various elastic tensors that fell within layers up to 25 km thick were merged and weighted based on the initial radial distance. Subsequently, through an average of the fast azimuths and time delays, the SKS splitting measurements were obtained for each receiver.

3.2.4 Strength of anisotropy

For anisotropic media with orthorombic anisotropy symmetry, the elastic tensor C_{ij} can be expressed as

$$
\begin{bmatrix}
C_{11} & C_{12} & C_{13} & & & \\
C_{21} & C_{22} & C_{23} & & & \\
C_{31} & C_{32} & C_{33} & & & \\
& & & C_{44} & & \\
& & & & C_{55} & \\
& & & & & C_{66}
\end{bmatrix}
$$

with $C_{11}, C_{22}, C_{33}, C_{44}, C_{55}, C_{66}, C_{12}, C_{13}, C_{23}$ independent elastic constants and $C_{12} = C_{21}, C_{13} = C_{31}, C_{23} = C_{32}$. For such anisotropic media and considering that in our 2-D geodynamic models the y-axis is the vertical direction, one can compute the following radial anisotropy parameters

$$A = 3/8(C_{11} + C_{33}) + 1/4C_{13} + 0.5C_{55} \tag{3.11}$$

$$C = C_{22} \tag{3.12}$$

$$L = 0.5(C_{44} + C_{66}) \tag{3.13}$$

$$N = 1/8(C_{11} + C_{33}) - 1/4C_{13} + 0.5C_{55} \tag{3.14}$$

$$F = 0.5(C_{12} + C_{23}) \tag{3.15}$$

and from these the azimuthally averaged effective radial anisotropy (Montagner & Nataf, 1986) as

$$\eta_{effective} = \frac{F}{A - 2L} \tag{3.16}$$

and the strength of radial (R_p, R_s) and azimuthal (A_p, A_s) anisotropy for P and S-wave (Song & Kawakatsu, 2012), respectively, as

$$Rs = \sqrt{N/L} - 1 \tag{3.17}$$

$$Rp = \sqrt{A/C} - 1 \tag{3.18}$$

$$As = \sqrt{C_{66}/C_{44}} - 1 \tag{3.19}$$

$$Ap = \sqrt{C_{11}/C_{33}} - 1 \tag{3.20}$$

3.3 Results

3.3.1 2-D geodynamic model

The geodynamic evolution of the 2-D subduction model is shown in Figure 3.2. After an initial stage during which the oceanic plate reaches the bottom of the domain, a steady-state poloidal flow pattern characterized by mantle upwelling below the ridge, horizontal flow in the intra-oceanic region and downwelling near the subductinig slab establishes. This large scale flow pattern is locally superimposed by smaller scale convection currents forming above and below the slab to compensate mantle downwelling through the permeable bottom boundary.

3.3.2 Micro-scale strain-induced LPO

Before computing upper mantle fabrics in the 2-D subduction models, I have tested the D-Rex software fundamental parameters, already discussed in section 3.2.2 (i.e. λ, M and χ), on a single crystal aggregate with either dunitic or harzburgitic composition. These parameters where then calibrated and validated by comparison with recent high-strain experimental data.

Figure 3.3 shows the results of three numerical experiments named Test 1, Test 2, Test 3. Table 3.2 summarizes the selected parameters. Test 1 was carried out on a 100% olivine aggregate with $M = 125$, $\lambda = 5$ and $\chi = 0.3$.
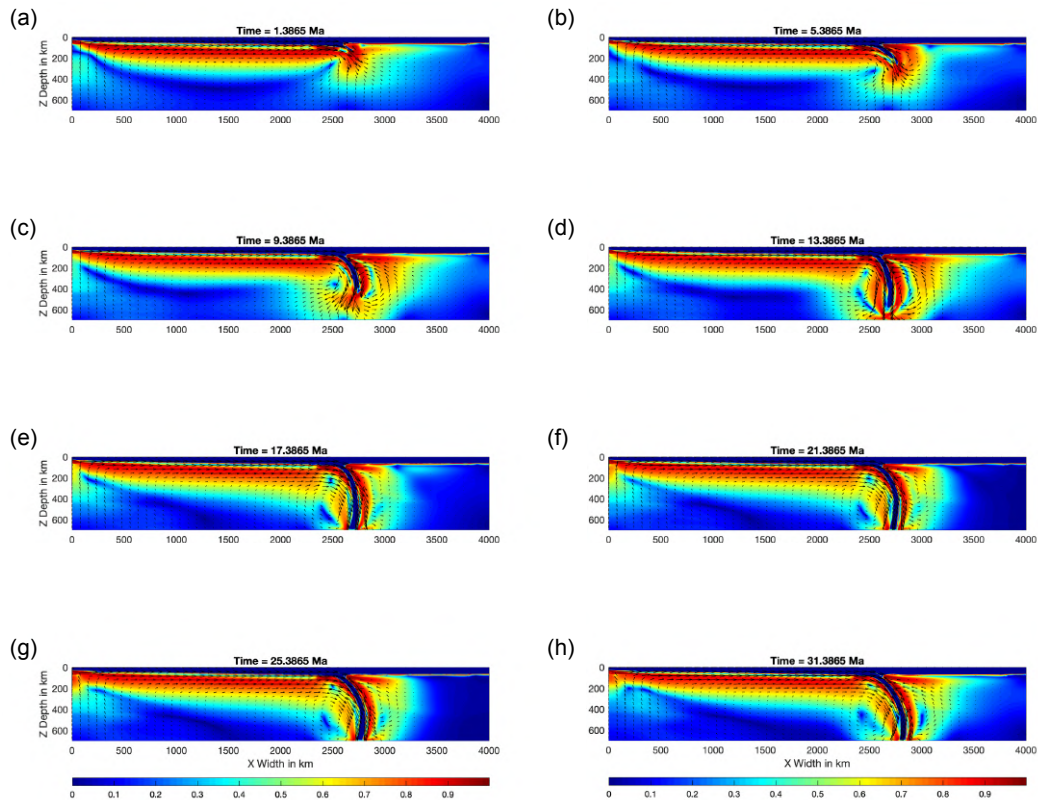
Figure 3.2: *Snapshots of the geodynamic evolution showing the fraction of dislocation creep (fd) with increasing time.*

These are the parameters initially identified by Kaminski et al. (2004) by fitting low strain deformation experiments by Zhang and Karato (1995). As can be seen in Figure 3.3(h-i), this type of parameterization reproduces a fabric that I name A-type I with dominant [100] (010) slip system (Nicolas et al., 1973; Zhang & Karato, 1995) in which the olivine fast and slow axes are oriented, respectively, parallel and normal to the shear direction. The strong fabric results in a high degree of anisotropy of the aggregate (i.e. tending toward the single crystal behavior). Test 2 was carried out on a multiphase aggregate (70% olivine + 30% enstatite) by imposing values of $M = 10$, $\lambda = 5$, $\chi = 0.3$ (Boneh et al., 2015). The test reproduces a different olivine fabric that I call A-type II (Figure 3.3j,k). Although similar to the previous case, the anisotropy magnitude is weaker. This is due to the diluting effect of orthopyroxene (whose mean fast and slow axes orient parallel to, respectively, the mean

slow and fast axes of olivine) and to the less efficient dynamic recrystalliza-
tion. Finally, Test 3 was also carried out on a multiphase aggregate of olivine
and pyroxene but imposing values of $M = 1$, $\lambda = 5$ and $\chi = 0.9$ and, more
importantly, by setting same nCRSS for the [100](010) and [001](010) slip sys-
tems. This combination of parameters reproduces the mixed AG-type olivine
fabric characterized by the presence of a girdle of [100] fast axes in the slip
plane (Figure 3.3l,m).

To validate the numerical results, micro-scale strain induced anisotropy
was compared to laboratory experiments (Hansen et al., 2014; Tasaka et al.,
2017; Warren et al., 2008). I used the scalar M-index (Skemer et al., 2005), in-
dicator of the strength of the anisotropy that is independent from the number
of measured grains. Its calculation is based on the distribution of the misori-
entation angles, i.e. on the angular difference necessary to bring two crystals
to the same orientation with respect to a common axis. Figure 3.3a shows the
evolution of the M-index with increasing strain (i.e. from $\gamma = 0$ up to $\gamma = 25$)
for Test 1, 2 and 3. Values of M-index close to 0 are typical of a random distri-
bution of the axes, thus typical of isotropic aggregates, while values close to 1
are characteristic of anisotropic single crystals. Therefore, crystal aggregates
with M-index ~ 1 indicate that the behavior of the aggregate is similar to that
of the single crystal, hence strongly anisotropic in the case of olivine.

The three curves in Figure 3.3a show the behavior of the crystal aggre-
gates for Test 1 (black line), Test 2 (green line) and Test 3 (blue line). It can be
observed that for Test 1, obtained by imposing an efficient dynamic recrystal-
lization, the value of M-index rapidly reaches its maximum (> 0.4) already
at low strains ($\gamma \cong 1$), remaining constant for the rest of the experiment. This
numerical simulation exhibits an overestimation of seismic anisotropy and
the trend of the black curve is similar to that observed by Hansen et al. (2014)
(purple dots). Test 2 and 3, which result in A-type II and AG-type fabric
respectively, show much lower M-index values, with a maximum peak at
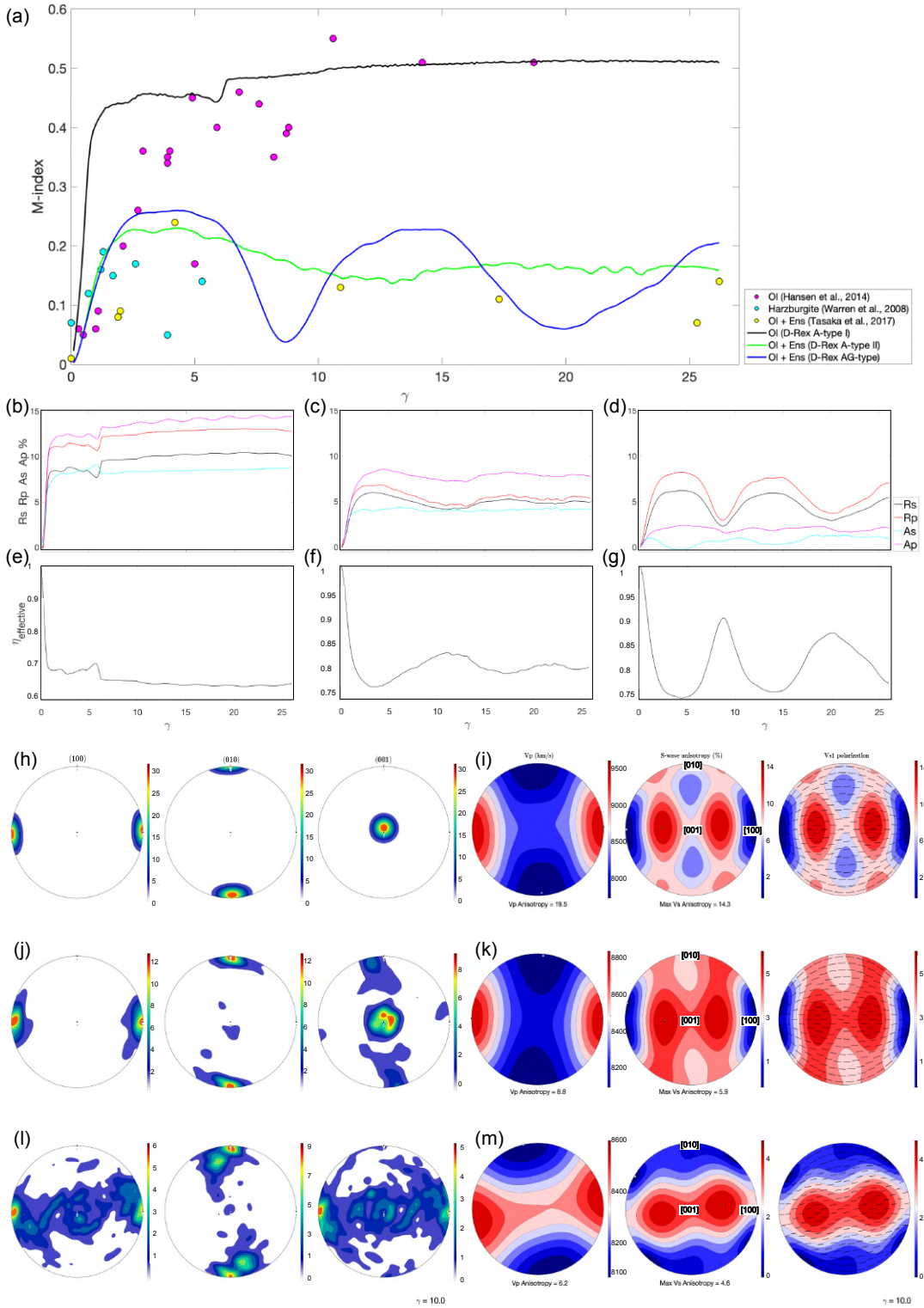
Figure 3.3: *Comparison between Test 1, Test 2 and Test 3. (a) M-index with increasing strain (γ). (b-g) Radial (R) and azimuth (A) anisotropy for P and S waves, and anisotropic parameter η$_{effective}$ (not to be confused with the effective viscosity) with increasing strain for (b,e) Test 1, (c,f) Test 2 and (d,g) Test 3. See legend. Pole figures showing olivine crystals LPO at strain γ = 10 and V$_P$ and S-wave anisotropy for (h,i) Test 1, (j,k) Test 2 and (l,m) Test 2.*

~0.2-0.25 and trends similar to those observed by Tasaka et al. (2017) (yellow dots). In the case of Test 2, after reaching the maximum peak, these values slightly decrease and then remain constant at about 0.17 for $\gamma > 10$. In Test 3, the curve shows an alternation of maximum (~ 0.25) and minimum (~ 0) values.

Another measure of the strength of strain-induced anisotropy is showed in Figure 3.3(b-g). The curves exhibit the evolution of radial and azimuthal anisotropy for S and P waves (R_s, R_p, A_s, A_p) as well as of the anisotropic parameter $\eta_{effective}$ with increasing strain calculated for Voight average for the three tests on single aggregates (eq. 3.16-3.20). Figure 3.3b shows an overestimation of strain-induced LPO when olivine single crystal aggregates are considered and an efficient dynamic recrystallization is imposed. Lower values are instead showed in Figure 3.3c and 3.3d for Test 2 and Test 3, respectively.

3.3.3 Macro-scale strain-induced LPO

The best set of parameters for modeling A-type I, A-type II and AG-type fabrics was then applied to model mantle fabrics and elastic properties in the large-scale models of oceanic plate tectonic evolution.. The obtained radial anisotropy is shown in Figure 3.4(a-c), for the three cases, i.e. Test 1, 2 and 3, respectively. We observe that radial anisotropy is higher where the mantle flow is horizontal (see also Figure 3.2d). On the contrary, lower radial anisotropy values (< 1) are observed in correspondence of vertical flows, i.e. beneath the ridge and the trench.

3.3.4 Predicted SKS splitting measurements

In order to validate the elastic properties of the models I performed SKS splitting measurements. The results obtained for the three models are shown in map view at the top of each panel of Figure 3.4. For model 1, with fabric
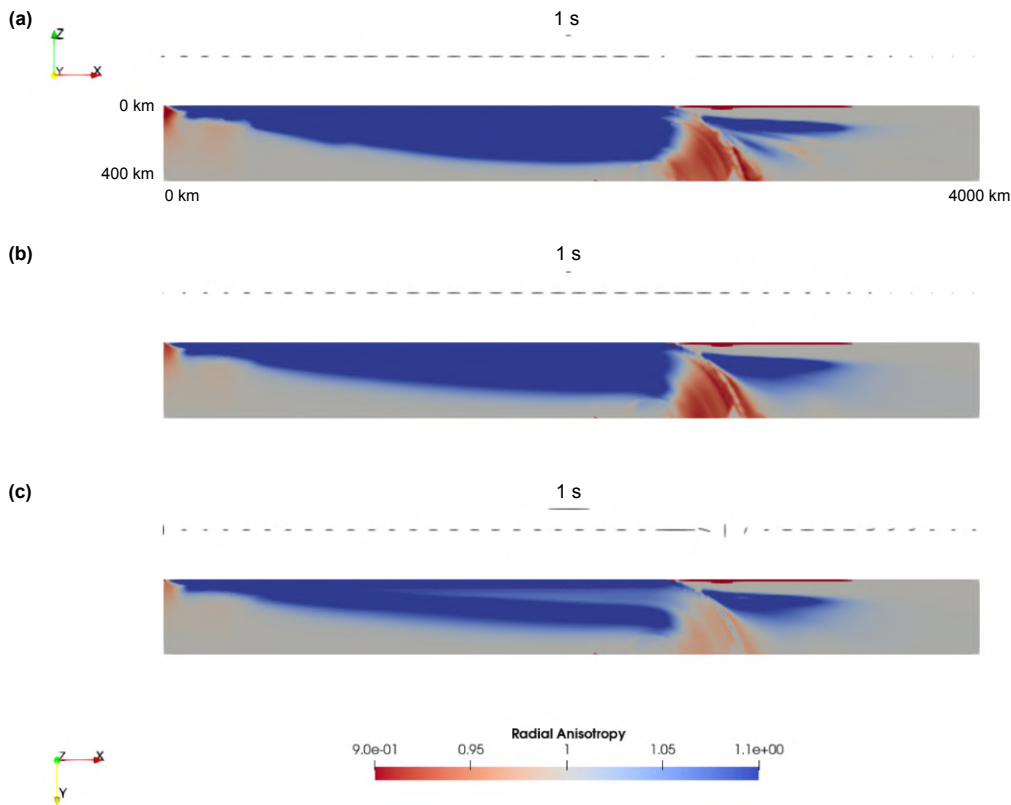
Figure 3.4: *Vertical cross view of radial anisotropy for (a) Test 1, (b) Test 2 and (c) Test 3. For each test, SKS splitting measurements from top view are plotted above. 1 s indicates the split time scale.*

A-type I, the preferential direction of the splitting is oriented in the trench-perpendicular direction along the entire model (Figure 3.4a). Similarly, model 2, with fabric A-type II, exhibits SKS splitting azimuths oriented in the trench-perpendicular direction and split-times proportional to those observed for model 1 (Figure 3.4b). The two cases differ in correspondence of the trench, where model 1 shows splitting magnitude = 0 s (i.e. isotropic behavior), while model 2 exhibits trench-perpendicular azimuths with split-time $\sim 3s$. Model 3 (Figure 3.4c), characterized by the AG-type fabric, exhibits SKS split-ting measurements with trench-perpendicular azimuths in the areas with high values of radial anisotropy (i.e. in correspondence with the oceanic plate) and trench-parallel in the area with low radial anisotropy (i.e. close to the trench and the ridge), exhibiting a tilt of $\sim 90°$.

3.4 Discussion

From the comparison between our micro-scale numerical simulations and laboratory experiments (Hansen et al., 2014; Tasaka et al., 2017; Warren et al., 2008) (Figure 3.3a) I observed that the trend of Test 1, i.e. A-type I fabric (black line), is similar to that observed by Hansen et al. (2014) on single aggregates of olivine crystals (purple dots). Test 2 (i.e., A-type II fabric, green line) and 3 (i.e., AG-type fabric, blue line) exhibit trends that partially reproduce that observed by Tasaka et al. (2017) on multiphase aggregates of olivine and pyroxene. As Test 2 and 3 are performed on multiphase aggregates (i.e. olivine:enstatite = 70:30 in volume proportion), in these two cases the slow axes of the enstatite tends to align parallel to the olivine fast axes. It follows that incorporating pyroxene into the crystal aggregate results in the decrease of strength of anisotropy (Kaminski et al., 2004). Imposing a lower *M* parameter with respect to Test 1 (i.e. 125, 10 and 1 for Test 1, 2 and 3, respectively), results in less efficient dynamic recrystallization, that reduces the M-index values, and thus weakens the resulting LPO. However, I note that this comparison is limited to the small number of available samples and more high-strain experiments are required to better constrain the model parameters.

Similarly to Figure 3.3c and 3.3d for Test 2 and 3, in intra-oceanic settings the average values of azimuthal anisotropy are equal to 2%, P-wave radial anisotropy equal to 4%, S-wave anisotropy equal to 3% and η equal to 0.95 (Beghein & Trampert, 2004; Dziewonski & Anderson, 1981; Kaminski et al., 2004; Kustowski et al., 2008).

Figure 3.4 shows radial anisotropy for the three tests performed at the geodynamic model scale. It exhibits positive values beneath the horizontal plate and negative beneath the ridge and the trench. S wave radial anisotropy is $\xi = (V_{SH}/V_{SV})^{1/2}$, where V_{SH} and V_{SV} are the velocity for horizontally and

vertically polarized shear waves, respectively. Areas with values of $V_{SH} > V_{SV}$ will therefore have radial anisotropy values > 1. This is the case of regions of the model where the movement of the oceanic lithosphere induces horizontal flows, generating anisotropic fabrics oriented according to it. On the contrary, areas with $V_{SH} < V_{SV}$ will have radial anisotropy lower than 1 as in proximity of oceanic ridges and subduction zones, where the vertical flows orients the crystals to form fabrics whit the fast axes aligned in the vertical direction. Figure 3.4 also exhibits age-dependent seismic anisotropy, i.e. the thickness of the body at high anisotropy values increases as the age of the lithosphere increases. This behaviour is in contrast with global radially anisotropic model (e.g., Auer et al., 2014) but often observed in geodynamic models.

Furthermore, a comparison between the predicted SKS fast azimuths and split-times from our large-scale models (Figure 3.4) and those observed by other authors (e.g., Long & Becker, 2010) allowed to validate the obtained results at the scale of subduction zone models. It is observed that most of the splitting measurements in correspondence of the subduction zones exhibits trench-parallel oriented azimuths (Long & Silver, 2009a). This orientation is also strictly correlated to the dip angle of the slab (Christensen & Abers, 2010; Currie et al., 2004; Hicks et al., 2012; Song & Kawakatsu, 2012). I observed that our large-scale simulations (Figure 3.4) in proximity of the subduction zone exhibits trench-perpendicular orientation when the fabric is A-type I and II and trench-parallel when the fabric is AG-type. However, although the AG-type olivine fabric well fits SKS splitting azimuths in forearc, the sinusoidal trend of Test 3 observed in Figure 3.3, that results from the competition between two predominant [100] (010) and [001] (010) slip systems, has never been observed in laboratory experiments so far.

From these comparisons it emerged that the A-type olivine fabric well reproduces the behaviour of dunitic mantle (100% olivine), while for a more

fertile mantle (e.g., harzburgitic) it is necessary using a combination of D-Rex parameters that weaken the strength of anisotropy.

3.5 Conclusion

By performing micro- and 2-D macro-scale flow simulations, I have constrained numerical modelling parameters for estimating strain-induced seismic anisotropy. Through a comparison with laboratory experiments it emerged that the A-type I olivine fabric matches fabrics of pure olivine aggregates, while it tends to overestimate seismic anisotropy of harzburgitic or more fertile mantle compositions. When applied to a larger-scale model of oceanic plate formation at the ridge and subduction at the trench, it results into trench-perpendicular SKS fast azimuths along the entire model. On the contrary, I observed that the AG-type olivine fabric better fits the multiphase aggregates laboratory experiments and when used in the larger scale goedynamic model, results into trench-parallel SKS splitting where vertical flow is present, i.e. in proximity of the ridge and the trench. I note that SKS splitting azimuths and times strongly depend on the choice of the D-Rex parameters (i.e. M, λ and χ). Specifically, I observe that imposing a poorly efficient dynamic recrystallization together with same activities of [100](1010) and [001](010) slip systems and a combination of 70% olivine and 30% entstatite yields numerical results that better fit seismological observations.

Acknowledgments

Chapter 4

SLAB GEOMETRY AND UPPER MANTLE FLOW PATTERNS IN THE CENTRAL MEDITERRANEAN FROM 3D ANISOTROPIC P-WAVE TOMOGRAPHY

F. Rappisi[1]**, B. P. VanderBeek**[1]**, M. Faccenda**[1]**, A. Morelli**[2] **and I. Molinari**[2]

A similar version of this manuscript has been published as: "Rappisi, F., VanderBeek, B. P., Faccenda, M., Morelli, A., & Molinari, I. (2022). Slab geometry and upper mantle flow patterns in the Central Mediterranean from 3D anisotropic P-wave tomography. Journal of Geophysical Research: Solid Earth, e2021JB023488". All the authors conceived the study. FR performed the inversions and wrote the first draft of the manuscript. BPV prepared the initial setup and resolution tests. MF helped in the geodynamic interpretation of the tomographic results. All the authors contributed equally to the discussion of the results and to the conclusions of this study.

---

[1]Dipartimento di Geoscienze, Università di Padova, Padova, Italy
[2]Istituto Nazionale di Geofisica e Vulcanologia, Bologna, Italy

Abstract

We present the first 3D anisotropic teleseismic P-wave tomography model of the upper mantle covering the entire Central Mediterranean. Compared to isotropic tomography, it is found that including the magnitude, azimuth, and, importantly, dip of seismic anisotropy in our inversions simplifies isotropic heterogeneity by reducing the magnitude of slow anomalies while yielding anisotropy patterns that are consistent with regional tectonics. The isotropic component of our preferred tomography model is dominated by numerous fast anomalies associated with retreating, stagnant, and detached slab segments. In contrast, relatively slower mantle structure is related to slab windows and the opening of back-arc basins. To better understand the complexities in slab geometry and their relationship to surface geological phenomena, we present a 3D reconstruction of the main Central Mediterranean slabs down to 700 km based on our anisotropic model. P-wave seismic anisotropy is widespread in the Central Mediterranean upper mantle and is strongest at 200-300 km depth. The anisotropy patterns is interpreted as the result of asthenospheric material flowing primarily horizontally around the main slabs in response to pressure exerted by their mid-to-late Cenezoic horizontal motion, while sub-vertical anisotropy possibly reflects asthenospheric entrainment by descending lithosphere. Our results highlight the importance of anisotropic P-wave imaging for better constraining regional upper mantle geodynamics.

Plain Language Summary

This study presents a new 3D model of the Earth's interior below the Central Mediterranean constructed from numerous observations of distant earthquakes. This seismic image constrains changes in the speed at which waves

propagate through the Earth that can be related to temperature and composition. Unlike many previous images of the region, our model accounts for seismic anisotropy–the directional dependence of wave propagation velocity– allowing us to also infer directions of mantle flow. It is found that the Central Mediterranean is underlain by many distinct regions of lithosphere descending into Earth's mantle. The recent motion of these lithospheric slabs drives regional mantle flow patterns that are largely consistent with our anisotropy observations.

4.1   Introduction

The Central Mediterranean region is an active plate margin characterized by the presence of both oceanic and continental lithosphere. The recent tectonic history is marked by intense seismic and volcanic activity triggered by episodes of continental collision and slab rollback leading to the formation of mountain ranges and extensional basins (Faccenna et al., 2014). Our understanding of the structural heterogeneity and tectonic complexity of this region requires accurate imaging of the subsurface. For this reason, since the late 1990s numerous seismological studies have been carried out to constrain upper mantle structure beneath the Mediterranean region (e.g., Piromallo & Morelli, 2003; Scarfi et al., 2018; Spakman, 1990; Spakman et al., 1993; Spakman & Wortel, 2004). However, despite a few notable exceptions (e.g., Eberhart-Phillips & Mark Henderson, 2004; Hua et al., 2017; Wei et al., 2019), P-wave tomographic models at regional and global scales generally neglected the phenomenon of seismic anisotropy, approximating the medium as elastically isotropic. Although this assumption simplifies the imaging approach, unmodelled anisotropic heterogeneities generate artefacts that could bias our understanding of the Earth's internal structure and dynamics (Bezada et al., 2016; VanderBeek & Faccenda, 2021). Delays from

anisotropic heterogeneities can in fact be as strong, if not stronger, than those from isotropic structure and consequently anisotropy could be mapped to a perturbation in the isotropic velocity (Blackman & Kendall, 1997; Blackman et al., 1996; Grésillaud & Cara, 1996; Kendall, 1994; Lloyd & Van Der Lee, 2008; Sieminski et al., 2007; Sobolev et al., 1999) resulting in misguided interpretations.

Seismic anisotropy in the Central Mediterranean upper mantle has been mostly measured by exploiting surface waves and shear wave splitting. The former generally suffer from poor lateral resolution owing to the long periods used for mantle imaging. The splitting of shear body waves, most commonly SK(K)S, has instead a poor vertical resolution due to their near vertical ray paths. To date, for the Central Mediterranean area, only a single P-wave azimuthal and radial anisotropic tomography study performed in the Alpine region exists (Hua et al., 2017). In this study teleseismic P-wave delay times are used to infer the isotropic and anisotropic (fabric strength, azimuth, and dip) velocity structures of the Earth's mantle in the Central Mediterranean region. Importantly, our work is the first to consider dipping fabrics in addition to the azimuth and strength of anisotropy which Vander-Beek and Faccenda (2021) demonstrated is key to reducing isotropic imaging artefacts. Specifically, our work focuses on the upper mantle where the main source of seismic anisotropy is related to the presence of intrinsically anisotropic minerals, predominantly olivine and to a lesser extent pyroxene. From our anisotropic tomography model, we attempt to answer some fundamental questions regarding Central Mediterranean mantle structure. To what extent could isotropic anomalies be artefacts related to neglected anisotropic heterogeneity? What is the present day configuration of subducting slabs? What is the geometry of mantle flow in relation to the slabs?

4.1.1 Recent tectonic history

The recent tectonic evolution of the Mediterranean region is characterized by the coexistence of episodes of subduction and collision that expanded and compressed the continental and oceanic lithosphere (Faccenna et al., 2014; Romagny et al., 2020; van Hinsbergen et al., 2014). Bordered at the north by the presence of the Alpine mountain range, whose orogeny dates back to the Late Cretaceous (Rosenbaum et al., 2002a), the area is still tectonically evolving. The collision between the African and the Eurasian plates, with the consequent closure of the Tethys Ocean, represents only the beginning of this articulated and complex geological history.

Since the Oligocene, two oceanic trenches surrounding the Alpine-Dinaric collision have dominated the evolution of the Mediterranean region. To the west the Liguro-Provençal or Tyrrhenian trench and to the east the Hellenic one. The slow southward retreat of the two trenches begun in the Middle Eocene - Early Oligocene when the subduction rate of the Ionian slab segments exceeded the convergence rate of the Africa and Eurasia plates. This resulted in a transition from compressional to extensional deformation regime related to the roll back of the oceanic slabs that led to the present day surface and deep structures observed South of the Alps.

From ∼32-30 million years (My) to ∼16-15 My, the south-eastward migration of the western portion of the Ionian plate triggered the separation of the Corsica-Sardinia block from the rest of the European continent with a consequent anticlockwise rotation of about 40°. This rotation caused the opening of the Liguro-Provençal basin (Carminati et al., 2012; Dewey et al., 1989; Faccenna et al., 2014; Faccenna et al., 2007; Faccenna et al., 2004; Gueguen et al., 1998; Jolivet et al., 2009; Malinverno & Ryan, 1986; Rosenbaum et al., 2002b; Wortel & Spakman, 2000) and the collision of the Corsica-Sardinia block with the westernmost part of Adria which gave rise to the Apennines orogeny

(Patacca et al., 1993). The retreat of the western portion of the oceanic Ionian plate continues to this day, and from about 15 million years ago (Ma) it has contributed to the fast opening of the Tyrrhenian basin and the southward migration and over-thrusting of European allochthonous terranes over NE Sicily and North Africa (i.e. Peloritani and Kabylides). More to the West, the Ionian plate experienced a clockwise rotation and westward retreat forming the Alboran-Betic arc.

Retreat on the eastern side of the Ionian ocean began at 45 Ma and accelerated at 15 Ma as a consequence of the Hellenic slab tearing as documented by mantle tomography (Brun et al., 2016).

Faccenna et al. (2014) in their figure 9 show the evolution of the Mediterranean region starting from 35 Ma. Here, Figure 4.1a shows the current position of the main trenches in the Central Mediterranean area in relation with the three main tectonic plates Africa, Eurasia and Adria.

4.1.2   Mantle structure from isotropic tomographic images

Several seismic tomographic models have been developed in recent decades with the aim of mapping the P and S wave velocity structures of the mantle in the Mediterranean (Bijwaard et al., 1998; El-Sharkawy et al., 2020; Hua et al., 2017; Kästle et al., 2019; Koulakov et al., 2009; Lippitsch et al., 2003; Lyu et al., 2017; Piromallo & Morelli, 2003; Spakman et al., 1993; Zhao et al., 2016; Zhu et al., 2012). The various studies indicate that the area is characterized by significant structural heterogeneity. Several fast anomalies interpreted as slab fragments are found with variable lateral and vertical dimensions including continuous slabs reaching the transition zone, hanging slabs and completely detached slabs. While the large-scale distribution of fast slab anomalies generally agree between studies, the vertical and lateral continuity of these features may vary significantly owing to different methodologies and datasets

employed.

Over the years particular attention has been paid to the Alpine area but its complexity and proximity to the Apennines makes the interpretation of the tomographic results particularly difficult. In the Western Alps, for example, some tomographic models have imaged a shallow hanging slab (80-150 km; Kästle et al., 2019) while others have observed a much deeper slab (250-300 km; Hua et al., 2017; Koulakov et al., 2009; Lyu et al., 2017; Zhao et al., 2016). Overall, the Alpine slab appears to be segmented in between Central and Eastern Alps, and dipping at very high angles, especially below the Eastern Alps. The latter feature is particularly problematic as it poses an ambiguity on whether the vertical slab belongs to the European or Adria plates.

The presence of a high-speed anomaly lying in the Northern Apennines area has been identified by numerous studies (Bijwaard et al., 1998; Giacomuzzi et al., 2011; Kästle et al., 2018; Koulakov et al., 2009; Lucente et al., 1999; Piromallo & Morelli, 1997, 2003; Spakman & Wortel, 2004; Van der Meer et al., 2018; Zhao et al., 2016) but its vertical continuity is still debated. For example Piromallo and Morelli (2003) show evidence of a continuous slab below Tuscany while Spakman and Wortel (2004) propose that a short (300-400 km) slab is hanging below the Northern Apennines. In the Central Apennines, a slab window of variable vertical extent is imaged ranging from 140 km (Giacomuzzi et al., 2011) to 250 km (Spakman & Wortel, 2004) depth. However, at greater depths the fast Apennine anomaly appears continuous connecting with the Calabrian slab to the south. The high-velocity Calabrian slab anomaly is observed extending to the transition zone and progressively narrowing at shallower depths as a result of the lateral migration of slab tears (El-Sharkawy et al., 2020; Giacomuzzi et al., 2012; Neri et al., 2009; Scarfì et al., 2018). Continuing westard, other lithospheric remnants now form the Kabylides slab which extends along the north Africa margin, and the Alboran slab in the Gibraltar area which falls at the far western edge of the study

region.

In the Dinaric Alps area several seismic tomographic images (Bijwaard & Spakman, 2000; El-Sharkawy et al., 2020; Koulakov et al., 2009; Piromallo & Morelli, 2003) found a long slab extending from north to south below the entire mountain range reaching varying depths. For example, El-Sharkawy et al. (2020) describes a model with a shorter slab in the northern portion (∼150 km) and deeper one (∼300 km) in the southern portion dipping in a northeast direction. Toward the South East, a broad fast anomaly is imaged below the Hellenic arc down to a depth of at least 1000 km (Piromallo & Morelli, 2003; Zhu et al., 2012).

The most relevant slow anomalies detected in these studies are those present in the shallow mantle beneath areas that over the Cenozoic experienced extensional deformation (e.g., Liguro-Provençal, Thyrrenian, Aegean, Pannonian basins) or volcanic activity (e.g., Massif Central and Central-Western Italy; Granet et al., 1995a; Granet et al., 1995b; Peccerillo, 2017). Other prominent slow velocity anomalies which have no clear connection to surface processes and structures are those imaged beneath the Adriatic and Ionian Seas (Piromallo & Morelli, 2003; Spakman & Wortel, 2004), or below the slab subducting beneath the Western Alps (Zhao et al., 2016).

4.2   Seismic Data

Within our study area, seismic stations are distributed fairly evenly throughout Europe with coverage extending as far south as Northern Africa. However, the marine areas of the Tyrrhenian, Adriatic, and Ionian Seas and the Strait of Sicily remain poorly sampled resulting in uneven seismic data coverage of the Central Mediterranean (Figure 4.1b).

The dataset used for this work consists of direct P-wave delay times reported by the International Seismological Centre EHB bulletin (ISC-EHB) for
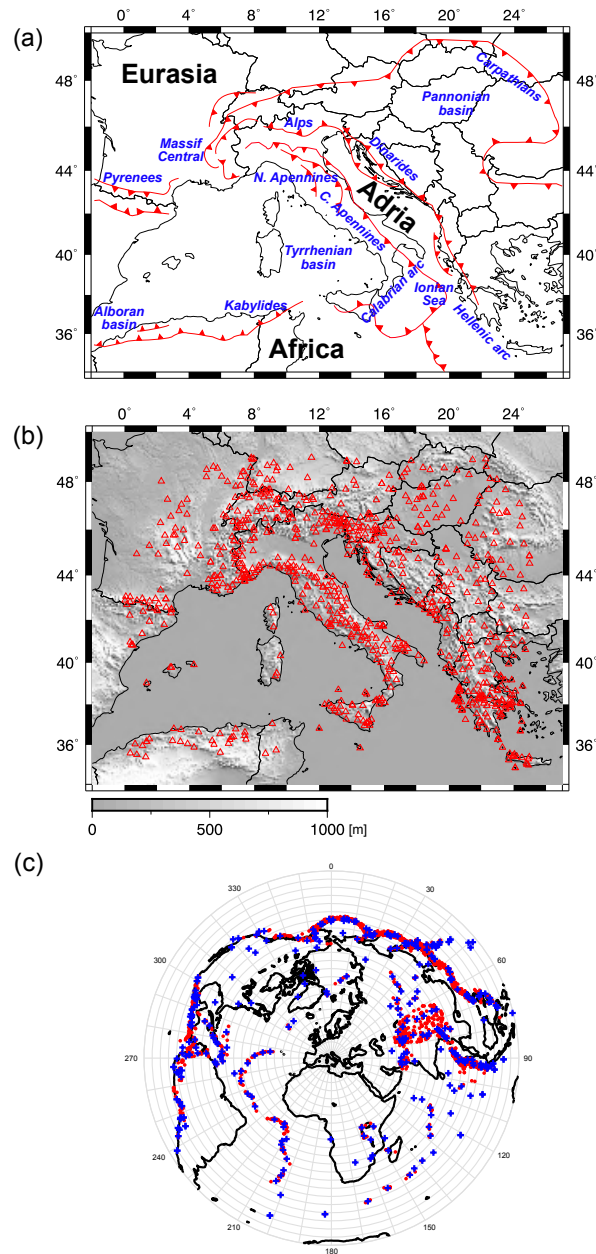
Figure 4.1: *(a) Current plate tectonic setting of the Central Mediterranean adapted from Faccenna et al. (2014). (b) Distribution of seismic stations (red triangles) used in this study. (c) Distribution of teleseismic events considered in this study. All events are shown as red points and binned events used for imaging are depicted with blue crosses. The bins are shown by grey lines and defined by 10° back-azimuthal and 5° range intervals. Not illustrated are the 50 km depth interval bins.*

the time interval 2000-2018. Delays are measured with respect to AK135 (Kennett et al., 1995) predictions and, as it is common in regional teleseismic tomography (e.g., Lévêque & Masson, 1999; Masson & Romanowicz, 2017), delays are demeaned by event to remove signal originating from structure

outside the array. In an effort to select high-quality data, only ISC bulletin arrivals that met the following criteria were selected: (i) events with magnitude $\geq$ 6; (ii) epicentral distance of at least 30° from the edges of the study area; (iii) to ensure an event is well recorded across the study area, it was required that at least 90 stations ($\sim$10% of the array) recorded each event; (iv) to exclude potentially poor quality instruments, each station must record no less than 10 events; (v) delays with respect to AK135 (Kennett et al., 1995) exceeding 4 standard deviations (4 s) of the entire delay time dataset are considered outliers and excluded (these data compose only 0.34% of all delays). Following preliminary isotropic inversions, the dataset was further culled by removing arrivals associated with the tails of the residual histogram that extended beyond three standard deviations of the collective residuals ($\sim$1.8 s). This amounted to a loss of 2% of data ($\sim$ 1636 arrivals excluded). Lastly, to reduce biases associated with preferential sampling of certain back azimuths (BAZ), the original 2918 events were binned in 5° arc distance, 10° BAZ and 50 km depth intervals (Figure 4.1c). For a given station, delays from events located in the same bin were averaged into a single observation. Our final dataset consists of 346 events, 810 stations and includes 89,456 delay times. Mean station delays prior to inversion are shown in Supplementary Figure 4.8. Inversions using raw (i.e. not binned) data with and without the aforementioned outlier arrivals were explored but no significant influence was observed on the tomographic solutions. The main benefit of binning the data was to reduce computational time and minimise the influence of potentially erroneous delays. The final delay time dataset has an RMS of 800 ms.

4.3   Seismic Imaging Method

4.3.1   Tomography Algorithm

We use a novel anisotropic seismic imaging method described in detail by VanderBeek and Faccenda (2021) and briefly summarised below. The tomographic algorithm solves simultaneously for perturbations to P-wave slowness (i.e. the inverse of velocity) and three additional parameters that define the anisotropic magnitude, azimuth, and dip in a simplified hexagonally symmetric medium. The method differs from other recent anisotropic P-wave inversion algorithms that include arbitrarily oriented fabrics (e.g., Munzarová et al., 2018) in that our parameterisation does not require an anisotropic starting model which could potentially bias results if not sufficiently close to the true solution. Another notable feature of our tomographic method is the use of 3D ray tracing through a user-defined 3D velocity model that explicitly incorporates elevation (Toomey et al., 1994). As demonstrated by Bodmer et al. (2020), elevation and complex shallow 3D structure can account for more than 1 s of teleseismic delay. Moreover, simply using undamped station static corrections to account for such structure was found to introduce artefacts in the tomographic image. Thus, elevation and shallow velocity variations are best treated explicitly in teleseismic imaging. Lastly, we note that our tomography algorithm can include approximate finite frequency kernels (Schmandt & Humphreys, 2010; VanderBeek & Faccenda, 2021). However, without details regarding the methods and frequency bands used in identifying arrival times in the ISC catalog, we use the infinite frequency approximation in the present study.

Ray theoretical travel-times through the modelling volume are computed using a shortest-path algorithm (Moser, 1991) while the tau-p method (Crotwell et al., 1999) is used outside the study area where a 1D radial Earth velocity model is assumed. Travel-times predictions from AK135 are then subtracted

from the shortest path time and the resulting residuals for each event are demeaned to yield relative delay time consistent with the observed data. Partial derivatives of the delay times with respect to the model parameters are computed along the discretized ray paths. The resulting system of equations is solved using the LSQR method (Paige & Saunders, 1982) subject to smoothing and damping constraints that are required to regularise the otherwise ill-posed inverse problem. As a consequence of the evolving 3D ray paths and non-linear relationship between the travel-times and anisotropic parameters, multiple iterations are required for the solution to converge.

4.3.2   Starting model, discretization and regularization

For the forward calculation of ray paths and travel-times, a regular grid with uniform 10 km node spacing was employed. The model domain extends 1200 km to the east and west of 12.5°E, 1000 km north and south of 42°N, and 700 km in depth. The initial model contains 3D crustal thickness and isotropic velocity variations from the 1°-resolution EPcrust (Molinari & Morelli, 2011), which at present is the only crustal model covering the entire area, in addition to elevation from Ryan et al. (2009). The crustal and Moho interfaces in the EPcrust model are linearly interpolated to our model grid and the laterally variable layer velocities in the EPcrust model are interpolated to nodes contained within each layer. Nodes that fall beneath the EPcrust Moho are assigned isotropic mantle velocities from AK135 (Kennett et al., 1995) corresponding to their depth beneath the crust-mantle interface. Elevation is included by vertically shearing the model grid with additional travel-time corrections made for differences between the true station elevation and the elevation on the ray tracing grid surface (see Toomey et al., 1994). An Earth flattening transform (Müller, 1971) is applied to the model velocities to account for Earth's curvature in our cartesian model domain.

We solve for perturbations to mean P-wave slowness and three anisotropic parameters (see VanderBeek & Faccenda, 2021) on a coarser grid with dimensions of 61x51x20 with uniform 40 km node spacing. Note that purely azimuthally anisotropic inversions were not considered as VanderBeek and Faccenda (2021) demonstrated that these can introduce significant artefacts in areas where dipping anisotropy is to be expected. The resulting perturbations are linearly mapped to the finer model used for travel-time computations upon each iteration. To further limit the number of inversion parameters, anisotropic perturbations were restricted to the upper 400 km where mineral physics predicts mantle anisotropy to be most significant (Karato et al., 2008) and where there is the best ray crossing. Furthermore, inversions without depth-restricted anisotropy did not significantly improve the fit to the data nor appreciably alter the final image. Our isotropic inversions converge after 3 iterations (where one iteration comprises the forward computation of ray paths and delay times and subsequent inversion for new model perturbations) while the anisotropic inversions converge after 6 iterations.

The selection of regularization parameters that enforce the Laplacian spatial smoothness of the model perturbations (i.e. smoothing factor, λ_s) and limit the norm of the model perturbational vector (i.e. damping factor, λ_d) is the most subjective aspect of a tomographic inversion. To avoid preferentially making isotropic perturbations whose partial derivatives are generally larger in magnitude relative to the anisotropic variables, the slowness regularisation equations are inversely weighted by the starting model slowness. In this way, damping and smoothing is applied to fractional changes in model parameters which are expected to be on the order of 1% for both isotropic and anisotropic perturbations. To identify appropriate regularisation values, we constructed L-curves (e.g., Aster et al., 2018) which plot the squared-norm of the data residual vector against the squared-norm of the model perturbational vector. Ideal solutions are considered those near the

corner of the L-curve where an increase in model norm does not result in an appreciable decrease in data residuals. Further discussion about the choice of the regularization parameters is addressed in Text S1 in the supporting information file (SI). The L-curves are shown in Supplementary Figure 4.9. The parameters adopted for our preferred isotropic and anisotropic solutions are listed in Table 4.1 in the SI.

Event and damped station correction terms are also included in the inversion. Event statics account for hypocentral errors and structure sampled outside the imaging volume. Station corrections are traditionally used to account for shallow structure that cannot be resolved by the teleseismic data (e.g. elevation changes and crustal heterogeneity). Considering our starting model contains elevation and 3D crustal velocities, we follow Bodmer et al. (2020) and solve for damped station correction terms. The damping factor is chosen such that the RMS station correction is ∼300 ms. This corresponds to a ∼3.75% change in average crustal velocity or 8 km change in crustal thickness.

The RMS delay time residuals from our preferred isotropic solution (referred to as iso-NEWTON21 in reference to the name of the European Research Council grant funding this work; see Supplementary Dataset S1) is 500 ms corresponding to a 61% variance reduction in the initial RMS delay time. In comparison, our preferred anisotropic solution, ani-NEWTON21 (Supplementary Dataset S2), has an RMS delay time of 488 ms corresponding to a 63% variance reduction. The similar data fit offered by the two models may reflect the true error in our delay time dataset and more accurate delay times may allow us to better distinguish between them in the future. While the small improvement in data fit alone does not justify the inclusion of additional anisotropic parameters, we assert that the ani-NEWTON21 model is the more optimal solution for the following reasons. (1) While the anisotropic model has more free parameters, it is the simpler solution. The total norm of

the fractional velocity perturbations (i.e. change in isotropic velocity normalized by the starting model value) and anisotropic magnitude perturbations can be used as an indication of model complexity with higher values corresponding to a greater magnitude and/or number of anomalies. The norms are comparable as both fractional velocity anomalies and anisotropic magnitude describe perturbations to seismic propagation velocity and are expected to be similarly valued (i.e. a few percent). From the L-curves (Supplementary Figure 4.9), it is clear that anisotropic models consistently fit the data better with less heterogeneity. (2) Unlike the isotropic model, the anisotropic solution can explain many patterns observed in independent SKS splitting parameters and is thus more consistent with observations. (3) As evidenced by numerous SKS splitting studies, the central Mediterranean is underlain by rather complex anisotropic structure and it is known that P-wave traveltimes are particularly sensitive to anisotropy (Sieminski et al., 2007) such that assuming an isotropic Earth can lead to significant imaging artefacts and possible erroneous interpretations (e.g., Bezada et al., 2016; VanderBeek & Faccenda, 2021). Therefore, neglecting anisotropy in body wave imaging is problematic and both isotropic and anisotropic inversions should be conducted to understand the nature of mantle heterogeneity. (4) Both ours and the synthetic tests of VanderBeek and Faccenda (2021) demonstrate both isotropic and anisotropic heterogeneity can be resolved by teleseismic P-weave delays and that there is not a one-to-one trade off in these parameters. Furthermore, true isotropic structure is not prone to yielding anisotropic artefacts. However, anisotropic structure can generate significant isotropic artefacts (VanderBeek & Faccenda, 2021). Thus, isotropic features in the anisotropic model are likely to be more robust.

4.3.3   Model resolution

Anisotropic imaging with teleseismic delay times has some important limitations. We summarise these issues in Text S2 in the SI and present in the next lines metrics for model resolution and results of synthetic tests to evaluate the effects of these limitations on our results.

Directly assessing model resolution for large scale tomographic problems remains a challenge. The large number of free parameters generally prohibits the direct computation of resolution matrices and non-linear inversion methods capable of systematically exploring model space quickly become computationally infeasible. Hence, three more indirect measures of model fidelity are tested, (1) ray density and directional sampling metrics, (2) synthetic reconstruction tests, and (3) predictive capability of the tomographic model.

The derivative weight sum (DWS; Toomey & Foulger, 1989) is the summation of travel-time partial derivatives with respect to slowness at each perturbational node. As demonstrated by Zhang and Thurber (2007), the DWS provides an indirect estimate of parameter resolution attaining higher values in more densely sampled regions of the model.

The DWS lacks information regarding how directionally well-sampled are the model parameters which is important for assessing resolution of anisotropic structure. To assess directional bias, we use the azimuthal mean resultant length (AMRL; Fisher, 1995; Zhang et al., 2009) defined as the length of the vector resulting from an averaging of the x- and y-components of all ray segment unit vectors sampling a given perturbational node. Maps of the DWS (Supplementary Figure 4.10) and AMRL (Supplementary Figure 4.11) for our study are shown in the SI together with their discussion in Text S2.

Directional sampling in the vertical plane is poor compared to the azimuthal plane owing to the steep incidence angles of teleseismic wavefronts.

Supplementary Figure 4.12 shows the mean incidence angles of rays throughout the imaging volume which primarily vary as a function of depth with values ranging between 20° - 40°. Despite the limited sampling of incidence angles, good azimuthal coverage is sufficient to resolve dipping anisotropic fabrics (VanderBeek & Faccenda, 2021) but results in limited vertical resolution of anisotropy as shown by our synthetic inversions discussed below.

A number of synthetic inversions is performed to address potential imaging problems highlighted in Text S2 and to evaluate isotropic and anisotropic parameter resolution in general. Ray theoretical synthetic delay times are predicted for various test models using the same station-event pairs defined in our binned dataset (section 4.2) with event demeaning to be consistent with the true observations. Random errors from a normal distribution with a standard deviation of 450 ms (i.e. a value comparable to the RMS-error of our preferred tomographic solutions) are added to the synthetic datasets. Unless otherwise noted, all synthetic tests are performed using the preferred anisotropic inversion parameters listed in Table 4.1 in the SI.

To assess resolution of isotropic structure and its trade-off with anisotropic parameters, checkerboard reconstruction tests were performed for purely isotropic cubic anomalies with alternating amplitudes of ± 4% and dimensions of 100 km (Figure 4.2a-d) and 200 km (Figure 4.2e-h). It is found that lateral and vertical variations in isotropic structure on the scale of at least 100 km are well-resolved in areas where the DWS $>\sim$ 100. However, as is common in ray-theoretical tomography, amplitudes are generally under-recovered. The degree to which the anomaly amplitudes are underestimated depends in part on their spatial extent. We recover $\sim$50% of the 100 km^3 block amplitudes and 75%-80% of the 200 km^3 blocks. Despite the potential of the checkerboard-pattern isotropic anomalies to impart a directional dependence in delay times, only minor anisotropic anomalies (generally <1%) are imaged indicating minimal leakage of truly isotropic heterogeneity into

anisotropic parameters. Lastly, it is worth noting that purely isotropic inversions for these models did not improve amplitude recovery or alter the solution in any appreciable way.

To investigate to what extent anisotropic heterogeneity can be isolated, additional checkerboard tests were performed for purely anisotropic anomalies. Two models were considered composed of 300 km x 300 km x 200 km anisotropic domains centered at (i) 100 km (Figure 4.3a) and (ii) 300 km depth (Figure 4.3b). Each block contains 6% P-wave anisotropy with fast axis azimuths alternating between 22.5° and -67.5°, while the dip varies between 0° and 45°. To visualise the effects of vertical smoothing, anisotropic perturbations were not limited to the [0 km, 400 km] depth interval as in our preferred solution. Strong lateral changes in anisotropic fabric are well-imaged at the scale of ~300 km where the AMRL $<\sim$0.5. On average, 50%-70% of the anisotropic amplitudes are recovered. The median error in fast axis azimuths for both tests is 14° and 10° for the dip using angular errors on a [0°, 90°] interval. As seen in Figure 4.3d, the anisotropic domains are reasonably well-localized in depth with the inversions recovering the strongest anisotropic magnitudes at depths coinciding with the anomaly centers. However, the peak recovered magnitude for the shallow block is offset deeper by ~50 km. Vertical smoothing does smear some anisotropic structure throughout the upper mantle. Because of the poor sampling of incidence angles, synthetic tests involving strong vertical changes in anisotropy orientations are poorly resolved and tend to yield a depth-averaged fabric. This explains why our preferred anisotropic solution presented in section 4.4.2 does not vary significantly with depth. Compared to the isotropic checkerboard tests, it is clear that anisotropic parameters are generally less-well resolved and yield more pervasive isotropic artefacts with magnitudes around 1% (Figure 4.3a-b).

To further investigate the resolution of dipping fabrics, we performed two additional synthetic tests (Supplementary Figures 4.13 and 4.14) discussed in

Text S3.

Checkerboard tests represent rather complex and geologically unrealistic structure. As discussed by VanderBeek and Faccenda (2021), strong lateral variations in anisotropic fabrics are ideal anomalies for regional teleseismic data as their signals are not easily removed by demeaning. To determine if our dataset is capable of constraining more realistic and smoother anisotropic heterogeneity, we construct a synthetic test based on SKS splitting observations from the area (Figure 4.3c). The target model contains a 200 km thick azimuthally anisotropic layer centered at 200 km depth; parameters do not vary with depth in the layer. The fast-axis azimuths within the layer are linearly interpolated from the station-averaged fast SKS polarization directions in the Becker et al. (2012) database (updated December 6, 2020). Station-averaged SKS split times (DT) are also interpolated to the layer and converted to P-wave anisotropic magnitude by the expression $1.51v_s DT/200$, where v_s is the mean shear-wave velocity between 100 and 300 km depth in the AK135 velocity model (4.55 km/s) and the factor of 1.51 is the ratio between P- and S-wave anisotropy measured for a peridotite sample by Kern (1993). Relative delay times accurately reconstruct such an anisotropic layer (Figure 4.3c). The median azimuthal error in the solution is 12°. The depth of the anisotropic layer is correctly imaged albeit with vertical smoothing throughout the upper 400 km and ~50% of the true anisotropy amplitude are recovered (Figure 4.3d). If SKS splits reflect the complexity of mantle anisotropy beneath the study area, then relative delay time tomography should yield an unbiased recovery of such heterogeneity.

To further explore possible trade-offs between isotropic and anisotropic parameters, synthetic inversions were ran aimed at reconstructing our preferred isotropic (Figure 4.4) and anisotropic (Figure 4.5) models presented in section 4.4. To test if velocity anomalies present in our preferred isotropic

model could yield erroneous anisotropy, delays predicted through this solution were inverted for both isotropic and anisotropic parameters. Isotropic anomalies were faithfully recovered with minimal (generally <1%) anisotropic perturbations (Supplementary Figure 4.15). Delays predicted through our preferred anisotropic model were then inverted without (Supplementary Figure 4.16) and with (Supplementary Figure 4.17) anisotropy. Neglecting anisotropy yielded a solution nearly identical to our preferred isotropic model (Figure 4.4 vs Supplementary Figure 4.16) indicating that the anisotropic heterogeneity can be mapped into significant isotropic perturbations. The anisotropic inversion (Supplementary Figure 4.17) accurately recovered fabric strength and orientations (median azimuthal and dip error of 8° and 6°, respectively) as well as isotropic velocity structure.

Lastly, the fidelity of our anisotropic model is assessed by its ability to predict independent SKS splitting observations. Numerous SKS splitting studies have been carried out across Europe (see compilations by Becker et al., 2012; Wüstefeld et al., 2009) and the mantle anisotropic structure imaged by P-waves should be consistent with these observations. A detailed description of the method used to model the effect of anisotropy on a SKS waveform is addressed in Text S4 in the SI. The results of this analysis are presented in relation to the recovered P-wave anisotropy in section 4.5.2, where we show that our P-wave model predicts most of the observed SKS splitting patterns.

4.4   Tomographic Model

We present two tomographic models for the central Mediterranean region; one is purely isotropic (Figure 4.4) while the other includes 3D anisotropic
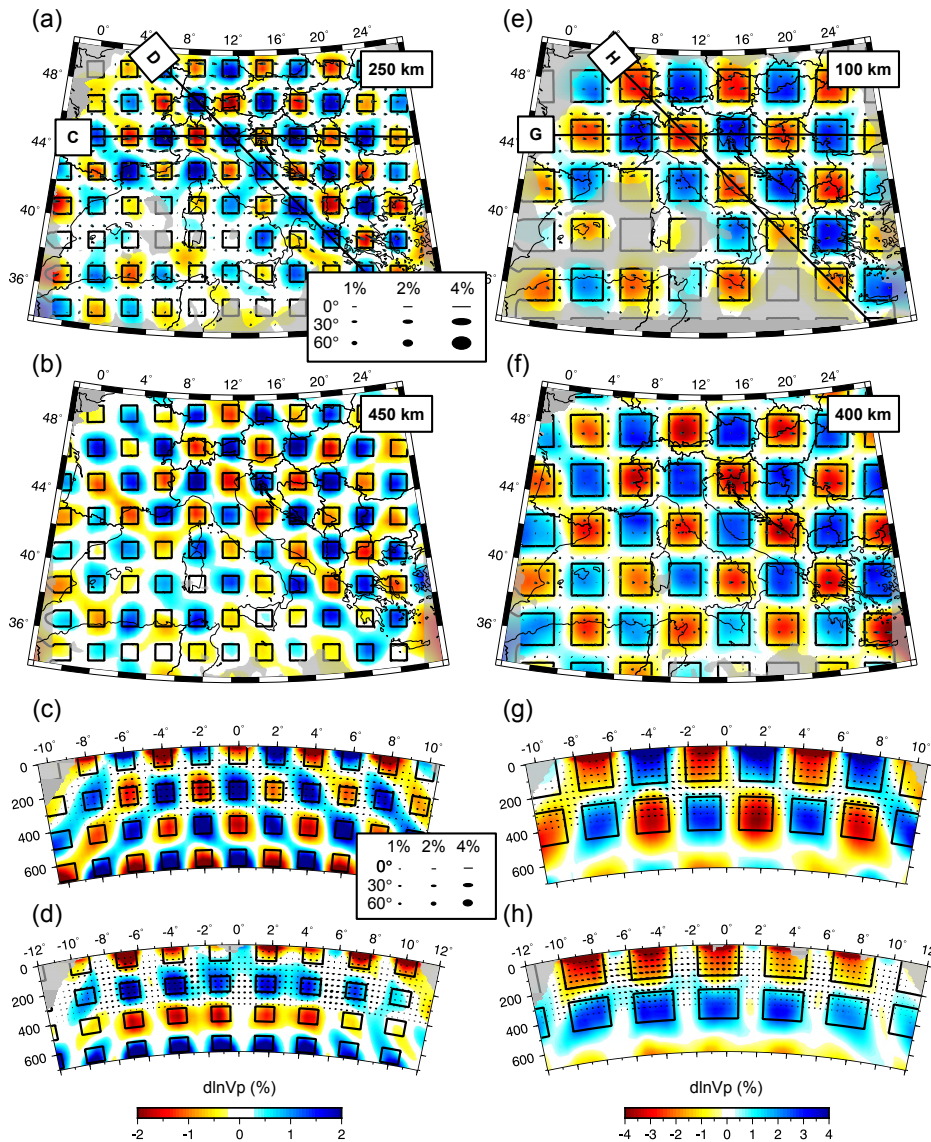
Figure 4.2: *Isotropic checkerboard test results. Reconstruction of 100 km cubic anomalies at (a) 250 km and (b) 450 km depth with cross-sections shown in (c) and (d) along the corresponding profiles drawn in (a). Reconstruction of 200 km cubic anomalies are shown at (e) 100 km and (f) 400 km depth with cross-sections shown in (g) and (h) along the corresponding profile lines in (e). In each panel, the location of the true anomalies are outlined in black and defined by alternating isotropic perturbations of +/-4%. While no anisotropic structure is present in the target model, the inversion does introduce some anisotropic perturbations. Anisotropy is represented by ellipse symbols where the major axis of the ellipse parallels the fast-direction and the minor axis scales linearly with the symmetry axis dip into the view plane such that fabrics parallel and normal to the cross-sections plot as lines and circles, respectively. In (a-b) and (e-f), small black quivers on the ellipses indicate the direction of dip into the earth. Legends in (a) and (c) depict reference ellipses for different fabric strengths and dips in the horizontal and vertical cross-sections, respectively. Areas of poor data coverage are masked in grey. Note the change in colorscale between panels a-d and e-h. While both synthetic models were defined with the same anomaly amplitudes, the amplitudes of the smaller blocks are more underestimated and a narrower value range is used so that the geometry of the imaged blocks is easily observed.*
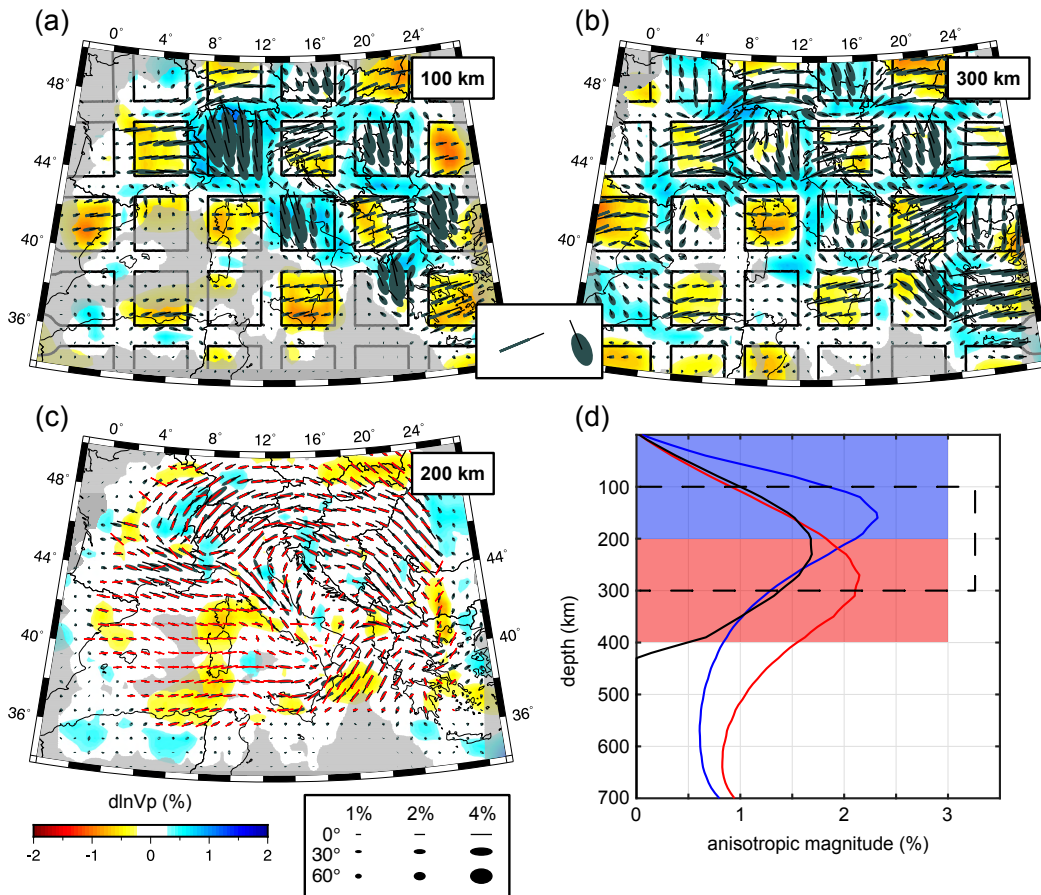
Figure 4.3: *Anisotropic checkerboard tests. Reconstruction of 300 km x 300 km x 200 km anisotropic blocks centered at (a) 100 km and (b) 300 km depth. Location of true anomalies are outlined in black and contain 6% P-wave anisotropy. The azimuth of anisotropy alternates between 22.5° and -67.5° while the dip varies from 0° to 45°. Symbols corresponding to the true fabrics are shown in the legend between panels (a) and (b). In (c), we plot the recovery of a 200 km-thick anisotropic layer centered at 200 km depth in which fast-axes parallel the fast SKS splitting direction and anisotropic magnitude is proportional to the split time (see section 4.3.3 for details). True orientations and magnitudes are shown by red quivers. No isotropic structure is present in the test models though the inversions introduce some isotropic artefacts. The average anisotropic magnitude as a function of depth is shown in (d) for the solutions in (a; blue curve) (b; red curve) and (c; black curve). The true depth distribution of anisotropy is shown by the shaded blue and red regions for models (a) and (b) and the dashed black line for model (c). Colorscale and anisotropy symbol legend (see Figure 4.2 for description) are shown beneath (c).*

heterogeneity (Figure 4.5). We first describe the primary P-wave speed per-turbations in our preferred isotropic solution and then consider how the in-clusion of anisotropic parameters modifies these anomalies. Lastly, we de-scribe anisotropic patterns beneath the Mediterranean as seen by teleseismic P-wave delays. We focus on mantle structures deeper than ~100 km and shallower than ~700 km where we have the best data coverage.

4.4.1 Purely isotropic solution

Our preferred isotropic tomographic model, iso-NEWTON21, is presented in Figure 4.4 (see Supplementary Figure 4.18(a-b) for additional maps at 500 km and 600 km depth and Supplementary Figure 4.19(a-f) for broader colorscale limits). It contains a number of fast anomaly features broadly consistent with previous seismic imaging studies. Specifically, the large-scale high-velocity zones underlying the Apennines, Calabrian arc, Alps, and Dinarides.

A prominent fast velocity feature is imaged extending along the Apennines (Apennines Fast Anomaly, ApFA) that at shallow depths (<200 km) is divided into a northern and southern segment by the Apennines Slow Anomaly (ApSA; Figure 4.4a). At depths greater that ~150 km, the ApFA is continuous throughout Italy and curves towards Sicily becoming the Calabrian Fast Anomaly (CFA; Figure 4.4b-d). Together, the ApFA and CFA form a single hook-shaped high-speed belt throughout the Italian peninsula. This high-speed belt dips toward the Tyrrhenian Basin and can, in most places, be traced to 600 km depth (Figure 4.4e-g).

Further north, the Alpine Fast Anomaly (AlFA) extends SW-NE across the entire Alps. Near 400 km depth (Figure 4.4d) the AlFA amplitudes become less laterally continuous separating into eastern- and western-AlFA segments. In cross-section H (Figure 4.4h), the central AlFA dips steeply to the southeast in the upper 400 km and then becomes horizontal at ~500 km. This trend is not evident in the western and eastern AlFA where the anomaly appears more vertically oriented.

At shallow depths (<200 km) the elongated Dinaric Fast Anomaly (DFA) can be traced from the eastern Alps to Greece following the trend of the Dinarides. The amplitude of this feature quickly diminishes below ~300 km (Figure 4.4b-d). The DFA generally appears to dip eastward in cross-section (Figure 4.4e-f).

Notable fast anomalies are imaged also underlying the Aegean Sea and Hellenic Peninsula (AeFA) and Carpathian Mountains (CaFA). Another high-speed feature is the Kabylides Fast Anomaly (KFA) along the North African margin that follows the Atlas Mountains and appears to connect with the Alboran Fast Anomaly (AFA) present eastward of the Strait of Gibraltar. The AeFA is characterised by high amplitudes (>2%) dipping northeastward and extending beneath Greece. The CaFA manifests as a small circular (∼200 km diameter) anomaly at 100-200 km depths becoming more laterally expansive around 300-400 km depth at which point it appears to connect with the AeFA. The KFA and AFA are weaker anomalies (0.5-1%) observed at depths greater than 200-300 km and down to ∼600 km (Figure 4.4e-f). Below ∼400 km depth, the KFA appears to connect with the deep portion of the ApFA (Supplementary Figure 4.18). The AeFA, CaFA, KFA and AFA are notable given their spatial correspondence with prominent geologic features. However, we note that they are near the edges of our study area and may be less-well resolved.

Several slow anomalies can also be observed in the iso-NEWTON21 model. Among them is the previously mentioned central-ApSA, located in central-west Italy along the Tyrrhenian coast. This anomaly interrupts the lateral continuity of the ApFA creating a well-known window (e.g., Kästle et al., 2018; Lucente et al., 1999; Piromallo & Morelli, 2003; Van der Meer et al., 2018) that separates the northern and southern ApFA at shallow depths; below ∼200 km the central-ApSA is no longer observed and the ApFA is continuous (Figure 4.4a-d). A prominent slow anomaly is imaged in the south of France (SFSA), in correspondence of the Massif Central already detected by Granet et al. (1995b) and Granet et al. (1995a). The SFSA stretches in the NW-SE direction in the first 100 km and, although with ever smaller magnitudes and dimensions, it persists down to 400 km of depth. A weaker (<1%) smaller-scale slow anomaly can be identified at shallow depths (<200

km) beneath the Po Plain (PpSA). A strong slow anomaly is detected at the boundary beneath the Adriatic and Ionian seas (AISA) off the southeastern tip of Italy where velocities are reduced by $<$-2% at $\sim$300 km (Figure 4.4c). Curiously, this feature is not spatially associated to any superficial geologic phenomenon. While the AISA is observed in other isotropic tomographic models (e.g., Li et al., 2008; Piromallo & Morelli, 2003; Spakman & Wortel, 2004), its origin is unclear. The Carpathian and Aegean Sea Slow anomalies (CaSA and AeSA, respectively) are two laterally extensive low-velocity zones restricted to the upper 200 km of our isotropic result. Lastly, we note the African Slow Anomaly (ASA) south of and generally parallel to the KFA. Above 100 km, the ASA manifests as three circular high magnitude anomalies ($<$-2%) and becomes more laterally continuous with depth.

4.4.2 Anisotropic solution

Our anisotropic model, ani-NEWTON21, is presented in Figure 4.5. Additional maps are shown at 500 km and 600 km depth in Supplementary Figure 4.18(c-d), with broader colorscale limits in Supplementary Figure 4.19(g-l) and differences in isotropic anomaly amplitudes between iso-NEWTON21 and ani-NEWTON21 in Supplementary Figure 4.20. The first-order effect of including anisotropic parameters in the inversion is to reduce the magnitude of isotropic anomalies (Supplementary Figure 4.20). The amplitude reduction is generally more significant for low-velocity relative to high-velocity zones. This is mostly due to the anisotropic symmetry system assumed for the mantle. Upper mantle anisotropy is largely the result of the preferential alignment of olivine crystals which tend to generate fabrics characterised by orthogonal symmetry with a single fast and two slower P-wave speed propagation directions (Karato et al., 2008). Because the anisotropic fabrics in our model tend to be oriented sub-horizontally, steeply propagating teleseismic

P-waves preferentially sample slower directions of the velocity surface resulting in an overall slower model requiring smaller reductions in isotropic velocity. This effect is particularly evident for the SFSA and AISA whose amplitudes are strongly reduced in coincidence with regions of elevated P-wave anisotropy ($\sim$2%; Figure 4.5) and strong shear wave splitting ($\sim$1.5 s; Becker et al., 2012). At greater depths (300-400 km), the SFSA appears more spatially concentrated occupying a roughly circular region defined by slightly stronger P-wave speed reductions with respect to iso-NEWTON21. A similar effect is seen around the Pannonian Basin and the ASA where strong subhorizontal anisotropy is present. In contrast, the amplitude of the central-ApSA in ani-NEWTON21 is similar to iso-NEWTON21 as it occupies a region of relatively weak P-wave anisotropy.

The geometry of the high-velocity features in our ani-NEWTON21 model remains largely unchanged but we do observe a general reduction in magnitude (Supplementary Figure 4.20). This is most evident in the central-ApFA and in the AeFA. The amplitude reduction associated with the central-ApFA is coincident with an area of relatively weak P-wave anisotropy while the amplitude reduction in the Aegean region is associated with the presence of strong NNW-trending anisotropy dipping moderately ($> 30°$) to the north.

Model ani-NEWTON21 exhibits a large-scale circular pattern in anisotropy azimuth around the Italian peninsula most evident in map view at 200 and 300 km depth in Figure 4.5(b-c). Other primary anisotropic structures recovered by the inversion include the one located beneath the Alps where the fast axes of P-waves coincide with the elongation direction of the AlFA, trending WSW-ENE. Near the Eastern Alps the azimuths gradually turn toward SE-NW. These fabrics persist throughout the Dinarides and Pannonian Basin. The fast axes continue to rotate clockwise becoming more N-S in Adriatic Sea and SW-NE around Calabria. Throughout northern Africa fast axes aligned E-W are observed. On a smaller scale, anisotropic azimuths normal

to the strike of the adjacent fast anomalies are imaged immediately eastward of the northern-ApFA and northward of the CFA.

A diversity of dip angles are also observed in our tomographic model. Near-horizontal fabrics are widespread in the Ionian and Adriatic Seas as well as throughout the Dinarides and Pannonian Basin. In contrast, more steeply dipping fabrics are observed around the western edge of the Alps near the SFSA and in the areas surrounding the Northern Apennines, Aegean Sea and ASA. The steepest dipping fabrics are observed within the CFA and AeFA ($>30°$).

The magnitude of P-wave anisotropy recovered throughout the study area is generally 2-3%. Notable areas of weak anisotropy include the AlFA and central-ApFA/ApSA, while the strongest anisotropy is observed in association with the circular pattern around the southern edge of Italy and the AeFA.

4.5   Discussion

We focus our discussion on the geodynamic interpretation of the anisotropic model and how it differs from the purely isotropic solution and previously published isotropic and anisotropic models. First, we discuss the isotropic anomalies recovered by the ani-NEWTON21 model by presenting a 3D reconstruction of lithospheric slabs geometry, and by providing interpretations for the low-velocity features (section 4.5.1). Following a comparison between the anisotropic component of our P-wave model to anisotropy patterns derived from other studies (section 4.5.2), we take advantage of recently published geodynamic models to discuss the nature of upper mantle flow in the Central Mediterranean in light of the new anisotropic patterns (section 4.5.3).
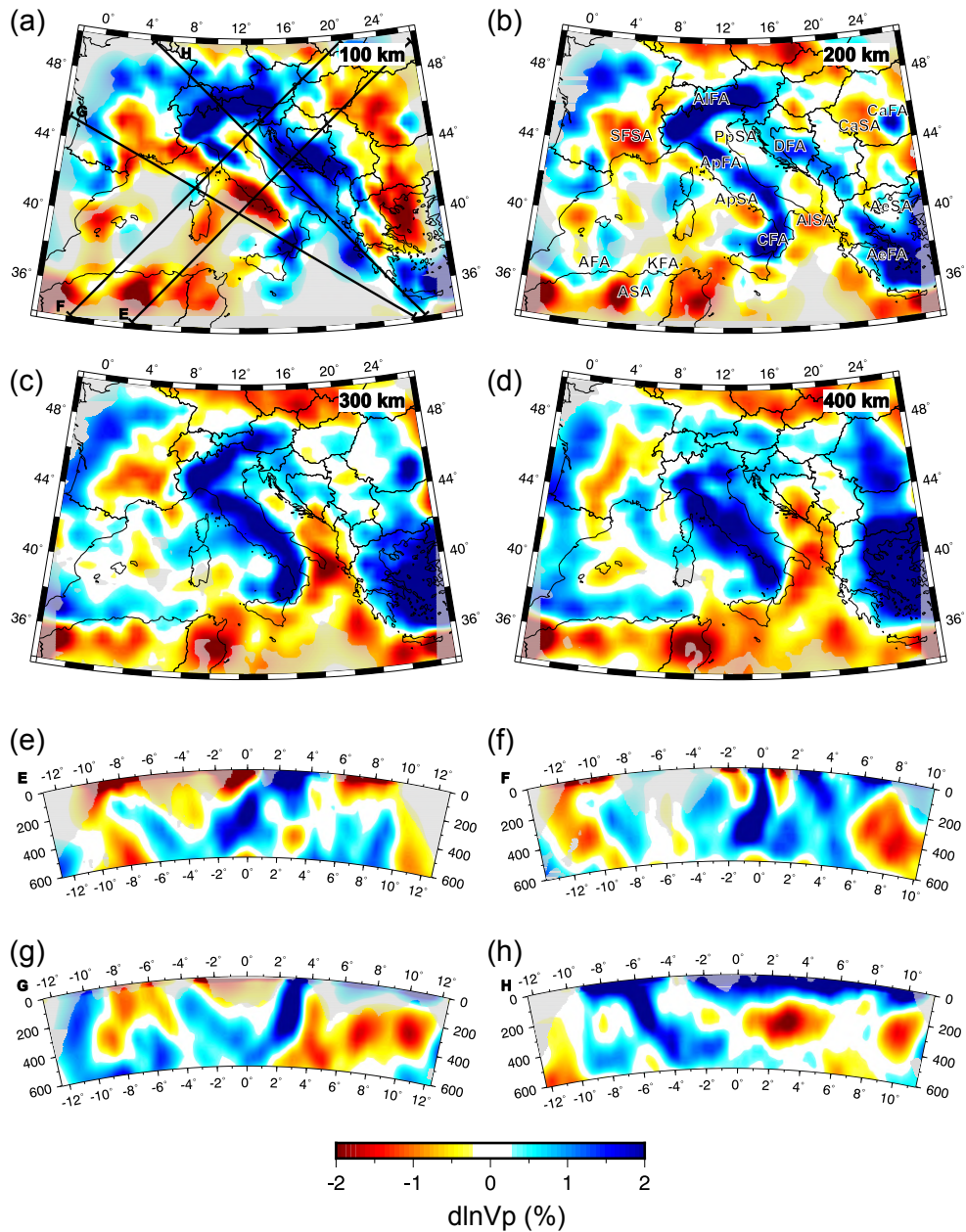
Figure 4.4: *The iso-NEWTON21 model. Depth slices are shown at (a) 100 km, (b) 200 km, (c) 300 km, and (d) 400 km depth. Vertical cross-sections are shown in (e-f) along the corresponding profile lines drawn in (a). Major anomalies discussed in the text are labeled in (b). Isotropic anomalies are plotted with respect to starting model. Areas of poor data coverage are masked in grey. See text for description of acronyms.*

4.5.1   A 3D Model of Central Mediterranean Slabs and Origin of Low-Velocity Zones

Consistent with previous studies, we interpret the major fast anomalies in ani-NEWTON21 (i.e. AlFA, ApFA, CFA, KFA, AFA, DFA, and AeFA) as
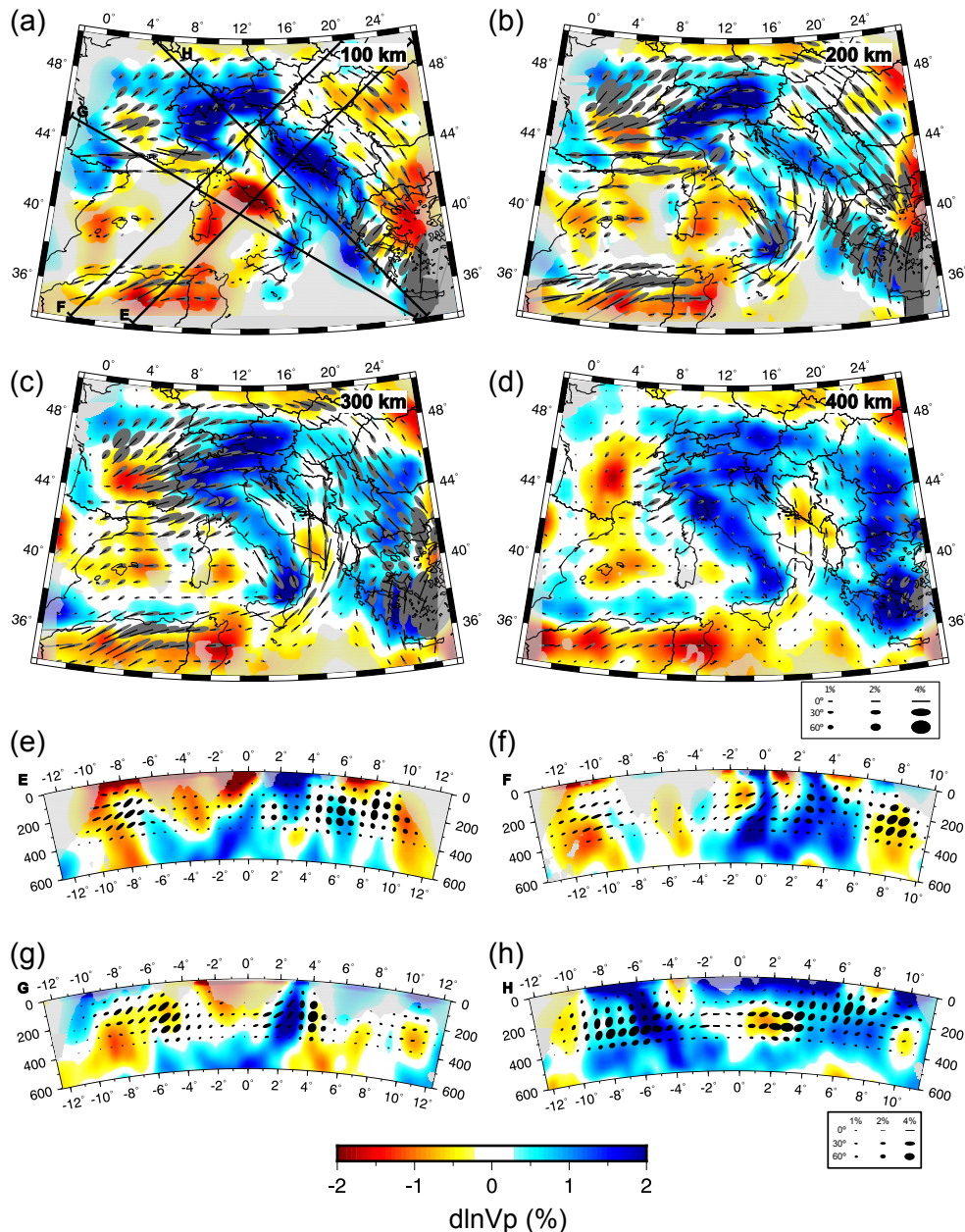
Figure 4.5: *The ani-NEWTON21 model. Depth slices are shown at (a) 100 km, (b) 200 km, (c) 300 km, and (d) 400 km depth. Vertical cross-sections are shown in (e-f) along the corresponding profile lines drawn in (a). Isotropic anomalies are plotted with respect to starting model. Anisotropy is plotted using ellipses as described in Figure 4.2. Areas of poor data coverage are masked in grey.*

descending lithospheric slabs. In Figure 4.6, Supplementary Movie S1 and Supplementary Dataset S3 we present a 3D model for the major slab segments present in the Central Mediterranean derived from these anomalies. Interpreting slab fragments from tomographic images can be difficult. Researchers often present either an interpretive cartoon (e.g., Hua et al., 2017;

Zhao et al., 2016) or chose a single velocity contour to capture a feature of interest (e.g., Paffrath et al., 2021). The former is an idealised representation of the data, while the later can often highlight extraneous features that obscure the structures of interest. Here, we follow a modified version of the strategy outlined by Portner and Hayes (2018) to extract interpretive but data-driven slab geometries from the tomographic model. For each potential slab fragment, the approximate trend of the slab is picked in multiple cross-sections normal to the strike of the high-velocity feature of interest. These slab guides are then sampled at regular 10 km intervals. At each sample point, the highest positive velocity anomaly within 100 km normal to the user-defined slab trend is chosen as the slab core. A smooth surface is then fit to the cloud of slab core points. Finally, any tomography model node within 20 km (i.e. two node spacings) of this surface with a velocity anomaly >0.8% is considered a slab core point. Together, these slab core points produce a surface that is rendered in ParaView. In total, we identify four main slab segments (Figure 4.6a) which are discussed in detail below.

The AlFA is interpreted as the Alpine slab composed of European lithosphere descending southward beneath the Adriatic plate (Figure 4.5; 4.6a,b). The Alpine slab is further divided into an Eastern, Central, and Western segment characterised by changes in dip. The Eastern Alps slab is nearly vertical as previously imaged by several seismic tomographic models (Hua et al., 2017; Kästle et al., 2019; Koulakov et al., 2009; Lippitsch et al., 2003; Paffrath et al., 2021; Zhao et al., 2016). The ani-NEWTON21 model does not identify any subducting body in the first 200-250 km of depth at the far eastern edge, which might indicate an ongoing shallow horizontal slab tear. The Central Alps slab dips steeply towards the southeast becoming more horizontal at ~500 km (Figure 4.6b) and may be separated at depth from the eastern Alpine slab by a vertical tear (Figure 4.6a). However, the smoothness of the tomographic image makes it difficult to discern if the reduction in slab

amplitude in this region represents a true absence of lithospheric material. The western Alpine slab dips more steeply southward relative to the central portion and does not flatten at depth. All three segments of the Alpine slab reach the transition zone. This is in contrast to previous studies which generally image a much shallower western Alpine slab (Hua et al., 2017; Kästle et al., 2019; Koulakov et al., 2009; Lyu et al., 2017; Zhao et al., 2016). However, the distinction between the northern ApFA and western AlFA become more ambiguous with depth.

At shallow depths ($<\sim$ 200 km), the ApFA and DFA are interpreted as the westward and eastward descending margins of the Adria plate. The two dipping bodies reflect the double-sided subduction of the Adria plate as described by Király et al. (2018). Deeper portions of the ApFA form a continuous band with the CFA (Figure 4.5a-d) which are interpreted as the subducting and retreating Ionian lithosphere (Figure 4.6a,c). The northern most segment, anchored to the surface beneath the Northern Apennines, dives almost vertically and continuously down to a depth of $\sim$660 km where it begins to flatten across the mantle transition (Figure 4.5f) zone as predicted in models by Lucente et al. (2006) and Piromallo and Morelli (2003). As described in previous studies (Amato et al., 1993; Lucente et al., 1999; Piromallo & Morelli, 2003; Selvaggi & Chiarabba, 1995; Spakman et al., 1993; Spakman & Wortel, 2004; Van der Meer et al., 2018; Zhu et al., 2012), the southern end of the Ionian slab, often referred to as the Calabrian slab, subducts northwestward ultimately flattening and stagnating in the mantle transition zone (Figure 4.5g). Consistent with prior seismic imaging results (El-Sharkawy et al., 2020; Giacomuzzi et al., 2012; Neri et al., 2009; Scarfì et al., 2018), the Calabrian slab appears to be progressively tearing apart in eastern Sicily (Figure 4.6a,c). The geometry of the window between the Northern Apennines and Calabrian slabs is widely debated. Its origin is uncertain but may have been

generated from a laterally expanding tear initiated in response to the subduction of a thick continental promontory located in the Central Apennines (e.g., Lucente et al., 2006). This mechanism was reproduced numerically by Lo Bue et al. (2021) who showed that the presence of structural heterogeneities within the Adria plate may have played a role on the formation of the slab window below the Central Apennines.

The upper 200 km of the northern Dinaric slab sinks steeply toward the NE into the asthenospheric mantle (Figure 4.5f; 4.6d). At greater depths, this slab segment appears to reverse dip toward the SW. However, its true trend is difficult to discern due to the vicinity of the AlFA and a nearby fast anomaly that could also reflect the continuation of the Dinaric slab in a more NE direction. Further south, the shallow portion ($<\sim$ 250 km) of the Dinaric slab continues to dive in the NE direction. We observe a laterally extensive gap from $\sim$200 km to $\sim$300 depth that separates the shallow Dinaric slab from possibly related deeper NE trending lithospheric remnants (Figure 4.6a,d). Moving toward the Aegean Sea the model captures a portion of the Hellenic slab subducting north-eastward into the lower mantle as imaged by prior larger-scale studies (e.g., Zhu et al., 2012). Near the surface, a gap separates the Hellenic from the Dinaric slab but they may be attached at depth (Figure 4.6d).

Lastly, the KFA and AFA along the northern edge of the African continent are interpreted as possible pieces of the Kabylides and Alboran slabs (Chertova et al., 2014; van Hinsbergen et al., 2014; Van der Meer et al., 2018). While these two slab fragments are separated by a large gap (Figure 4.6a), we note that they may be poorly resolved as they are near the less well-instrumented southern edge of our model. Together with the ApFA, we suggest that the CFA, KFA and AFA are portions of the subducted Ionian oceanic lithosphere that since the Oligocene rolled back partly towards the italian peninsula and partly towards the Maghreb area (Chertova et al., 2014).

A variety of geodynamic processes may explain the low-velocity zones present in our ani-NEWTON21 model. The SFSA could reflect a thermal and or melt anomaly associated with an asthenospheric plume that may have driven Massif Central volcanic activity in the Cenozoic (Granet et al., 1995a; Granet et al., 1995b). The upwelling could generate from buoyancy forces internal to the plume material or in response to the subduction of the Ionian plate (Faccenna et al., 2010; Yang & Faccenda, 2020). We note that the SFSA circular shape in the ani-NEWTON21 model is more consistent with geodynamic predictions of a localised upwelling rather than the elongated SFSA shape observed in iso-NEWTON21. The ApSA likely reflects the thermochemical anomalies caused by the opening of the slab window below the Central Apennines and that led to the emplacement of the volcanic fields active in central West Italy over the last 1 My (Peccerillo, 2017). Most low velocity anomalies at shallow depths, such as the one beneath eastern Sardinia and in the Liguro-Provençal basin, correspond to oceanic regions of the Central Western Mediterranean and can be related to the opening of back-arc basins (Zhu et al., 2012). The AeSA is attributable to the extensional tectonic regime and continental lithosphere thinning induced by the rollback of the Hellenic slab.

Although generally the presence of low-speed anomalies is attributed to changes in the temperature of the upper mantle, our results show how including anisotropy in the inversion greatly reduces their magnitude (Supplementary Figure 4.18). Consequently, it can be deduced that not only temperature or compositional variations, but also anisotropy has a strong effect on the appearance of such anomalies in seismic images. Bezada et al. (2016) and VanderBeek and Faccenda (2021) clearly demonstrate how neglecting anisotropy could lead to errors in the interpretation of isotropic velocity models in subduction zone settings. In particular, the slow anomalies appearing below the Adriatic and Ionian Seas (AISA) in our isotropic model iso-NEWTON21

and in many body-wave tomographic images and whose interpretation remained elusive, are not present in ani-NEWTON21. The AISA is located in a region of sub-horizontal anisotropy fabrics highlighting its potential anisotropic origin.

The location and geometry of the fast anomalies interpreted as sinking slabs do not differ substantially between the iso- and ani-NEWTON21 models. An exception is the appearance of the deeper portion of the Dinaric slab in ani-NEWTON21 as a result of the positive velocity shift occurring when the effect of the sub-horizontal anisotropy is taken into account. At depths greater than 400 km further differences between the fast anomalies in the two models are found in the western part of the study region (Supplementary Figure 4.18). As demonstrated by previous studies (e.g., Faccenna et al., 2001; Lo Bue et al., 2021) this area, at these depths, is mainly influenced by the presence of the stagnating Ionian slab lying beneath the Central Mediterranean basin as in model ani-NEWTON21 and not beneath Southern France and Northern Spain as in model iso-NEWTON21 where such fast anomalies appear to be artifacts due to having neglected the seismic anisotropy. The fact that fast anomalies appear to be mildly affected by including anisotropy can be explained with the strong temperature difference (up to 1000 °C) likely existing between the slab cold core and the surround hot mantle. Such a thermal contrast produces strong isotropic (true) fast anomalies that are seen in both the isotropic and anisotropic inversions. On the other hand, positive thermal anomalies at sub-lithospheric depths are on the order of few 100s °C causing relatively small variations in isotropic elastic moduli. The resulting slow velocity anomalies are thus more likely to trade-off with anisotropic structures and, in general, different inversion methods.
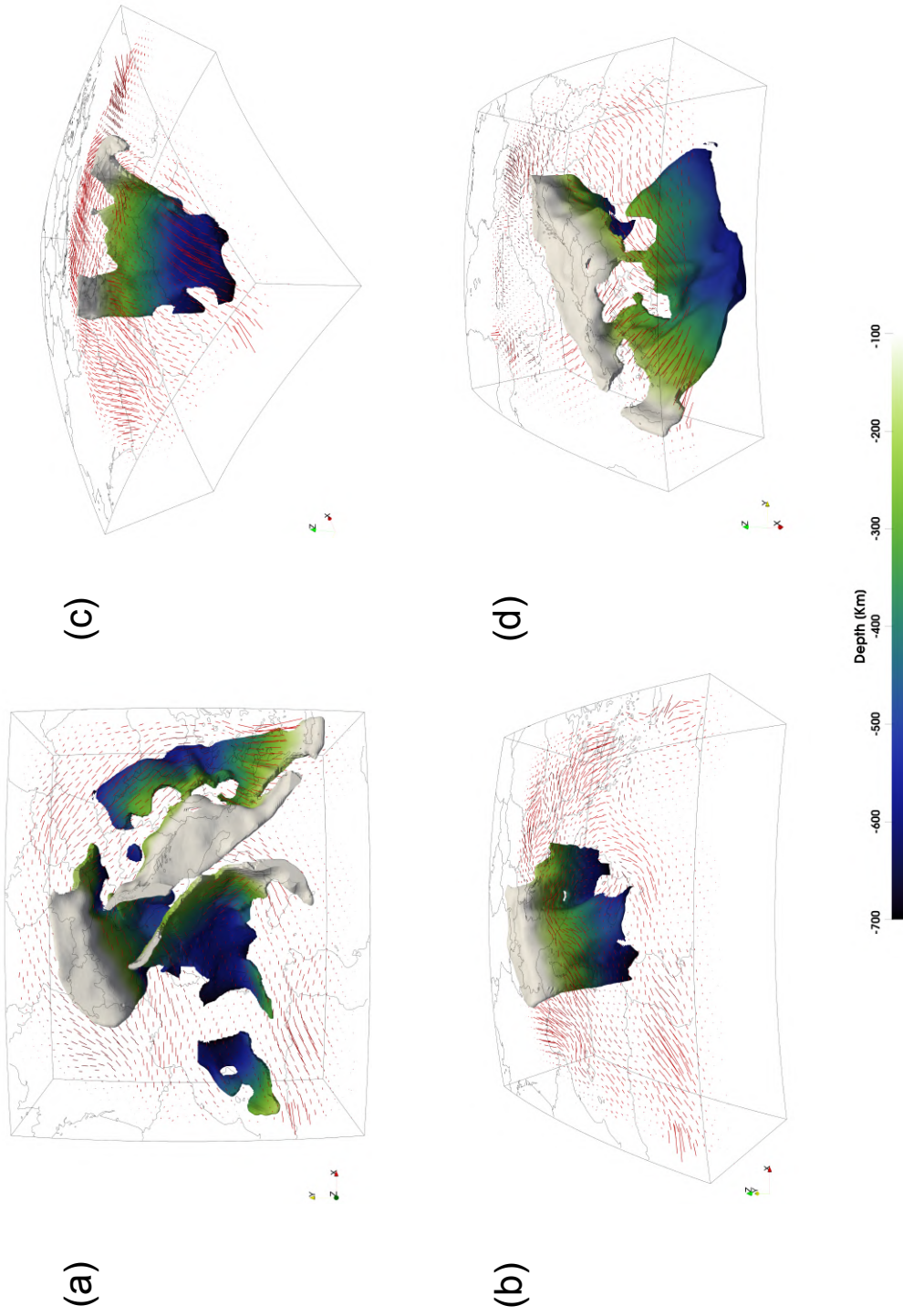
Figure 4.6: *A 3D reconstruction of slab geometries beneath the central Mediterranean with P-wave fast axes at 200 km depth. All slab segments are show from above in (a) with perspective views of the (b) Alpine, (c) Ionian, and (d) Dinaric and Hellenic slabs shown in subsequent panels. Slabs are coloured by depth. Cartesian x-, y-, and z-coordinates correspond to east, north, and vertical directions. Anisotropy quivers are scaled by magnitude.*

4.5.2   Comparison of Anisotropic Structure with Observations

Provided our ani-NEWTON21 accurately images mantle anisotropic structure, it should be able to independently predict SKS splitting observations in the Central Mediterranean. In Figure 4.7, SKS splits from the database of Becker et al. (2012) (updated December 6, 2020) averaged in 0.5° bins are compared to those predicted through ani-NEWTON21 as described in section 4.3.3. While SKS splits are a depth integrated measurement, they have good lateral resolution (depending on station spacing) and are primarily sensitive to upper mantle anisotropy with limited sensitivity to isotropic velocity (e.g., Sieminski et al., 2007) and thus provide an ideal basis for comparison.

While the ani-NEWTON21 model generally predicts spatially smoother trends in fast splitting directions, they are largely consistent with the observations; the prediction error is $<22°$ for 50% of the observations and $<19°$ if we only consider split times ≥ 1 s (Supplementary Figure 4.21); errors are larger by 1° if we consider station-averaged rather than geographically binned splitting parameters. Fast directions agree well through the southern tip of the Italian peninsula into Sicily, the Alpine region and along southern margin of France into Spain. Observations and predictions also match in the Carpathians, drawing a large-scale circular pattern that from the Bohemian Massif continues south to the Hellenic peninsula. Recent studies interpret the predominantly NW-SE orientation also observed in the present work, as due to the compression exerted by the Adriatic plate (Qorbani et al., 2016), while the circular pattern as the result of a toroidal flow associated with the subduction of the aforementioned plate (Song et al., 2019).

Notable areas of disagreement include the Northern Apennines, Dinarides, and the Massif Central in southern France where errors in the predicted fast axes approach 90°. Such discrepancies could be attributed to a number of factors. For example, poorly constrained anisotropy in the upper ~100

km. SKS splitting is biased toward the anisotropic structure at shallower depths where teleseismic P-wave raypaths become more vertical and, consequently, less sensitive to anisotropy. Including local earthquake arrivals into the inversion to better constrain shallower structure could yield an anisotropic model more consistent with the SKS data. Another possibility could be changes in the mineral fabric type creating the seismic anisotropy. Here we have assumed anisotropy is largely due to olivine A-type fabrics with a fast symmetry axis (e.g., Karato et al., 2008). However, A-type or AG-type fabrics (Mainprice, 2010) characterised by a slow symmetry axis are also possible which would manifest as a 90° rotation of the imaged symmetry axis in the ani-NEWTON21 model. Elastic anisotropy from lower-order symmetry systems (e.g., orthorhombic) could also generate discrepancies between P-wave fast axes and fast SKS splitting directions. Additionally, unresolved dipping fabrics could yield orthogonal P and SKS polarization fast axes (see Supplementary Figure 4.22; Song & Kawakatsu, 2012), thus explaining the discrepancies between the SKS splitting azimuths predicted from P-wave models and those observed. Lastly, we acknowledge that split times are not particularly well-fit considering the residual mean and standard deviation are -0.672 s and 0.965 s, respectively (Supplementary Figure 4.21). This could be related to the aforementioned factors as well as assumptions made in converting P-wave anisotropy parameters into an elastic tensor (section 4.3.3).

A particularly interesting area of disagreement between predicted and observed SKS fast directions is the Northern Apennines where our model predicts ENE-WSW splitting which is nearly orthogonal to the observed NNW-SSE trends. Our results (both in terms of SKS splitting and P-wave fast azimuths) are consistent with azimuthal P-wave tomography of Hua et al. (2017) who also incorporated local earthquake arrival times. Recent ambient noise tomography by Kästle et al. (2022) also constrains E-W fast propagation directions at crustal depths suggesting the SKS splits are not likely the result

of crustal fabrics. Using Pn arrivals, Díaz et al. (2013) constrain mantle anisotropic velocity structure just below the Moho and find fast P-wave propagation directions that generally parallel SKS splits in the Northern Apennines. Similar orientations are also constrained by adjoint surface wave tomography in the depth range 75-125 km (Zhu & Tromp, 2013). Together, these observations suggest strong lithospheric/shallow mantle fabrics control SKS splitting and such anisotropy is not well-constrained by our teleseismic P-wave dataset.

The azimuthal anisotropy component of ani-NEWTON21 (Figure 4.5) is generally consistent with the larger-scale anisotropic Rayleigh wave tomography of Zhu and Tromp (2013). For example, the sub-circular anisotropy pattern observed by Zhu and Tromp (2013) in their model EU_{60} at 125 km of depth beneath Eastern Alps and Pannonian basin is recovered by model ani-NEWTON21 as well and found at all depths (Figure 4.5). Consistently with ani-NEWTON21 in the Central and Eastern Alps, the P-wave anisotropic tomography of Hua et al. (2017) shows fast velocity directions parallel to the mountain chain from the surface down to ∼500 km of depth. The same result is confirmed by shear-wave splitting studies of Barruol et al. (2011) and Bokelmann et al. (2013). The authors showed an arc-shaped anisotropy pattern beneath Western and Eastern Alps, consistent with our result along the southern French coast and beneath Central and Eastern Alps. On the contrary a mismatch is observed in correspondence of the Western Alps, where Barruol et al. (2011), Hua et al. (2017), and Zhu and Tromp (2013) observe NW-SE azimuths, interpreted by the latter as the results of the mantle flow induced by subduction and retreating and the peaks of anisotropy magnitude around the Alpine fast anomaly as induced by the sub-lithospheric mantle deformation.

With the exception of the Southern France, model ani-NEWTON21 (Figure 4.5) exhibits steep dipping fabrics mainly in the areas near subduction

zones (e.g., Calabria, Alps, Northern Apennines and Hellenic peninsula). This may be caused by the near-vertical subduction of the slabs largely observed in the first 400 km depth, e.g. in the Western Alps and Northern Apennines, that induces near-vertical mantle flow. In agreement with the fact that positive radial anisotropy ($V_H > V_V$) is associated with horizontal flow and negative radial anisotropy ($V_V > V_H$) is associated with vertical flow, Hua et al. (2017) show negative V_P radial anisotropy (i.e. $V_{PV} > V_{PH}$) in correspondence of dipping fast velocity anomalies, i.e. close to the nearly-vertical European and Adriatic slabs (i.e. Alps and Apennines). At ~410 km depth, the model proposed by Hua et al. (2017) exhibits a widespread positive radial anisotropy (i.e. $V_{PH} > V_{PV}$), thus a dominant horizontal mantle flow. This is confirmed by our ani-NEWTON21 model that, despite the assumption of isotropy below 400 km depth, exhibits a gradual decrease in dip angles with respect to the shallower layers (~<400 km) in correspondence of the main subduction zones, that may have induced nearly-horizontal mantle flows.
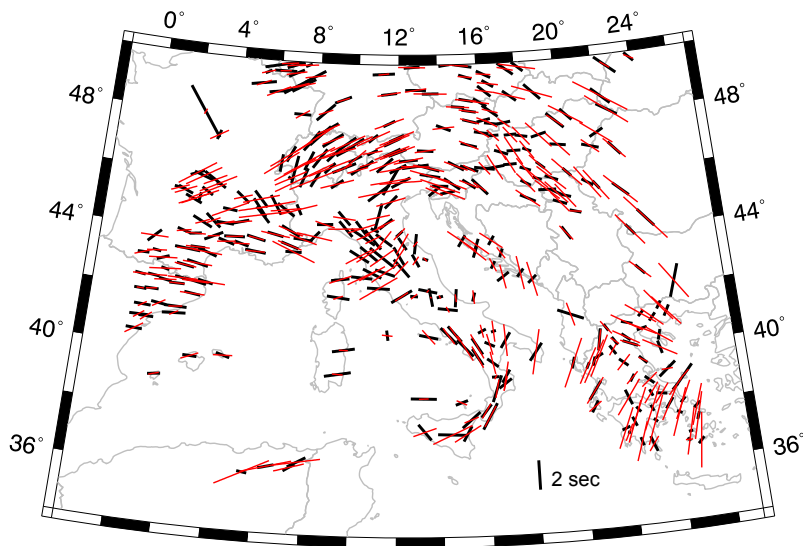
Figure 4.7: *Comparison between predicted (red) and observed (black) SKS splits. Black bar at 36°N, 18°E is the 2 s scale for the splits.*

4.5.3   Comparison of Anisotropic Structure with Geodynamic Predictions

The P-wave anisotropic structure agrees well with geodynamic models of the region (e.g., Lo Bue et al., 2021), according to which the anisotropic patterns can be interpreted with sub-vertical flows generated by subduction and the presence of horizontal flows of asthenospheric material around the main slabs related to the pressure exerted by their Mid-to-Late Cenozoic horizontal motion. This is true especially in the Central-Eastern Alpine and Calabrian arcs where the fast azimuths preferentially orient trench-parallel. In the Alpine area, this pattern can be explained with the retreat of the slabs attached to the Eurasian plate southern margin as a result of their negative buoyancy and of the compression exerted by the Adria plate. In the Calabrian arc, trench-parallel anisotropy is likely related to the southeastward retreat of the Ionian slab (Civello & Margheriti, 2004; Faccenna et al., 2014; Faccenna et al., 2007; Jolivet et al., 2009). Similarly to what has been previously demonstrated by (Faccenda & Capitanio, 2013) on a similar synthetic scenario, the mantle below the subducting plate is subject to the pressure exerted by the slab rollback. Consequently, a horizontal flow and trench-parallel extension establishes below the trench. The mantle flow is directed toward the slab lateral margins and beyond toward regions of lower pressure, i.e., back-arc basins, where it orients trench-perpendicular. The predicted and observed SKS splitting data confirm the first of these two situations, while the trench-perpendicular fabric is suggested only by our anisotropic P-wave model due to the lack of receivers in the Tyrrhenian Sea for measuring SKS splitting. Therefore, the splitting measurements together with the P-wave anisotropy are in agreement with what Faccenda and Capitanio (2013) observed for a similar modelled scenario. The trench-parallel P- and SKS-wave fast azimuths in the Dinarides can be related to (i) the

NE-oriented compression exerted by the eastern Adria plate margin causing trench-parallel extension and seismic anisotropy, and/or the strong influence exerted by the retreating Aegean trench that is drawing mantle material from the Alpine area and toward the Aegean back-arc basin.

4.6 Conclusions

We presented new isotropic and anisotropic tomographic images of the upper mantle in the Central Mediterranean area, obtained by inverting relative P-wave delay times from teleseismic events reported by the International Seismological Centre. The primary effect of including anisotropic parameters in the inversion is a reduction in the magnitude of low-velocity anomalies highlighting how such features could be artefacts in purely isotropic images. A three-dimensional reconstruction of the lithsopheric slabs beneath the Central Mediterranean is derived from our preferred anisotropic velocity model, ani-NEWTON21. Three main segments of subducting lithosphere are identified belonging to the (1) Eurasian, (2) Ionian, and (3) Adria plates. These slab segments are further interrupted by a number of slab windows and tears. The entire Central Mediterranean upper mantle is characterised by substantial heterogeneity in P-wave anisotropic structure particularly at 200-300 km. In general, the fast P-wave azimuths trend parallel to the trenches in the foreland and progressively rotate toward the trench retreating direction in the mantle wedge/back-arc region. These P-wave derived anisotropic fabrics are largely consistent with those inferred from SKS splitting and Rayleigh wave tomography studies and with predictions from geodynamic models. Our study demonstrates the importance of including anisotropy in the inversion of teleseismic P-waves as it pertains to the imaging of isotropic heterogeneity as well as generating seismic models that are consistent with other independent datasets (e.g. SKS splitting). Considering the success of

this study using ISC bulletin delays, we expect higher resolution anisotropic models could be obtained using a rigorously quality controlled dataset of multi-frequency delay time measurements such as that recently generated for the Alpine region (Paffrath et al., 2021).

4.7   Data Availability Statement

Included with the publication of this manuscript are the iso-NEWTON21 (Supplementary Dataset S1), ani-NEWTON21 (Supplementary Dataset S2), and our model for central Mediterranean slabs (Supplementary Dataset S3) all stored as NetCDF 4 files. These files are available for download via FigShare.

Acknowledgments

Supplementary Material

Additional Supporting Information (Files uploaded separately)

Dataset S1 iso-NEWTON21 Tomographic Model

Dataset S2 ani-NEWTON21 Tomographic Model

Dataset S3 Central Mediterranean Slab Model

Movie S1 A 3D reconstruction of slab geometries beneath the central Mediterranean with P-wave fast axes shown by quivers (scaled by anisotropic magnitude) at 200 km depth.

Text S1. Selection of regularization parameters

To identify appropriate regularization values (i.e. damping and smoothing factors, λ_d and λ_s, respectively), we constructed L-curves (Supplementary Figure 4.9) which plot the squared-norm of the data residual vector against the squared-norm of the model perturbational vector.

The model norm comprises the fractional velocity perturbations (i.e. the change in velocity with respect to the starting model inversely weighted by the initial model velocities) and the anisotropic magnitude perturbations both of which are on the order of a few percent. Because both values describe changes in velocity, they are directly comparable.

Ideal solutions are considered those near the corner of the L-curve where an increase in model norm does not result in an appreciable decrease in data residuals.

We first ran a series of purely isotropic inversions at different λ_d values for different fixed ratios of λ_s/λ_d such that the relative influence of damping versus smoothing on each solution remained constant. The preferred λ_s/λ_d ratio was selected such that further reductions in this ratio did not yield appreciable reductions in data residuals while smoother solutions more rapidly

degraded the data fit and generally required a greater number of perturbations to achieve similar RMS residual values relative to less smooth solutions (Supplementary Figure 4.9). A series of anisotropic inversions were subsequently run in which the damping applied to the mean P-wave slowness perturbations was varied across different ratios of slowness-to-anisotropic parameter damping assuming the same λ_s/λ_d for both parameter sets identified from the aforementioned isotropic inversions. Considering that both isotropic and anisotropic heterogeneity are likely significant beneath the study area, we chose the anisotropic damping ratio such that the norm of the fractional velocity perturbations equals the norm of the anisotropic magnitude perturbations. The L-curve for the anisotropic inversions using this ratio is shown in Supplementary Figure 4.9. The parameters adopted for our preferred isotropic and anisotropic solutions are shown in Table 4.1.

Text S2. Model resolution

Anisotropic imaging with teleseismic delay times has some important limitations. Because the delay times are demeaned, they only illuminate changes in velocity relative to an unknown average value. The implication for anisotropic imaging is that there may be a systematic bias in the recovered anisotropic parameters as demeaning effectively removes the average back-azimuthal signal in delay times. For this reason, a laterally homogeneous isotropic or anisotropic layer spanning the entire model cannot be imaged. However, provided that the imaging volume contains heterogeneous anisotropic structure, this back-azimuth trend will amount to a constant value and not impart any bias on the recovered anisotropic parameters. See section 4 of VanderBeek and Faccenda (2021) for further discussion. Considering the variety of splitting parameters observed across the central Mediterranean, the mantle appears sufficiently heterogeneous such that anisotropy can be accurately recovered–an inference that has been verified through our synthetic

tests.

The steep incidence angles of teleseismic ray paths also adversely affect model resolution. In particular, resolution is poor at depths ∼75 km where rays are steepest and ray crossing is limited. Therefore, anomalies in the uppermost lithosphere are not interpreted. Limited sampling of incidence angles can result in poor vertical resolution of anisotropic fabrics. However, good azimuthal teleseismic ray coverage is sufficient to constrain anisotropic domains characterized by horizontal or dipping fabrics (VanderBeek & Faccenda, 2021). Another consequence of restricted incidence angle coverage is that the full magnitude of directional velocity variations are not sampled causing an underestimation of anisotropy strength as shown in our synthetic tests. Lastly, with imperfect data coverage, trade-offs between isotropic and anisotropic parameters are likely. However, the trade-off appears to be largely one-sided in that unaccounted for or poorly imaged anisotropic heterogeneity creates significant isotropic artefacts but truly isotropic structure does not tend to generate anisotropic artefacts as demonstrated by Vander-Beek and Faccenda (2021) and our own synthetic tests.

The derivative weight sum (DWS; Toomey & Foulger, 1989), i.e. the summation of travel-time partial derivatives with respect to slowness at each perturbational node, provides an indirect estimate of parameter resolution attaining higher values in more densely sampled regions of the model. Based on the checkerboard resolution tests discussed in section 4.3.3 of the main text, we find that isotropic structure in areas with DWS > 100 is generally well-recovered. We present maps of the DWS in Supplementary Figure 4.10 from which we can see that the upper mantle beneath Italy and mainland Europe is well sampled by teleseismic rays. In contrast, the dearth of stations throughout the Mediterranean Sea and north Africa results in a clear reduction in DWS and by inference less wellresolved velocity structure. However,

teleseismic rays travelling to stations throughout mainland Europe do illuminate this area at depths greater than ∼150 km.

The DWS lacks information regarding how directionally well-sampled are the model parameters which is important for assessing resolution of anisotropic structure. To assess directional bias, we use the azimuthal mean resultant length (AMRL; Fisher, 1995; Zhang et al., 2009) defined as the length of the vector resulting from an averaging of the x- and y-components of all ray segment unit vectors sampling a given perturbational node. If a node is directionally well-sampled, the AMRL tends toward zero while the AMRL will approach 1 in areas with a strong directional bias. Based on our checkerboard tests (section 4.3.3), AMRL < 0.5 indicates a node is sufficiently directionally sampled to image anisotropic structure. Maps of the AMRL for our study are shown in Supplementary Figure 4.11. It is found that the AMRL reflects the DWS (Supplementary Figure 4.10) indicating that areas of high data density correspond to areas of good directional coverage. The Mediterranean Sea region is primarily sampled by rays coming from the south and east, and travelling to stations on mainland Europe resulting in high AMRL values.

Text S3. Resolution of dipping fabrics

To further investigate the resolution of dipping fabrics, we performed two additional synthetic tests for three 300 km x 300 km x 200 km anisotropic anomalies centered at 200 km depth beneath the Western Alps, Dinarides, and Calabria–three areas with unique anisotropic fabrics in the preferred tomographic solution. We prescribed 6% anisotropy to these three anomalies with an azimuth at a high-angle to that imaged in the preferred model and created two synthetic datasets for shallowly (30°) and steeply (60°) dipping

fabrics. The true and recovered anomalies are shown in Supplementary Figures 4.13 and 4.14. Both the azimuth and dips are well-imaged for both synthetic models with amplitudes being more under-estimated for the steeper fabrics.

Text S4. SKS from P-wave tomography

We use the method of Rümpker and Silver (1998) to model the effect of anisotropy on a SKS waveform approximated as a Ricker wavelet with a central period of 10 s. The method involves progressively rotating and time shifting a waveform, initially linearly polarised in the back-azimuth direction, through a series of anisotropic layers. The splitting parameters (i.e. time delay and fast direction) are computed on the resulting waveform following Silver and Chan (1991). To compute the time shifts for each layer, we use the Christoffel equations and take into account variations in ray incidence. The elastic tensor in principal coordinates at every point in our model is defined from the P-wave velocities as:

$$
\begin{bmatrix}
[v_p(1-f_p)]^2 & C_{11}-2C_{66} & C_{11}-2C_{66} & 0 & 0 & 0 \\
 & [v_p(1-f_p)]^2 & C_{11}-2C_{66} & 0 & 0 & 0 \\
 & & [v_p(1+f_p)]^2 & 0 & 0 & 0 \\
 & & & [gv_p(1+hf_p)]^2 & 0 & 0 \\
 & \text{Symmetry} & & & [gv_p(1+hf_p)]^2 & 0 \\
 & & & & & [gv_p(1-hf_p)]^2
\end{bmatrix}
$$

where vp is the mean isotropic P-wave velocity; fp is the anisotropic magnitude; g is a constant compressional-to-shear wave speed ratio assumed here to be 1.81; and h is a constant compressional-to-shear wave anisotropy magnitude ratio assumed to be 1.51. These values were taken from laboratory measurements of a peridotite sample by Kern (1993) who found $C_{12} \approx C_{13}$ and $C_{13} = C_{23}$. The tensor is then rotated such that the C_{33}-direction

parallels the P-wave fast direction in our model. SKS splits are computed for all stations in the study area with observations listed in the compilation of Becker et al. (2012 updated 2020). Ray paths are predicted via the TauP toolkit (Crotwell et al., 1999) using the reported event-station back-azimuths and ranges. Ray paths are discretised into 10 km segments through which the splitting effect is computed. We present the results of this analysis in the discussion of our preferred tomographic models (section 4.5.1) and simply note here that our P-wave model predicts many patterns observed in prior SKS studies.

Table 4.1: *Inversion parameters summary table. Damping (λ_d) and smoothing (λ_s) factors, type of data (isotropic/anisotropic), rms, perturbation vector (dm) norm (calculated as $|dlnV| + |df|$, where dlnV is the fractional velocity perturbation vector and df is the anisotropic magnitude perturbation vector), iteration at convergence.*

name	λ_s/λ_d	λ_d	λ_s	data	rms	dm norm	iterations
iso-NEWTON21	200	6	1200	isotropic	0.5	2.73	3
ani-NEWTON21	200	6	1200	anisotropic	0.48	4.64	6
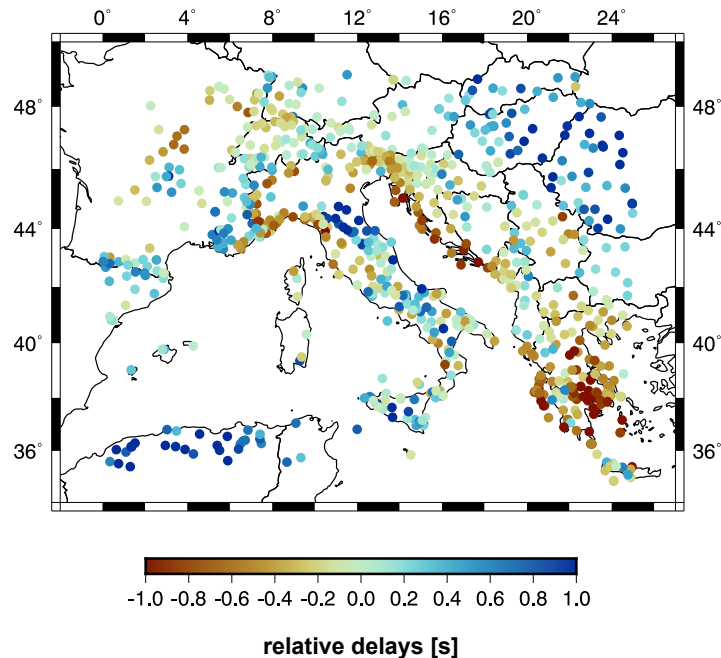
Figure 4.8: *Mean station delays with respect to model AK135.*
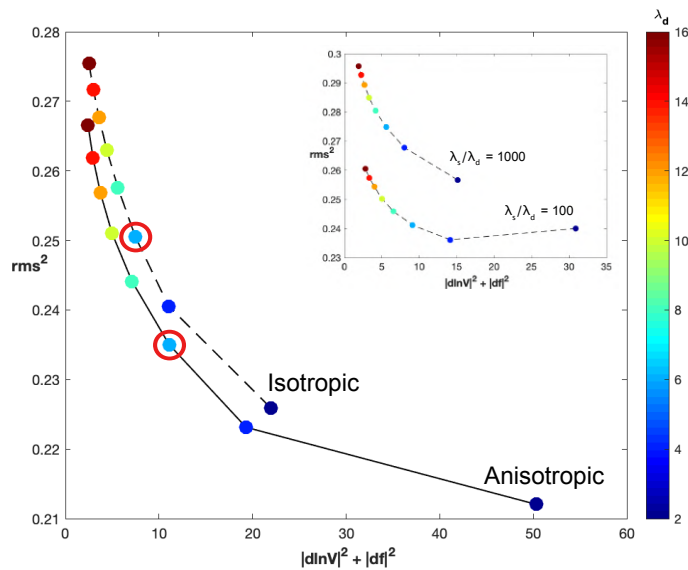
Figure 4.9: *Trade-off curves for damping and smoothing multiplier selection. The squared RMS is plotted as function of the squared model norm, $|dlnV|^2 + |df|^2$, where dlnV is the fractional velocity perturbation vector and df is the anisotropic magnitude perturbation vector. The dashed and solid lines are, respectively, the trade-off curve for purely isotropic and anisotropic inversion. The values λ_s/λ_d are kept fixed at 200 for both the isotropic and anisotropic cases. Colorbar represents different values of damping factor for slowness. Red circles indicate the preferred solutions presented in section 4.4, corresponding to $\lambda_d = 6$. Insert shows the trade-off curves from two isotropic tests with $\lambda_s/\lambda_d = 100$ and 1000.*
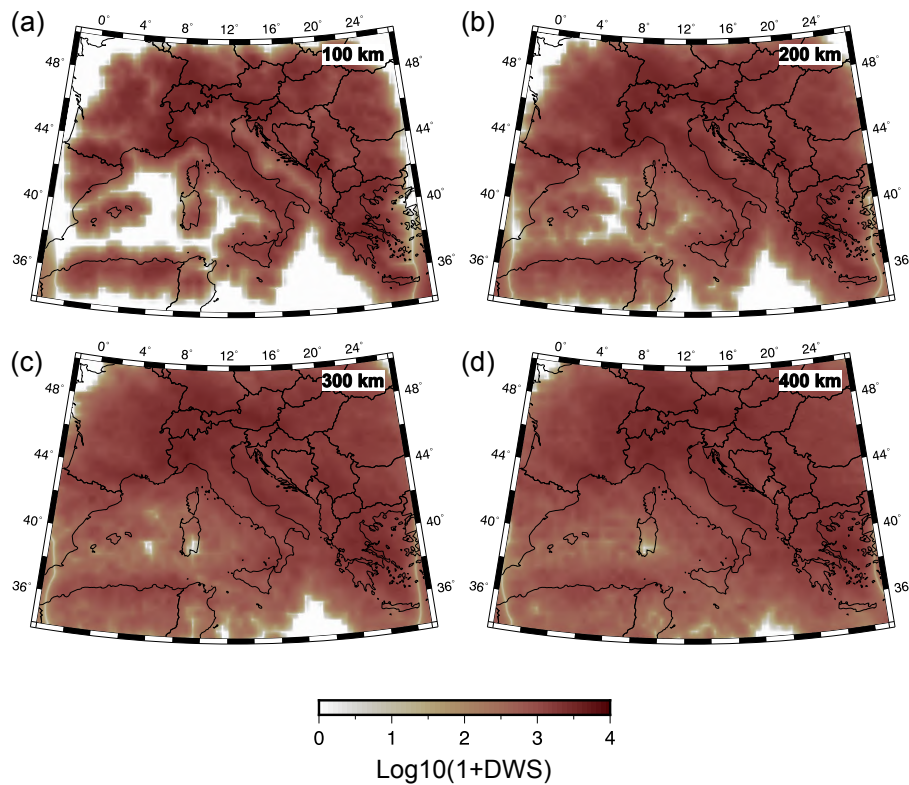
Figure 4.10: *Derivative weighted sum (DWS) at (a) 100 km, (b) 200 km, (c) 300 km, (d) 400 km depth.*
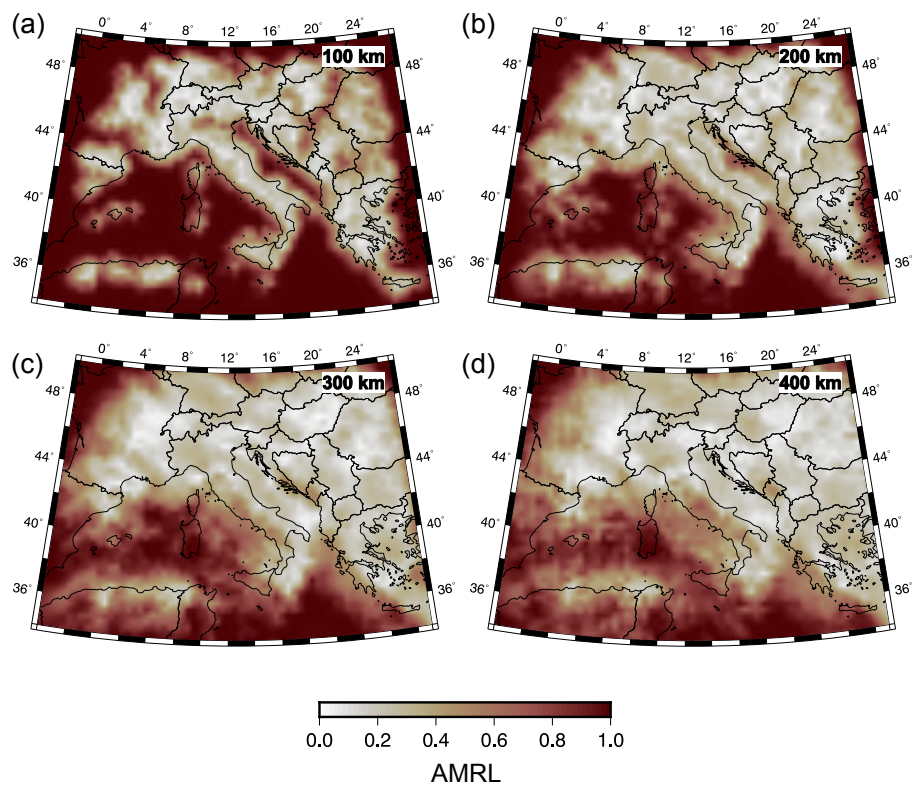
Figure 4.11: *Azimuthal mean resultant length (AMRL) at (a) 100 km, (b) 200 km, (c) 300 km, (d) 400 km depth.*
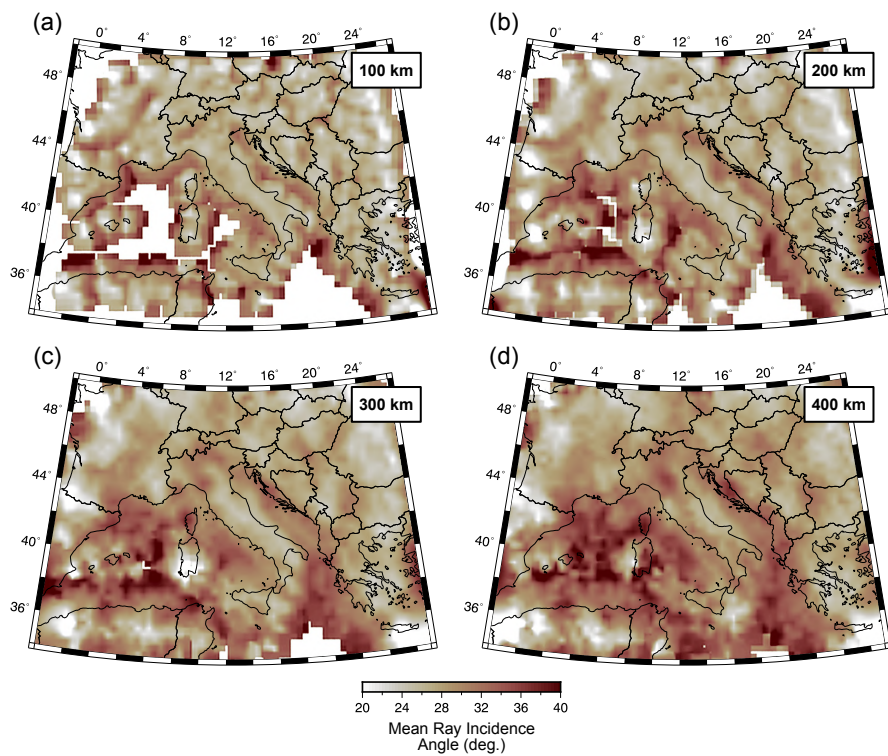
Figure 4.12: *Mean ray incidence angles at (a) 100 km, (b) 200 km, (c) 300 km, and (d) 400 km depth.*
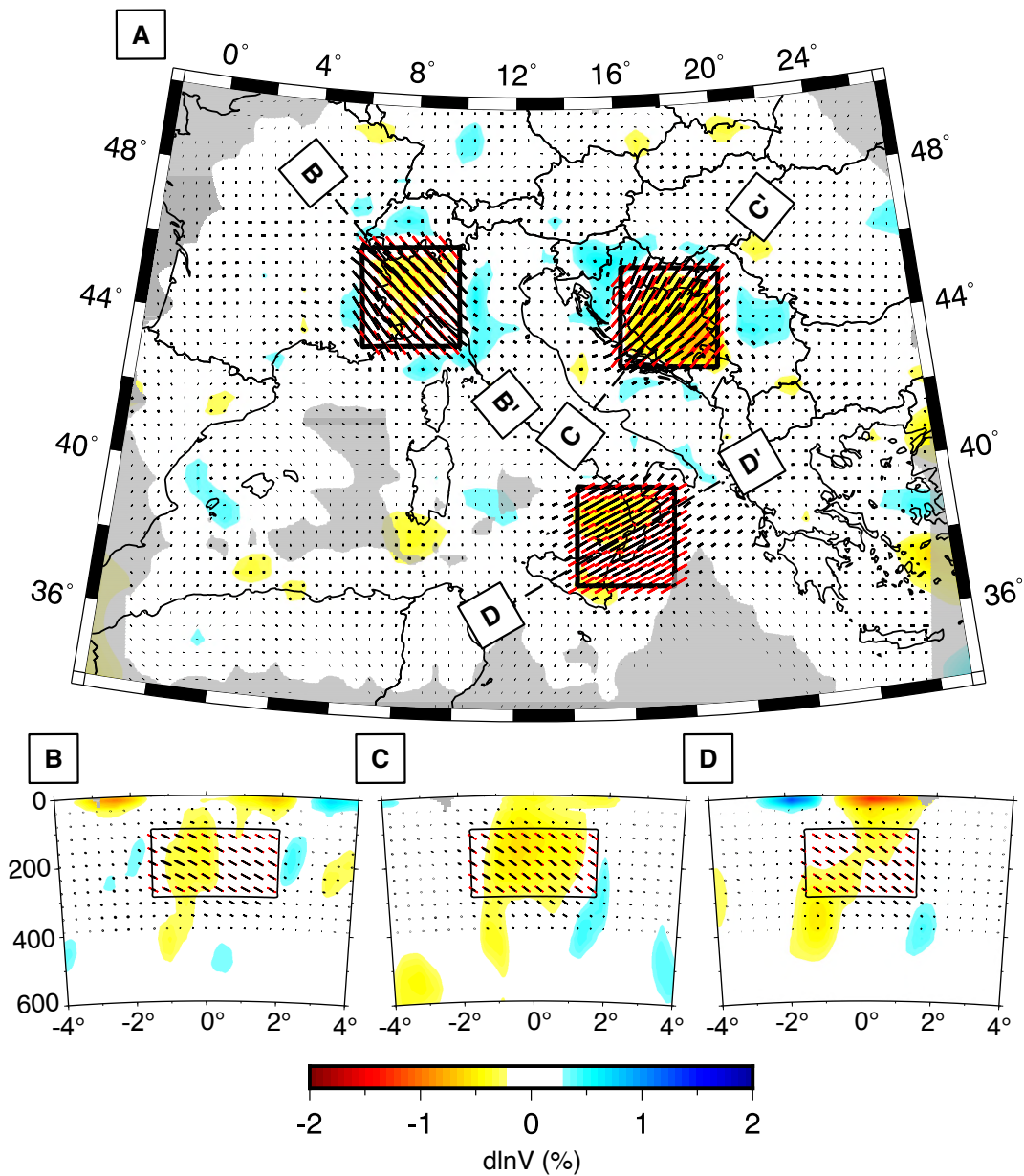
Figure 4.13: *Recovery of shallow dipping (30°) anisotropic fabrics. The true anisotropic anomalies have dimensions of 300 km x 300 km x 200 km and are centered at 200 km depth; no isotropic heterogeneity is present in the true model. (A) Map view at 200 km depth of imaged anisotropic and isotropic structure. Cross-section through the (B) Western Alps, (C) Dinarides, and (D) Calabrian anomalies are plotted along the corresponding cross-section lines in (A). In all panels, red quivers show the true anisotropic fabric orientations whose length is scaled by the anisotropic magnitude (6%) and the black box outlines the extent of the anomalies. Black quivers are the recovered anisotropic orientations.*
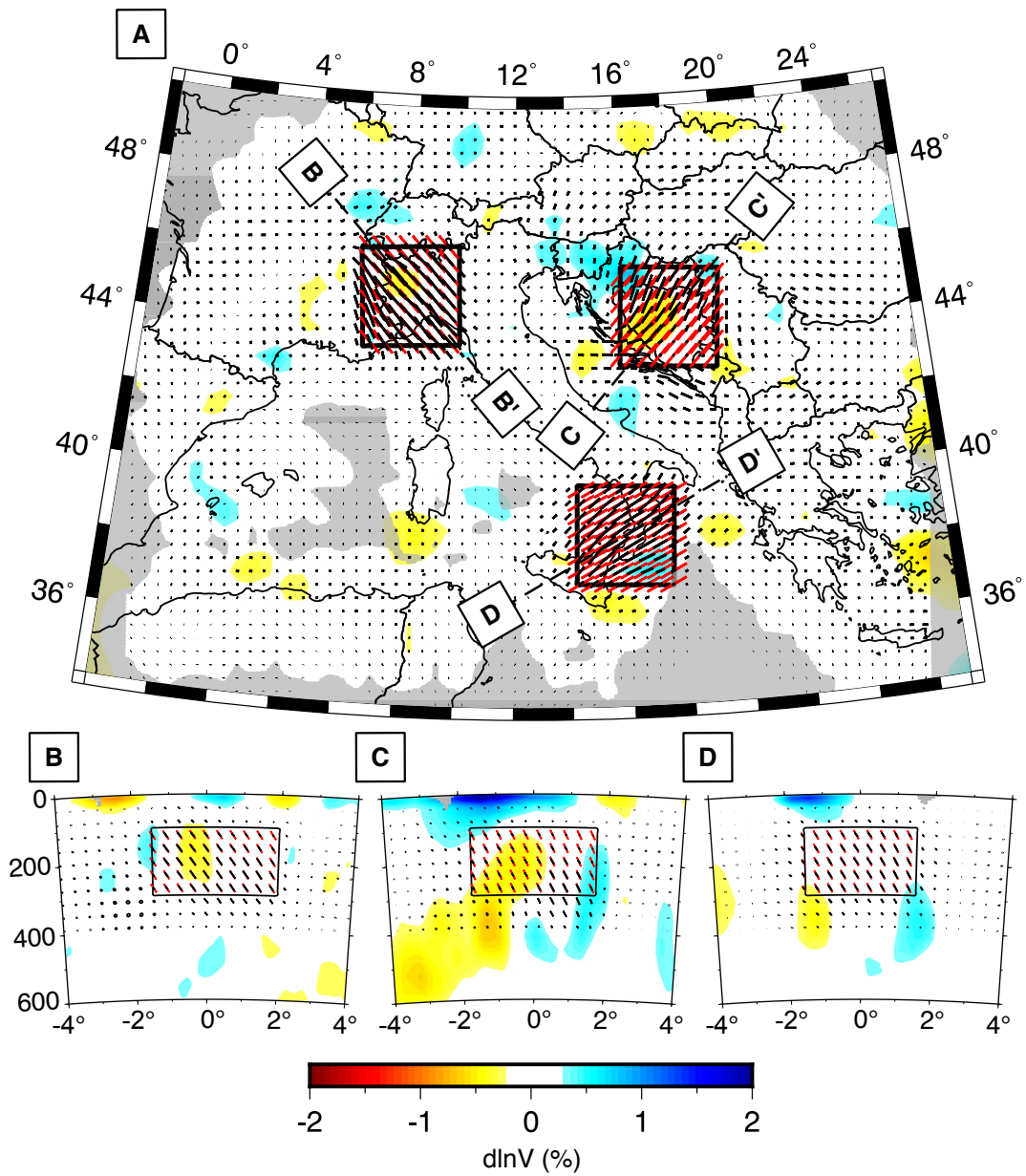
Figure 4.14: *Same as Supplementary Figure 4.13 but for steeply dipping (60°) anisotropic fabrics.*
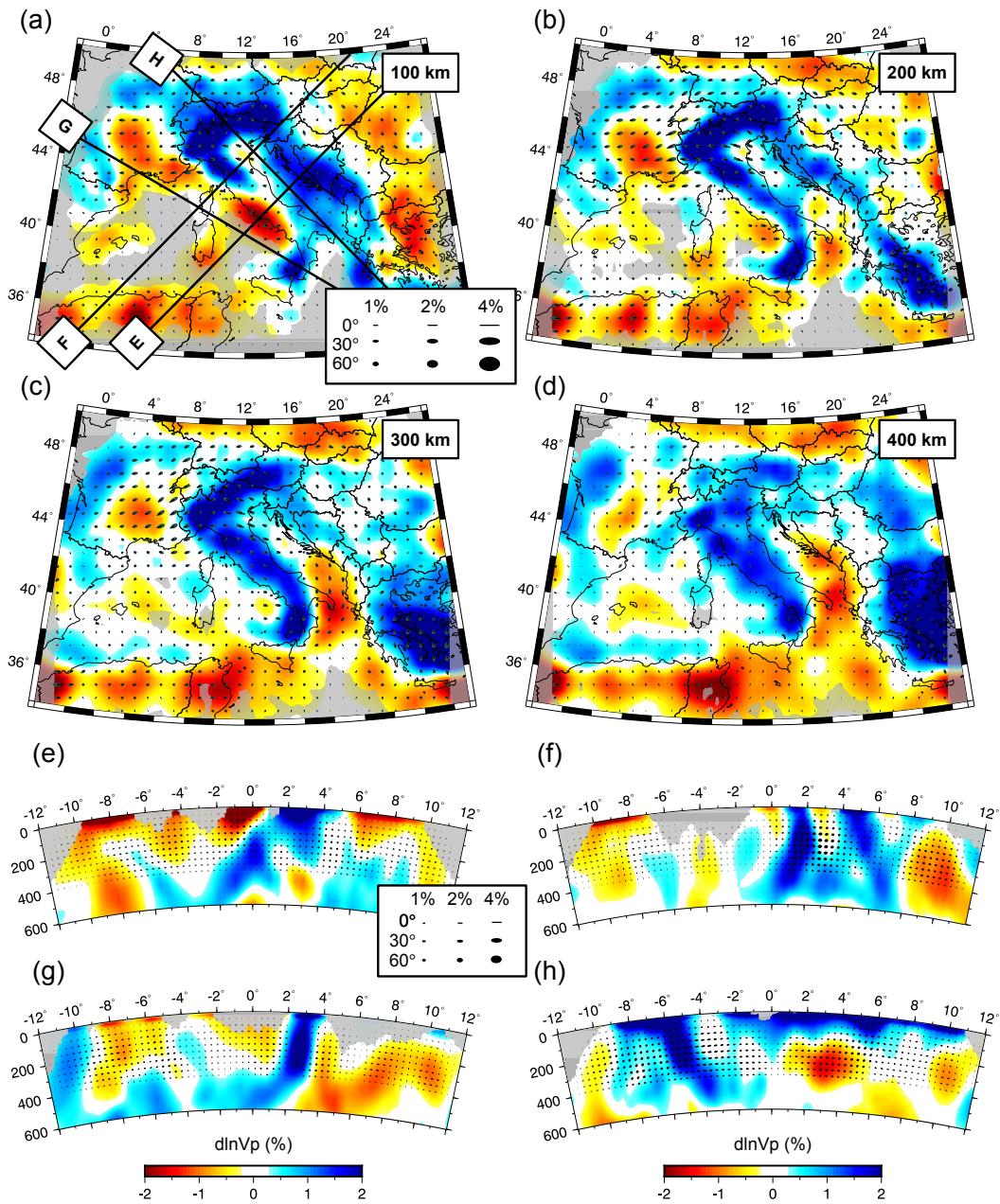
Figure 4.15: *Isotropic restoration synthetic test (see section 4.3.3 for details). Anisotropic inversion for our preferred isotropic model depicted in Figure 4.4*
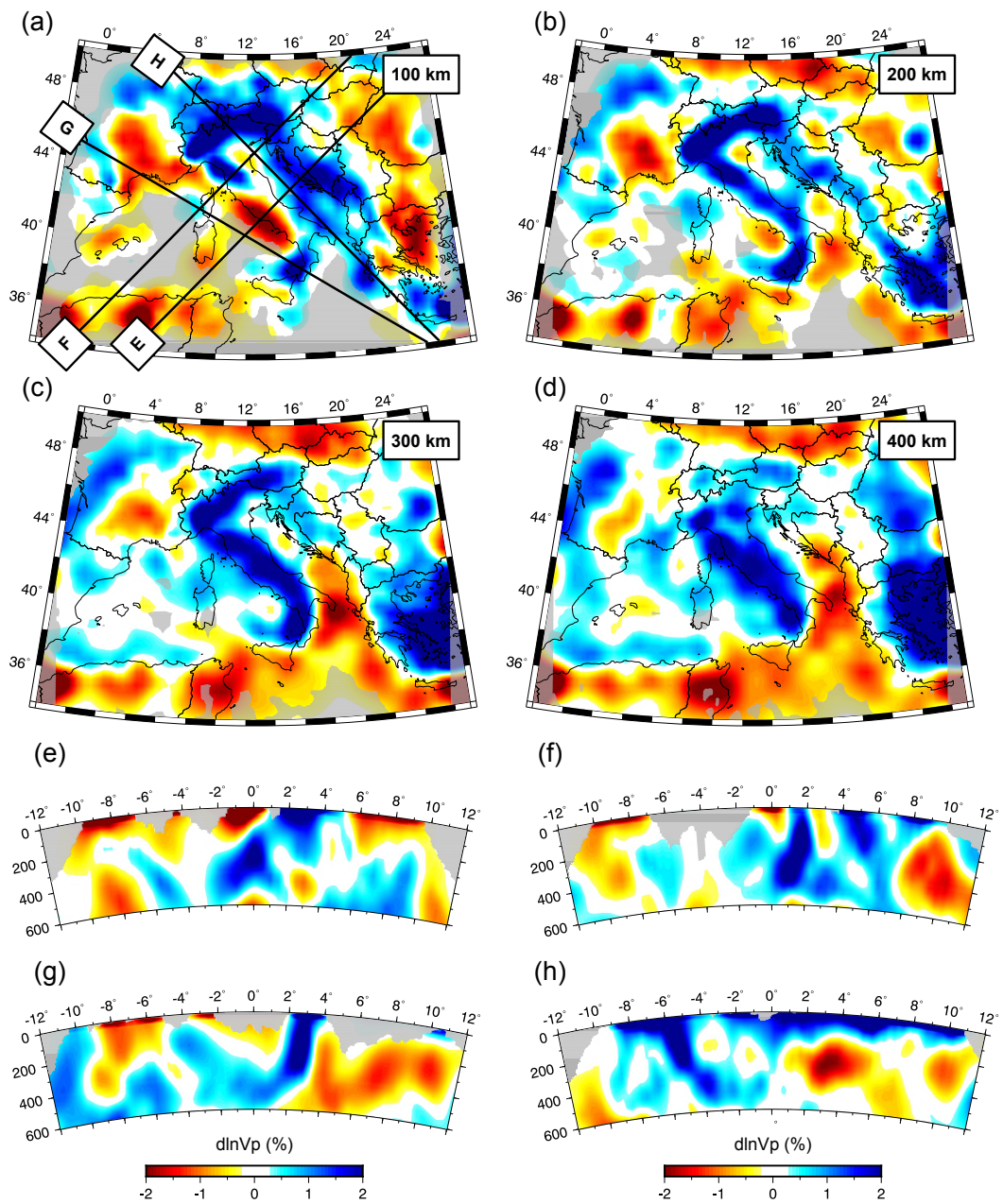
Figure 4.16: *Anisotropic restoration synthetic test (see section 4.3.3 for details). Isotropic inversion for our preferred anisotropic model depicted in Figure 4.5. Note similarity of this solution to the preferred isotropic model (Figure 4.4).*
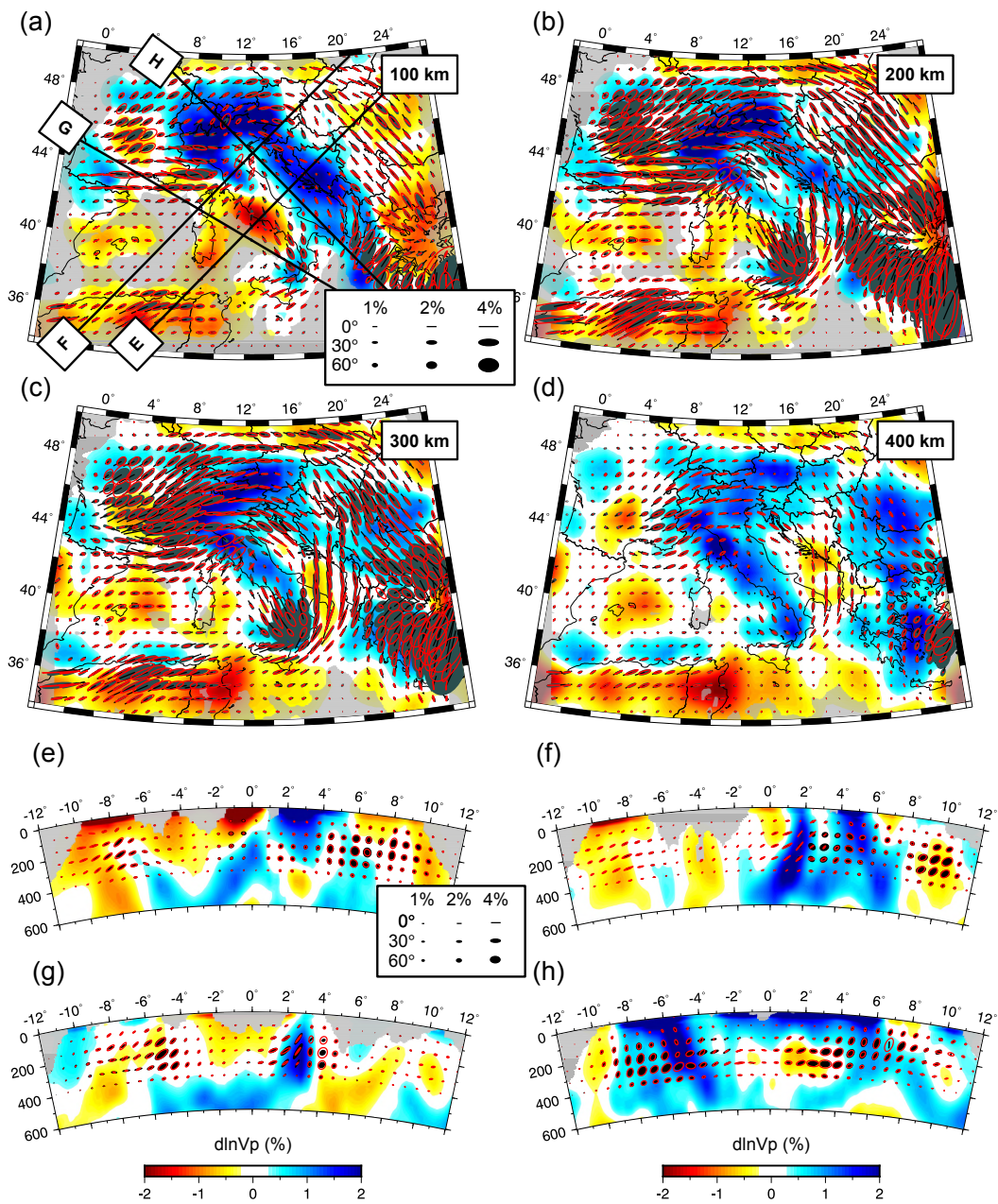
Figure 4.17: *Anisotropic restoration synthetic test (see section 4.3.3 for details). Anisotropic inversion for our preferred anisotropic model depicted in Figure 4.5. For ease of comparison, the true/target anisotropic fabrics are shown by the red ellipses.*
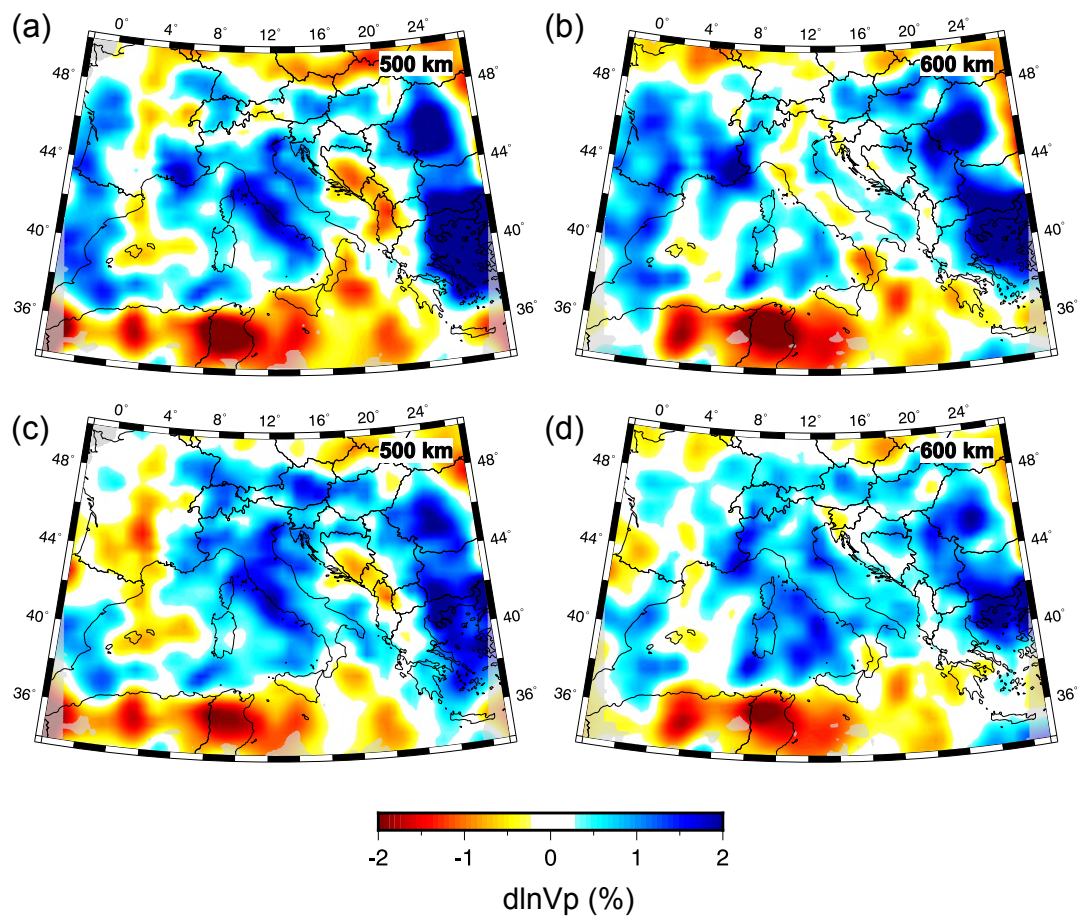
Figure 4.18: *Depth slices at 500 km and 600 km depth for model iso-NEWTON21 (a, b) and ani-NEWTON21 (c, d). P-wave velocity anomalies shown with respect to reference model AK135.*
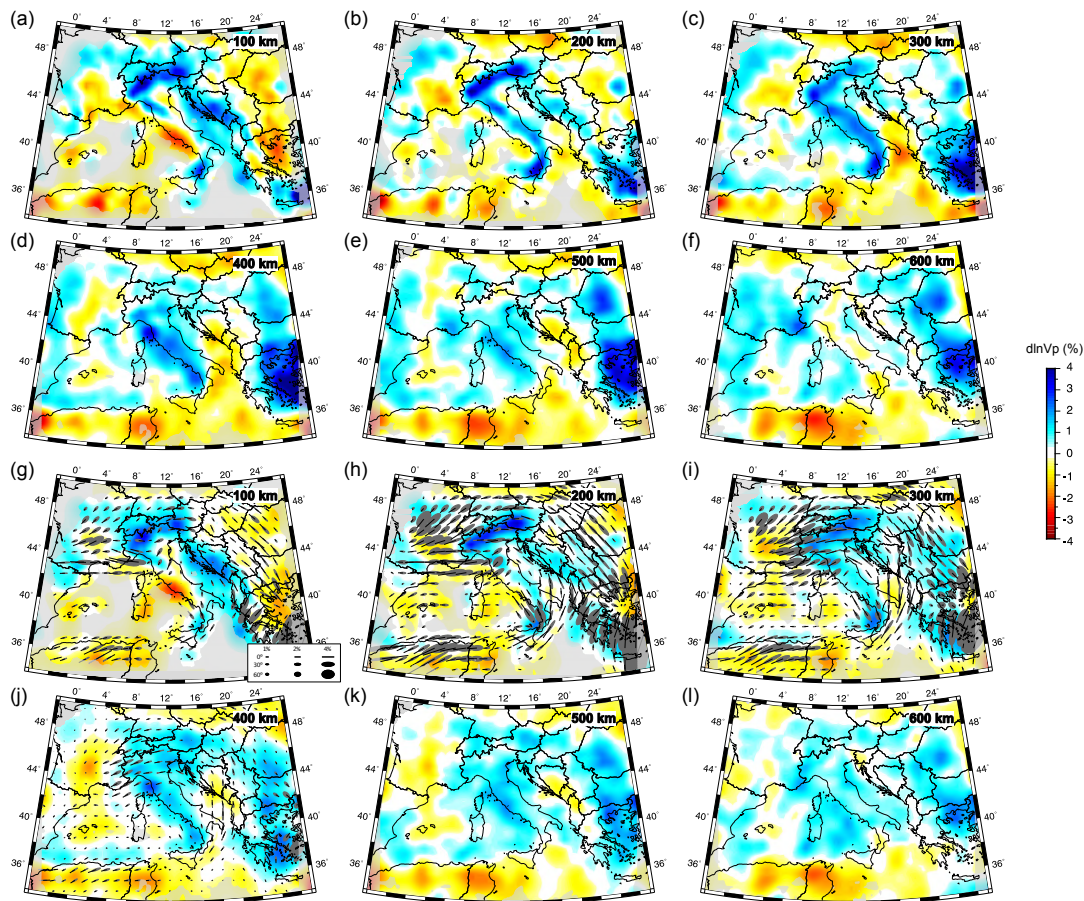
Figure 4.19: *(a-f) Iso-NEWTON21 and (g-l) ani-NEWTON21 with broader colorscale limits with respect to Figure 4.4 and Figure 4.5. Depth slices are shown at (a,g) 100 km, (b,h) 200 km, (c,i) 300 km, (d,j) 400 km, (e,k) 500 km and (f,l) 600 km depth. Isotropic anomalies are plotted with respect to starting model. Anisotropy is represented by ellipse symbols where the major axis of the ellipse parallels the fast-direction and the minor axis scales linearly with the symmetry axis dip into the view plane such that fabrics parallel and normal to the cross-sections plot as lines and circles, respectively. Areas of poor data coverage are masked in grey.*
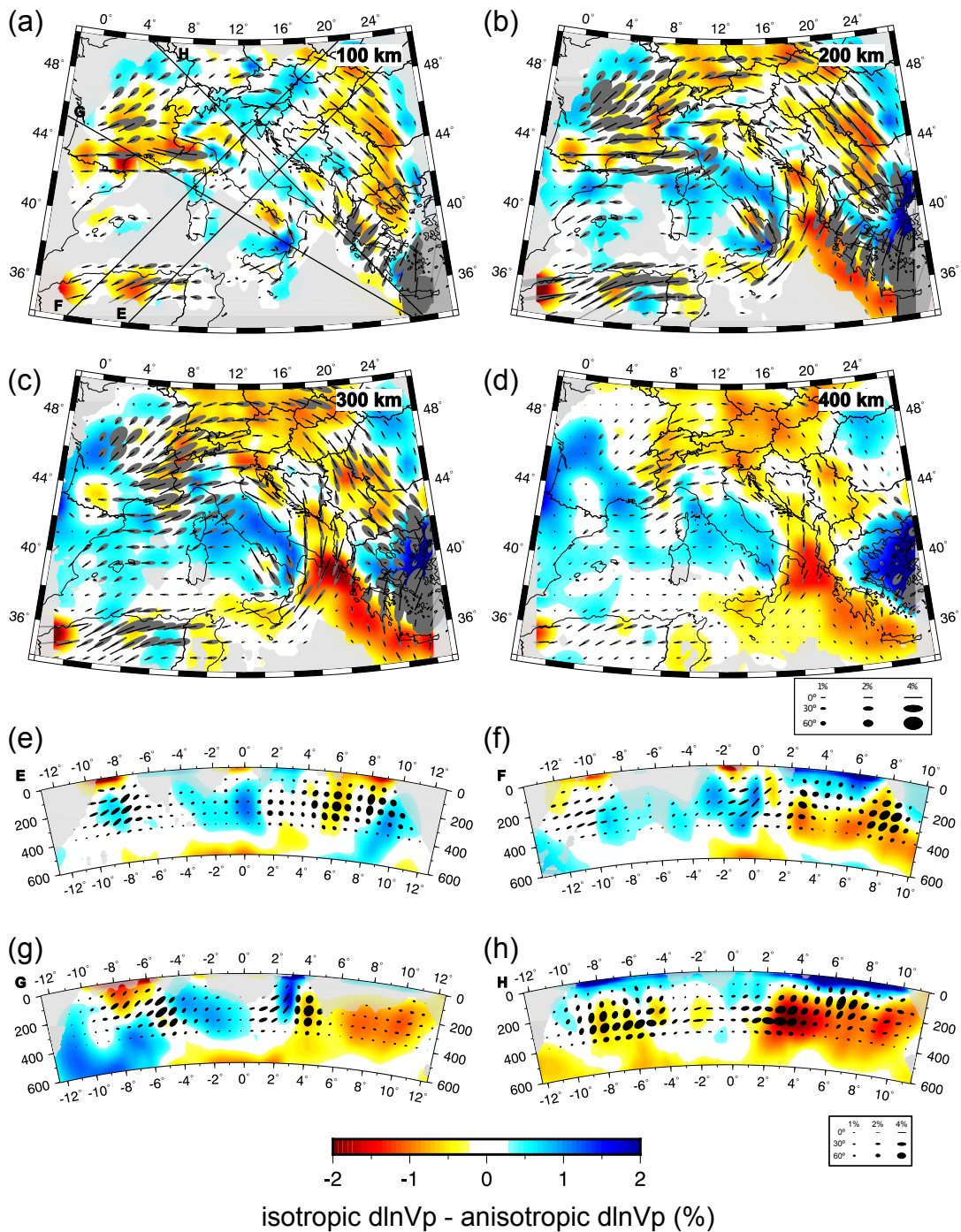
Figure 4.20: *Differences between iso-NEWTON21 and ani-NEWTON21 isotropic anomalies. Horizontal cross-sections are shown at (a) 100 km, (b) 200 km, (c) 300 km, and (d) 400 km depth. Vertical cross-sections are shown in (e-f) along the corresponding profile lines drawn in (a). Anisotropy from ani-NEWTON21 is plotted using ellipses as described in Figure 4.2. Areas of poor data coverage are masked in grey.*
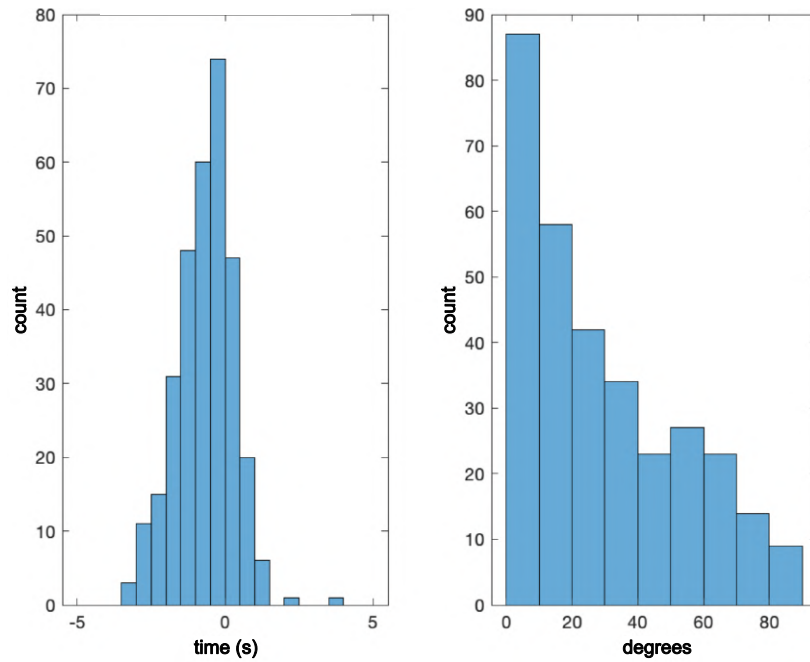
Figure 4.21: *Time (left) and azimuth (right) errors between predicted and observed SKS splitting measurements. The split time mean error is -672 ms with a standard deviation of 965 ms; the split azimuth median error is 22 for the entire dataset 19 if only considering split times greater than 1 s.*
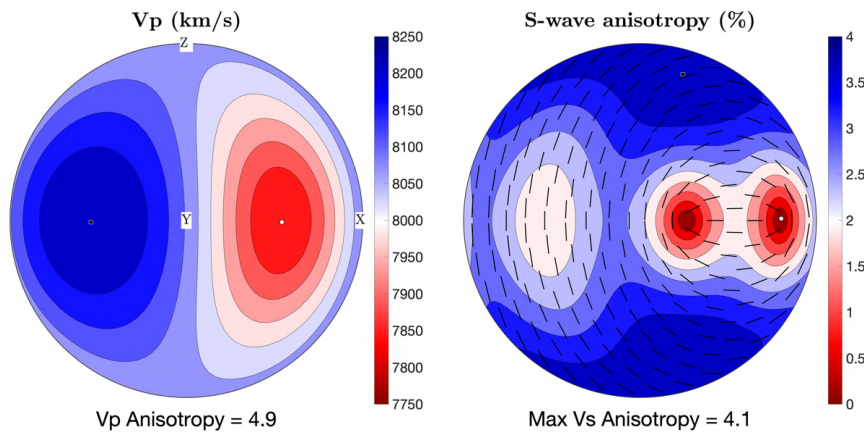
Figure 4.22: *Seismic velocities pole projections for an elastic tensor representative of the asthenospheric mantle as defined in Song and Kawakatsu (2012). The tensor is characterized by orthorhombic symmetry and has been rotated by 45° around the N-S axis. (left) P-wave velocity in m/s; (right) S wave anisotropy (%) = $(V_{S1} - V_{S2})/(V_{S1} + V_{S2}) * 200$. The black bars indicate the azimuth of the fast S-wave component for different seismic ray propagation directions. In both panels, the black square and white circle indicate, respectively, the seismic ray direction yielding max. and min. values. For teleseismic rays with high incidence angles (i.e., close to the center of the circle) the azimuth of the fast S-wave is N-S, which is at 90° from the fast Pwave oriented in the E-W plane. This discrepancy is found for dipping angles > 30°. Pole projections plotted with MTEX (Mainprice et al., 2011).*

Chapter 5

TOMOGRAPHIC IMAGE INTERPRETATION AND CENTRAL-WESTERN MEDITERRANEAN-LIKE UPPER MANTLE DYNAMICS FROM COUPLED SEISMOLOGICAL AND GEODYNAMIC MODELING APPROACH

R. Lo Bue[†,1], F. Rappisi[†,1], B. P. Vanderbeek[1] and M. Faccenda[1]

This manuscript is under review in Frontiers in Earth Science - Solid Earth Geophysics. All the authors conceived the study. RLB performed the geodynamic and seismological (i.e. strain-induced fabric estimation and SKS splitting calculations) numerical modeling. FR performed the seismological forward and P-wave tomography. RLB and FR wrote the first draft of the manuscript. BPV and MF supervised the findings of this work. All the authors contributed equally to the discussion of the results and to the conclusions of this study.

[†]indicates the first authors.
[1]Dipartimento di Geoscienze, Università di Padova, Padova, Italy

Abstract

The Central-Western Mediterranean (CWM) is one of the most complex tectonic setting on Earth. Episodes of slab rollback, break-off and tearing, the opening of back-arc extensional basins (i.e., Liguro-Provençal, Alboran, Algerian and Tyrrhenian basins), the presence of large mountain ranges, active volcanoes and violent earthquakes have made the Mediterranean an ideal environment to study a wide range of geodynamic processes and an important target for seismological studies (e.g, seismic tomography). Here we build a geodynamic model which, although it does not reproduce its exact tectonic structure (e.g., due to the limits of the numerical method, approximations in the initial setup, etc), presents multiple and geometrically complex subduction systems analogous to those found in the CWM. The tectonic evolution of this model is estimated with petrological-thermo-mechanical 3D simulations, then, we dynamically compute the upper mantle fabrics and seismic anisotropy as a function of the strain history and local P-T conditions. After comparing the model with SKS splitting observations in order to quantify the discrepancies with the true Central-Western Mediterranean, we use the elastic tensors predicted for the modeled configuration to perform 3D P-wave anisotropic tomography by inverting synthetic P-wave delay times. Using the geodynamic model as reference, we evaluate the capabilities of a recently developed seismic tomography technique to recover the isotropic anomalies and anisotropy patterns related to a complex subduction environment in different conditions, such as poor data coverage and bad data quality. We observe that, although P-wave tomography still remains a powerful tool to investigate the upper mantle, the reliability of the retrieved structures strongly depends on data quality and data density. Furthermore, the recovered anisotropic patterns are consistent with those of the target model, but in general an underestimation of the anisotropy magnitude in the upper mantle

is observed. In the light of future developments, our study suggests that by combining micro- and macro-scale geodynamic simulations and seismological modeling of seismic anisotropy it will be possible to reproduce, at least to a first order, the tectonic evolution of real study regions (e.g., the Mediterranean) thus providing fundamental constraints on the processes that have contributed in shaping their current geological scenario.

5.1 Introduction

Since the early 1990s numerous seismological studies have been carried out to image the Earth's upper mantle and seismic tomography proved to be a fundamental tool for constraining the past and present-day mantle dynamics and structure (Liu & Gu, 2012; Rawlinson et al., 2014; Romanowicz, 2021; Van der Meer et al., 2018). Tomographic methods (e.g. P-, S- and surface-wave tomography) yield wave velocity models that are commonly used to infer distributions in physical and chemical properties affecting seismic-wave propagation such as density, temperature, melt fraction and volatile content.

At the same time, petrophysical analysis of exhumed rock samples and micromechanical laboratory experiments (Blackman & Kendall, 2002; Faccenda, 2014; Kaminski et al., 2004; Karato et al., 2008; Long & Becker, 2010; Ribe, 1989; Savage, 1999; Skemer & Hansen, 2016) have shown that the development of mineral and compositional fabrics mainly associated with rock deformation can create significant directional variations in seismic velocities known as seismic anisotropy. Although the presence of seismic anisotropy in Earth's upper mantle is well-established, scientists have often assumed the Earth's interior as seismically isotropic. This approximation certainly simplifies the computational approach but at the same time it can introduce notable imaging artefacts and, consequently, errors in the interpretation of the tomographic results (Bezada et al., 2016; Blackman & Kendall, 1997; Blackman et

al., 1996; Kendall, 1994; Lloyd & Van Der Lee, 2008; Menke, 2015; Sobolev et al., 1999; VanderBeek & Faccenda, 2021).

Recently, VanderBeek and Faccenda (2021) and Wang and Zhao (2021), have independently developed a methodology to invert for P-wave isotropic (mean velocity) and anisotropic (magnitude of hexagonal anisotropy, azimuth and dip of the symmetry axis) parameters. When tested on a relatively simple, 3D geodynamic model of subduction, VanderBeek and Faccenda (2021) found that the new inversion technique produces a much more accurate reconstruction of the upper mantle isotropic and anisotropic structures. In contrast, ignoring for seismic anisotropy (isotropic approximation) or allowing for only azimuthal variations in seismic velocity (i.e., no dipping fabrics) generates strong imaging artifacts. From these tests it follows that taking into account seismic anisotropy can provide new insights into the 3D upper mantle structure and dynamics. Despite these encouraging results, it remains unclear whether isotropic and anisotropic structures of the Earth's mantle can be simultaneously recovered by P-wave anisotropic inversions in real and more complex tectonic settings.

Along with seismic imaging techniques, over the last decades numerical geodynamic modeling became an essential approach for understanding the long-term and deep evolution of a wide range of geological processes, which otherwise would remain unconstrained due to the lack of geological data (Gerya, 2019). Owing to the development of increasingly high performance computers and more advanced numerical techniques, it is nowadays possible to simulate the multiscale tectonic evolution of 3D complex settings for 10s or 100s of millions of years (van Zelst et al., 2021). However, despite being a powerful tool, numerical modeling is also affected by several limitations that could potentially bias the final output, such as uncertainties in the employed initial model geometry, physical parameters (mainly viscosity), chemical compositions, and limited computational power.

In order to test the limitations of the tomographic and numerical modeling methods, a promising approach is combining micro- and macro-scale geodynamic modeling simulations of mantle flow to predict mantle isotropic and anisotropic structures and then perform seismological synthetics (Confal et al., 2018; Faccenda & Capitanio, 2012, 2013; Hu et al., 2017; Lo Bue et al., 2021; Zhou et al., 2018). We decided to apply this combined methodology to the Central Western Mediterranean (CWM) region. In the last 20-30 million years, this area has experienced complex tectonic activity characterized by back-arc extension related to slab retreat in the Liguro-Provençal, Alboran, Algerian and Tyrrhenian basins and episodes of slab break-off, lateral tearing and interactions between slabs (Carminati et al., 1998; Carminati et al., 2012; Faccenna et al., 2014; Faccenna et al., 2007; Faccenna et al., 2004; Jolivet et al., 2008; Jolivet et al., 2006; Jolivet et al., 2009; Király et al., 2018; Lonergan & White, 1997; Mauffret et al., 2004; Platt & Vissers, 1989; Rosenbaum et al., 2002b; Spakman et al., 1988; Spakman & Wortel, 2004; van Hinsbergen et al., 2014; Van Hinsbergen et al., 2020; Vignaroli et al., 2008; Wortel & Spakman, 2000) and a wealth of geological and geophysical data are available. Numerous tomographic models and geodynamic studies focusing on the CWM upper mantle are available, which can be used here to test the reliability of our approach.

We first extend the modeling methodology of Lo Bue et al. (2021) to create a geodynamic model that resemble observed slabs morphology and anisotropic mantle fabrics of the CWM. The geodynamic model is then exploited as synthetic case study to test the capabilities and limitations of P-waves isotropic and anisotropic inversions in recovering complex geological scenarios using the methodology of VanderBeek and Faccenda (2021).

In this work, we attempt to answer some fundamental questions. How well does P-wave anisotropic tomography recover the modeled isotropic and anisotropic structures? How reliable are the inferred anisotropic patterns

with respect to the upper mantle fabrics? Which are the main artefacts introduced in the tomographic image when neglecting seismic anisotropy? To which extent vertical smearing bias the inverted structures when only using teleseismic P-wave travel times?

5.2   Methodology

5.2.1   Geodynamic Numerical Modeling

We construct a 3D petrological-thermo-mechanical numerical model of the Central-Western Mediterranean convergent margin using I3MG (Gerya, 2019), which is based on the finite difference method (FDM) combined with a marker-in-cell (MIC) technique. The mass, momentum and energy conservation equations are solved on a staggered Eulerian grid while the physical properties are interpolated to the Lagrangian markers for advection. The Earth's mantle is treated as a highly viscous incompressible medium. Visco-plastic deformation is simulated by combining a Drucker-Prager yielding criterion with dislocation, diffusion and Peierls creep mechanisms.

In this paper we refer to our geodynamic model as Model CWM (Central Western Mediterranean Model). This model is an updated version of the Reference Model CM of Lo Bue et al. (2021). Here, the computational domain has been enlarged and has dimensions of 3700 x 700 x 2200 km (373 x 101 x 229 nodes) along the $x - y - z$ coordinates, with y being the vertical direction. As in Model CM, subduction modeling is self-consistent, driven only by internal buoyancy forces. Velocity boundary conditions are free slip everywhere. We impose a constant incoming heat flux of 2 mW/m^2 at the bottom boundary, while the top boundary is characterized by a constant temperature of 273 K. The side boundaries are insulating. The models account for frictional
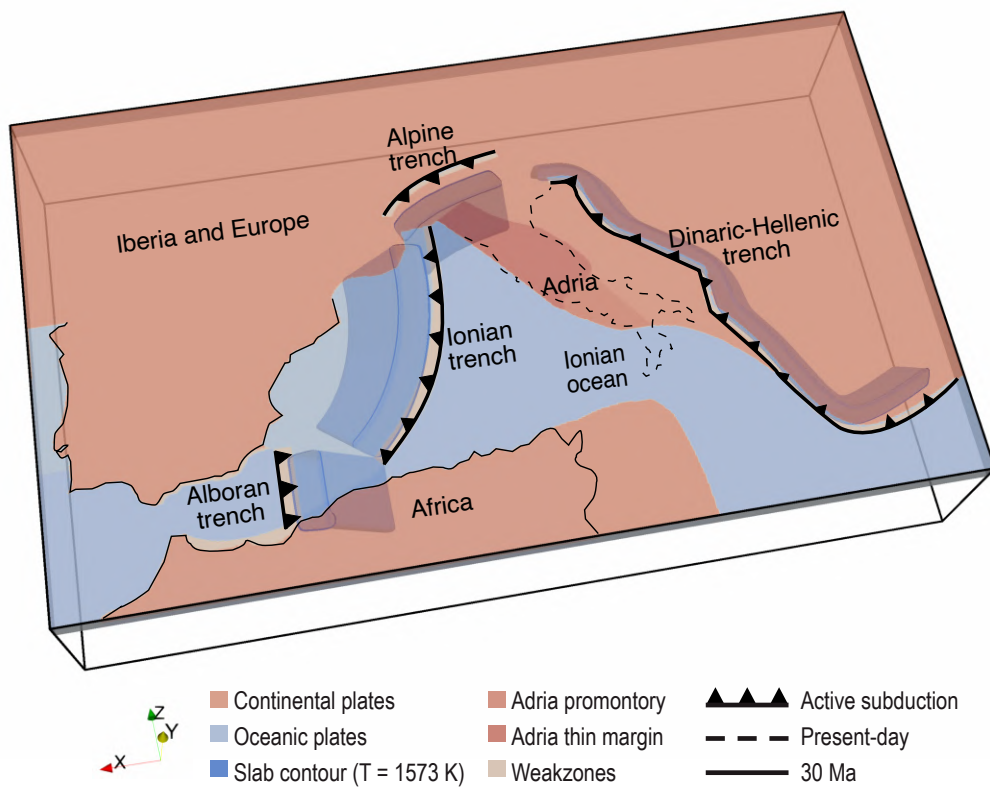
Figure 5.1: *Initial model setup for Model CWM. It consists of a subducting oceanic plate (Ionian Ocean;light blue) surrounded by lateral continental blocks (Adria, Africa, Iberia and Europe; salmon pink) drawn according to paleogeographic reconstructions at ∼30 Ma proposed by Faccenna et al. (2014), Romagny et al. (2020), and van Hinsbergen et al. (2014). The Adria plate is characterized by the presence of a stiffer continental promontory (peach pink) and a thin continental margin (red) as proposed by Lo Bue et al. (2021), Lucente et al. (2006), and Lucente and Speranza (2001). Multiple subducting slabs are positioned according to the chosen reconstructions (i.e., Alboran and Ionian trenches as in Romagny et al. (2020); Alpine and Dinaric-Hellenic trenches as in Faccenna et al. (2014)) and taking into account the limitations imposed by numerical modeling. The solid black line indicates the coastlines at ∼30 Ma as in van Hinsbergen et al. (2014), while the dashed black line the present-day coastlines of peninsular Italy. The plates are opacified for a better visualization of the subducted slab.*

and adiabatic heating, and for thermal and dynamic effects of phase changes (except that the medium is assumed to be incompressible).

We used the MATLAB toolbox geomIO (Bauville & Baumann, 2019) to create the 3D initial temperature and compositional fields. The tectonic plate geometry has been designed according to the paleogeographic and tectonic reconstructions at ∼30 Ma proposed by Faccenna et al. (2014), Lucente et al.

(2006), Lucente and Speranza (2001), Romagny et al. (2020), and van Hins-
bergen et al. (2014) although some simplifications were required due to limi-
tations imposed by numerical modeling.

In the initial setup (Figure 5.1), a subducting oceanic plate, that represents
the Ionian Ocean, is surrounded by lateral continental blocks corresponding
to the Adria, Africa, Iberia and European plates. The position of the plates in
the Oligocene-Miocene was adapted from a reconstruction of van Hinsber-
gen et al. (2014). It is worth noting that, not having applied a convergence
rate between the plates (self-consistent subduction), their relative position
slightly differs from the present-day one. However, an initial geometry de-
fined in the Oligocene-Miocene should not have a strong impact on man-
tle flow directions and splitting parameters as the slow Africa-Europe plates
convergence has not caused a drastic change in plates position over this time
span.

In Model CWM, we considered a more realistic paleo-tectonic configura-
tion of the region, which is characterized by the presence of multiple sub-
ducting slabs rather than a single one as in Model CM.

Subduction in the Ionian plate occurs along two trenches as in Romagny
et al. (2020). The longest one stretches from the Alps to the southeast of
the Baleares and is associated with a slab dipping 40° NW and extending
down to 300 km in the upper mantle. A second one is placed in the Albo-
ran domain, where a slab with the same dipping angle but an opposite ver-
gence extends down to 350 km in the upper mantle (Romagny et al., 2020).
Throughout the manuscript we use "Ionian slab and Ionian trench" to in-
dicate the former subduction zone and "Alboran slab and Alboran trench"
when referring to the latter. It is worth noting that to trigger slab roll-back
self-consistently, the Ionian trench has been positioned further south as in
Lo Bue et al. (2021) and the initial depth of the Alboran and Ionian slabs
has been increased compared to tectonic reconstructions. This could cause

a difference in rates of slabs retreat when compared to those reported in the literature and be representative of a more recent stage of the Central-Western Mediterranean history rather than the 30 Ma assumed here.

Two large collisional suture zones, are present in the continental Adria and European plates as in Faccenna et al. (2014). To the north, we find the Alpine trench with its characteristic arcuate shape and, to the east of the model, the Dinaric-Hellenic trench that extends from Eastern Alps to the southernmost tip of the Hellenic peninsula (Faccenna et al., 2014). In both trenches the slab dips almost vertically into the upper mantle to a depth of about 350 km to simulate locked collision zones. In this area slabs extended down to 350 km depth to model flow barriers due to the presence of subducted slab.

In the area of the model corresponding to the present-day Apenninic chain, we use the same initial configuration as in Lo Bue et al. (2021), characterized by lithospheric heterogeneities which are fundamental for the development of key tectonic features such as a prolonged eastward retreat of the Ionian plate and the formation of a slab window below the modelled central Apennines. The Adria plate consists of a thin continental lithosphere in the Umbria-Marche region and of a stiffer continental promontory in its central portion corresponding to the Abruzzo-Laziale platform (Calcagnile & Panza, 1980; Geiss, 1987; Lo Bue et al., 2021; Lucente et al., 2006; Lucente & Speranza, 2001; Maino et al., 2013; Miller & Piana Agostinetti, 2012; Panza et al., 2003). The African plate structure, nearby Sicily and the Sicilian Channel area, is characterized by a slightly thinner margin (Arab et al., 2020; Lo Bue et al., 2021).

The initial lithosphere thermal structure was modeled using the half-space cooling equation (Turcotte & Schubert, 2014), while the underlying asthenosphere consists of a 0.5 K/km constant adiabatic temperature gradient. The thermal age of the Ionian oceanic plate is 80 Myr, while that of the two slabs

is 70 Myr to simulate partial heating upon subduction. The age of the continental plates (Africa, Africa eastern margin, Iberia, Adria and Adria promontory) is 150 Myr while an age of 90 Myr was imposed for the thinned portion of Adria continental lithosphere. To activate a self-consistent subduction, the Ionian plate north of the two trenches is composed of a young lithospheric portion (1 Myr - the young age is justified by assuming a well-developed continental rifting system North of the Balearics and Corsica-Sardinia block). Furthermore, rheologically weak zones (constant viscosity of 10^{18} *Pa s* and constant density of 3200 kg/m^3) have been inserted (i) on the slabs top surface to lubricate the initial contact between the overriding and the subducting plates, and (ii) around southwest Iberia and northwest Africa to facilitate the Alboran trench retreat (e.g., Chertova et al., 2014). The plates thermal structures and flow law parameters have been tuned to allow a self-consistently subduction and simultaneously to reproduce the main tectonic events as close as possible to the geological reconstructions. This may cause a too weak rheology and faster rates of mantle convection once self-sustained subduction has started due to the non-linear viscous behaviour of the mantle.

The density is computed using the thermodynamic databases generated with PERPLE_X (Connolly, 2005) and tested by Mishin et al. (2008) for a pyrolytic mantle composition. The continental crust density is calculated as being that of the mantle minus 400 kg/m^3, except for the Adria thin margin where we subtract 200 kg/m^3 to model a less buoyant continental lithosphere. Instead, for the crust of the Adria promontory we use a constant value of 2700 kg/m^3. More details about the physical parameters used in the geodynamic model can be found in Lo Bue et al. (2021).

5.2.2 Predicting mantle anisotropy and SKS splitting

The development of seismic anisotropy in the upper mantle is calculated using a modified version of D-Rex (Kaminski et al., 2004), which incorporates the deformation mechanisms inducing LPO (plastic deformation, dynamic recrystallization and grain-boundary sliding) and accounts for deformation history and non-steady-state evolution of geodynamic systems (Faccenda, 2014; Faccenda & Capitanio, 2013).

A large number of Lagrangian particles representing mineral aggregates are regularly distributed throughout the numerical domain (25 *km* reciprocal distance along the 3 directions, for a total of 364672 aggregates). Each particle consists of 1024 randomly oriented crystals, which results in an initially isotropic upper mantle. We use a harzburgitic upper mantle composition (70% olivine and 30% orthopyroxene modal abundance) and a more fertile pyrolitic mantle composition in the transition zone (60% spinel and 40% majoritic garnet) (Faccenda, 2014). The Eulerian velocity field obtained by the macro-flow simulation is then used to passively advect the particles and LPO is generated at each time step through the re-orientation of such particles in response to the gradients in the velocity field. Since SKS splitting parameters are mostly sensitive to the upper mantle (Sieminski et al., 2008), we only model the anisotropy from the Moho to the 410 *km* discontinuity. We use the same dimensionless crystallographic parameters as in (Rappisi & Faccenda, 2019) with the nucleation rate $\lambda = 5$, the grain-boundary-mobility $M = 1$ and the threshold volume fraction $\chi = 0.9$, which generate weaker fabrics and seismic anisotropy more consistent with the observations.

Synthetic SKS splitting parameters are computed using the software package FSTRACK (Becker, 2006). Through the stiffness matrix the code recovers the elastic tensors for each aggregate and then, below each station and down to 400 *km*, it builds a vertical stack of horizontal layers (minimum thickness

of 25 *km*) where the elastic tensor of each layer is radially averaged within a distance of 50 *km*. Next, assuming an incident plane wave (5° for typical SKS arrivals) into the mantle over a range of frequencies from 0 to 25 Hz, using the inverse Fourier transform, it computes a pulse seismogram that will be further filtered to construct SKS waves (i.e. from 0.1 to 0.3 *Hz*). Finally, by applying the cross-correlation method of Menke and Levin (2003) and averaging all the fast azimuths and delay times at each station measured by rotating the vertical stack of elastic tensors by 5° intervals around the y-axis, the SKS splitting parameters are determined. The software for computing mantle aggregates fabrics and SKS splitting can be found in the open source software package ECOMAN.

5.2.3   3-D P-wave Anisotropic Tomography

We use the anisotropic seismic imaging method by VanderBeek and Faccenda (2021), that solves for perturbations to P-wave slowness and three additional parameters that define the anisotropic magnitude, azimuth, and dip in a hexagonally symmetric medium. The tomographic algorithm does not require an anisotropic starting model which could potentially distort the results if not close enough to the true solution as in the case of the anisotropic imaging method of Munzarová et al. (2018). Additionally, changes in elevation and surface velocity are explicitly addressed in teleseismic imaging using 3D ray tracing through a user-defined 3D velocity model that incorporates elevation (Toomey et al., 1994).

Ray theoretical travel-times are estimated (i) with the shortest-path algorithm (Moser, 1991) through Model CWM described in the previous section using the mantle aggregates full elastic tensor at ~21 Myr, and (ii) with the tau-p method (Crotwell et al., 1999) outside the study area using a 1D radial Earth velocity model. The geodynamic model was centered on 42°N 12.5°E

to match the main seismic structures with the real positions observed in current tomographic images.

Partial derivatives of the travel-times with respect to the model parameters are computed along the discretized ray paths. The LSQR method (Paige & Saunders, 1982) is used to solve the resulting linear system of equations relating changes in model parameters to changes in travel-times. To regularize the ill-posed inverse problem, damping and smoothing constraints are used. The choice of the regularization parameters that limit the norm of the model perturbational vector and enforce the Laplacian spatial smoothness of the model perturbations, thus controlling the length and the roughness of the solution vector relative to the length of the data residual vector, i.e. λ_d and λ_s respectively, is discussed in section 5.2.3.
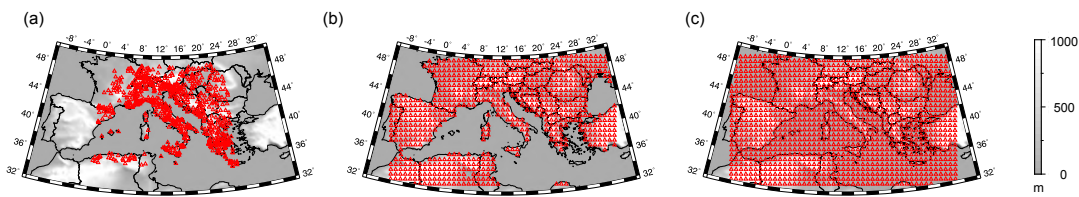
Figure 5.2: *Plot of the real land as in Rappisi et al. (2022) (a), ideal land (b) and ideal marine and land (c) station distribution.*

Starting model, discretization and regularization

We use a regular grid with uniform 10 km node spacing for the forward calculation of travel-times. The initial mantle velocity model is the isotropic 1D AK135 model (Kennett et al., 1995). We applied an Earth flattening transform (Müller, 1971) to account for Earth's curvature in our Cartesian model domain.

Perturbations to the three anisotropic parameters and the mean P-wave slowness (i.e. inverse of velocity, $u = 1/v$) are solved on a coarser regular grid with 40 km node spacing and then, at each iteration, linearly mapped

to the finer model used for travel-times calculation. Model CWM was considered down to 700 km depth, however, to limit the number of inversion parameters, anisotropic perturbations were restricted to the upper 400 km where there is the best ray crossing and mineral physics predicts mantle anisotropy to be most significant (Karato et al., 2008).

To resemble realistic conditions a first inversion was performed using delay times calculated through our Model CWM with the same distribution of sources (Supplementary Figure 5.12a) and receivers (Figure 5.2a), and the same regularization parameters as in the anisotropic tomography model of the Central Mediterranean by Rappisi et al. (2022) (Test 1). For this first test normally distributed errors with a standard deviation of 450 ms was added to the seismic data.

Next, several sets of inversions were run imposing a 1-sigma error of 125 ms applied to synthetic data and a smoothing-to-damping ratio (λ_s/λ_d) of 100 and damping values (λ_d) of 1,2,...9,10 with different synthetic datasets. For these sets of tests we used: (i) same sources (Supplementary Figure 5.12a) and station array as in Test 1 (Test2); (ii) an ideal on land receivers distribution (Figure 5.2b) (Test 3); (iii) an ideal marine and on land receivers distribution (Figure 5.2c) (Test 4). In the last two cases (Test 3 and 4) the receivers are equally spaced 75 km apart and the teleseismic events are placed at a distance from the center of the domain from a minimum of 35 ° up to a maximum of 110°, every 10° of azimuth (Supplementary Figure 5.12b), guaranteeing a perfectly homogeneous azimuthal events distribution, thus removing any bias associated with preferential sampling of certain back azimuths.

In addition we performed (iv) purely isotropic inversions in order to evaluate the effect of neglecting seismic anisotropy on the tomographic image (Test5), and (v) an inversion where the Model CWM is considered to be isotropic below 200 km to address vertical smearing of anisotropic structures (Test 6).

Table 5.1: *Inversions summary table. The type of inversion (isotropic/anisotropic), receivers distribution, true model, standard deviation of normally distributed data errors, damping and smoothing factors and relevant figures for each inversion are listed. In bold the λ_d corresponding to the preferred solution.*

	Type	Receivers Distribution	True Model	Data error	λ_d	λ_s/λ_d	Figures
Test 1	Anisotropic	Real land (Rappisi et al., 2022)	Anisotropic down to 400 km	450 ms	6	200	5.6e-h; 5.16c-d; 5.17e-h
Test 2	Anisotropic	Real land (Rappisi et al., 2022)	Anisotropic down to 400 km	125 ms	1,2,3,...,10	100	5.6i-l; 5.13a; 5.16a-f; 5.17i-l
Test 3	Anisotropic	Ideal Land	Anisotropic down to 400 km	125 ms	1,2,3,...,10	100	5.8a-d; 5.13c; 5.16g-h
Test 4	Anisotropic	Ideal Marine + Land	Anisotropic down to 400 km	125 ms	1,2,3,...,10	100	5.6m-p; 5.13b; 5.16i-j; 5.17m-p
Test 5	Isotropic	Ideal Marine + Land	Anisotropic down to 400 km	125 ms	1,2,3,...,10	1000	5.8a-d; 5.13d; 5.16k-l
Test 6	Anisotropic	Ideal Marine + Land	Anisotropic down to 200 km	125 ms	2	100	5.8e-h; 5.16m-n

We constructed L-curves (Aster et al., 2018) plotting the squared model norm ($|dm|^2$) as a function of the squared norm of the delay time residuals normalized by the estimated data uncertainty (χ^2) for different values of damping factor (λ_{du}) (Supplementary Figure 5.13). Ideal solutions are considered those near the corner of the L-curve where an increase in model norm does not result in an appreciable decrease in data residuals. For each test, convergence is usually reached before or at iteration 3.

Reliability of the tomographic results

To explore possible trade-offs between isotropic and anisotropic parameters, a synthetic inversion was aimed at reconstructing the isotropic component of model CWM. To test if velocity anomalies present in our preferred isotropic model could yield erroneous anisotropy, delays predicted through this model –not considering the anisotropic components– were inverted for both isotropic and anisotropic parameters. The result is showed in Figure 5.3. Isotropic anomalies were faithfully recovered with minimal anisotropic perturbations throughout the entire study area (generally <1%) with the exception of higher-magnitude anisotropic perturbations (<2%) in the Southern Tyrrhenian sea, Ionian sea and Sicilian Channel.

Permuted data test similar to Bijwaard et al. (1998), Rawlinson and Spakman (2016), and Spakman (1991) was performed in order to assess the model amplitude error as the anomaly amplitudes are interpreted in terms of geodynamic features and errors could potentially bring to wrong interpretations. The inverted dataset is the data vector of the last iteration of Test 2, randomly permuted. The "permuted dataset" can be considered noise that has the same average, standard deviation and distribution of the delay times "not permuted" used for Test 2. By permuting the data vector order, there is no more correlation between the delay times and the raypaths. The starting model is the tomography obtained at the last iteration of Test 2. This

choice allows to guarantee that the ray geometry of the permuted data test is comparable to that in Test 2. The result is showed in Figure 5.4. We do not observe regions with systematic anomaly patterns, on the contrary, random anomalies are recovered with delay time residual $\chi^2 \approx 8.8$ and the RMS amplitude variations $\approx 0.99\%$. This value is much bigger than the data residual observed for Test 2 (i.e. $\chi^2 \approx 0.95$; Supplementary Figure 5.13a) and for Test 3, 4 and 5 as well (i.e. $0.85 < \chi^2 < 3.6$; Supplementary Figure 5.13b-d). The random distribution of the retrieved anomalies and the low data fit obtained for the permuted data test compared with the higher data fit of the correlated (i.e. the data vector not permuted) data test suggest that the results of our tests (i.e. Test 1-6) are reliable.
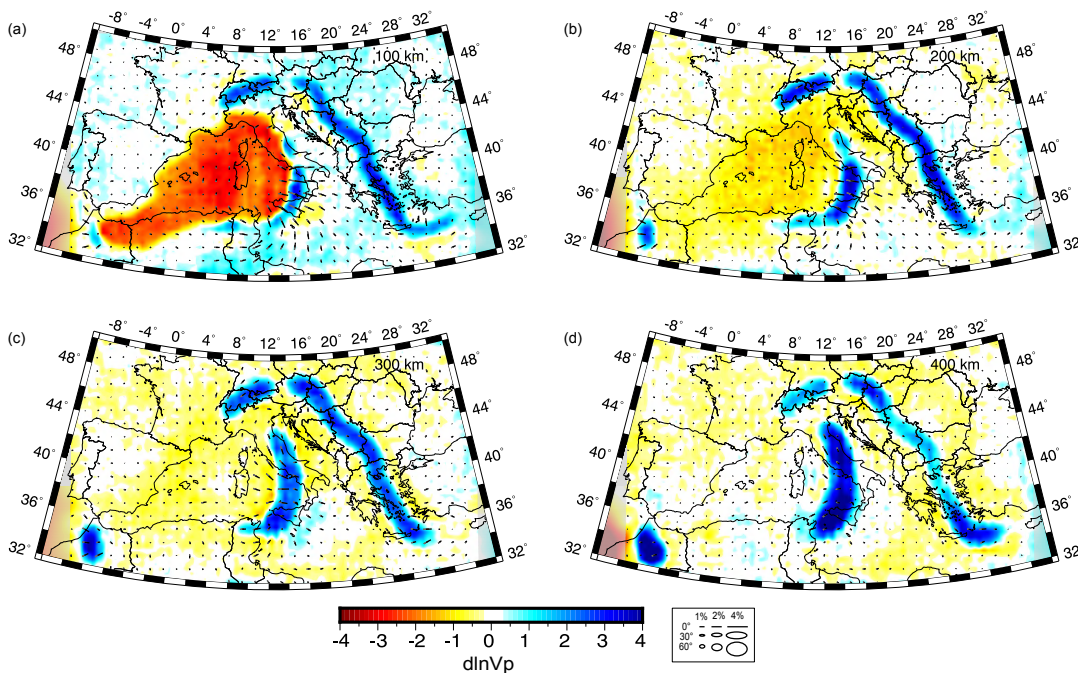
Figure 5.3: *Isotropic restoration synthetic test. Anisotropic inversion of purely isotropic synthetic data calculated through our model CWM, i.e., non taking into account the anisotropic patterns. While no anisotropic structures have been considered when performing the forward problem, the inversion does introduce some anisotropic perturbations. Anisotropy is represented by ellipse symbols where the major axis of the ellipse parallels the fast-direction and the minor axis scales linearly with the symmetry axis dip into the view plane such that fabrics parallel and normal to the cross-sections plot as lines and circles, respectively. Anisotropic perturbations were restricted to the upper 400 km. See legend. Areas of poor data coverage are masked in grey.*
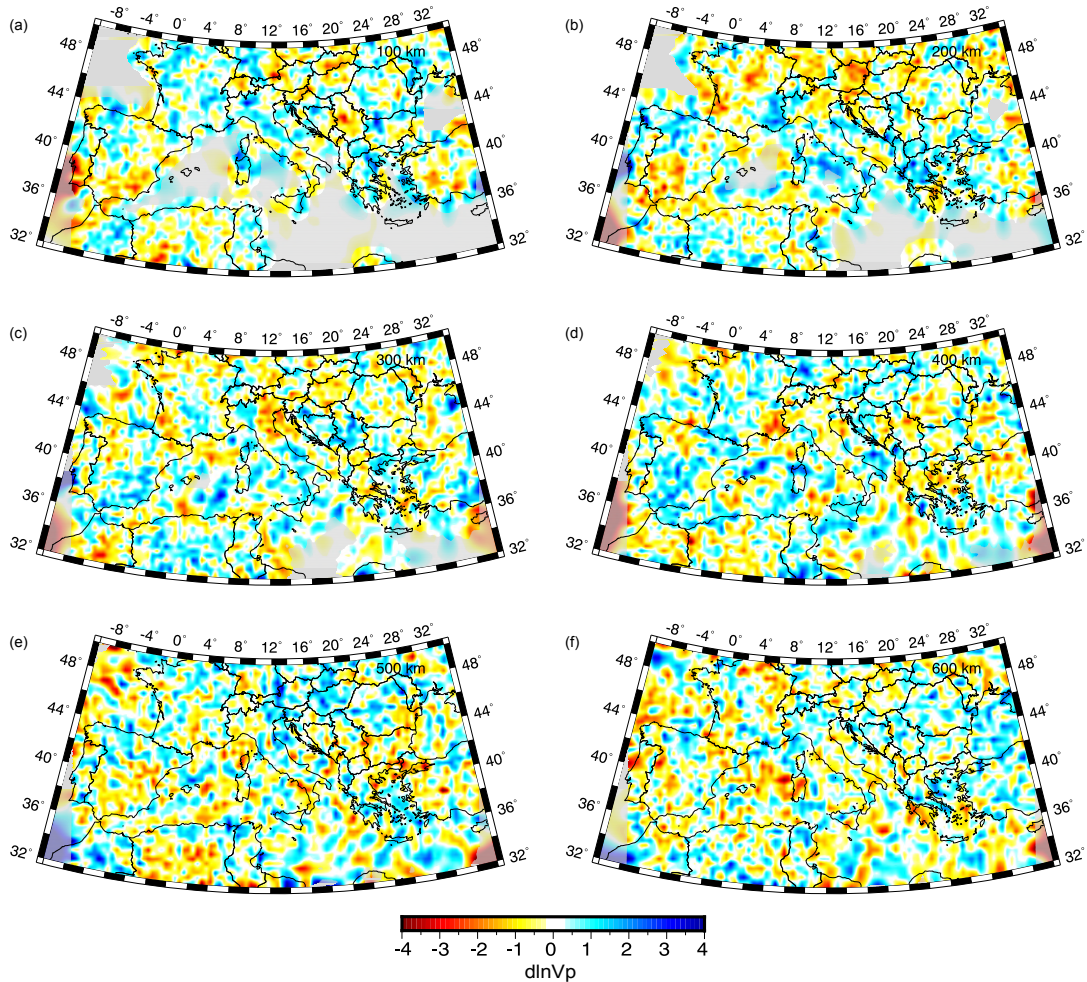
Figure 5.4: *Permuted data test. P-wave velocity anomalies obtained from the inversion of randomly permuted delay times.*

5.3 Results

5.3.1 Geodynamic evolution of the Central Western Mediterranean (Model CWM)

In this section the geodynamic evolution of Model CWM is addressed (Supplementary Movie S2). The following discussion focuses on a mere description of our geodynamic model evolution. Analogies and differences between Model CWM and the real tectonic evolution of the Central-Western Mediterranean region will be discussed in section 5.4.1. The Alpine and Dinaric slabs have been included in the Model CWM only to evaluate their influence in the mantle flow below the Adria plate surrounding regions, but they also
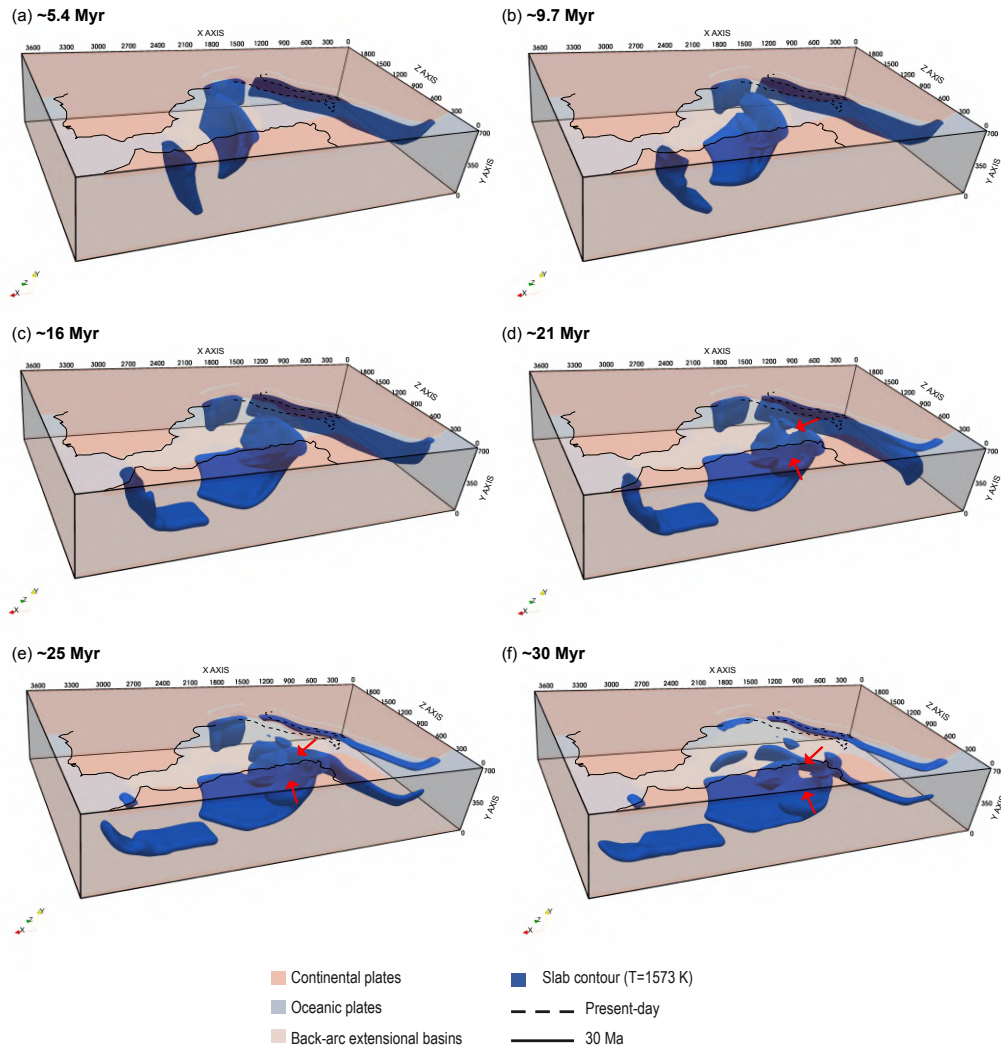
Figure 5.5: *Snapshots of the Model CWM geodynamic evolution. In blue the subducted slabs (contour at T=1573 K) below ~100 km depth. The plates are partially transparent for a better visualization of the subducted slabs. The solid black line indicates the coastlines in the Oligocene-Miocene (van Hinsbergen et al., 2014), while the dashed black line indicates the present-day coastlines of peninsular Italy. The red arrows indicate the two slab windows beneath the Central Apennines and the Africa continental plate.*

represent important targets to be recovered by our tomographic inversions. Their geodynamic evolution is characterized by further slab verticalization and final break-off.

The slabs negative buoyancy drives the evolution of the two active oceanic subductions. The oceanic plates progressively sink down to the the mantle transition zone and after bending start to rollback accompanied by a stretching of the overriding lithosphere. The Ionian slab migrates south-eastward while the Alboran slab south-westward. The rollback of the two slabs evolves

with episodes of lateral tearing, segmentation and break-off when trenches impact with a continental margin.

The tectonic evolution of the Ionian slab is similar to that of Model CM (Lo Bue et al., 2021). In a few million years (~ 4 Myr), the western part of the Ionian trench collides with the African plate inducing slab tearing along the passive margin and subduction of continental crust fragments. The tear propagates along the African margin, favouring the eastward slab rollback (Figure 5.5a). Subsequently, the northeastern edge of the trench reaches the thin northwestern Adria margin progressively causing subduction of the Adria continental crust, slab lateral tearing along the oceanic-continental lithosphere transition, and the formation of a curved trench due to the variations of buoyancy along it. Meanwhile, the Alboran slab rapidly rolls back westward, accommodated by lithosphere tearing along the African and Iberian margins (Figure 5.5a,b). In $\sim$10 Myr, both subducting slabs are already stagnating horizontally in the mantle transition zone at the bottom of the model.

After $\sim$16 Myr (Figure 5.5c), the Alboran slab reaches the area of the model corresponding to the current Gibraltar region, after which a very slow trench retreat is observed until the complete detachment at $\sim$23 Myr.

The late evolution of the Ionian slab is instead more complex and important differences occur compared to the Model CM (Lo Bue et al., 2021). When the Ionian trench reaches Central Adria, part of the stiffer continental promontory subducts causing slab break-off. As in Lo Bue et al. (2021), this rupture generates a large slab window that splits the Ionian slab in two separate slabs. Contrary to Lo Bue et al. (2021), here, this phenomenon also occurs on the side of the African continent. This leads to a final geometry of the Ionian slab characterized by the presence of two wide windows, one below the area corresponding to the current Central Apennines and one beneath the north-eastern African margin (Figure 5.5d).

After ∼20 Myr (Figure 5.5d,e,f), slab remnants are found in model areas corresponding to the present-day Northern Apennines, Southern Tyrrhenian sea, Alboran sea and Kabylides. At ∼20 Myr, the Ionian slab (portions beneath the Northern Apennines and south of the Tyrrhenian Sea - Supplementary Figure 5.14a) and the Alboran slab extend continuously from the surface down to the mantle transition zone.

At ∼ 25 Myr, the Northern Apenninic and Kabylides slabs hang down to ∼150 km depth (Supplementary Figure 5.14b). The first one extends further deeper from ∼180 km down to about ∼660 km depth while a horizontal segment of the Kabylides slab is still joined to the Ionian slab from ∼180 km down to about ∼300. The remaining portion of the Ionian slab (south of the Tyrrhenian Sea) instead extends continuously from the surface down to the mantle transition zone. The Alboran slab is already detached. At ∼ 30 Myr, the Calabrian slab appears still anchored to the surface (Supplementary Figure 5.14c) showing clear evidences of break-off. The model evolves with the complete detachment of all the slabs (Figure 5.5f).

5.3.2 Upper Mantle Flow, LPO, and Synthetic Seismic Anisotropy

The subduction and rollback of the Ionian and Alboran slabs in the Model CWM induces a complex flow in the surrounding mantle characterized by the presence of poloidal and toroidal components (Supplementary Movie S2). The initial sinking of the two slabs (i.e. Ionian and Alboran) generates a dominant poloidal flow component and mantle upwelling in the mantle wedge (i.e., arrows pointing downward or upward in correspondence of slabs and basins, respectively - Supplementary Movie S2). Subsequently, toroidal cells are also generated by slab rollback that forces the mantle to flow
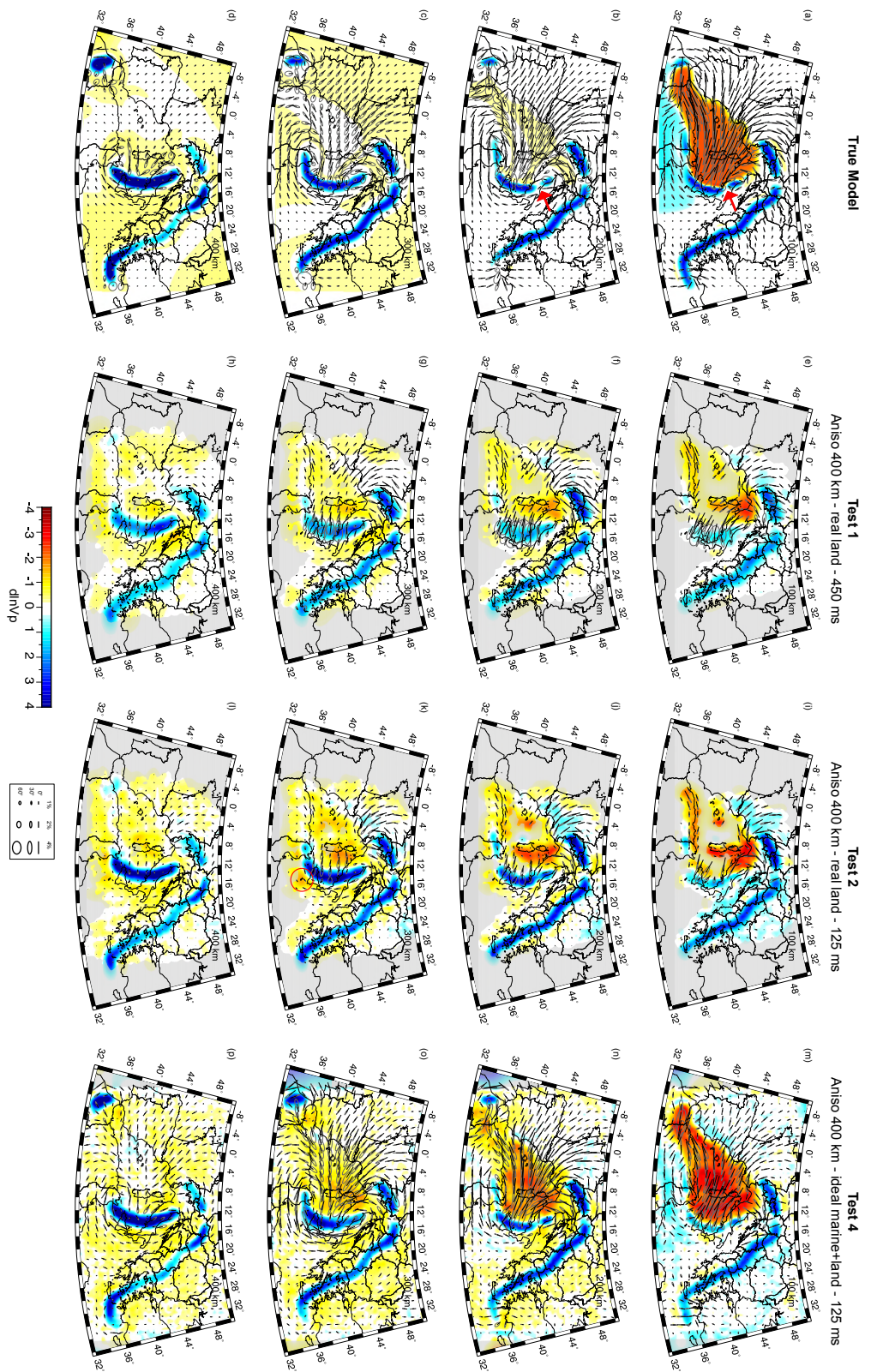
Figure 5.6: *True model and anisotropic tomography results. Depth slices are shown at 100 km, 200 km, 300 km and 400 km depth for the true model (a-d), the model resulting from Test 1 (e-h), Test 2 (i-l) and Test 4 (m-p). Isotropic anomalies are plotted with respect to the reference velocity model. We plot anisotropic fabrics as ellipses where the major axis of the ellipse parallels the fast-direction of anisotropy in the view plane and scales with the anisotropic magnitude while the minor axis scales linearly with the symmetry axis dip into the view plane. Thus, fabrics parallel and normal to the view plane plot as lines and circles, respectively; see legend. Areas of poor data coverage are masked in grey. The red arrows in panels a and b indicate the position of the slab window below the Central Apennines. The red circle in panel k indicates a low velocity artefact.*

circularly around the edges of the two slabs and through the slab windows
that are formed at later stages.

Here, compared to Model CM (Lo Bue et al., 2021), the complexity of the
mantle flow increases due to the presence of the multiple subducting slabs.
We observe the mantle flowing mainly horizontally toward southeast and
west directions in response to the horizontal motion of the Ionian and Alb-
oran slabs, respectively. The Dinaric and Alpine slabs act as a barrier to the
large toroidal flow patterns induced by the retreat of the Ionian plate found in
Model CM of Lo Bue et al. (2021). As a result, the mantle flows parallel to the
Dinaric slab in the region corresponding to the Adriatic sea and Dinarides,
as well parallel to the Alpine slab. The strongest upper mantle fabrics are ob-
served in the area surrounded by the Alboran and Ionian slabs, down to 400
km depth, while east of the Dinaric slab and in the eastern Ionian sea mainly
isotropic structures are found (Figure 5.6a-d). This is because Model CWM
only partially reproduces the retreat of the Aegean slab over the Cenozoic.
Trench-perpendicular azimuths are observed in the supra-slab upper man-
tle, corresponding to the Tyrrhenian and Alboran basins. The sub-slab upper
mantle portions (i.e. below Calabrian, Alboran and Alpine slabs) are instead
characterized by the presence of trench-parallel fabrics. Near-horizontal fab-
rics are found in the area of the Ionian sea and in the continental European
plate. More steeply dipping fabrics are instead observed in the Tyrrhenian
sea, Alboran basin and Northern Italy in correspondence of the subducting
slabs.

The upper mantle fabrics patterns are reflected in those of the synthetic
SKS splitting measurements shown in Figure 5.7. In the back-arc regions,
the fast azimuths orient parallel to the trajectory of the Ionian and Alboran
trenches migration. The delay times in these regions are very high ($\delta t =
2 - 3.2s$), reflecting fabrics that are consistent within the entire upper mantle,
and are reduced in the areas near the two trenches ($\delta t = 1 - 1.5s$) due to the

superposition of mantle domains with contrasting fabric patterns. In the fore arc regions, the teleseismic fast shear wave components align trench-parallel, while around the slabs edges, they form a circular pattern highlighting the underlying return flow ($\delta t = 1 - 1.5s$).

5.3.3   Anisotropic tomography inversions

Tomography results are shown in Figure 5.6 and 5.8, with additional maps at 500 km and 600 km depth in Supplementary Figure 5.16 and narrower colorscale limits (i.e. [-2% − +2%]) in Supplementary Figure 5.17.

Following the workflow described in section 5.2.3, we first inverted a set of time delays computed through Model CWM using the distribution of sources and receivers as in Rappisi et al. (2022) (see Supplementary Figure 5.12a and Figure 5.2a; Test 1). We added random errors with a standard deviation of 450 ms to the data (i.e. a value corresponding to the amount of error usually encountered in real case studies). This solution reproduces realistic study conditions to test the ability of our method in recovering the main isotropic and anisotropic structures of the target (Figure 5.6 e-h).

The marine areas of the Tyrrhenian, Adriatic, Ionian Sea and Strait of Sicily are poorly sampled, resulting in a general loss of fast and slow anomaly amplitude. Nevertheless, the main isotropic structures (i.e. the Alpine, Northern Apennines, Calabrian and Dinaric-Hellenic slabs) are well recovered. The Northern Apenninic and Calabrian slabs are imaged as a single weak fast anomaly stretching along the N-S direction, while in the geodynamic model a ∼150 km wide window is present at shallow depth, i.e ∼100-200 km beneath central Italy (Figures 5.5d, 5.14a and 5.6a-b).

Test 1 exhibits a ∼-2% low velocity artefact in correspondence of the northern Tyrrhenian basin and Corsica-Sardinia block at ∼200 km depth (Figure 5.6f), indicating some vertical smearing of the true low velocity structure

confined in the upper 100 km of the domain. Anisotropy patterns are well recovered where seismic ray coverage is relatively abundant, e.g., the near-horizontal circular pattern of P-wave fast azimuths around the Western Alps in Southern France. Trench perpendicular steeply dipping fabrics are imaged above the Calabrian slab in the Tyrrhenian Sea, while E-W oriented fabrics are found in the Northern African margin.
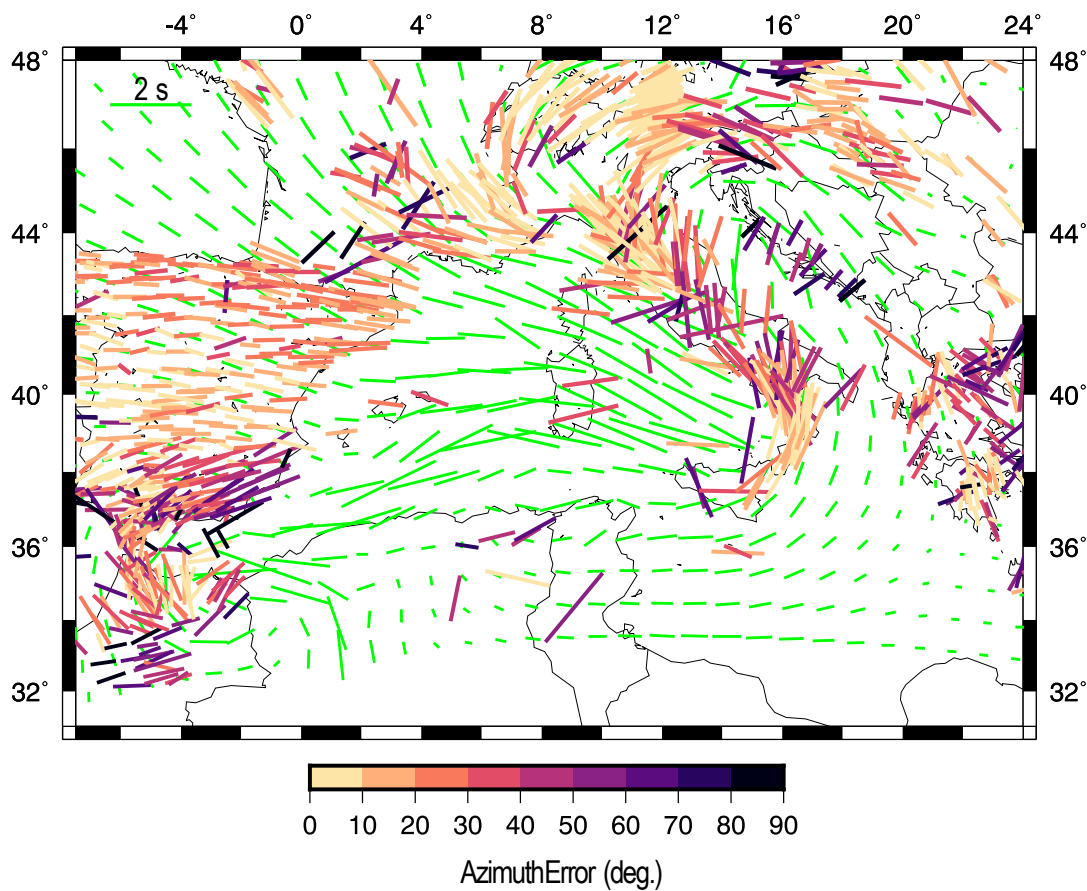
Figure 5.7: *SKS-splitting measurements in the Central-Western Mediterranean (Becker et al., 2012) color-coded by the angular misfit compared with synthetic SKS splitting measurements for Model CWM at ~20 Myr (green bars). The EW green bar in the upper left corner indicates 2 s. Time-delay misfits are shown in Supplementary Figure 5.15a.*

The recovered isotropic and anisotropic structures from the model resulting from Test 2 (Figure 5.6i-l) indicate that a better quality dataset increases the probability of better retrieving the magnitude and sharpness of the true anomalies. However, at the same time new and increased in magnitude tomography artefacts are observed. For example, the low velocity artefact at
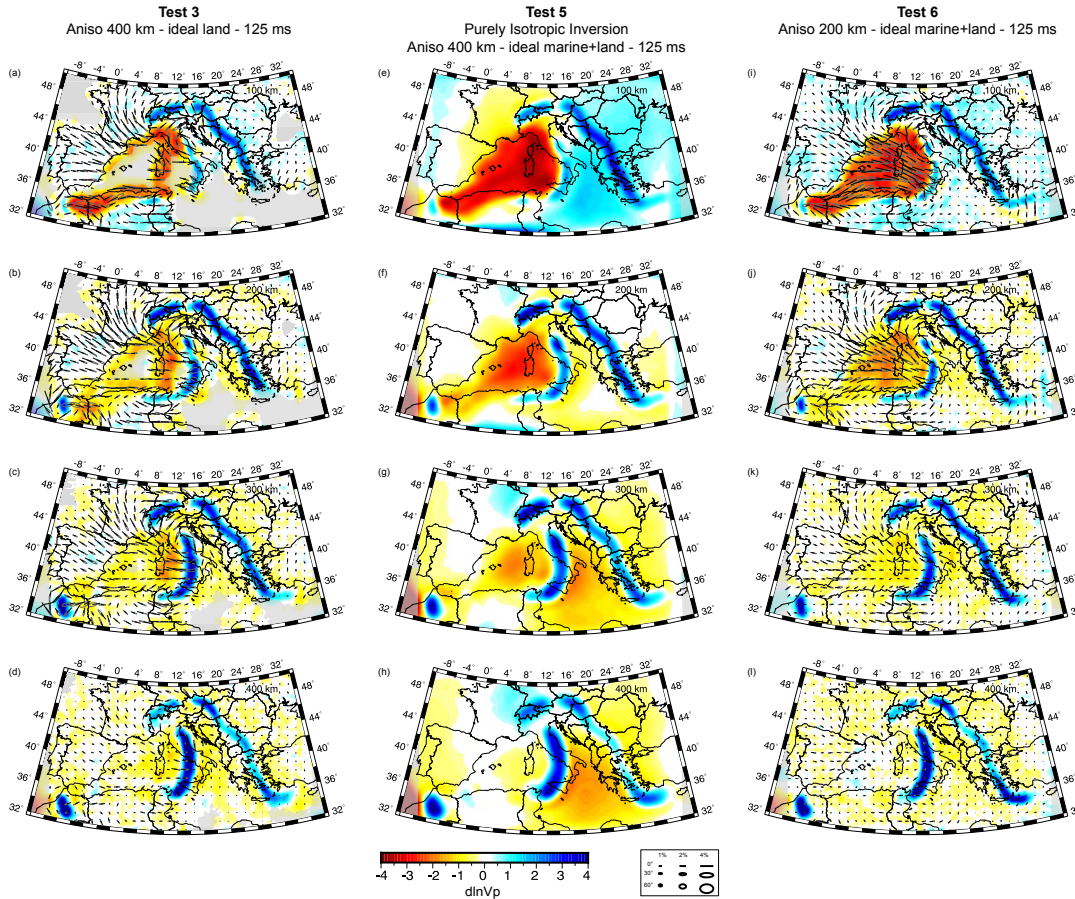
Figure 5.8: *Depth slices at 100 km, 200 km, 300 km and 400 km depth for the tomographic results from Test 3 (a-d), Test 5 (e-h) and Test 6 (i-j). Isotropic anomalies are plotted with respect to the starting model. Anisotropy is plotted using ellipses as described in Figure 5.6. Areas of poor data coverage are masked in grey.*

200 km depth (Figure 5.6j) in the Tyrrhenian sea, east of the Sardinia-Corsica block, is in Test 2 much stronger than it was in Test 1 (Figure 5.6f) with an increase in magnitude of ∼1%. And also, a new ∼100 km wide low velocity artefact (∼-2%) appears at 300 km depth south of Sicily (Figure 5.6k). High velocity artefacts already observed in Test 1, such as the one in Spain and west of the Alps, are in Test 2 much bigger (i.e. joined in a single broader anomaly) and slightly stronger in amplitude, covering the entire southern portion of France at 100 and 200 km depth (Figure 5.6i-j). Although the anisotropy patterns do not differ from the ones of Test 1, a reduction in their magnitude is observed above the Calabrian slab (i.e. in the Tyrrhenian Sea
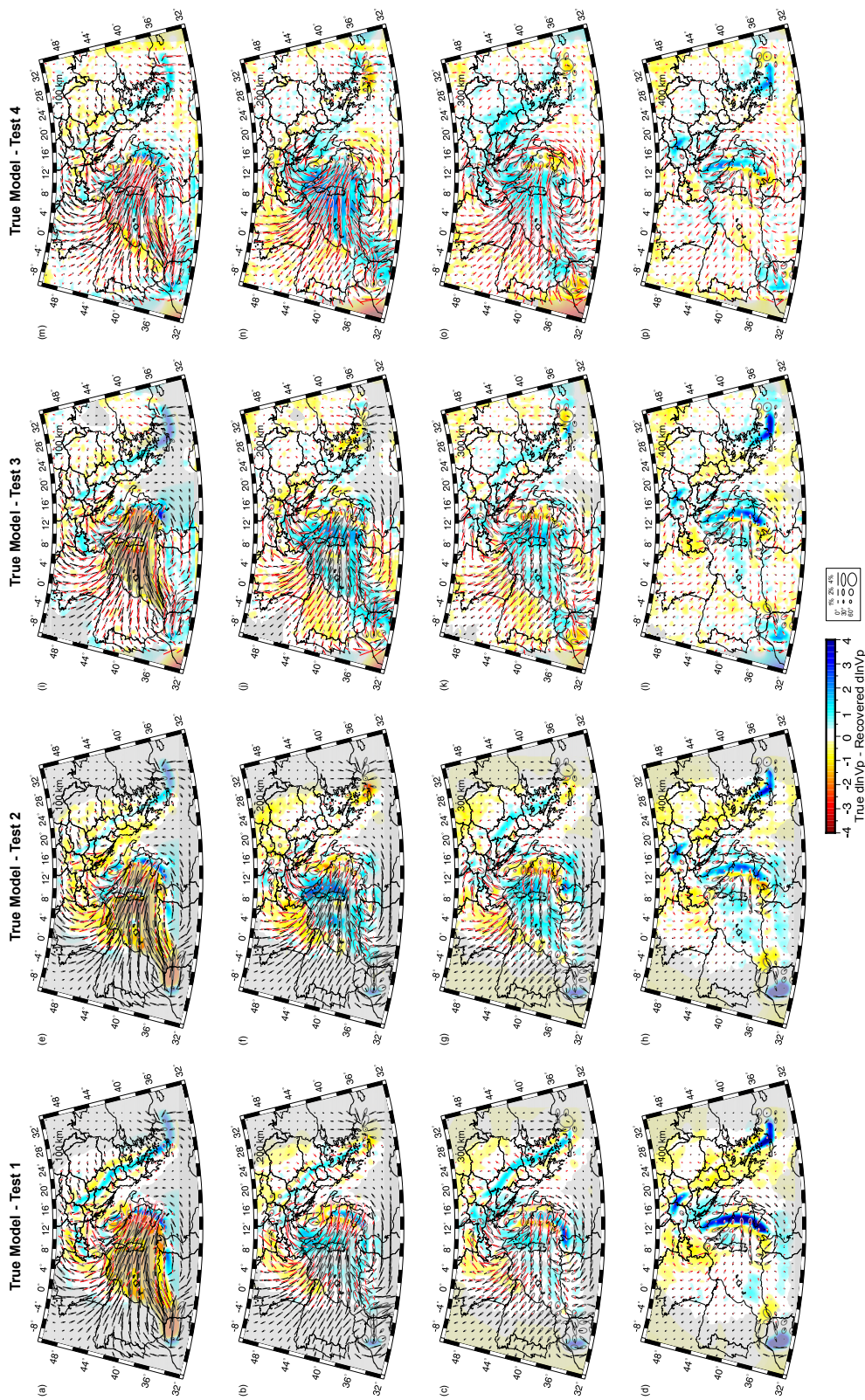
Figure 5.9: *Depth slices at 100 km, 200 km, 300 km and 400 km showing the differences between the true model and (a-d) Test 1, (e-h) Test 2, (i-l) Test 3 and (m-p) Test 4. Anisotropy is plotted using ellipses as described in Figure 5.6. Areas of poor data coverage are masked in grey.*
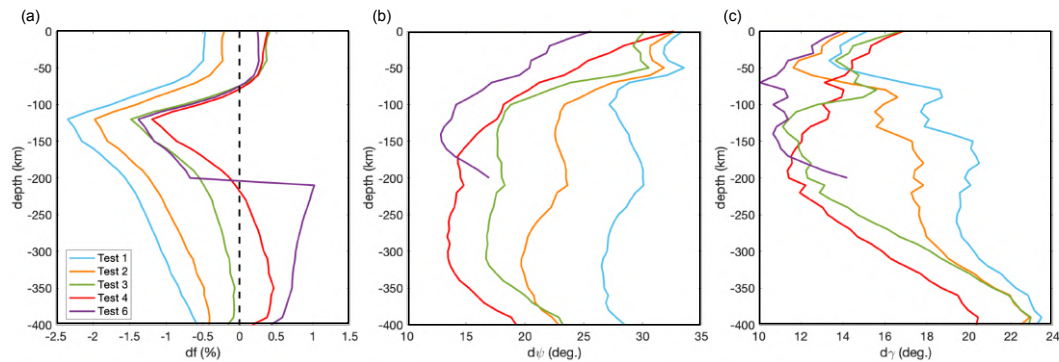
Figure 5.10: *Errors in recovered anisotropic parameters. Mean errors in the anisotropic (a) fraction, (b) azimuth, and (c) elevation as a function of depth are shown for Test 1 (blue line), Test 2 (orange line), Test 3 (green line), Test 4 (red line) and Test 6 (purple line).*

dipping fabrics). Probably due to the trade-off between isotropic and anisotropic components, it is worth noting that this reduction is associated with an increase in the magnitude of the isotropic fast anomaly.

In Test 4, with an ideal distribution of sources (Supplementary Figure 5.12b) and marine and land receivers (Figure 5.2c), the fast anomalies are better retrieved in terms of amplitude and spatial distribution (i.e. size and geographic position). However, many artefacts still persist, for example, at 100 km depth (Figure 5.6m) the Calabrian fast anomaly exhibits a weak magnitude (i.e., $\sim$1% vs. $\sim$3% in the true model). More importantly, at 200 km depth (Figure 5.6n) the slow velocity artefact located est of the Sardinia-Corsica block in the previous tests now affects the entire Liguro-Provençal and Tyrrhenian basins. Although the weak magnitude of the Calabrian fast anomaly, the gap between Northern Apennines and Calabrian slab is better retrieved at 100 and 200 km depth (Figure 5.6m, n) with respect to the previous Test 1 and Test 2. The Alboran fast anomaly is recovered as well and placed in the correct geographic position (Figure 5.6p). The high velocity artefact imaged in Test 2 beneath the southern France at shallow depth (100-200 km; Figure 5.6i-j), now disappears and the recovered model better resembles the target. The ideal station coverage also helps in retrieving anisotropic

patterns and magnitude at every depth slice, including the well sampled marine areas where the NW-SE fabrics are now recovered in the Tyrrhenian Sea. Similar results, i.e. about sensitivity of teleseismic P-wave tomography under different conditions, have been previously described (e.g., Lévĕque et al. (1993), Rawlinson and Spakman (2016), and Spakman and Nolet (1988)).

Considering that placing marine receivers is a costly procedure, we also performed a set of inversions with an ideal distribution of on-land receivers only (Figure 5.2b). The result is shown in Figure 5.8(a-d). The main effect of having reduced the number of receivers is the underestimation of anisotropy in poorly sampled areas. For example, the trench-parallel patterns bordering the eastern side of the Apenninic fast anomaly in Test 3 (Figure 5.8a-d) appears weaker than it is in the true model and in Test 4 (Figure 5.6a-d, 5.6m-p).

Figure 5.8 also shows the results of Test 5 and 6 performed, respectively, in isotropic approximation (Figure 5.8e-h; i.e. ignoring seismic anisotropy) or with a model that is anisotropic only in the top 200 km (Figure 5.8i-l). In both cases, we observe that the isotropic solution contains a number of fast anomaly features broadly consistent with the true model (Figure 5.6a-d). However, several slow velocity artefacts are imaged around and above the main slabs (i.e. Alpine and Calabrian slabs) especially when not considering seismic anisotropy (Figure 5.8e-h). Figure 5.8(i-l) indicate that seismic anisotropy is retrieved also at depths below 200 km where the true model is instead isotropic. This suggests that when only using teleseismic P-waves anisotropic structures are vertically smeared similarly to isotropic anomalies.

5.4 Discussion

5.4.1 How well does Model CWM fit seismological observations?

In this work we have extended the modeling methodology of Lo Bue et al. (2021) to build a structurally complex geodynamic model which was then exploited to test the capabilities of anisotropic P-wave seismic tomography to recover a Mediterranean-like subduction environment. With respect to Model CM of Lo Bue et al. (2021), the new geodynamic model CWM has been updated by using a different paleo-tectonic configuration characterized by the presence of additional subducting plates (i.e., Alboran, Alpine and Dinaric subduction zones).

Similarly to previous studies (Holt et al., 2018; Holt et al., 2017; Jagoutz et al., 2015; Király et al., 2018; Luth et al., 2013; Peral et al., 2020), here we notice that the presence of multiple subducting slabs influences the over-all force balance, the geometry and kinematics of the subduction systems, as well as the mantle flow patterns. The inclusion of additional subduction zones has partly improved the prediction of the mantle dynamics leading to a better correspondence between the modeled and observed surface and deep isotropic structures, and seismic anisotropy patterns when compared to Model CM of Lo Bue et al. (2021). A quantitative comparison between predicted and observed SKS splitting measurements (Figure 5.7; Becker et al. (2012) database updated December 6, 2020) shows a moderate improvement in terms of the average misfit angle from $\sim 26°$ in Model CM (Lo Bue et al., 2021) to $\sim 23°$ in Model CWM (Supplementary Figure 5.15). In detail, the general pattern of the synthetic 3D anisotropy calculations matches the observed data with a relatively lower misfit angle in the model areas corresponding to the Iberian peninsula and the Apennines chain if compared to

the Model CM (Lo Bue et al., 2021). In the Dinaric Alps area the synthetic fast splitting directions are trench parallel. Here, the average angular misfit between predicted and observed fast azimuths remains high, but with slightly reduced values of about $70 - 80°$ degrees, compared to $90°$ degrees of Lo Bue et al. (2021). Lastly, we acknowledge that split times are not particularly well-fit considering that the residual mean and standard deviation are 667 ms and 592 ms, respectively (Supplementary Figure 5.15). However, the magnitude of the average misfit of the whole model is mainly due to the broad mismatch found in the south of the Iberian Peninsula.

Uncertainties in the initial model geometry and in the modeled mantle rheology are likely responsible for the major discrepancies. Other sources of mismatch could be related to the modeling of the mantle textures, and to the presence of fossil fabrics within the oceanic and continental subducted lithosphere that have not been included here. Furthermore, the employed free slip boundary conditions prevent lateral mantle flow across the bottom and vertical boundaries. The large discrepancy in the area of the southern Iberian Peninsula may be partly due to the fact that the model does not account for the Cenozoic Eurasia-Africa convergence, and the relative position of the African plate has remained fixed since ∼30 Ma differing slightly from the present-day one. As such, the Alboran arc is positioned further south than its present-day position (under Morocco).

Although Model CWM is based on paleogeographic and tectonic reconstructions of the region in the Oligocene-Miocene (Faccenna et al., 2014; Lucente et al., 2006; Lucente & Speranza, 2001; Romagny et al., 2020; van Hinsbergen et al., 2014), geometrical assumptions, that could potentially bias the final output, were required due to limitations imposed by numerical modeling. First, the initial geometry and thermal ages of the subducting slabs were partly simplified and this could strongly influence the comparison with seismological data. This could be the case of the Alps and Dinarides where a

simplified initial portion of the subducted lithosphere was imposed to model flow barriers. We note that the detachment of Alpine slabs prior to collision is still debated in some areas, such as the Western Alps where Kästle et al. (2020) favor the interpretation of a recent European slab break-off, consistent with observations of strong exhumation and sedimentation that started around 2–7 Ma ago and is still ongoing (Escher & Beaumont, 1997; Fox et al., 2016; Kuhlemann, 2007; Nocquet et al., 2016). On the contrary, Zhao et al. (2016) document the lateral continuity of the European slab from the Western Alps to the Central Alps, and the downdip slab continuity beneath the Central Alps, ruling out the hypothesis of slab break-off to explain Cenozoic Alpine magmatism. The teleseismic P-wave tomography of Rappisi et al. (2022), referred as model ani-NEWTON21, exhibits a continuous slab beneath the Alps, divided into an Eastern, Central, and Western segment characterised by changes in dip. Similarly, the extent of the Dinaric slab at ∼30 Ma is largely debated. Post-collisional uplift and contemporaneous emplacement of igneous rocks (33-22 Ma) in the internal Dinarides may suggest either (i) "that the Oligocene-Miocene orogen-wide uplift was driven by post-break-off delamination of the Adriatic lithospheric mantle" (Balling et al., 2021), or (ii) verticalization of the Adria slab driven by slab pull and consequent upper plate extension, which is exactly what is modeled in our Model CWM. In conclusion, the available geophysical and geological data do not allow to discriminate between a model of post-collisional slab break-off and one of post-collisional slab verticalization (as modelled for the Alps and Dinarides in our Model CWM), as both would imply upper plate extension, uplift and magma emplacement (Faccenda et al., 2009; Faccenda et al., 2008).

Secondly, the tectonic reconstruction of Romagny et al. (2020) shows that ∼30 Ma the Mesozoic Tethyan lithosphere was consumed in two different trenches located from the Alps to the southeast of the Baleares and in the Alboran domain, respectively. Two incipient slabs (∼150-200 km) were already

subducted in the upper mantle. However, to trigger a "spontaneous" sub-
duction system, the Ionian trench has been initially positioned further south
with the slab extending to a depth of 300 km, while the Alboran one further
west with a 350 km deep slab, in order to model a more developed subduc-
tion and increase the slab negative buoyancy. This could cause a difference
in rates of Ionian and Alboran slabs retreat at the model early stage when
compared to those reported in the literature. However, we note that in the
reconstructions by Faccenna et al. (2014) and Romagny et al. (2020) the initial
plate geometry at ∼23 Ma does not differ substantially from that at ∼35 Ma,
and from our initial setup. This is likely related to the slow dynamics typical
of incipient subduction systems.

Despite the modeling limitations, Model CWM reproduces several episodes
of slab lateral tearing and break-off that have been proposed according to
geological and seismological data. The model is partly able to recover the
main features found in the seismic tomography models. After ∼20 Myr
(Figure 5.5d,e,f and Supplementary Figure 5.14) subducted lithospheric por-
tions are found below the areas corresponding to the Alboran, Kabylides
and Calabria-Apennine region where seismic tomographic methods have re-
vealed several positive velocities anomalies (Bezada et al., 2013; Calò et al.,
2012; Calò et al., 2013; Gutscher et al., 2002; Piromallo & Morelli, 2003; Spak-
man, 1991; Spakman et al., 1993; Spakman & Wortel, 2004; Van der Meer et
al., 2018; Wortel & Spakman, 2000; Wortel et al., 2009). For example, Model
CWM retrieves (a) the high-velocity body arranged horizontally over the 660
km discontinuity interpreted as the Ionian slab lying and broadening at the
base of the upper mantle by P-wave tomographic models (Amato et al., 1993;
Lucente et al., 1999; Piromallo & Morelli, 2003; Selvaggi & Chiarabba, 1995;
Spakman et al., 1993; Spakman & Wortel, 2004; Van der Meer et al., 2018);
(b) the portion of the slab under the Northern Apennines extending down to

150 km depth and from ∼180 km down to about 660 km depth (Supplementary Figure 5.14b) (El-Sharkawy et al., 2020; Giacomuzzi et al., 2012; Spakman & Wortel, 2004) and (c) the Calabrian slab continuous from the surface down to a depth of 660 km (El-Sharkawy et al., 2020; Giacomuzzi et al., 2012; Neri et al., 2012; Presti et al., 2019; Rappisi et al., 2022; Scarfì et al., 2018); (d) the portion of slab imaged under the north African margin of Algeria, hanging down to ∼150 km depth and from ∼200 km joining to the Calabrian slab (Supplementary Figure 5.14b) (Chertova et al., 2014; Van der Meer et al., 2018); (e) the presence of two wide windows in the Ionian slabs, one below the area corresponding to the present-day Central Apennines and one beneath the north-eastern African margin (Amato et al., 1993; Carminati et al., 1998; Faccenna et al., 2014; Faccenna et al., 2007; Lucente & Speranza, 2001; Magni et al., 2014; Piromallo & Morelli, 1997, 2003; Spakman & Wortel, 2004; Van der Meer et al., 2018).

On the contrary, the modeled Alboran slab, in addition to being in a wrong position (i.e. further south than its current position), possesses a morphology which is not entirely realistic. This is probably due to the imposed initially 350 km long slab and to the slab tearing occurring as soon as the trench interacts with the continental margins, thus preventing any arcuate shape of the margin. However, we note that the geometry and length of the Alboran slab in model CWM at 0 (initial conditions; Figure 5.1) and ∼20 Ma (Figure 5.5d) are similar to those obtained by Chertova et al. (2014) at -20 and 0 Ma (see Figure 8 and Figure 10 of Chertova et al. (2014)). The flat portion of our Alboran slab at ∼20 Ma (Figure 5.5) is consistent with the Spakman and Wortel (2004) model (as presented in Figure 3 of Chertova et al. (2014)).

5.4.2   How well does tomography recover the target model?

We performed seismological forward and inverse simulations by testing different types of data coverage and quality. To help the comparison between the different tests and evaluating their capabilities in recovering model CWM, Figure 5.9 shows the difference between the true model and the solution of Test 1, Test 2, Test 3 and Test 4, both in terms of isotropic and anisotropic structures (i.e. dlnVp = dlnVp true model - dlnVp tomography model). We observe that the average difference in retrieved isotropic velocity is in general low ($\sim$[-1%,+1%]) and gradually decreases moving from Test 1 to Test 4. For example, Figure 5.9(a-d) shows maximum values of dlnVp of $\sim$3% for Test 1, i.e. in the Apenninic slab at 400 km depth (Figure 5.9d), that gradually decrease to $\sim$1% for Test 4. For Test 4 (i.e. test with perfect data coverage), higher values are observed in the western side of the model, with peaks of $\sim$ 1.5% in the Liguro-Provençal basin at 200 km depth (Figure 5.9n). True and recovered anisotropy patterns are plotted in black and red, respectively, showing high degree of matching both in terms of azimuth and dip. With few exceptions of sparse differences in dip angles, no particular areas of discrepancy are identified.

From our results it emerged that even with a non-ideal source-station coverage the recovery of isotropic structures and anisotropic patterns is quite good, although anisotropy magnitude is overall underestimated (especially in poorly sampled areas). This suggests that the amount of mantle anisotropy could be higher than that retrieved by tomographic models with commonly uneven source-receiver distributions. The consequences of the inhomogeneous distribution of seismicity and stations on ray coverage and on retrieved tomographic images is known in isotropic tomographic models (e.g., Antolik et al., 2003; Boschi & Dziewonski, 1999; Bozdağ et al., 2016; Dalton &

Ekström, 2006; Masters et al., 1996; Ruan et al., 2019). Here we show that similar problems are also found in anisotropic seismic tomographic models (e.g., causing underestimation of anisotropy magnitude). In addition, it emerged that tomographic images calculated from data with a scarce seismic coverage are potentially affected by the presence of anomalies placed in a wrong geographic position. This is the case of the Alboran slab that in Figure 5.6(e-l) appears shifted toward the east. This kind of artefacts could bring errors in the tomographic model interpretation when fast anomalies are present close to the boundaries of the sampled area. Increasing data quality (i.e., decreasing data error; Test 2) helps in better retrieving the magnitude of the isotropic and anisotropic structures, but at the same time leads to an increase in the magnitude and size of the artefacts in poorly sampled areas (Figure 5.6e-l). In addition, Figure 5.6(m-p) shows that ideal data coverage allows for a more accurate retrieval of anomaly magnitudes without increasing artefact amplitudes. However, we note that the higher number of receivers (e.g., in the Tyrrhenian and Liguro-Provençal basins) at 200 km depth amplifies the smearing of the upper low-velocity layer with respect to Test 3 where, on the contrary, the limited number of stations (i.e. limited rays) reduces this effect.

In the inversions where seismic anisotropy is ignored (Test 5), we observe that several slow anomalies appear in the tomographic sections (Figure 5.8e-h). This is especially evident in the area north of the Alps (Figure 5.8a) and below the Calabrian slab (i.e. in the Ionian Sea, Figure 5.8b-d). Considering that these anomalies are not present in the true model and indeed completely disappear in the anisotropic inversions (Figure 5.6), it follows that they are seismic artefacts due to the isotropic approximation.

Lastly, the test carried out on the model isotropic only from 200 km depth down (Test 6), showed that both the isotropic and anisotropic features are subjected to vertical smearing (5.8g,h). This should be taken into account when interpreting teleseismic P-wave anisotropic tomography.

In order to further characterize model differences between true and tomographic models, we have computed the average misfit values for fraction of anisotropy (df), azimuth and dip angles (i.e. $d\psi$ and $d\gamma$) with increasing depth (Figure 5.10a-c) with respect to the true values. We observe that the average solution gradually improves, better resembling the true model, with decreasing data error and improving data coverage. The higher values of misfit are in fact observed for the model obtained from the inversion performed with the bigger data error (i.e. 450 ms, Test 1) and the worst receiver distribution. This is true for both df and $d\psi$, while for $d\gamma$ is valid below $\sim$70 km depth (Figure 5.10c). For all models the average azimuthal misfit is highest in the upper 50 km (due to the poor ray coverage at these depths by teleseismic P-waves), below which it rapidly decreases and remains roughly constant with depth except for a slight increase toward the bottom of the anisotropic domain. In contrast, the dip angle average misfit gradually increases with depth. The misfit curves for Test 4 and Test 6 show similar shapes but with shifted absolute values in the upper 150 km. This indicates that the presence of deeper anisotropy (Test 4) associated with poor vertical resolution deteriorates the quality of the retrieved shallower structures.

5.5 Conclusion

We applied the modeling methodology of Lo Bue et al. (2021) to simulate the geodynamic evolution over $\sim$20-30 Myr of a model that presents similar characteristics to those currently observed in the Central-Western Mediterranean region (e.g., detached or stagnating slabs, slab windows, etc). To quantify similarities and discrepancies between the obtained geodynamic model and the current tectonic setting, the model results were verified by comparing seismological synthetics (isotropic P-wave anomalies, P-wave anisotropy and SKS splitting) and major tectonic features (i.e., slab and trench geometry)

with observations. This comparison confirms that, with respect to the previous study of Lo Bue et al. (2021), using a more complex initial geometry (i.e. including the Alboran, Alpine and Dinaric-Hellenic slabs) allows us to perform a step forward toward the better recovering of the mantle flow, overall evolution and current tectonic beneath this region. However, we note that model CWM is still far from reproducing the exact evolution and present-day tectonic setting of the area and further studies need to be performed in this direction. For example, next-level numerical studies should attempt to improve the model geometry by considering the Earth's sphericity and the Africa-Eurasia plates convergence.

Despite the several limitation of the numerical methods (e.g., Cartesian coordinates system, no plates convergence, no fossil LPO, fabrics within the lithosphere, free slip boundaries, no mantle in/outflow, etc..) and the assumptions necessary to start and drive the simulation self-consistently (e.g., initial slab depths, mantle rheology parameters, etc..), we observe that at $\sim$20 Myr model CWM exhibits interesting geological features resembling those found in the Central-Western Mediterranean (e.g., Calabrian slab continuous from the surface down to the base of the upper mantle, the presence of two wide windows in the Ionian slab, etc). For this reason, we used the modeled elastic properties at this stage (i.e. the elastic tensors at $\sim$20 Myr), to perform 3D P-wave anisotropic tomography using the approach proposed by Vander-Beek and Faccenda (2021). Using the geodynamic model as reference model, we evaluated the capabilities of seismic tomography to recover a complex subduction environment in different conditions, such as poor station coverage and bad data quality. From the seismological inversions and the comparison between purely isotropic and anisotropic solutions it emerges that (i) it is fundamental to invert for anisotropy to improve the reliability of the tomographic result and (ii) even a non-ideal source-station coverage allows

to recover isotropic structures and anisotropic patterns from teleseismic P-wave tomography. Anisotropy magnitude, although consistent with those of the synthetic target model, is overall underestimated in the upper mantle especially in poorly sampled areas. In light of this, it is recommended to increase the number of marine and land stations and improve the accuracy of teleseismic arrival time measurements. However, it should be noted that perfect coverage of receivers does not guarantee an ideal tomographic solution. For example, Test 4, despite being performed with receivers distributed over the entire study area, presents various imaging artefacts. Future steps aiming at recreating a "perfect coverage" should be characterized by a good ray sampling, thus to include seismic rays that cover different directions in order to guarantee an excellent resolution (e.g., not only teleseismic events). Furthermore, although the synthetic inversions confirm that the developed methodology for P-wave anisotropic tomography is capable of retrieving with a good approximation the modeled upper mantle structures, the employed geodynamic simulations do not account for compositional variations, presence of fluids/melt and lithospheric fossil fabrics that can affect the seismic properties of natural tectonic settings. The presence of these further complexities remains to be tested, and it will be considered in future studies.

The synthetic tomography results demonstrated that using a combination of geodynamic and seismological numerical modeling techniques could represent a powerful tool to investigate mantle dynamics. Although the modeling limitations, we obtained a 3D complex mantle structure that partly resemble some main characteristics of the actual present-day mantle in the Central-Western Mediterranean. This opens new perspectives towards the future possibility of creating models of the geodynamic evolution that can be constrained by the structure and mantle anisotropy obtained from P-travel

time anisotropic tomography. To better constrain the initial tectonic configuration, an interesting future development would be to formulate a fluid dynamic inverse problem to reproduce unknown mantle flow back in time from seismic tomographic observations of the mantle and reconstructions of past plate motions using variational data assimilation (Bunge et al., 2003). Adjoint modeling is in fact a great opportunity to produce realistic mantle retrodictions models. However, the development of testing of this methodology is still far from being applicable to complex 3D tectonic settings such as the Mediterranean. This technique has been successfully applied to reproduce the recent dynamics in the South America and North America subduction zones (Hu et al., 2017; Zhou et al., 2018), However, we believe that exhumation back in time of the slabs stagnating in the mantle transition zone is non-trivial when the plate convergence rate is quite small (basically, by inverting gravity there is not easy way to exhume back at the surface these slabs), which is one of the reason why we choose to model forward in time the Central-Western Mediterranean dynamics. Reuber and Simons (2020), although showing the potentials (and limitations) of this technique on quite simple 2D and static (not dynamic) model configurations, concluded that the method "needs to be thoroughly tried and tested on real-world examples". Adding mantle fabrics to improve the mantle flow retrodictions is an ongoing research activity in our group, that we hope to include in our models in the near future.

Acknowledgments

found inside the ECOMAN. The MATLAB toolbox geomIO was used to define the geometry of the model initial setup. Paraview was used for graphic visualization of the model output. Tomographic maps were created using Generic Mapping Tools (Wessel et al., 2019) with colormaps developed by Crameri (2018a, 2018b). The manuscript was significantly improved thanks to the constructive feedback and comments from the editor, Wim Spakman and an anonymous reviewer.

Supplementary Material

Supplementary Movie

Supplementary Movie S2. Model CWM evolution. Initial setup is shown in Figure 5.1. In blue the subducted slab (contour at T=1573 K) below ∼100 km depth. The continental plates of Adria, Africa and Iberia and the oceanic plate were opacified for better visualization of the subducted slab. The arrows indicate the velocity field at ∼200Km depth, and their length is proportional to the velocity magnitude.

Supplementary Figures
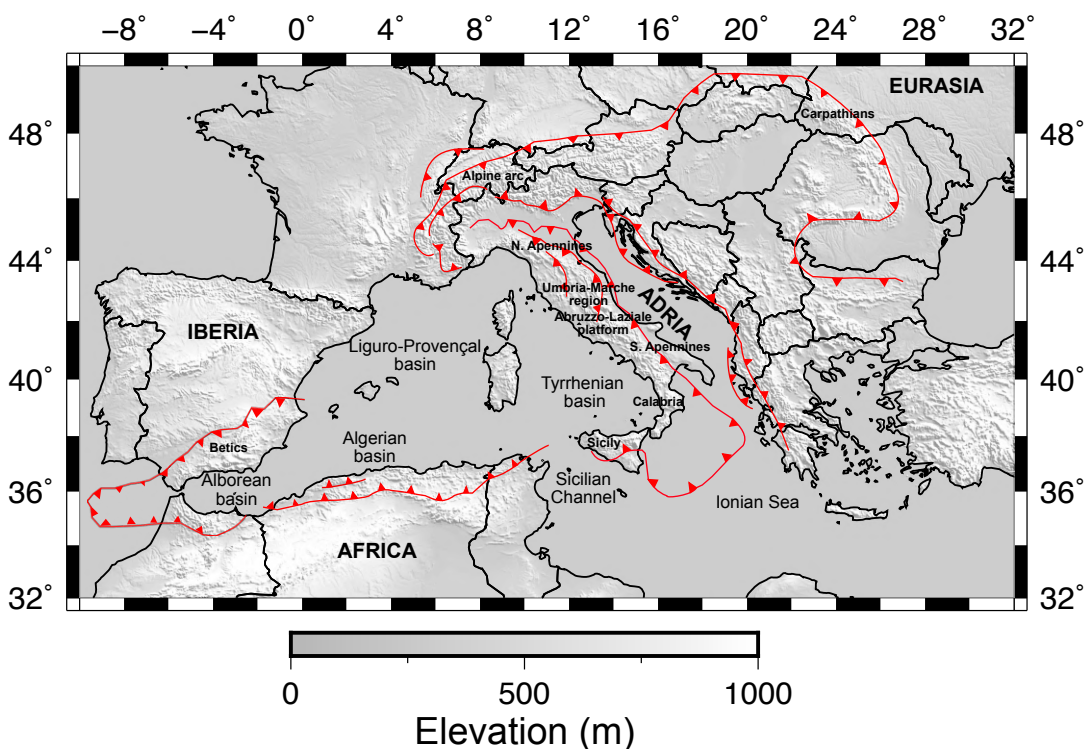
Figure 5.11: *Tectonic setting of the entire Mediterranean region adapted from Faccenna et al. (2014) showing the main structures, mountain ranges, subduction zones, back-arc basins, etc.*
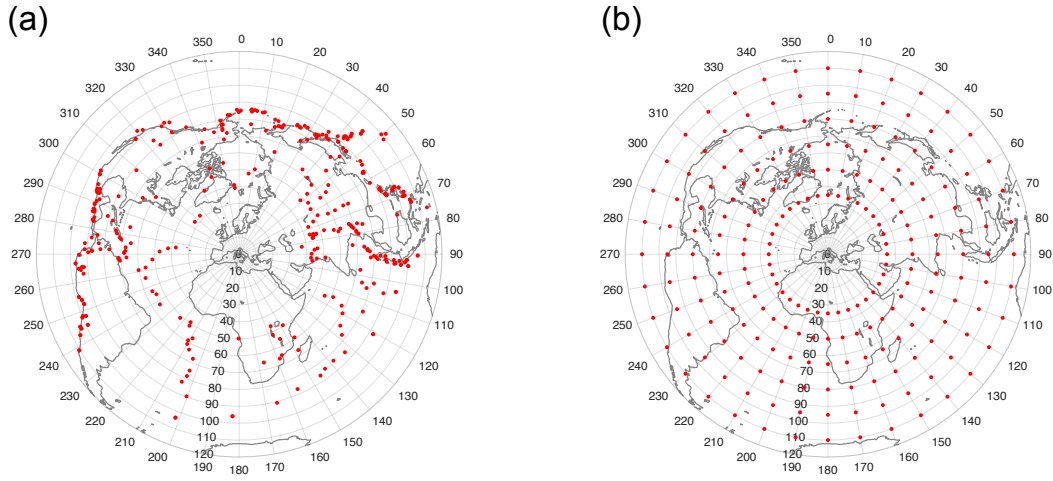
Figure 5.12: *Events distribution for (a) Test 1, 2 and (b) for Test 3, 4, 5 and 6.*
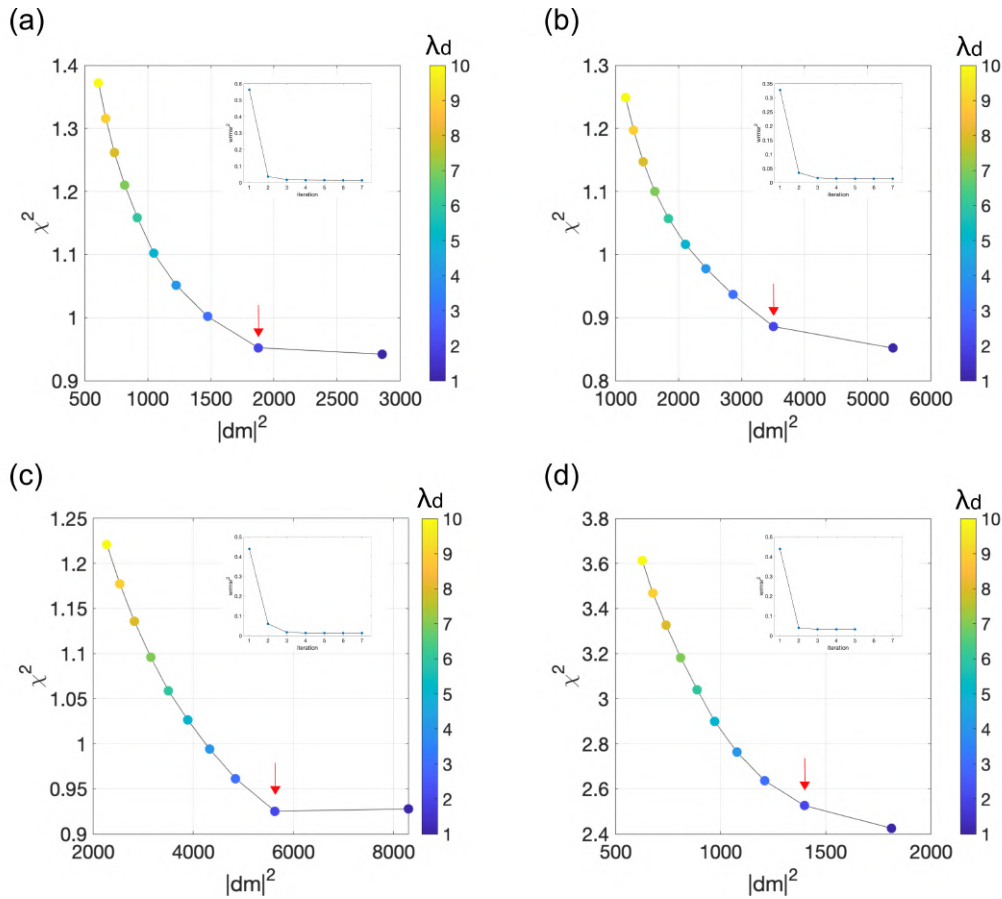
Figure 5.13: *L-curves for model selection. Normalized data residual ($\chi^2 = ddt^2/\epsilon^2$; where ddt is the delay time residual and ϵ is the uncertainty in the time measurements) is plotted as function of the squared of the model norm ($|dm|$). L-curves for (a) Test 2, (b) Test 3, (c) Test 4, and (d) for the purely isotropic Test 5. Curves (a), (b) and (c) are constructed using $\lambda_s/\lambda_d = 100$, while curve (d) using $\lambda_s/\lambda_d = 1000$. Red arrows indicate an ideal solution. Insets at the top-right corner of each panel show the convergence of the preferred solution.*
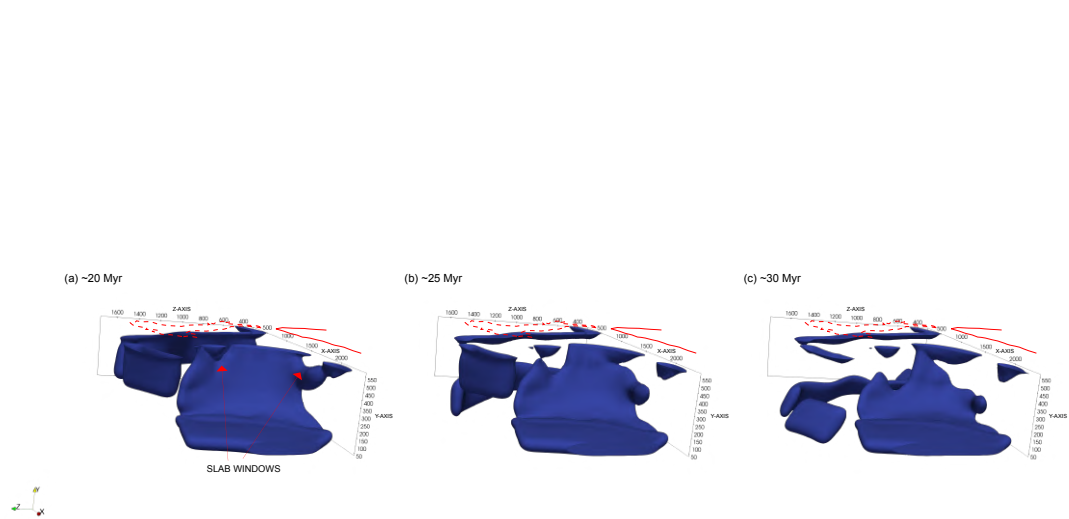
Figure 5.14: *Zoom of the Ionian slab of the Model CWM at (a)∼20 Myr, (b)∼25 Myr and (c)∼30 Myr. The red arrow indicates the slab windows below the Central-Apennines and Africa continental plate. The solid red line indicates the Africa coastlines in the Oligocene-Miocene (van Hinsbergen et al., 2014), while the dashed red line indicates the present-day coastlines of peninsular Italy.*
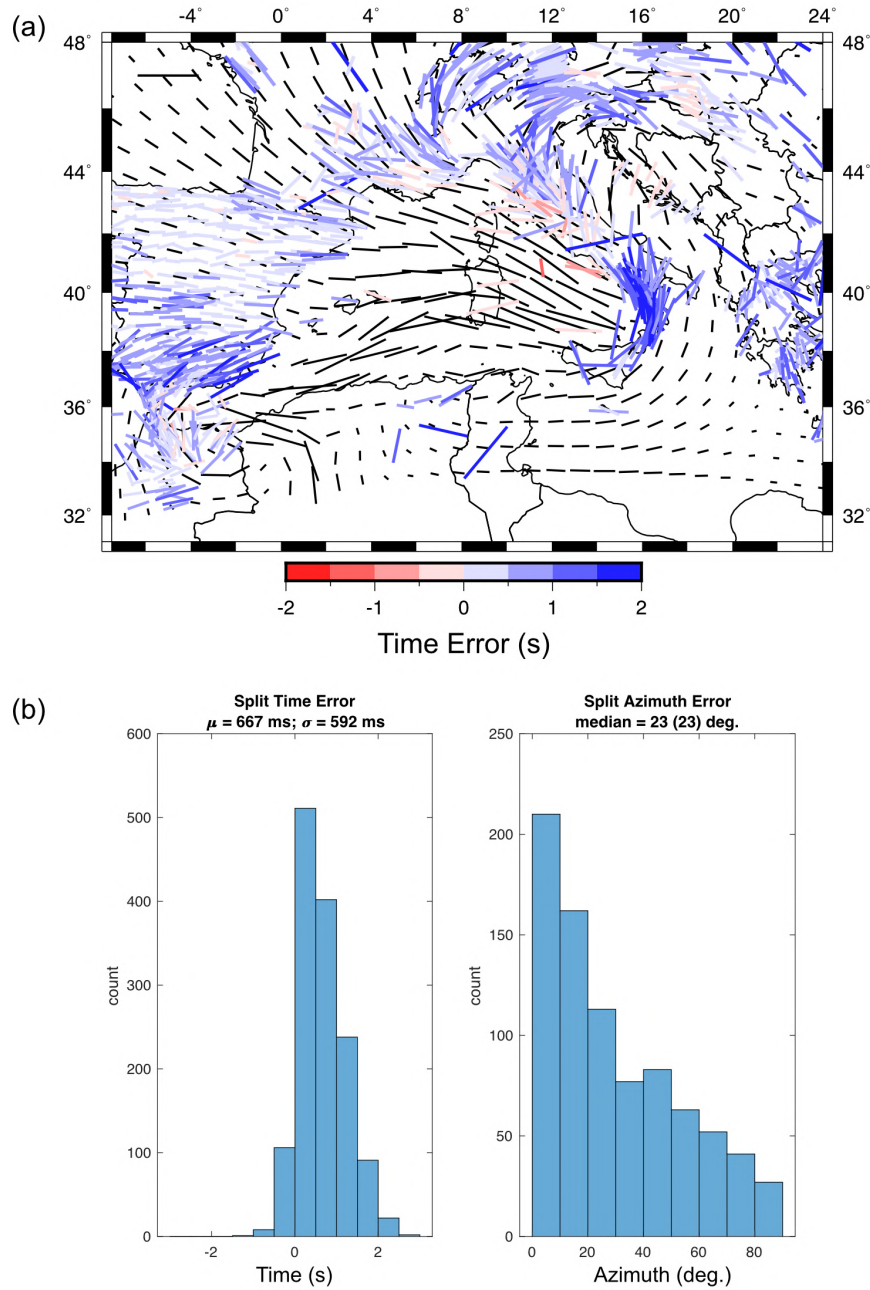
Figure 5.15: *(a) SKS-splitting measurements in the Central-Western Mediterranean (Becker et al., 2012) color-coded by the delay time misfit compared with synthetic SKS splitting measurements for Model CWM at ∼20 Myr (black bars). The EW black bar in the upper left corner indicates 2 s. (b) Split time error and split azimuth error histograms for the Model CWM at ∼20 Myr.*
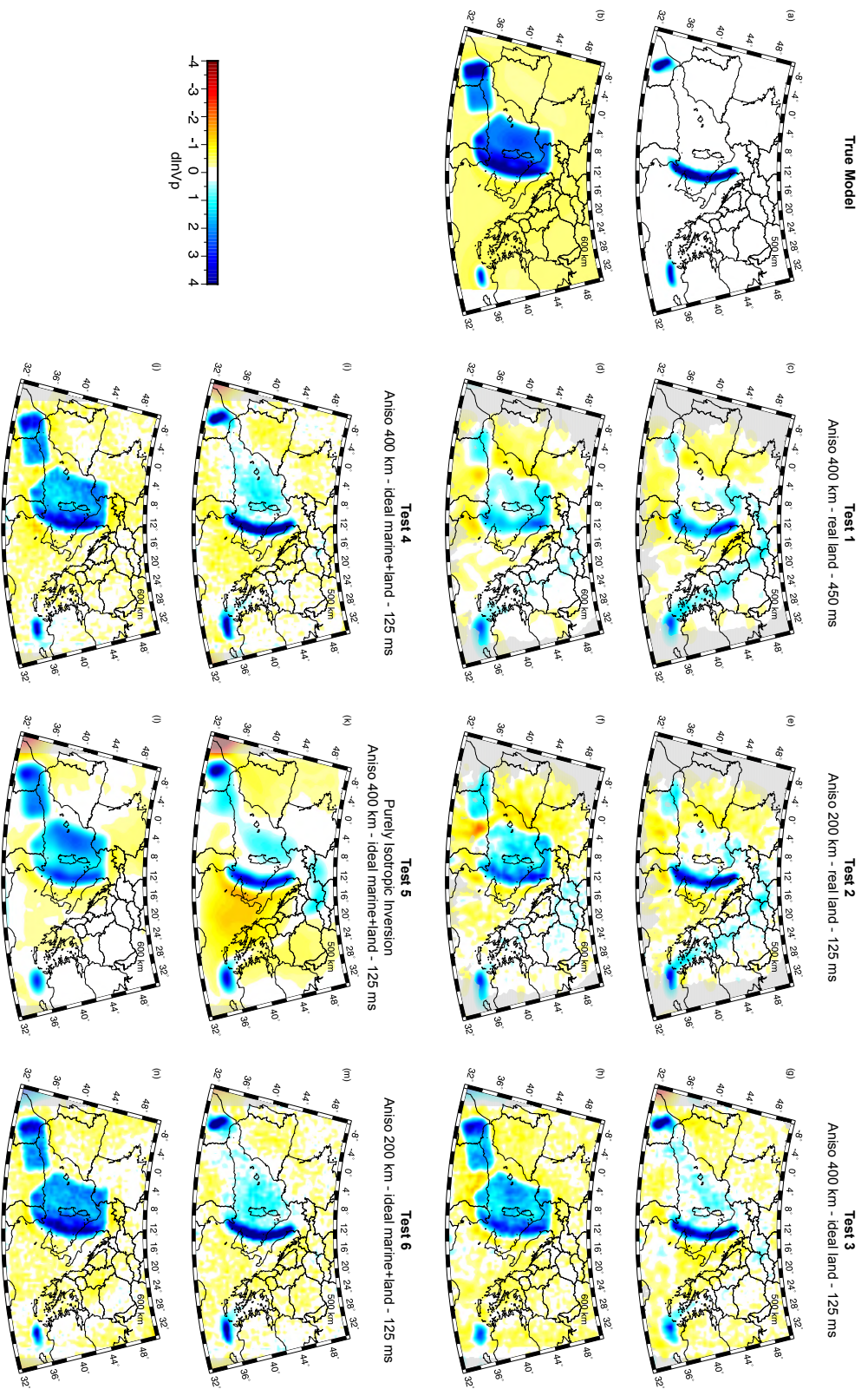
Figure 5.16: *Depth slices at 500 km and 600 km depth for (a-b) the true model, (c-d) Test 1, (e-f) Test 2, (g-h) Test 3, (i-j) Test 4, (k-l) Test 5, and (m-n) Test 6.*
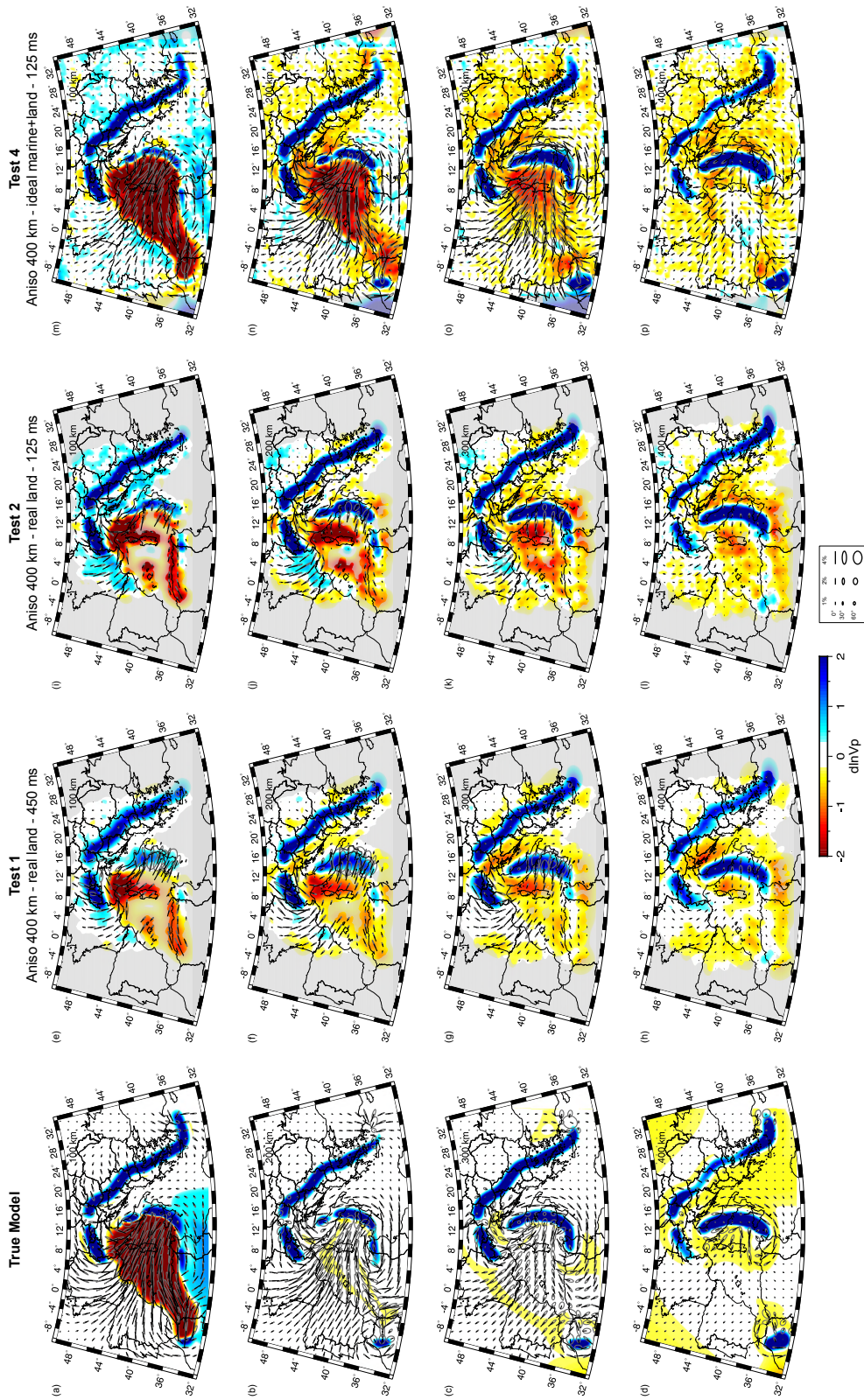
Figure 5.17: *Depth slices as in Figure 5.6 with smaller colorscale limits. Anisotropy is represented by ellipse symbols where the major axis of the ellipse parallels the fast-direction and the minor axis scales linearly with the symmetry axis dip into the view plane such that fabrics parallel and normal to the cross-sections plot as lines and circles, respectively. Anisotropic perturbations were restricted to the upper 400 km. See legend. Areas of poor data coverage are masked in grey.*

Chapter 6

IMAGING UPPER MANTLE ANISOTROPY WITH TELESEISMIC S-WAVE DELAYS: INSIGHTS FROM TOMOGRAPHIC RECONSTRUCTIONS OF SUBDUCTION SIMULATIONS

B. P. Vanderbeek[1], R. Lo Bue[1], F. Rappisi[1] and M. Faccenda[1]

This manuscript is in preparation. BPV and MF designed the study. BPV developed the method. MF created the geodynamic model. FR performed the picking of S-waves and preliminary tomographic models to tune the input parameters. RLB performed all the S-wave tomography inversions. RLB, FR and BPV wrote the first draft of the manuscript. All the co-authors contributed to the final polishing of the manuscript.

[1]Dipartimento di Geoscienze, Università di Padova, Padova, Italy

Abstract

It is well established that flow and deformation in the mantle produces a considerable amount of seismic anisotropy. However, the construction of tomographic models, in particular those derived from body waves, typically relies on the assumption of seismic isotropy. Recent studies have demonstrated that neglecting anisotropy in P-wave tomography can lead to notable imaging artifacts and misinterpretations. Less attention has been given to the effect of anisotropy on S-wave tomography partly because, unlike P-waves, there is not a simple ray-based methodology for modelling S-wave travel-times through anisotropic media. Here, we evaluate the bias introduced when ignoring seismic anisotropy in shear wave tomographic models using a new methodology for the inversion of teleseismic S-wave delays for upper mantle isotropic velocity and hexagonal anisotropy. We model the teleseismic shear wavefield through an elastically anisotropic geodynamic subduction model created via petrologic-thermomechanical modelling. We explore how the chosen coordinates system in which S-wave arrival times are measured (e.g., radial versus transverse) affects the imaging results. We observe that when S-wave travel-times are measured in the direction of polarisation, the apparent anisotropic shear velocity can be approximated using sinusoidal functions of period π and 2π. The sinusoidal approximation allows us to use ray-based methods to predict S-wave travel-times through anisotropic domains and to recover velocity models displaying 3-D patterns of mantle fabrics and where the imaging artifacts are substantially reduced.

6.1 Introduction

Since its discovery in the 1960s (e.g., Anderson, 1965; Anderson, 1961b; Hess, 1964; McEvilly, 1964), seismic anisotropy has been extensively mapped in many regions of the Earth, from crust to core. In the mantle, anisotropy is mainly caused by the non-random distribution of intrinsically anisotropic minerals (lattice/crystal-preferred orientation - LPO/CPO) as a response to mantle deformation (Kaminski & Ribe, 2001; Karato et al., 2008; Nicolas & Christensen, 1987; Wenk, 2016; Zhang & Karato, 1995) or from the alignment of structures such as faults, tabular intrusions, gas or fluid-filled cracks, and layered media with different elastic properties (shape preferred orientation - SPO). Petrophysical analysis of exhumed and experimentally deformed rock samples, together with micromechanical flow models (Blackman & Kendall, 2002; Faccenda, 2014; Kaminski et al., 2004; Karato et al., 2008; Long & Becker, 2010; Ribe, 1989; Savage, 1999; Skemer & Hansen, 2016) have shown that anisotropic structures of the Earth can create significant directional variations in seismic velocities, which allows to study mantle dynamics exploiting the anisotropic properties of the seismic wavefield.

Despite the well-established anisotropic nature of the Earth's upper mantle, conventional tomographic models, in particular those derived from body waves, are typically constructed based on the assumption of an isotropic Earth. This approximation simplifies the computational problem as taking into account seismic anisotropy involves the introduction of new unknowns in an already underdetermined inverse problem. However, this is a poor assumption considering that (i) body waves exhibit strong sensitivity to anisotropic fabrics and neglecting anisotropy can lead to notable imaging artifacts and misinterpretations (Bezada et al., 2016; Blackman & Kendall, 1997; Blackman et al., 1996; Kendall, 1994; Lloyd & Van Der Lee, 2008; Menke, 2015;

VanderBeek & Faccenda, 2021); (ii) the magnitude of seismic velocity anomalies caused by anisotropy can be even greater than those due to changes in temperature, composition or mineralogy (Anderson, 1989); (iii) tomographic models are used to constrain geodynamic simulations and infer mantle flow and structure (Becker & Boschi, 2002; Faccenna & Becker, 2010; Simmons et al., 2006; Wang & Becker, 2019). It is therefore crucial to include seismic anisotropy when imaging the mantle to advancing our understanding of the physical state and dynamics of the mantle.

A popular and conventional means for detecting upper mantle seismic anisotropy is through the analysis of shear wave splitting (SWS) and surface waves. Several techniques have been proposed to measure SKS splitting (e.g., Chevrot, 2000; Savage, 1999; Sieminski et al., 2007; Silver & Chan, 1988; Vinnik et al., 1989) and this has provided important insights on mantle flow patterns, especially in subduction zone settings (Crampin, 1984; Huang et al., 2011a, 2011b; Long, 2013; Long & Becker, 2010; Long & Silver, 2008, 2009b; Savage, 1999; Silver, 1996). However, the SWS measurements have a poor depth resolution and limited sensitivity to the dip of anisotropic fabrics (Beller & Chevrot, 2020; Chevrot, 2006; Chevrot & Van Der Hilst, 2003). Surface waves, on the other hand, are particularly sensitive to variations in depth in both azimuthal and radial anisotropic structures, but they have a poor lateral resolution (hundreds of kilometers). These drawbacks could be overcome by considering seismic anisotropy in the tomographic inversion of body wave data.

Recently, VanderBeek and Faccenda (2021) and Wang and Zhao (2021) have independently developed a new inversion strategy that yields accurate reconstructions of the upper mantle isotropic and anisotropic structures.

This new approach simultaneously inverts for P-wave slowness (i.e., the inverse of velocity) and three anisotropic parameters (magnitude of hexagonal anisotropy, azimuth and dip of the symmetry axis respectively). VanderBeek and Faccenda (2021) show that unaccounted for seismic anisotropy (isotropic approximation) or allowing for only azimuthal variations in seismic velocity (i.e., no dipping fabrics) generates strong imaging artifacts in the tomographic results. On the contrary, this new inversion strategy strongly minimizes the artifacts. While anisotropic imaging strategies have been developed for P-wave delay times in an effort to reduce such artifacts, no such ray-based anisotropic imaging strategies exist for S-waves partly because, unlike P-waves, there is not a simple ray-based methodology for modelling S-wave travel-times through anisotropic media. However, the elastic tensor is only partially resolved by knowledge of P-wave anisotropy, and S-wave anisotropy is also necessary to constrain fully the elastic tensor (Mochizuki, 1995; Wu & Lees, 1999). Several studies have successfully been performed using jointly P and S wave arrival times to image anisotropy in the Earth's mantle. Liu and Zhao (2016c) presented azimuthal anisotropic images of the Japan subduction zone assuming a weak orthorhombic anisotropic medium (i.e. with 3 orthogonal symmetry axes). However, the authors ignored the polarization of S-waves by assuming that all S-waves were polarized in the radial direction. Calò et al. (2016) by jointly inverting the high frequency P-waves, long period surface waves and group dispersion data infer profiles of radial anisotropy, imaging layered structure in the upper mantle beneath North America. More recently, Beller and Chevrot (2020) performed full waveform inversion (FWI) including both P and S phases generating high-resolution images of upper mantle anisotropic fabrics. However, although FWI is capable of solving for the 21 elastic coefficients, thus leading to a more linear imaging problem, it is limited by the computational resources and dense high-quality seismic data. Lloyd and Van Der Lee (2008)

investigate regional S and Rayleigh waves, concluding that anisotropy can be mapped as artifacts in S-wave tomographic images when not accounted for in the inversion process. However, the authors state that the bias introduced in the tomography by the isotropic assumption is small with respect to the magnitude of the velocity anomalies interpreted by seismologists. Furthermore, it is worth noting that Lloyd and Van Der Lee (2008) performed a poor-resolution study and do not consider dipping fast axes. Nevertheless, the nature of anisotropy-induced artifacts has not been largely characterized for only teleseismic shear wave tomography.

Here we present a new methodology to invert teleseismic S-wave delays for upper mantle isotropic velocity and hexagonal anisotropy. By performing waveform modelling through geodynamic subduction simulations, realistic synthetic seismic datasets are created. The geodynamic models include elastic anisotropy predicted from micromechanical flow models of polymineralic aggregates advected through the simulated flow field. We performed isotropic and anisotropic (i.e., azimuthal and fully anisotropic) inversions to show the ability of different imaging strategies in recovering subduction zones structures. The influence on the imaging results of the chosen coordinates system in which S-wave arrival times are measured (e.g., radial or transverse) is addressed. We observe that when S-wave travel-times are measured in the direction of wave polarisation, the apparent anisotropic shear velocity can be approximated using simple sinusoidal functions describing hexagonal anisotropy. The sinusoidal approximation allows us to use ray-based methods to predict S-wave travel-times through anisotropic models. We show that this parameterisation can be used to invert S-wave travel-times for the orientation and strength of anisotropy analogously to the anisotropic P-wave travel-time tomography by VanderBeek and Faccenda (2021), and that artifacts are strongly minimized. Our results highlight that shear wave anisotropy can be accounted for in a ray theoretical framework to constrain

realistic mantle anisotropic fabrics and improve imaging of isotropic features. Future applications of our methodology to real seismic datasets could bring new insights into upper mantle isotropic and anisotropic structures and dynamics.

6.2 Methods

6.2.1 Approximating Shear Wave Anisotropic Velocities

The primary issue preventing anisotropic S-wave travel-time tomography is that no simple strategy exists for modelling such travel-times in a ray-theoretical framework. This is because, unlike P-waves, S-waves may split into two orthogonally polarised quasi-shear waves that propagate at different speeds upon entering a region of elastic anisotropy. Provided that the time delay between the quasi-shear waves is small (i.e. less than the period of the seismic wave), their propagation is coupled and ray theory is not valid for independently tracing the quasi-shear phases (Coates & Chapman, 1990). This is indeed the case for teleseismic S-waves which are typically observed at periods of $\sim$10 s while the delay between fast- and slow-polarised waveforms is generally <2 s. Furthermore, the splitting process will be repeated upon encountering a change in anisotropy or ray geometry and even if ray theory were valid it is not clear which quasi-shear wave should be traced to the observation point. Another complication is that two quasi-shear waves are not produced when the shear wave polarisation parallels a symmetry axis or symmetry plane. The final waveform observed at the surface will generally contain two arrivals within the S-wave observation window that reflect the integrated effects of splitting along the ray path. Which arrival should we measure and can we relate its travel-time to anisotropic properties along the ray path in a manner suitable for a linearised inversion scheme? Here

we propose inverting S-wave travel-times measured in the direction of the initial linear polarisation. We chose this orientation because anisotropy does not significantly perturb the incoming wavelet for small splitting times relative to its period (Chevrot, 2000; Silver & Chan, 1988; Vinnik et al., 1989); this is beneficial for array processing techniques common in teleseismic analyses (e.g., multi-channel cross-correlation; VanDecar & Crosson, 1990).

We posit–and later support this supposition via waveform modelling– that the S-wave observed in the polarisation direction propagates at a velocity between the two quasi-shear wave speeds. We assume that the polarisation of a shear wave entering the imaging volume is approximately linear and remains so as it propagates through the model. In reality, anisotropy will cause elliptical particle motion but provided the splitting time remains small relative to the period of the waveform ($T/\Delta t \lesssim 5$) the displacement will not deviate significantly from the initial polarisation direction (Rümpker & Silver, 1998). A similar assumption is made in the modelling of splitting intensity (Chevrot, 2000; Chevrot et al., 2004; Sieminski et al., 2007). Given an anisotropic seismic velocity model, we can estimate the velocity of the two quasi-shear waves (v_1 and v_2) from the ray path orientation. We then assume that the propagation velocity varies sinusoidally between v_1 and v_2 and is a function of the angle between the incoming shear wave polarisation and the quasi-shear wave whose displacement is in the plane containing the anisotropic symmetry axis. The details of this approach are provided below.

Numerous studies have demonstrated that elastic anisotropy within the Earth is dominated by hexagonal symmetry (e.g., Becker et al., 2006a; Brownlee et al., 2017; Ismaıl & Mainprice, 1998; Russell et al., 2019). Assuming that the magnitude of anisotropy is relatively weak (<10-20%), the speed at which two orthogonal quasi-shear waves will propagate through an anisotropic layer can be approximated as periodic functions of 2α and 4α where α is the angle between the hexagonal symmetry axis and the S-wave ray path

(Backus, 1965; Thomsen, 1986).

$$v_1 = \overline{v_1} \left[1 \pm g \cos(2\alpha) \right] \tag{6.1}$$

$$v_2 = \overline{v_2} \left[1 \mp h \cos(4\alpha) \right], \tag{6.2}$$

where $\overline{v_1}$ and $\overline{v_2}$ are the mean or isotropic velocities and g and h are the fractional magnitude of the velocity variations associated with the 2α- and 4α-cosines, respectively. The velocities for a ray parallel to the symmetry axis are controlled by the sign of the anisotropic fraction. Note that g and h tend to be of opposite sign with $g > 0$ for mantle anisotropy produced by olivine A-type fabrics. We also note that, $v_1(\alpha = 0) = v_2(\alpha = 0)$ so that $\overline{v_2} = \overline{v_1}[1 \pm g][1 \mp h]^{-1}$ reducing the number of parameters required to describe S-wave anisotropy.

We wish to write the two quasi-shear wave speeds as a function of the symmetry axis azimuth (ψ) and elevation (γ). After some trigonometric manipulation and noting that $\cos(\alpha)$ is given by the dot product between the ray unit vector and the anisotropic symmetry axis unit vector, we can expand Equations 6.1 and 6.2 as,

$$v_1 = \overline{v_1} \left[1 \pm g \left(2 \left[\cos(\theta) \cos(\gamma) \cos(\phi - \psi) + \sin(\theta) \sin(\gamma) \right]^2 - 1 \right) \right], \tag{6.3}$$

$$\begin{aligned}
v_2 = \overline{v_1} \frac{(1 \pm g)}{(1 \mp h)} \Big[1 \mp h \Big(& 8 \left[\cos(\theta) \cos(\gamma) \cos(\phi - \psi) + \sin(\theta) \sin(\gamma) \right]^4 \\
& - 8 \left[\cos(\theta) \cos(\gamma) \cos(\phi - \psi) + \sin(\theta) \sin(\gamma) \right]^2 + 1,
\end{aligned} \tag{6.4}$$

where θ and ϕ are the ray elevation and azimuth, respectively. We then parameterise the velocity at which the shear wave observed in the direction of polarisation travels as,

$$v = \frac{(v_2 + v_1)}{2} \left[1 + \frac{(v_2 - v_1)}{(v_2 + v_1)} \cos(2\omega - 2\psi') \right], \tag{6.5}$$

where ω is the angle of shear wave polarisation and ψ' is the orientation of the symmetry axis projected into the ray-normal plane. See Figure 6.1 for an illustration of the coordinate system. The frequency-dependent anisotropic shear wave travel-time is given by the volume integral,

$$t = t' + \int_V (u - u')KdV, \tag{6.6}$$

where t' is the travel-time predicted through the 1-D reference slowness (i.e. inverse of velocity) model u'; u is the true 3-D slowness model; and K is the approximate Born sensitivity kernel defined in Equations 4 and 5 of VanderBeek and Faccenda (2021). In Equation 6.6, u is defined by $1/v$ and each node in the kernel K maps to a specific ray segment whose orientation is used to define the slowness at that point via Equations 6.3-6.5. See VanderBeek and Faccenda (2021) for further details on the finite-frequency travel-time approximation used here.

6.2.2   Validation of Anisotropic Shear Wave Travel-times

Equations 6.3-6.5 provide a means to estimate the anisotropic propagation velocity and travel-time of a linearly polarised shear wave. To assess the accuracy of this approximation, we measure travel-time delays of teleseismic S-waves propagated through an anisotropic subduction zone model using SPECFEM3D and compare these measured delays to those predicted using Equations 6.3-6.5.

We use the synthetic waveform dataset created by VanderBeek and Faccenda (2021) and briefly summarise its key features below. The teleseismic wavefield is modelled using the spectral element code SPECFEM 3-D (Chen & Tromp, 2007; Komatitsch & Tromp, 1999) with the AxiSEM grid-injection technique (Monteiller et al., 2013; Nissen-Meyer et al., 2014). The anisotropic elastic model used in the waveform modelling is the result of a geodynamic
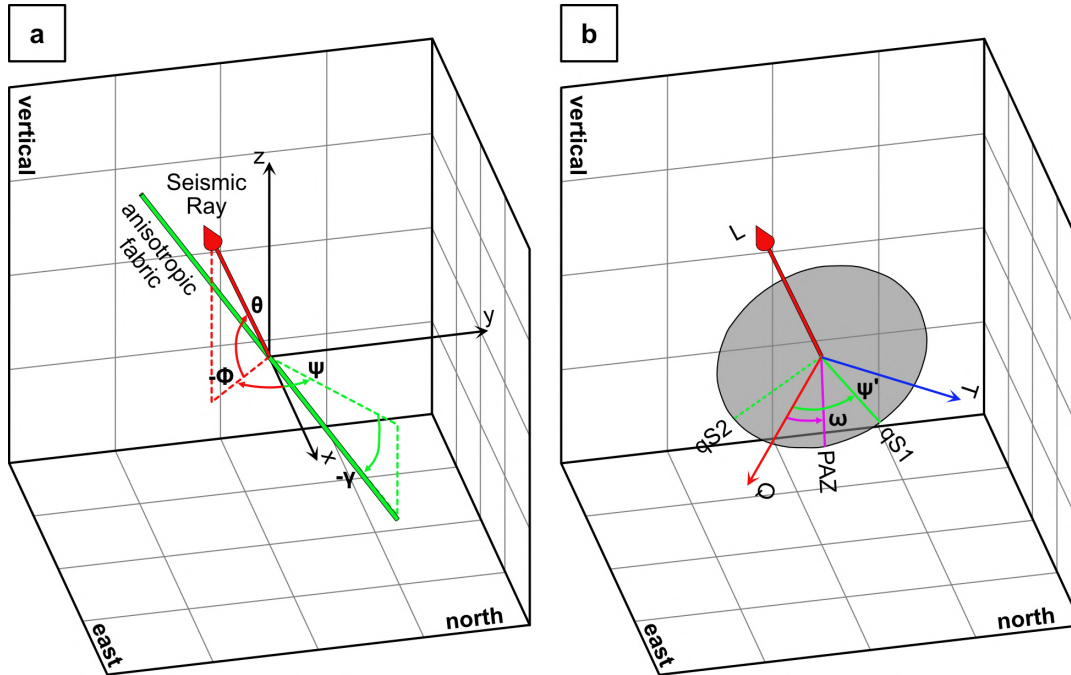
Figure 6.1: *Coordinate system depicting parameters used to model shear wave anisotropy. (a) The S-wave ray path (red arrow) is shown in relation to the orientation of the anisotropic symmetry axis (green bar). The ray and symmetry axis azimuths (ϕ and ψ) are measured positive counter-clockwise from the +x-axis while the ray and symmetry axis elevation are measure positive counter-clockwise from the x,y-plane. (b) The ray-aligned QTL-coordinate system. The shear-wave polarisation direction (ω; pink line labeled PAZ) is shown in the ray-normal plane (grey shaded region) in addition to the two quasi-shear wave polarisations (qS_1 and qS_2). Note that the qS_1 polarisation coincides with the projection of the symmetry axis into the ray-normal plane (ψ'; green line). Angles are measured positive counter-clockwise with respect to the Q-axis in the QT-plane.*

simulation of a slab (1000 km-long half-width) subducting freely in response to its negative buoyancy. Fully anisotropic elastic tensors are predicted via micromechanical modelling of polymineralic aggregates advected through the simulated mantle flow field (see Faccenda, 2014; Faccenda & Capitanio, 2013; Kaminski et al., 2004). The tensors are subsequently simplified by extracting the dominant hexagonally symmetric component. This simplification was also made to maintain focus on the accuracy of the imaging methodology specifically designed to approximate hexagonal anisotropy. Outside of the local imaging volume the 1-D radial Earth model IASP91 (Kennett & Engdahl, 1991) is used to define seismic wave speeds.

The isotropic component of the synthetic subduction zone is shown in Figure 6.2 and contains only one significant anomaly–the seismically fast slab.   The anisotropic component of the synthetic model is shown in Figure 6.3 and contains five significant imaging targets that provide insight into the structure and dynamics of the subduction zone.   (1) Throughout the upper 300 km, toroidal mantle flow generates a circular pattern in the symmetry axis orientations around the slab edges (Figure 6.3a).   (2) At greater depths beneath the incoming plate there is a region of trench-parallel anisotropy (Figure 6.3b). (3) Surrounding the subducting lithosphere, flow entrainment produces anisotropic symmetry axes that follow the trajectory of the descending plate (Figure 6.3c,d).   (4) The subducting lithosphere also contains frozen-in anisotropic fabrics characterised by 5% S-wave speed varia-

Figure 6.2: *Isotropic structure, array geometry and distribution of teleseismic sources considered in the present study. (a) Seismic stations (black triangles) are uniformly spaced 75 km apart and plotted over isotropic velocity heterogeneity in the true model at 150 km depth. Inset shows location of teleseismic sources (stars) relative to the experiment centre. Sources are located at distances of 50° and 80° and evenly distributed in backazimuth. An east-west cross-section through the centre of the true isotropic model at 0°N is shown in (b). Note that the isotropic structure is symmetric about 0°N.*

tions oriented east-west. (5) Mantle circulation within the wedge generates a corner-flow type pattern in anisotropy fabrics near the mid-plate that becomes less evident towards the edges (Figure 6.3c,d).
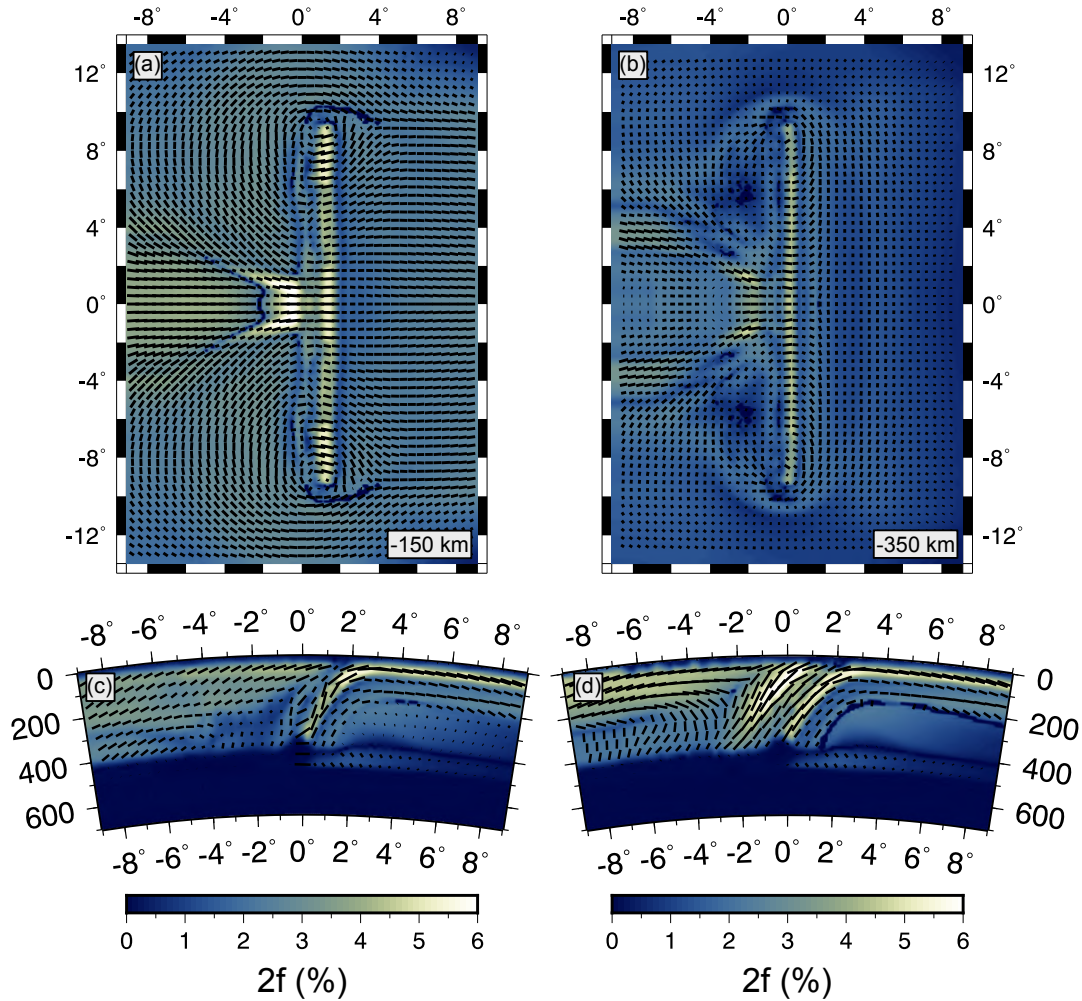
Figure 6.3: *Cross-section through the true anisotropic model. Hexagonal symmetry axis vectors are plotted over the peak-to-peak magnitude of S-wave velocity anisotropy at (a) 150 km and (b) 350 km depth. East-west cross-section are shown at (c) 0°N and (d) 4°30'S. Symmetry axis vectors are scaled by the anisotropic magnitude and projected onto the cross-section plane. Note that the anisotropic structure is symmetric about 0°N.*

The teleseismic wavefield propagated through this model is recorded by an array of 770 receivers equally spaced 75 km apart (Figure 6.2a) yielding a station density comparable to the USArray. In total 16 double-couple sources are modelled; 8 at a range of 50° and another 8 at 80° equally distributed in back-azimuth (Figure 6.2a). The dominant period of the waveforms is 15 s. A second waveform dataset was created in which only the isotropic component of the elastic tensors are considered and used to derive a reference set of delay times without any anisotropic signal.

We measure relative S-wave travel-time delays following the multi-channel

cross-correlation method of VanDecar and Crosson (1990). A second order bandpass filter with corners at 15 s and 40 s is applied to the synthetic seismograms. We measure delays in two coordinate systems. First, we analyse shear waves observed in the transverse direction–a common choice for many teleseismic studies. Second, we measure S-wave delays in the direction of polarisation, or more precisely, parallel to the major axis of the particle motion ellipse. The shear wave polarisation can be determined given the ray orientation and moment tensor. However, in practice moment tensors may be unknown or the polarisation may have been perturbed prior to entering the regional imaging volume. To avoid such issues, we suggest estimating the incoming polarisation for each event using the array-averaged S-waveform. For a given event, we first pick and align S-wave arrivals on the transverse channel. We then stack the aligned traces and perform a polarisation analysis on the stacked three-component signal via an eigendecomposition of the trace covariance matrix (e.g., Flinn, 1965); a 15 s window about the S-waveform is used in this analysis. Each seismogram is then rotated into the principal coordinate system determined by the eigendecomposition and S-wave delays are re-measured in the direction corresponding to the largest eigenvalue. The polarisation angle in the QT-plane (ω; Figure 6.1b) is stored for each event and used for computing travel-times (Equation 6.5). Note that we have assumed ω is constant across the array for a given event which is reasonable for teleseismic phases recorded by regional-scale or smaller arrays. For all sources modelled by VanderBeek and Faccenda (2021), $\omega = 47°$ and the results of the polarisation analysis outlined above agree to within 1°.

By comparing the delay times measured from the SPECFEM generated waveforms to those predicted by our ray-theoretical tomographic method, we can assess the error in our approximation for S-wave anisotropy. We find that the root-mean-square error (RMSE) between the observed and predicted

delays is 241 ms while RMSE for delays predicted without considering anisotropy is 600 ms. The error in our ray-theoretical anisotropic delays is comparable those estimated for modern day S-wave delay time measurements ($\sim$250 ms; Byrnes et al., 2017) and less than the accuracy of most modern tomographic models ($\sim$400 ms). Thus, our approximation appears sufficient for tomographic imaging.

6.2.3   Imaging Method

Having validated equations that relate shear-wave travel-times to mean velocity and the strength and orientation of seismic anisotropy, we formulate an inversion procedure for recovering these anisotropic parameters from the travel-time observations. In constructing our anisotropic model, we seek to minimise the least-squares objective function defined by,

$$\chi^2 = (\Delta\mathbf{t} - \mathbf{J}\Delta\mathbf{m})'\mathbf{C}_t^{-1}(\Delta\mathbf{t} - \mathbf{J}\Delta\mathbf{m}) + \lambda_d\Delta\mathbf{m}'\mathbf{C}_m^{-1}\Delta\mathbf{m} + \lambda_s\Delta\mathbf{m}'\mathbf{C}_s'\mathbf{C}_s\Delta\mathbf{m}, \quad (6.7)$$

where $\Delta\mathbf{t}$ is a (N x 1) vector of travel-time residuals with respect to the current model vector $\mathbf{m}$; $\mathbf{J}$ is the (N x M) Jacobian matrix that relates a change in travel-time to a change in the model parameters; $\Delta\mathbf{m}$ is the model perturbation vector for which we are trying to solve; $\mathbf{C}_t$ is the (N x N) data covariance matrix which we assume to be diagonal and composed of the inverse of the squared data uncertainties (250 ms for our dataset); $\mathbf{C}_m$ is the (M x M) model covariance matrix which we assume to be diagonal and composed of the inverse of the squared parameter uncertainties; $\mathbf{C}_s$ is an (M x M) matrix that defines the model roughness (i.e. the discretised 3-D Laplace equation for each parameter); lastly λ_d and λ_s are Lagrangian multipliers that limit the size and roughness of the model perturbation vector. These parameters are required to regularise the otherwise under-determined and ill-posed inverse problem and their selection is discussed below (section 6.2.4). To minimise

Equation 6.7, we solve the system of equations defined by,

$$
\begin{bmatrix}
\mathbf{C}_t^{-1/2}\mathbf{J} \\
\lambda_d \mathbf{C}_m^{-1/2} \\
\lambda_s \mathbf{C}_s
\end{bmatrix}
\Delta\mathbf{m} =
\begin{bmatrix}
\mathbf{C}_t^{-1/2}\Delta\mathbf{t} \\
\mathbf{0} \\
\mathbf{0}
\end{bmatrix}.
\tag{6.8}
$$

The solution is obtained via the LSQR algorithm (Paige & Saunders, 1982).

To evaluate Equation 6.8, we must define the linear equations that populate the rows of the Jacobian matrix $\mathbf{J}$ which are obtained by differentiating the travel-time equation (Eq. 6.6) with respect to the anisotropic model parameters. Rather than invert directly for the mean velocity ($\overline{v}$) and the strengths (g, h), azimuth (ψ), and elevation (γ) of anisotropy, we follow VanderBeek and Faccenda (2021) and parameterize the inversion using the mean slowness ($\overline{u} = 1/\overline{v}$) and three anisotropic parameters defined as,

$$
A = g \cos(\gamma) \cos(2\psi)
\tag{6.9}
$$

$$
B = g \cos(\gamma) \sin(2\psi)
\tag{6.10}
$$

$$
C = \sqrt{g} \sin(\gamma)
\tag{6.11}
$$

Under this parameterisation, Equations 6.3 and 6.4 become,

$$
v_1 = \overline{v_1} \left[1 \pm (Q - G - C^2) \right],
\tag{6.12}
$$

and

$$
v_2 = \overline{v_1} \frac{(1 \pm [G + C^2])}{(1 \mp r_{hg}[G + C^2])} \left[1 \pm r_{hg} \left(2Q^2[G + C^2]^{-1} - 4Q + G + C^2 \right) \right].
\tag{6.13}
$$

For notational convenience, we have introduced the terms Q and G defined as

$$
\begin{aligned}
Q &= [A\cos(2\phi) + B\sin(2\phi) + G]\cos^2(\theta) + 2C^2\sin^2(\theta) \\
&\quad + \sqrt{2}C\left[s_1(G+A)^{1/2}\cos(\phi) + s_2(G-A)^{1/2}\sin(\phi)\right]\sin(2\theta)
\end{aligned}
\tag{6.14}
$$

with $s_1 = \text{sign}(\cos\gamma\cos\psi)$, $s_2 = \text{sign}(\cos\gamma\sin\psi)$ and $G = \sqrt{A^2 + B^2}$. To further limit the number of free parameters, we have also added the term r_{hg} which is the ratio h/g and is assumed constant throughout the inversion. Appropriate values for r_{hg} can be inferred from laboratory measurements of relevant anisotropic fabrics. Here we use $r_{hg} = -0.1746$ which is the average value of the geodynamically modelled elastic tensors. Note also that the sign term ($\pm$) that appears in these equations is selected *a priori* in accordance with the expected symmetry system and is fixed throughout the inversion. Here we use the convention (+,-) for ($\pm,\mp$) corresponding to a seismically fast symmetry axis and slow propagation plane normal to the symmetry axis. Finally, we can write the elements of **J** as,

$$
J_{ij} = \frac{\partial t_i}{\partial m_j} = -w_{ij}\left(\frac{\partial u_{ij}}{\partial v_{ij}}\right)\left(\frac{\partial v_{ij}}{\partial m_j}\right)
\tag{6.15}
$$

where w_{ij} expresses the relative influence the model parameter m at the jth location has on the ith travel-time observation in units of km where m_j is one of the anisotropic parameters ($\bar{u}_j$, A_j, B_j, or C_j). For ray theoretical travel-times, w_{ij} is simply the length of the ray segment that is mapped to the jth model node (or $K_{ij}dV_{ij}$ for finite-frequency travel-times). The partial $\partial u_{ij}/\partial v_{ij}$ is given by $-v_{ij}^{-2}$ (i.e. the squared anisotropic slowness for the ith observation at the jth location) and the partials $\partial v_{ij}/\partial m_j$ can be derived from Equations 6.5 and 6.12-6.14.

Clearly, the partial derivatives in Equation 6.15 are non-linear and depend upon the current model. Therefore, we iteratively solve Equation 6.8. At each

iteration, we recompute the Jacobian given the current model, solve Equation 6.8 for new model perturbations, and then update the model (i.e. $\mathbf{m}_{n+1} = \mathbf{m}_n + \Delta\mathbf{m}_n$ for iteration n). Iterations stop once the $||\Delta\mathbf{t}||^2$ converges to a stable value (4-6 iterations for our synthetic tomography problem). Further details regarding the imaging methodology can be found in VanderBeek and Faccenda (2021).

6.2.4   Model Discretisation, Regularisation, and Resolution

The unknown model perturbations are discretised on a regularly spaced 50-km grid with each node being described by the four anisotropic parameters $\overline{u}, A, B,$ and C. Appropriate smoothing and damping values were selected via the construction of a series of L-curves in which the squared-residual norm is plotted against the squared-model norm. Solutions near the corner of the L-curve are considered ideal as a further increase in model complexity (i.e. larger model norm) does not substantially improve the data prediction while simpler models rapidly increase the residual norm. To identify an appropriate ratio of λ_s-to-λ_d, we constructed several L-curves at fixed λ_s/λ_d values and systematically varied λ_d. From this analysis, we found $\lambda_s/\lambda_d = 100$ provided good fitting models while less smooth solutions did not improve the datafit and smoother solutions generated larger residuals. For the isotropic inversion, we found $\lambda_d = 5$ corresponded to the corner of the L-curve. Considering that anisotropic structure is likely as heterogeneous as isotropic structure, we adopted the same λ_s-to-λ_d ratio for the anisotropic inversions and equally damped isotropic and anisotropic perturbations. After performing a series of anisotropic inversions across different λ_d values, we again found that $\lambda_d = 4$ provides an optimal solution for the anisotropic inversions. A selection of L-curves for isotropic and anisotropic inversions are plotted in Figure 6.11.

Assessing model resolution is an important aspect of tomographic reconstructions considering that the solutions are generally non-unique. In this work, we focus on the imaging of a known and geologically-relevant target synthetic structure allowing us to assess model resolution by direct comparison. We refer to VanderBeek and Faccenda (2021) for a more general discussion on the resolution of teleseismic travel-times to anisotropic heterogeneity.

6.3 Results and Discussion

We performed a series of inversions to show the ability of different imaging strategies in recovering subduction zones structures and upper mantle flow patterns using teleseismic S-waves. We started with isotropic inversions and proceeded by gradually adding anisotropy through AB- and ABC-anisotropic inversions, i.e. azimuthal and fully anisotropic, respectively. Using trade-off curves we quantitatively compared the results of the different inversion strategies, evaluating their ability to recover the isotropic and anisotropic structures of the true model.

6.3.1 Isotropic solutions

At the early stages of our work we inverted a dataset of delay times computed from a purely isotropic model (Figure 6.4). Not considering the effect of anisotropy on seismic tomography allows to recover, within the limits of the capabilities of the method (e.g. finite-frequency approximation, imperfect data coverage, manual picking), the geometry of the isotropic structures. This solution will represent the reference model for future comparisons. Figure 6.4 shows a fast anomaly (FA), corresponding to the true slab, extending in the N-S direction at 150 km (Figure 6.4a) and 350 km (Figure 6.4b) depth with no significant imaging artifacts. Weak (∼-1%) slow anomalies (SAs) are imaged all around the slab. Cross sections in Figures 6.4(c,d) present SAs
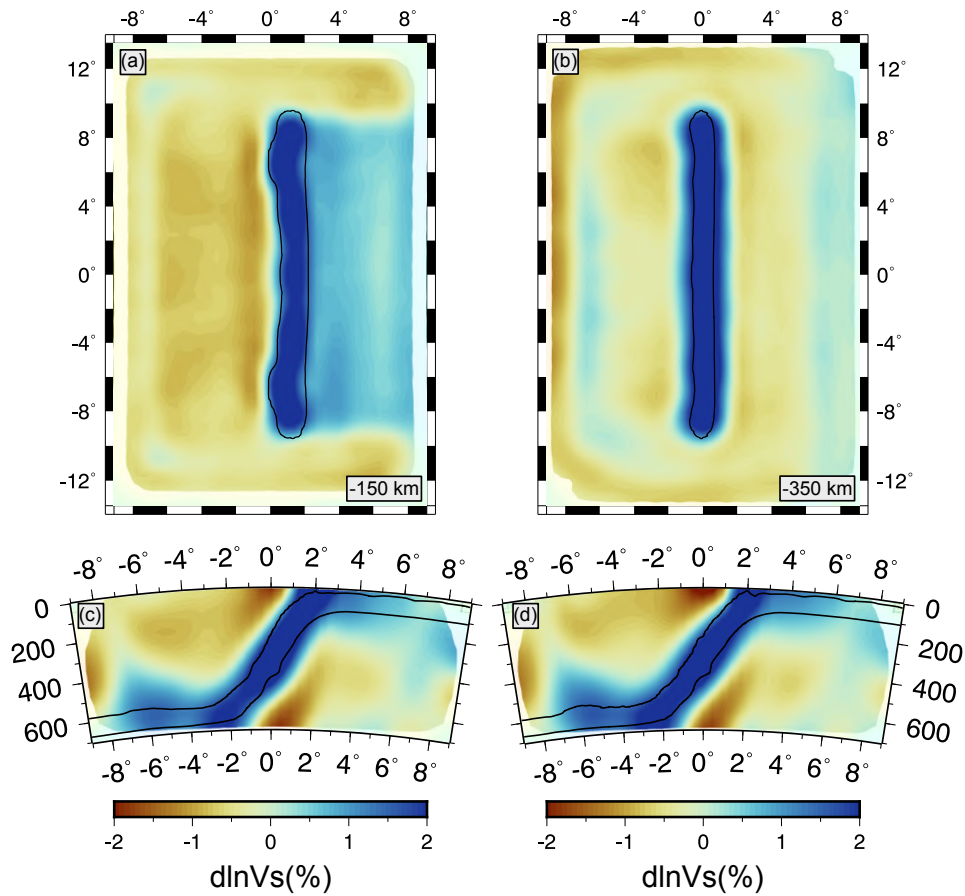
Figure 6.4: *Isotropic inversion of isotropic data. Top view of the velocity perturbations with respect to the 1-D starting velocity model at (a) 150 km and (b) 350 km depth. East-west cross-sections at (c) $4°30'N$ and (d) $0°N$. The black line represents the 1% velocity contour in the true model and outlines the true slab geometry. Areas with poor data coverage are masked.*

with stronger-magnitude-peaks (i.e. ∼-2%) above and below the slab. The latter sinks into the mantle down to 700 km depth showing a good later symmetry along the latitude plane. However, cross sections exhibit a significant loss of resolution resulting in the smoothing of the FA in the deeper layers.

Successively, we performed isotropic inversions with anisotropic delays (Figure 6.5 and 6.6) that we first picked from the transverse component (Figure 6.5 and 6.6, left columns). In contrast with the purely isotropic results of Figure 6.4, a significant number of artifacts were captured by the new inversion in isotropic approximation (Figure 6.5 and 6.6, left columns). The magnitude of both fast and slow anomalies strongly increased, e.g., this is
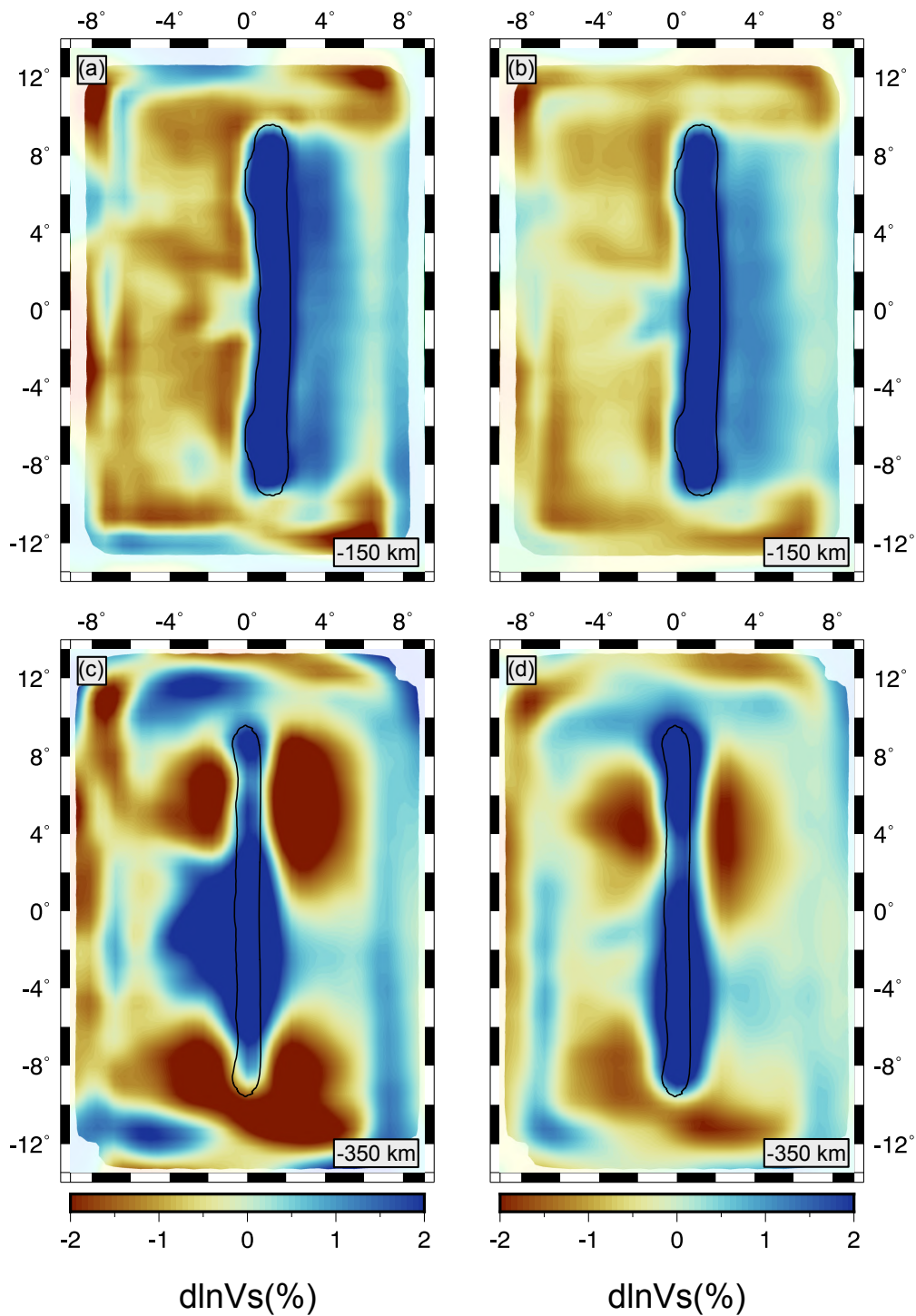
Figure 6.5: *Isotropic inversion of anisotropic delays picked from the transverse component (left column) and the S-wave polarization direction (right column). Velocity perturbations with respect to the 1-D starting velocity model are plotted at (a and b) 150 km and (c and d) 350 km depth. Slab contour and mask as in Figure 6.4.*

particularly evident for the SAs in the areas surrounding the slab. This effect is attributable to the presence of strong anisotropy in these regions. Although
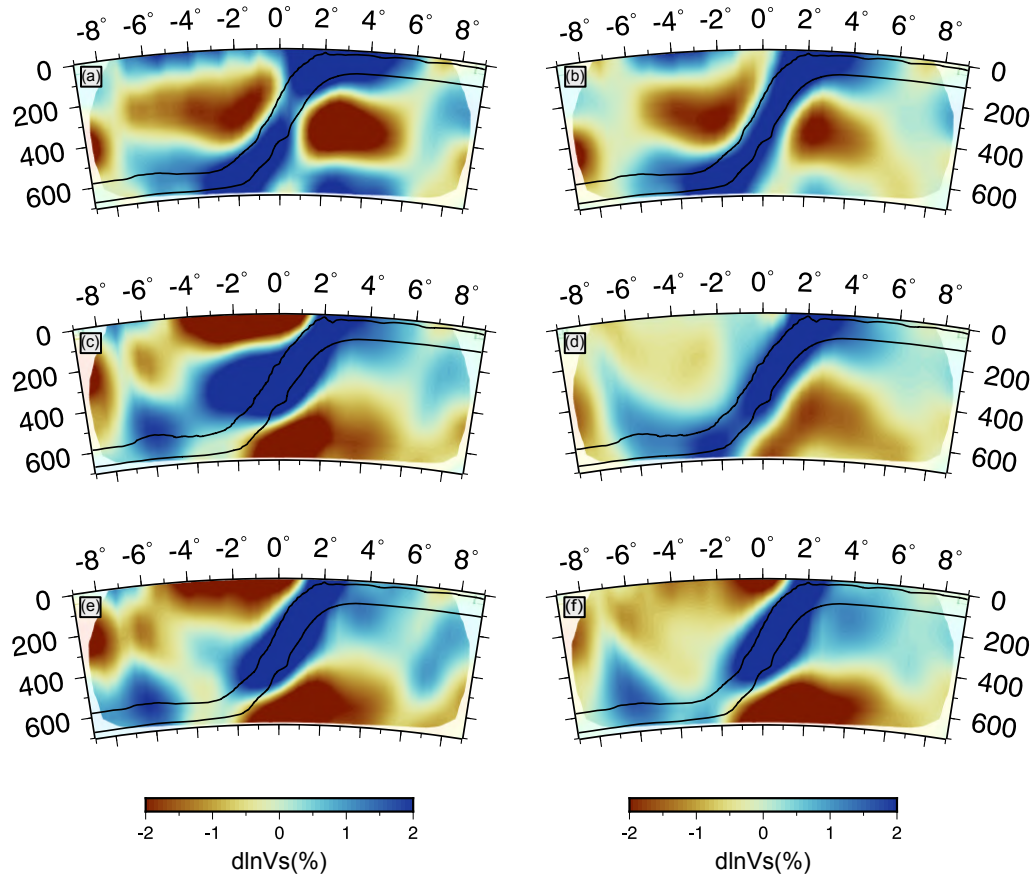
Figure 6.6: *Isotropic inversion of anisotropic delays picked from the transverse component (left column) and the S-wave polarization direction (right column). East-west cross-sections are plotted at (a and b) $4°30'N$, (c and d) $0°N$ and (e and f) $4°30'S$. Slab contour and mask as in Figure 6.4.*

in the first kilometers of depth the slab geometry is well recovered (Figure 6.5a), significant distortions are found with increasing depth (Figure 6.5c). Cross sections in Figure 6.6a, 6.6c and 6.6e exhibit a deformed slab varying with latitude. E.g., Figure 6.6(a) presents a weakening (i.e. a lower magnitude portion) in the center of the FA at ~200-250 km depth, which could be interpreted as slab detachment; on the contrary, Figures 6.6(c) exhibits a wider slab stagnating at ~400 km depth; Figure 6.6(e) shows instead a ~500 km slab penetrating into the mantle.

A second set of inversions was performed using delay times picked on the S-wave polarization direction (Figure 6.5 and 6.6, right columns). With

respect to the previous case, i.e. with data picked on the transverse component, we observe a general reduction in the amplitude of the slow anomalies and the geometry of the slab is better recovered (Figure 6.5b), although a general worsening with increasing depth (6.5d) still persists. However, Figure 6.5d partly allows to distinguish the N-S elongated shape of the FA which instead was not recovered at this depths (i.e. 350 km depth) when inverting the transverse component (Figure 6.5c). Strong distortions remain on the latitude plane. Cross sections in Figure 6.6b, d and f show the presence of seismic imaging artifacts below and above the slab that, in Figure 6.6b and 6.6d, penetrates down to 700 km stagnating at that depth, while in Figure 6.6f appears detached at ∼500 km depth with some remnants stagnating at the transition zone.

The presence of these artifacts in the tomographic model does not allow to recover the correct geometry of the slab thus potentially leading to wrong interpretations of the seismic images when inverting in isotropic approximation.

6.3.2 AB anisotropic solutions

In this section we show the results of the inversions for the azimuthal anisotropy parameters only (Figure 6.7, 6.8, 6.9 and 6.10, left columns). Considering that among the isotropic tests showed in section 6.3.1 the best results is attributable to that performed using delays picked on the polarization direction, we decided to proceed the anisotropic tests using the polarization component only (i.e., not performing inversions with data picked on the transverse component).

Differently from what VanderBeek and Faccenda (2021) observed for P-wave tomography, due to the fact that teleseismic S-waves are more sensitive to azimuthal variations than P-waves are, we note that the first order effect
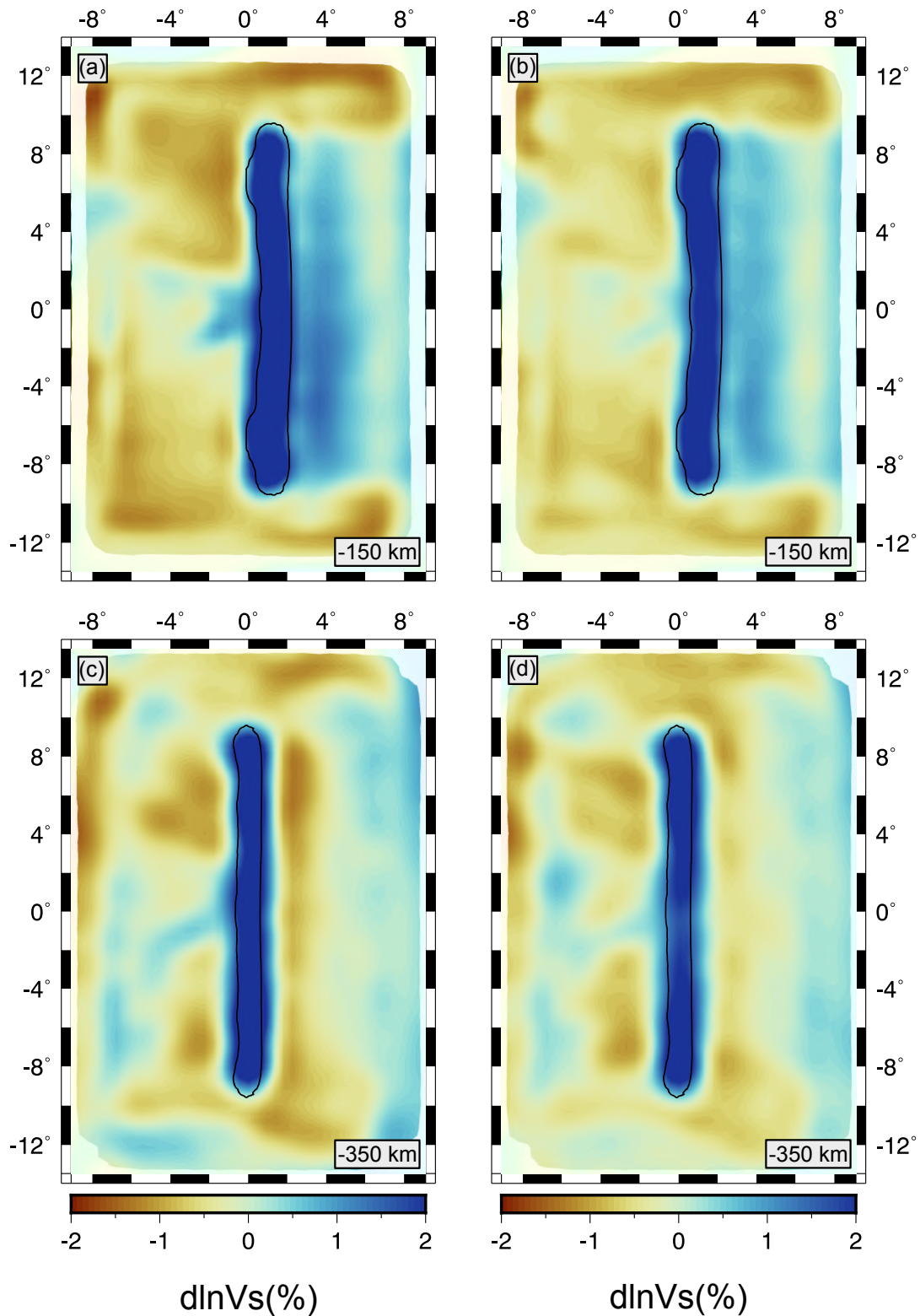
Figure 6.7: *Isotropic structure recovered from azimuthally anisotropic inversion (left column) and from anisotropic inversion that includes symmetry axis azimuth and dip (right column). Velocity perturbations are plotted as in Figure 6.5. Slab contour and mask as in Figure 6.4.*
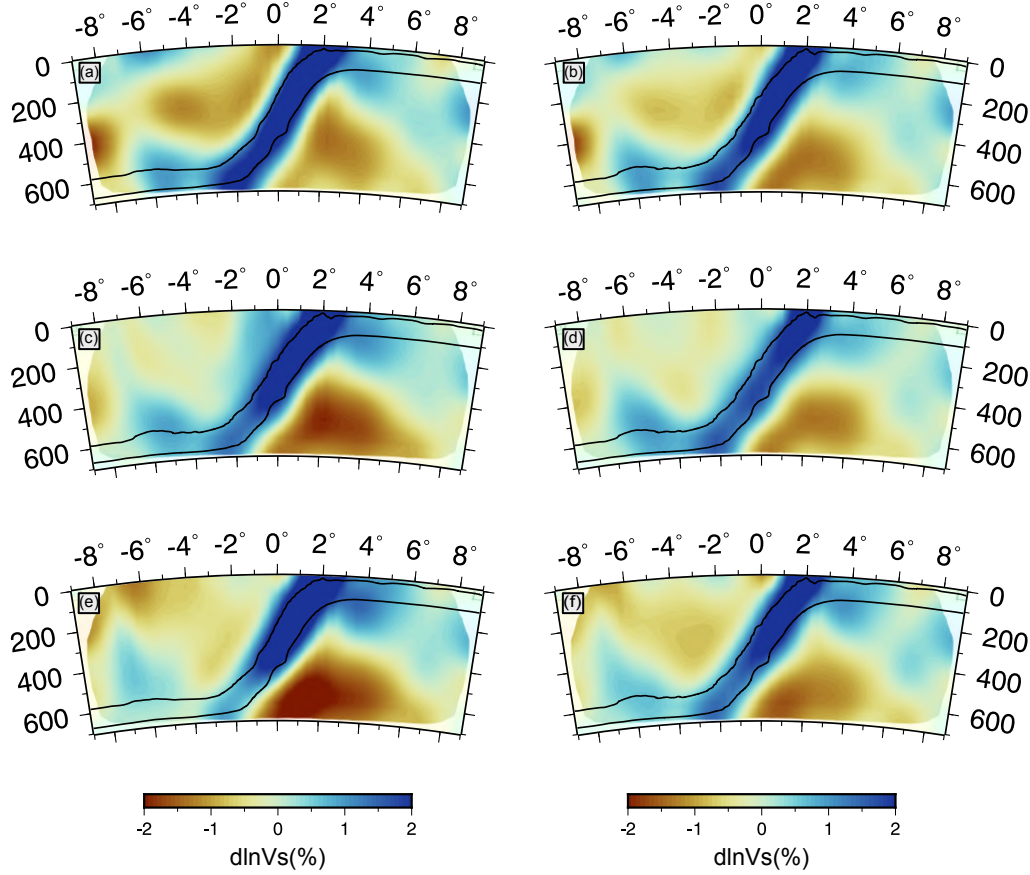
Figure 6.8: *Isotropic structure recovered from azimuthally anisotropic inversion (left column) and from anisotropic inversion that includes symmetry axis azimuth and elevation (right column). Velocity perturbations are plotted as Figure 6.6. Slab contour and mask as in Figure 6.4.*

of including only the azimuthal anisotropic parameters (i.e., A and B) in the inversion is to reduce the number and the magnitude of velocities artifacts, consequently to allows for a better recover of the slab geometry (Figure 6.7a,c and 6.8a,c,e). However, the SAs above and beneath the slab still persists (Figure 6.8a,c,e).

Important insights on mantle dynamics come from the azimuthal anisotropic patterns showed in Figure 6.9 and 6.10 (left columns). The torodial flow, typical of many subduction zones, is retrieved at the edges of the slab (Figure 6.9a) and trench-perpendicular azimuths are observed beneath the incoming plate. With increasing depth the azimuthal assumption introduces several artifacts. Among them, shown in Figure 6.9c, is the presence of apparent

isotropic bodies and the not recovering of the toroidal patterns.

Despite including azimuthal anisotropy helps to better recover the isotropic structures with respect to the purely isotropic cases, it is true that neglecting anisotropy dip leads to isotropic and anisotropic imaging artifacts which make the interpretation of the model particularly difficult.

6.3.3   ABC anisotropic solutions

We performed anisotropic inversions for perturbations to S-wave slowness (u) and all the three anisotropic parameters (A, B and C) that define the anisotropic magnitude, azimuth and dip (Figure 6.7, 6.8, 6.9 and 6.10, right columns).

In Figure 6.7(b, d) and 6.8(b, d, f) we observe that the low velocity artifacts are significantly reduced and the solution closely resembles the ideal recovery of the isotropic structure in Figure 6.4. The geometry of the slab is well recovered both at shallower layers and in depth. Vertical sections at the center and at the edges of the model (Figure 6.8b,d and f) show the slab fast anomaly continuously dipping down to 700 km depth. No significant changes in magnitude and geometry are found between the three cross sections, imaging a symmetric slab with respect to the latitudinal plane. The magnitude of the SAs below and above slab is strongly reduced with respect to the purely isotropic (Figure 6.5 and 6.6) and azimuthal anisotropic (Figure 6.7a, c and 6.8a, c, e) inversions of anisotropic delays.

The recovered anisotropic patterns (Figure 6.9b, d) capture the toroidal flows at the edges of the slab at 150 km and 350 km depth. The trench perpendicular anisotropy in the incoming plate is now well recovered and the number and size of the anisotropic artifacts are strongly reduced. Although the slight overestimation of the anisotropy magnitude observed in the central portion of the slab at 350 km depth ($\sim$5%, Figure 6.9), its geometry is well
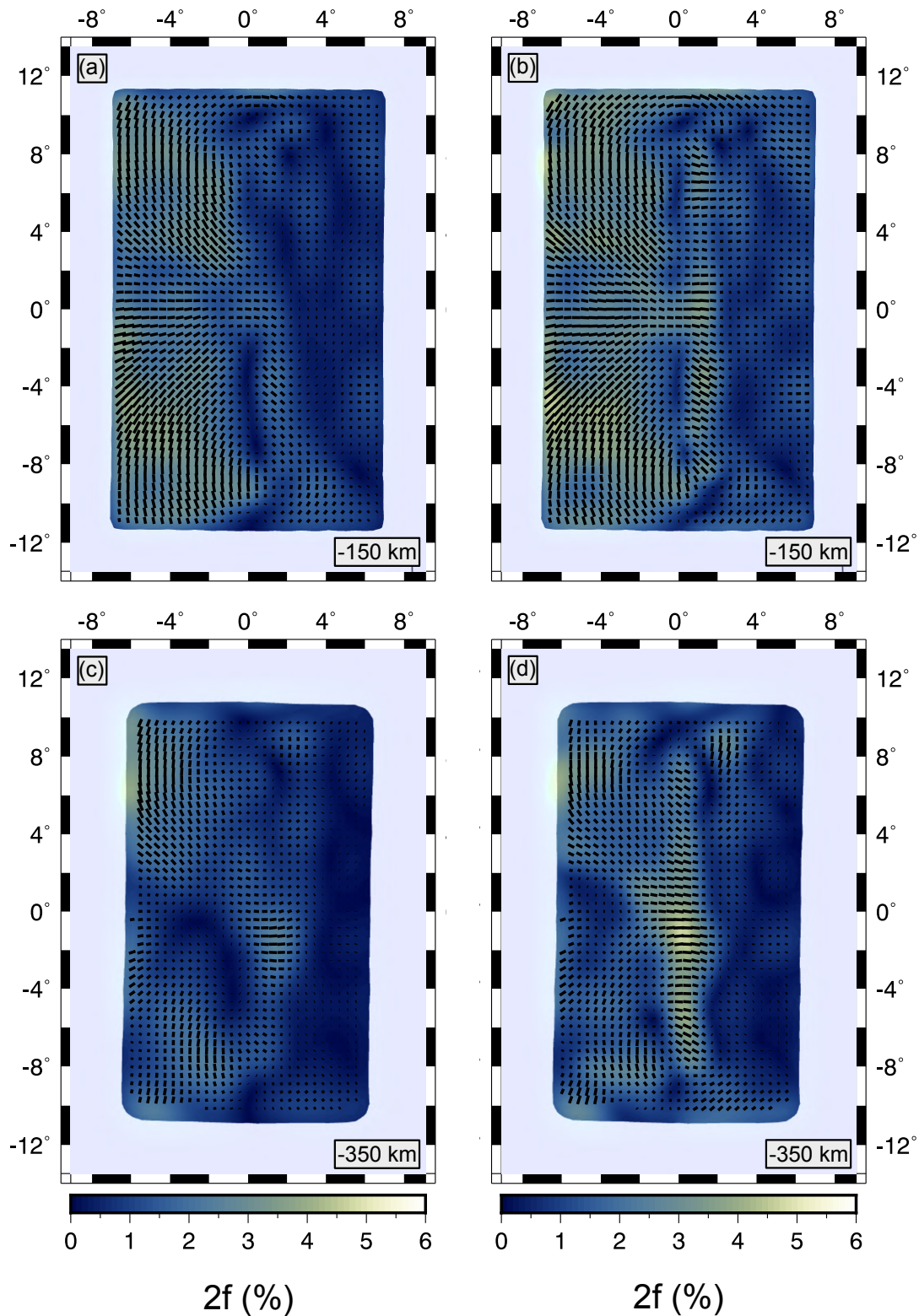
Figure 6.9: *Azimuthal anisotropic structure recovered from inversion for u, A and B terms (left column) and from inversion for u, A, B and C terms (right column). Seismic anisotropy is plotted as in Figure 6.3. Areas with poor directional sampling are masked.*
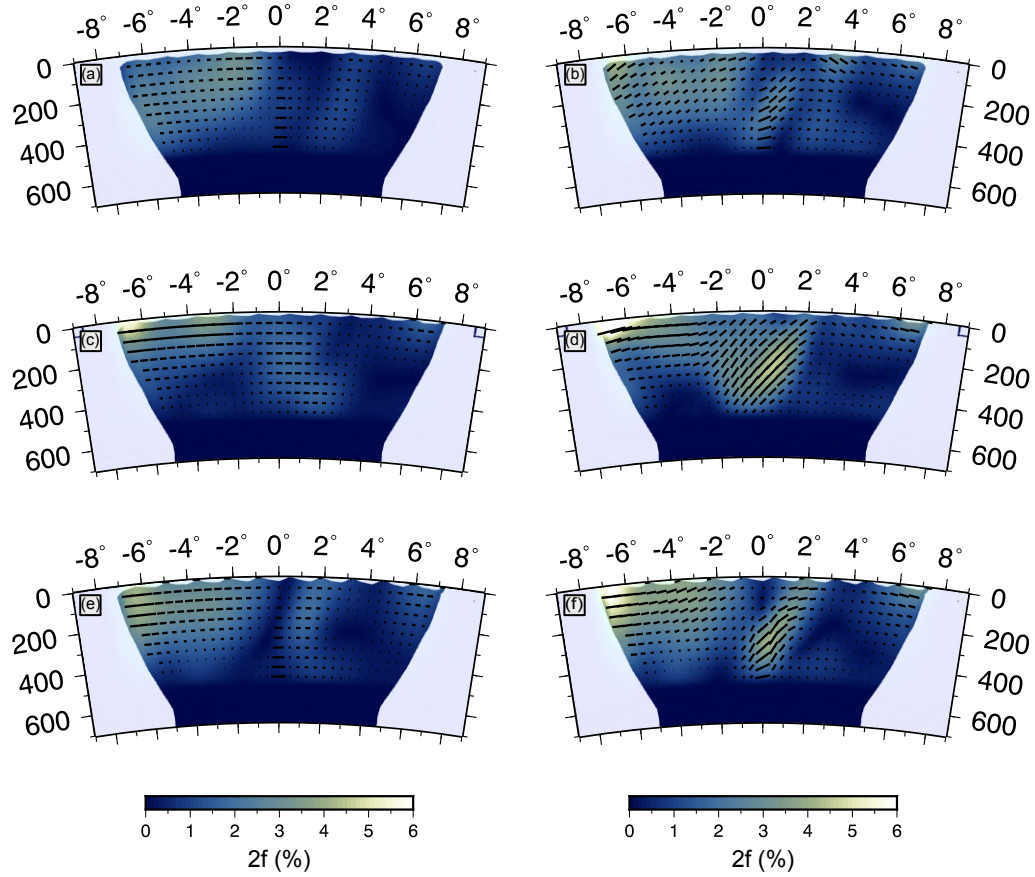
Figure 6.10: *Azimuthal anisotropic structure recovered from inversion for u, A and B terms (left column) and from inversion for u, A, B and C terms (right column).Seismic anisotropy is plotted as in Figure 6.3. Areas with poor directional sampling are masked.*

constrained by the fraction of anisotropy. Anisotropic vertical sections in Figure 6.10b, d, f show the anisotropic patterns and magnitude with depth. We observe that dipping fabrics are found in the slab, and near-horizontal fabrics beneath the incoming plate.

6.3.4 Comparison between results

From a comparison between our results it emerges that inverting teleseismic S-waves delays simultaneously for perturbation to S-wave slowness and the three anisotropic parameters strongly reduces isotropic artifacts in seismic images, revealing upper mantle structure and dynamics.

Figure 6.11 shows the progressive improvement of the results with respect to the reference model (i.e. isotropic inversion of isotropic data; black curve) in terms of RMS residual values (rms^2) and model norm ($|dlnV|^2 + |df|^2$). The purely isotropic inversion of the delay times picked on the transverse component (orange curve in Figure 6.11) exhibits the highest values of both data fitting and model complexity (rms^2 and $|dlnV|^2 + |df|^2$, respectively). This results in the presence of several isotropic artifacts in the tomographic image as shows in Figure 6.5 and 6.6 (left panels). Notably, improvements are observed when inverting the data picked on the polarization component (red curve in Figure 6.11). We note that, despite the high number of artifacts still present in the seismic images, the trade-off curve exhibits lower values of data misfit and model norm.

Finally, the best results were obtained when the anisotropic parameters are included in the tomographic inversion. It is worth noting that, although the lowest value of rms^2 was obtained for the ABC-anisotropic inversion, the AB- and ABC-anisotropic inversions exhibit similar model complexity, i.e. similar model norm.

As observed in Figure 6.9 and 6.10 and confirmed by the L-curves (Figure 6.11), differently from what VanderBeek and Faccenda (2021) observed for P-wave anisotropic tomography, in the S-wave case analyzed here considering only azimuthal anisotropy represents a good approximation for recovering the isotropic velocity anomalies without introducing abundant artifacts.

6.4   Conclusion

We performed a series of isotropic and anisotropic inversions highlighting the ability of each imaging strategy to accurately capture subduction zone structure. Our tomographic results demonstrate that teleseismic S-waves are strikingly sensitive to anisotropy. This sensitivity is well documented by the
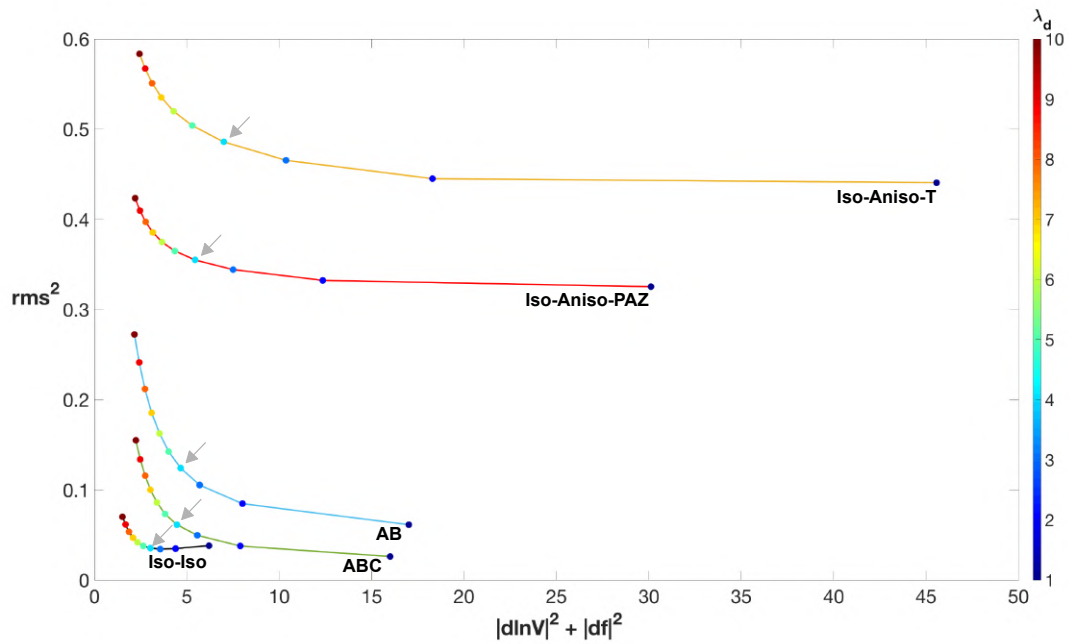
Figure 6.11: *Trade-off curves for damping and smoothing multiplier selection for the isotropic inversion of isotropic data (black line), the isotropic inversion of the anisotropic data picked on the transverse and polarization direction (orange and red lines, respectively) and for the azimuthal (AB, blue line) and fully anisotropic inversion (ABC, green line). The squared RMS is plotted as function of the squared model norm, $|dlnV|^2 + |df|^2$, where $dlnV$ is the fractional velocity perturbation vector and df is the anisotropic magnitude perturbation vector. The values λ_s / λ_d are kept fixed at 100 for both the isotropic and anisotropic cases. Colorbar represents different values of damping factor for slowness. Arrows indicate the preferred solutions, corresponding to $\lambda_d = 4$.*

appearance of several artifacts in the tomographic image when ignoring seismic anisotropy (isotropic assumption).

Unaccounted for anisotropic structure creates significant distortions in slab geometry (changes in dip and appearance of slab gaps) and appearance of several strong low-velocity features. This can significantly corrupt S-wave images of isotropic upper mantle velocities leading to erroneous inferences on subduction dynamics. Severity and geometry of slab distortions and low-velocity artifacts created by anisotropy are dependent on the orientation in which S-wave delays are measured (e.g., radial versus transverse). When measured in the direction of maximum S-wave energy, these artifacts are still present but appear at a generally reduced magnitude.

When anisotropic parameters (i.e., magnitude of hexagonal anisotropy,

azimuth and dip of the symmetry axis) are included in the inversion, all major artifacts are strongly minimized. Additionally, major patterns in anisotropic fabrics (e.g., toroidal flow pattern around slab edge, dipping fabrics associated with entrained flow) are well-recovered. These synthetic tests show that teleseismic S-wave alone can constrain 3-D upper mantle isotropic and anisotropic structure and modelling anisotropic structure is key to accurately recovering subduction zone shear velocity heterogeneity.

Furthermore, we find that travel-times of shear waves picked in the direction of maximum energy can be approximated by simple sinusoidal functions describing hexagonal anisotropy. This observation allows us to use ray-based methods to predict S-wave travel-times through anisotropic models. This parameterisation can be used to invert S-wave travel-times for the orientation and strength of anisotropy analogously to the anisotropic P-wave travel-time tomography by VanderBeek and Faccenda (2021). Therefore, shear wave anisotropy can be accounted for in a ray theoretical framework to constrain realistic mantle anisotropic fabrics and improve imaging of isotropic features.

We envisage that future studies should carefully assess the role of anisotropy on S-wave teleseismic tomography models to provide more robust interpretations of the upper mantle. Although our synthetic tests demonstrate the utility of teleseismic S-waves in constraining realistic upper mantle anisotropy, the proposed imaging strategy has important limitations that should be overcome. For example, estimating S-wave polarization requires high quality 3-components data or also use of relatively long period data (T > dts).

Ongoing research is aimed at applying our imaging strategy to real data, with a focus on the Cascadia and Central Mediterranean subduction systems. Possible future improvement could aim at jointly invert P-, S-waves and SKS splitting data. The use of both P and S phases and improving ray coverage by including teleseismic and local arrivals will allow for a new and more

precise parameterisation of the model. Finally, next studies will extend the current hexagonal symmetry (i.e. with 2 distinct anisotropy axes, 5 independent elastic coefficients) to orthorhombic (i.e. with 3 distinct anisotropy axes, 9 independent elastic coefficients), in order to better resolve the true anisotropy, thus better estimate mantle conditions.

Chapter 7

ON THE RESOLVING POWER OF (AN)ISOTROPIC TOMOGRAPHY: A SEISMO-GEODYNAMICS APPROACH

F. Rappisi[1], **M. Witek**[2], **M. Faccenda**[1], **A. M. G. Ferreira**[3] **and S.-J. Chang**[2]

This manuscript is in preparation. All the authors conceived the study. FR and MF created the geodynamic model and performed strain-induced fabric estimation tests. FR simulated seismic wave propagation to generate the synthetic database. MW performed the tomographic inversions. AF and SJC supervised the seismological part of the study. MF supervised the geodynamical interpretation of the tomography image. All the authors contributed equally to the discussion of the results and to the conclusions of this study.

---

[1]Dipartimento di Geoscienze, Università di Padova, Padova, Italy
[2]Division of Geology and Geophysics, Kangwon National University, Chuncheon, South Korea
[3]Department of Earth Sciences, University College London, London, UK

Abstract

Olivine crystallographic preferred orientation (CPO) due to mantle flow is the primary cause of seismic anisotropy in the Earth's upper mantle. Thus, observations of seismic anisotropy provide key information about mantle structure and dynamics. In this study we combine geodynamic simulations with seismological forward and inverse modelling to understand which realistic features in the Earth's mantle can be accurately imaged with current seismic tomography methods. We first create a ridge-to-slab 2-D geodynamic model and from its velocity field we compute mantle fabrics and strain-induced seismic anisotropy in the upper mantle. Using the 21 elastic constants obtained from the fabrics calculations we compute seismic waveforms, which are inverted for isotropic shear velocity and radial anisotropy in the mantle using the partitioned waveform inversion method. The synthetics obtained from the geodynamical model serve as a reference to test the limits and capabilities of the inverse method in different conditions. In addition to testing the limitations of the approximate inversion method used, we also compare results from inversion tests with different seismic data coverage. Moreover, we also test different levels of regularization and evaluate their effect on the tomographic results and thus on the geodynamical interpretation of the images. Our results show that in all inversion tests the retrieved isotropic images of subducted slabs show substantial artificial slab's thickening (from ~ 90 km in the input model to > 100 km in the output model) and loss of the slab's fast velocity signature below $\sim 100\text{-}150$ km depth. Further, by changing regularization we can obtain anisotropic models similar to the half-space cooling model, showing age-dependent lithospheric structures, or, conversely, obtain results similar to the plate cooling model, characterized by flat and age-independent lithospheric structures. Thus, enhanced data coverage and further complementary data types are needed to improve the

resolution of (an)isotropic tomography models.

7.1 Introduction

Global and regional seismic tomography have greatly progressed in the past decades thanks to the explosion in seismic data sets and to the development of sophisticated forward and inverse seismological methods (e.g., Chang et al., 2014; Liu & Gu, 2012; Rawlinson et al., 2010). In particular, many regional models of the Earth's uppermost mantle have been developed and different data types are used, ranging from body wave travel-times to surface wave dispersion measurements and waveforms, from both earthquakes and ambient noise (e.g., Emry et al., 2019; Estève et al., 2020; Mohammadzaheri et al., 2021; Rawlinson et al., 2016; Witek et al., 2021). While body wave data are invaluable to build tomography images in regions with dense data coverage, such as, e.g., subduction zones, offering excellent lateral resolution (e.g., Estève et al., 2020; Kim et al., 2021; Mohammadzaheri et al., 2021; Zhao et al., 1992), surface waves allow sampling regions with poor data coverage, such as the oceans (e.g., Forsyth et al., 1998; Kendall et al., 2021; Nishimura & Forsyth, 1989).

The use of huge volumes of high quality seismic data has made it necessary to introduce automatic approaches. While in the past manual studies were able to analyze $\sim 10^3$ seismograms (e.g., Van der Lee & Nolet, 1997), now new methods perform automatic analysis of $\sim 10^6$ seismograms (e.g., Debayle & Ricard, 2012; Schaeffer & Lebedev, 2014; Wang et al., 2019). Based on the partitioned waveform inversion (PWI) method (Nolet, 1990), Lebedev and Nolet (2003) introduced an automated multimode inversion (AMI) method, which was successively expanded to include azimuthal anisotropy variations, P-velocity variations and a reference 3-D model (Lebedev et al., 2005; Lebedev & Van Der Hilst, 2008; Schaeffer & Lebedev, 2013). Recently,

Witek et al. (2022) (in review) presented a new automated multimode wave-form inversion algorithm based on PWI able to jointly model isotropic and radially anisotropic Earth structure.

Studying seismic anisotropy is fundamental to infer the state of deformation in the crust and mantle, which in turn is strongly related to the present-day and past flow. Upper mantle seismic anisotropy, mainly generated by strain-induced lattice/crystal preferred orientation (LPO/CPO) of intrinsically anisotropic minerals (e.g., olivine), is used as a proxy to infer mantle flow and its relations with plate motions (Park & Levin, 2002). Radial anisotropy is the simplest type of anisotropy, which can occur in layered isotropic media with strong contrasts in material properties or any system displaying hexagonal symmetry (Anderson, 1961a). It can help distinguishing between horizontal and vertical mantle flow, and it has helped unravel exciting dynamic processes in the Earth's deep interior (e.g., Chang & Ferreira, 2019; Chang et al., 2016; Chang et al., 2015; Ferreira et al., 2019; Zhu et al., 2017).

Global isotropic shear wave velocity and radial anisotropy whole and upper mantle models (e.g., Auer et al., 2014; Chang et al., 2015; French et al., 2013; Moulik & Ekström, 2014; Panning et al., 2010; Ritsema et al., 2011; Schaeffer & Lebedev, 2013) exhibit several features in common in isotropic velocity structure, such as high velocity anomalies corresponding to subducting slabs stagnating or penetrating in the transition zone, high velocity anomalies beneath cratons and low velocity anomalies beneath ridges at ∼100–150 km depth, low velocity anomalies associated with Large Low Shear Velocity Provinces (LLSVPs) beneath Africa and the South Pacific observed in the lowermost mantle, etc. There are also some similarities between radially anisotropic models (e.g., SGLOBE-rani, Chang et al. (2015), S362WMANI +M, Moulik and Ekström (2014), SAW642ANb, Panning et al. (2010), SAVANI, Auer et al. (2014), SEMum2, French et al. (2013)), such as positive velocity

anomalies (i.e., faster V_{Sh}) beneath the Pacific at 150 km depth and negative velocity anomalies (i.e., faster V_{SV}) beneath the East Pacific Rise at 250 km depth. Nevertheless, there are still substantial inconsistencies between anisotropy tomography models. Independent tests of their robustness are needed to better quantify what can and cannot be resolved and interpreted.

Geodynamical simulations and fabrics calculations are useful tools to quantitatively interpret seismic tomography models. Faccenda and Capitanio (2013) presented a methodology to compute seismic anisotropy from upper mantle flow of 3-D numerical models resembling subduction zones. They used the full mantle flow field that develops during subduction to then compute strain-induced LPO, taking into account dynamic recrystallization and other creep mechanisms. In this study, similarly to Faccenda and Capitanio (2013), we carry out 2-D mechanical simulations of oceanic plate evolution from ridge to trench and estimate the associated strain-induced anisotropy. Successively, we apply the method of Witek et al. (2022) (in review) to synthetic seismic waveforms computed with the spectral element (Tromp et al., 2008) method using the Earth model obtained from the geodynamic simulations and mantle fabrics calculations. Hedjazian et al. (2017) performed a similar study, although without (i) considering plate subduction and (ii) computing waveform synthetics, but rather making comparisons with existing tomography images. We test two different receiver distributions, one ideal, with receivers close to each other and evenly distributed over the study area, and one more realistic emulating the distribution of seismic stations in the Pacific ocean. We discuss the methodology used in this study in section 7.2. In sections 7.3 and 7.4, we show and discuss the results obtained as well as their implications.

7.2 Method

In this section we describe the numerical methods used to compute mantle flow patterns, strain-induced mantle fabrics and seismological synthetics in this chapter.

7.2.1 Geodynamic modelling

We model oceanic plate formation, spreading and subsequent subduction with I2VIS (Gerya & Yuen, 2003) that is based on the finite difference method and the marker-in-cell technique. The code has been modified to solve the equations for conservation of mass (eq.7.1), momentum (eq.7.2-7.3) and energy (eq.7.4) in polar coordinates. In a Lagrangian reference frame and assuming incompressibility these equations take the form:

$$\frac{1}{r}\frac{\partial r v_r}{\partial r} + \frac{1}{r}\frac{\partial v_\phi}{\partial \phi} = 0 \tag{7.1}$$

$$\phi_{mom}: \frac{1}{r}\frac{\partial \tau_{\phi\phi}}{\partial \phi} + \frac{1}{r^2}\frac{\partial r^2 \tau_{\phi r}}{\partial r} - \frac{1}{r}\frac{\partial P}{\partial \phi} = 0 \tag{7.2}$$

$$r_{mom}: \frac{1}{r}\frac{\partial \tau_{r\phi}}{\partial \phi} - \frac{1}{r^2}\frac{\partial r^2 \tau_{\phi\phi}}{\partial r} - \frac{\partial P}{\partial r} = -\rho g_r \tag{7.3}$$

$$\rho C_p \frac{DT}{Dt} = -(\frac{1}{r}\frac{\partial r q_r}{\partial r} + \frac{1}{r^2}\frac{\partial q_\phi}{\partial \phi}) + H \tag{7.4}$$

where ϕ and r are the tangential and radial coordinates, respectively, $\overrightarrow{v}$ is the velocity vector, P is pressure, τ is the deviatoric stress tensor, ρ is density, g_r is the radial gravitational acceleration (9.81 m s^{-2}), C_p is the specific heat capacity, T is the temperature, D/Dt is the Lagrangian time derivative, $\overrightarrow{q}$ is the heat flux and H is a heat source term accounting for radiogenic, adiabatic and shear heating.

The model domain extends $0° \leq \phi \leq 40°$ in longitude and 700 km in depth, and is discretized using a regular grid with 1001 by 351 nodes. The

initial model setup (Figure 7.1a) is composed by the left plate defined by an age increasing from 0 to 60 Myr in the $0° \leq \phi \leq 25°$ range, and by the right plate with a constant 20 Myr age. These thermal ages are defined with the Half-Space Cooling Model (HSCM; Turcotte & Schubert, 2014) for a 90 km thick layer, below which a 0.5 K/km adiabatic gradient is imposed. The two plates are characterized by a 7 km thick and relatively weak oceanic crust (which lubricates the plates contact) and are separated by a $\sim 30°$ dipping weak zone. A 30 km thick sticky-air layer is placed at the top to model the free surface. A plate speed of 4 cm/yr is applied to the left plate, while the right plate is fixed. The model runs until a mature subduction scenario is established ($\sim$13 Myr; Figure 7.1b). Velocity boundary conditions are free slip everywhere, except for the lower permeable boundary where we apply external free-slip (Gerya, 2019). The side boundaries are insulating, while a constant T = 273 K is used for the sticky air layer and a T = 1890 K is employed for the bottom boundary.

A visco-plastic rheology based on deformation invariants (Ranalli, 1995) is used to model the mantle mechanical behaviour. For the oceanic crust we use the Plagioclase An_{75} flow law reported by Ranalli (1995). For the mantle, the effective viscosity is given by the harmonic average of the combined dislocation, diffusion and Peierls creep mechanisms (parameters and physical meaning are defined in Table 7.1):

$$\eta_{ductile} = \left(\frac{1}{\eta_{disl}} + \frac{1}{\eta_{diff}} + \frac{1}{\eta_{peierls}} \right)^{-1} \qquad (7.5)$$

where the dislocation and diffusion creep viscosities η_{disl}, η_{diff} are given by Karato and Wu (1993):

$$\eta = \frac{\tau_{II}}{2\dot{\varepsilon}_{II}}, \qquad (7.6)$$

with the strain rate being given by:

$$\dot{\varepsilon}_{II} = A \left(\frac{\tau_{II}}{\mu} \right)^n \left(\frac{b}{d} \right)^m exp \left(- \frac{E + PV}{RT} \right) \tag{7.7}$$

Table 7.1 gives the specific parameter values (pre-exponential factor A, activation energy E, activation volume V, stress exponent n, grain-size exponent m, gas constant R, shear modulus μ, Burgers vector b and gran size d) for the cases of diffusion (η_{diff}) and dislocation creep (η_{disl}), which are analogous to those used by Hedjazian et al. (2017).

At high deviatoric stresses (greater than 0.1 GPa) and low-T conditions, creep is accommodated via the Peierls mechanism as given by Katayama and Karato (2008):

$$\eta_{peierls} = 0.5 A \tau_{II}^{-1} exp \left\{ \frac{E + PV}{RT} \left[1 - \left(\frac{\tau_{II}}{\sigma_{Peierls}} \right)^p \right]^q \right\} \tag{7.8}$$

where τ_{II} and $\dot{\varepsilon}_{II}$ are the second invariant of the deviatoric stress and strain rate tensors, and all the other parameters are defined in Table 7.1.

A pseudo-plastic viscosity is also computed as:

$$\eta_{pl} = \frac{\tau_y}{2 \dot{\varepsilon}_{II}}, \tag{7.9}$$

where $\dot{\varepsilon}_{II}$ is the second invariant of the strain rate and the plastic strength τ_y is determined with a plastic Drucker–Prager criterion:

$$\tau_y = C_{DP} + \mu P \tag{7.10}$$

where $C_{DP} = C \cos \phi = 1 MPa$ is the cohesion, $\mu = \sin \phi$ is the friction coefficient and ϕ is the friction angle. To model strain-induced brittle weakening, the initial friction 0.6 coefficient is linearly decreased to 0.4 in the $0.5 \leq \varepsilon_p \leq 1.5$ range, where ε_p is the accumulated brittle/plastic strain. For the crust we use a constant $\mu = 0.05$ to ensure lubrication at the plate's contact. Finally, the effective viscosity is given by:

$$\eta_{eff} = min(\eta_{ductile}, \eta_{pl}) \qquad (7.11)$$

The lower and upper cutoff of η_{eff} are set to 10^{18} and 10^{25} $Pa\,s$, respectively. The set of rheological parameters used in this study is similar to that employed in previous numerical studies (e.g., Hedjazian et al., 2017; Lo Bue et al., 2021; Yang & Faccenda, 2020), and among other key features it reproduces a 100-120 km thick, low-viscosity asthenospheric channel dominated by dislocation creep (Figure 7.2).

TABLE 7.1: Creep parameters for mantle rocks.

Property	Symbol	Value	Unit
Diffusion Creep (Karato & Wu, 1993)			
Pre-exponential factor	A	$8.7 \cdot 10^{15}$	s^{-1}
Activation energy	E	300	$kJmol^{-1}$
Activation volume	V	6	cm^3mol^{-1}
Stress exponent	n	1	-
Grain-size exponent	m	2.5	-
Dislocation Creep (Karato & Wu, 1993)			
Pre-exponential factor	A	$3.5 \cdot 10^{22}$	s^{-1}
Activation energy	E	540	$kJmol^{-1}$
Activation volume	V	20	cm^3mol^{-1}
Stress exponent	n	3.5	-
Grain-size exponent	m	0	-
Peierls Creep (Katayama & Karato, 2008)			
Pre-exponential factor	A	$10^{7.8}$	Pa^2s
Activation energy	E	532	$kJmol^{-1}$
Activation volume	V	12	cm^3mol^{-1}
Peierls stress*	$\sigma_{Peierls}$	9.1	GPa
Exponent	p,q	1, 2	-,-

$R = 8.313 \, Jmol^{-1}K^{-1}$ is the gas constant, $\mu = 80 \, GPa$ is the shear modulus, $b = 0.5nm$ is the Burgers vector, $d = 1mm$ is the grain size. * (Evans & Goetze, 1979)

7.2.2 LPO development

We consider upper mantle aggregates with olivine:enstatite = 70:30 in volume proportion, mimicking a harzburgitic composition and with a regular 5 km spacing. The development of strain-induced LPO fabrics in the upper

mantle aggregates is computed with the modified version of D-Rex (Kaminski et al., 2004) included in the software package ECOMAN. For this study we selected the same parameters, $\lambda = 5$, M = 1 and $\chi = 0.9$, and same high activity for slip systems [100](010) and [001](010) as in Rappisi and Faccenda (2019), which result in an olivine fabric analogous to the AG-type characterized by (i) a girdle of a- and c-axes lying in the shear plane and spinning around its normal (which causes stain-dependent fluctuations in the fabric and anisotropy strength), (ii) being relatively weak, consistent with experimental and natural samples, and (iii) small but substantial azimuthal and radial anisotropy (Figure 3.3a,d,l,m). The A-type olivine fabrics are produced with D-Rex's widely used slip system activities and higher dimensionless grain boundary mobility and dimensionless threshold volume fraction below which grain-boundary sliding is active, i.e., M = 10 - 125 and $\chi = 0.3$, respectively (Boneh et al., 2015; Kaminski et al., 2004) (Figure 3.3a,b,c,h,i,j,k). However, the A-type fabrics generate stronger fabrics and seismic anisotropy relative to those of the AG-type fabric, which appear to be inconsistent with the observations when considering that in oceanic regions azimuthal anisotropy is typically 2% and P wave and S wave radial anisotropy are 4% and 3%, respectively (Song & Kawakatsu, 2012).

We assume that at 13 Myr, when subduction is well developed (Figure 7.1b,7.2b), the upper mantle flow field has reached a mature and steady-state stage. As such, we use this flow field to (i) initially perform advection backward in time such that all crystal aggregates are initially located below 400 km depth, (ii) and subsequently compute strain-induced LPO and forward advection until when the particles have reached the original position and regualr distribution. If an upper mantle crystal aggregate enters the transition zone, its LPO is reset and the aggregate is composed by randomly oriented spinel and majoritic garnet crystals. Strain-induced LPO is computed only for the fraction of deformation accommodated by dislocation

creep $f_{disl} = \eta_{eff}/\eta_{disl}$. As shown in Figure 7.2b, f_{disl} is high in hot mantle regions close to the oceanic plate and subjected to high deviatoric stresses (i.e., Sturgeon et al., 2019). The elastic properties of each crystal aggregate are finally computed as a function of the LPO and the single crystal elastic tensor is scaled by the local P-T conditions.

The resulting elastic tensor defined by 21 independent elastic constants is then interpolated to an Eulerian grid with lateral spacing $\Delta\phi = 0.1°$ and with depth spacing $\Delta r = 10$ km. The 2-D grid is then replicated along latitude θ each $0.1°$ with respect to the equatorial plane in the range between $-40°$ and $+40°$, and reflected with respect to the ridge axis, so that the final Eulerian domain in (Φ, R, Θ) is $80°$ x 700 km x $80°$. The resulting 3-D computational domain is then characterized by two subduction zones which are symmetric with respect to the central oceanic ridge.

7.2.3   Seismological forward modelling

We use the spectral element method (SEM; Chen & Tromp, 2007; Komatitsch & Tromp, 1999; Tromp et al., 2008) to simulate seismic wave propagation through the medium obtained from the geodynamical simulations and fabrics calculations presented in the previous sections. Chapter 2 of this Thesis presented the SEM, which is currently one of the most accurate methods to simulate seismic wave propagation in global and regional scales for realistic 3-D media.

The original SPECFEM3D_GLOBE code has been modified to allow loading (i) density and the 21 elastic moduli of the geodynamic model in the $24 \leq r \leq 670$ km depth range, and (ii) a 1-D reference model elsewhere (Figure 7.3). A crustal layer is characterized by two discontinuities at 14 km and 24.4 km depth.
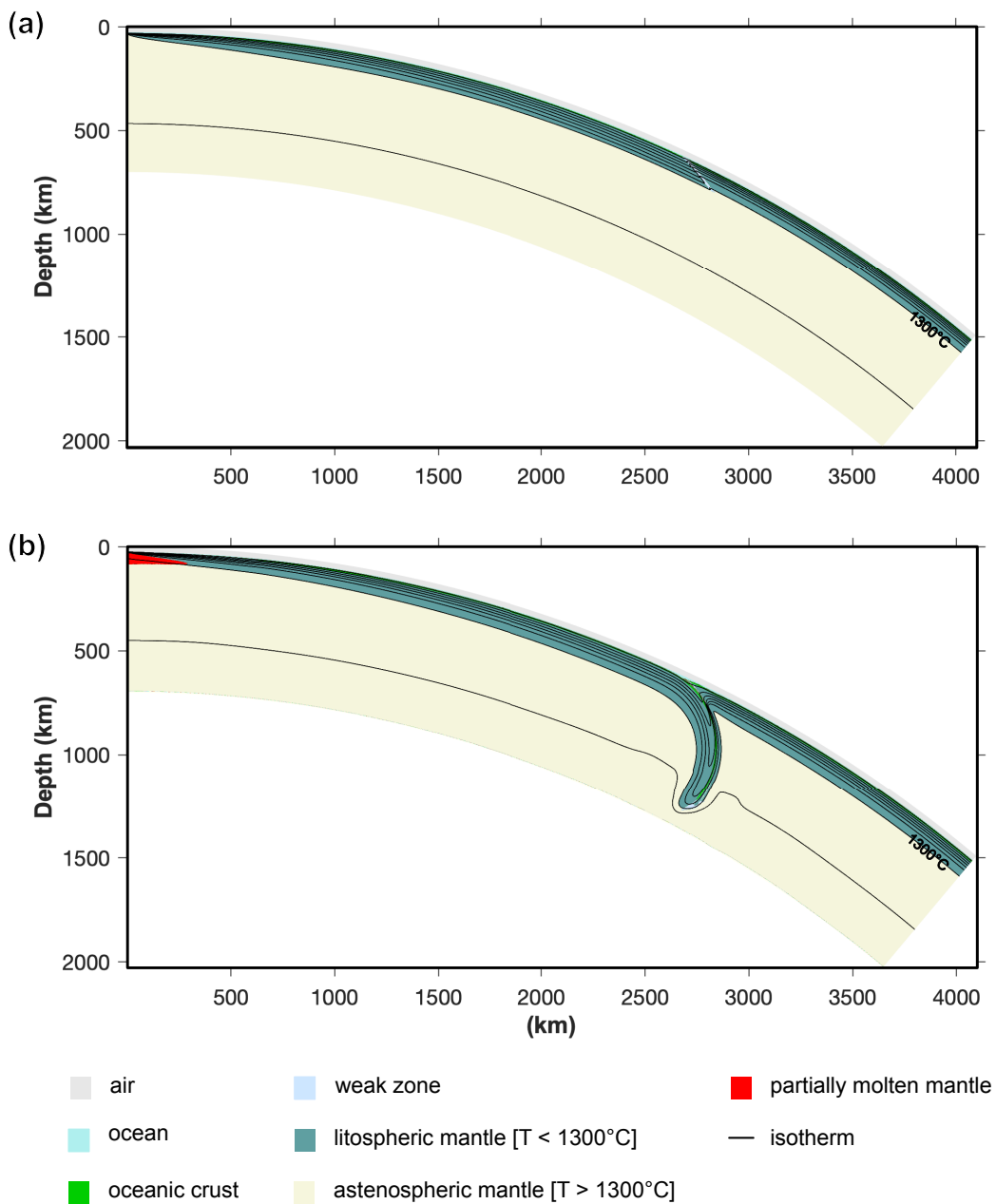
Figure 7.1: *(a) Initial model setup of 2-D oceanic plate formation at the ridge and subsequent subduction. (b) Snapshot at 13 Myr. The black lines are isotherms at every* 200°C.

We compute 60 minute-long synthetic seismograms recorded by 1302 stations equally spaced 1° apart. This array of stations was placed above the ridge (at 80°E) and the eastern slab (105°E) extending from 72°E to 113°E and from 15°N to 15°S. We use 43 earthquakes with magnitudes $5 < M_w < 8$ and at local and teleseismic distances with respect to the seismic array. Most of the events are placed in correspondence of the two subduction zones and at
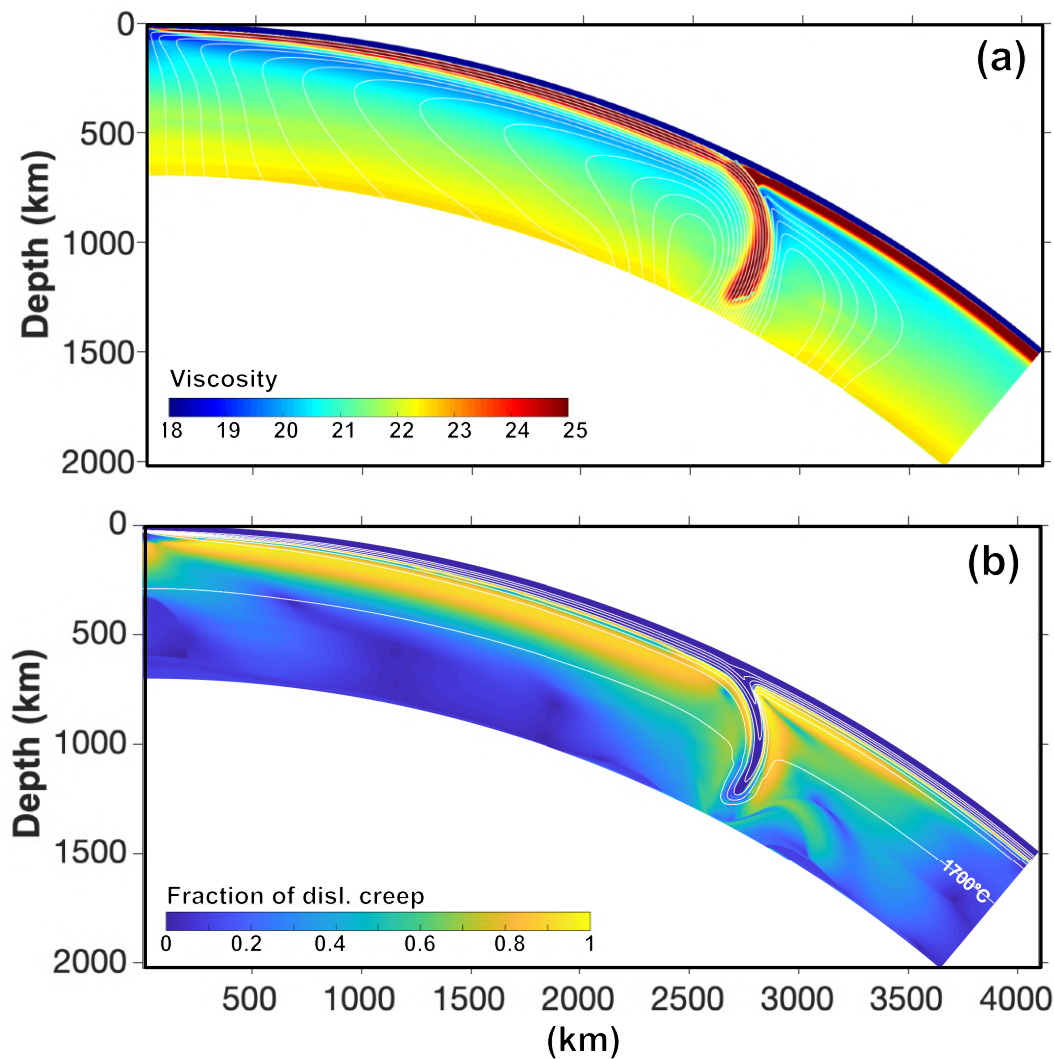
Figure 7.2: *(a) Viscosity and (b) Fraction of deformation accommodated by dislocation creep at 13 Myr; the white lines are streamlines in (a) and isotherms taken every 200°C in (b).*

the ridge (Figure 7.4).

In order to include teleseismic events in the analysis, we have expanded the domain along ϕ by 40° on each side of the geodynamic model so that the spectral-element domain is $(\Phi, R, \Theta) = (160° \times 6371 \text{ km} \times 80°)$ and the geodynamic model is centred at $\phi = 80°\text{E}$. After interpolation of the geodynamic model to the spectral element mesh, the physical properties of (isotropic) grid nodes at $\phi = 40°\text{E}$ and $\phi = 120°\text{E}$ are replicated to fill the mesh in the $0°\text{E} \leq \phi \leq 40°\text{E}$ and $120°\text{E} \leq \phi \leq 160°\text{E}$ ranges, respectively. Absorbing boundary conditions are applied on the two sides and bottom edges of the

spherical chunk. The number of spectral elements along longitude and latitude are, respectively, $n_\phi = 320$ and $n_\theta = 160$ and the horizontal resolution is about 0.5°. The vertical resolution is determined by the mesher so that its size varies with depth and is doubled at the main discontinuities (i.e. Moho, 670 km and core-mantle-boundary, CMB; see Figure 7.5). The minimum accurate wave period is

$$T_{min} = \frac{256}{n_\phi} \frac{\Phi}{90} \times 17 \approx 24.2s \,, \tag{7.12}$$

where Φ is the angular width in degrees. For simplicity, attenuation, gravity, ocean, topography and bathymetry effects on seismic wave propagation have been neglected.
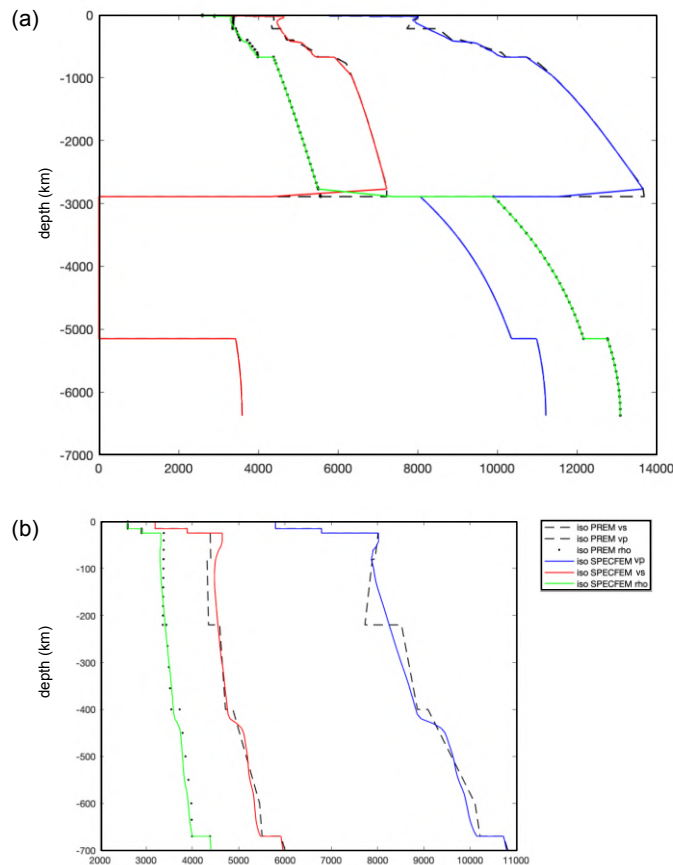
Figure 7.3: *Black dashed lines are the 1-D reference model; colored solid lines are the isotropic SPECFEM model for (a) the entire Earth and (b) upper mantle. Density, V_S and V_P in green, red and blue, respectively. The 1-D profiles have been taken at 0°N and 0°E.*
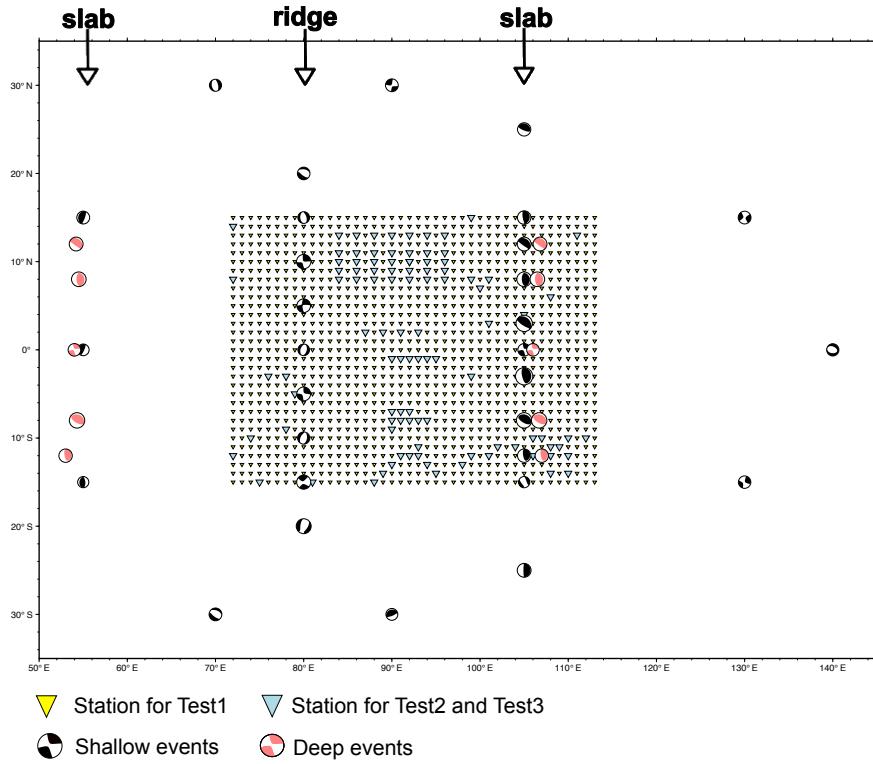
Figure 7.4: *Seismic array with sources (beachballs) and stations (triangles) distribution. Shallow events are in the range between 10 km and 20 km depth. Deep events goes from 100 km to 600 km depth.*

7.2.4   Waveform Inversion

Automated PWI method

In order to test the ability of widely used seismic tomography methods based on ray theory to retrieve the geodynamic model, the seismic waveforms are inverted using an automatic algorithm based on the partitioned waveform inversion (PWI) method (Nolet, 1990; Witek et al., 2022). A brief description of the method is given as follows. Waveforms are modelled along great circle paths using a local modes approach,

$$u(\omega) = \sum_n A_n(\omega) \exp\left\{ i \int k_n(\omega, s) ds \right\}, \tag{7.13}$$

where $u(\omega)$ is the displacement response at frequency ω, $A_n(\omega)$ is a complex excitation coefficient for mode n, and $k_n(\omega, l)$ is the local wavenumber for the position s along the great circle arc. The wavenumbers are calculated
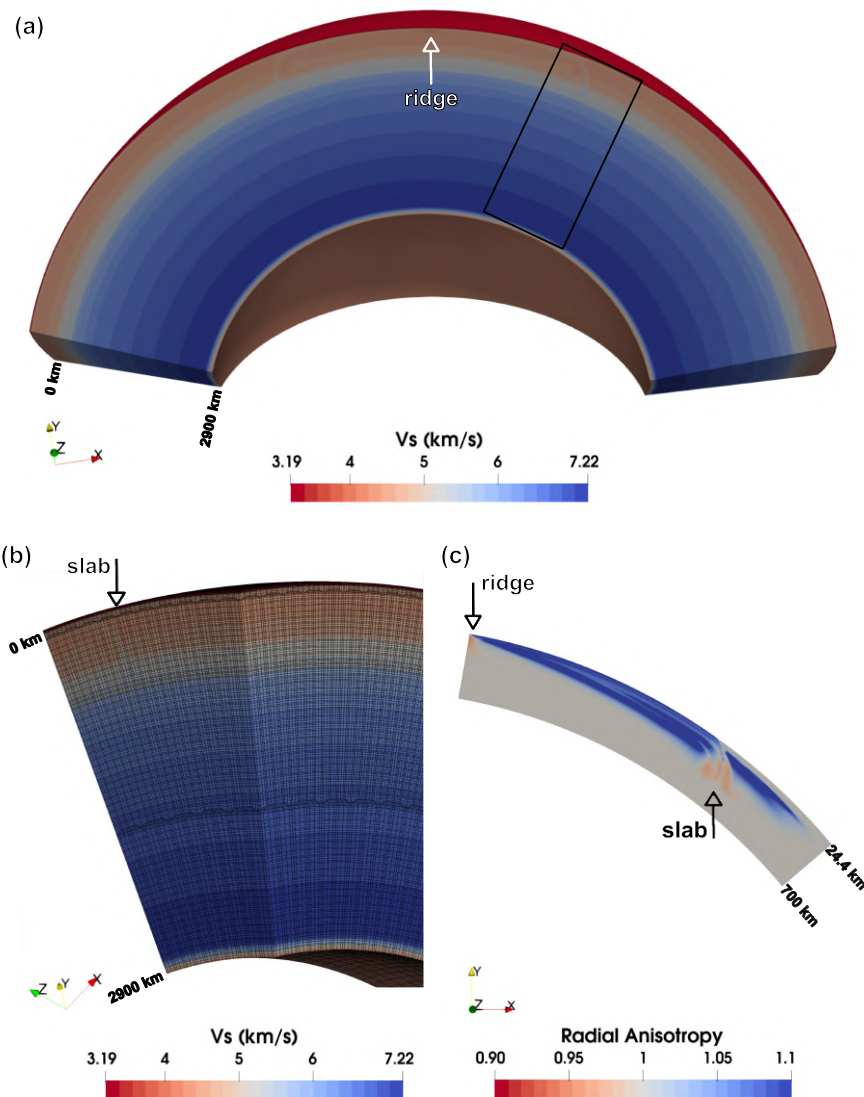
Figure 7.5: *(a) Isotropic shear velocity (V_S); (b) zoom of the SPECFEM3D_GLOBE mesh from 0 to 2900 km depth as shown by the black box in (a); (c) radial anisotropy of the 2-D section that is replicated along θ and reflected with respect to the ridge axis, from 24.4 km (Moho depth) to 670 km.*

by solving the normal mode eigenfrequency-eigenfunction problem for a 1-D Earth using a 1-D profile extracted from the 3-D model directly under the position s. More information on the reference 3-D model used in this study is given in Section 7.2.4. The excitation coefficients $A_n(\omega)$ include source effects and local receiver effects. Since the SEM waveforms used in this study are calculated without the effects of attenuation, attenuation due to Q structure along the ray path is also neglected here. Moreover, we performed extensive

validation comparisons of waveforms computed using the spectral element method and the forward modelling scheme used within our automated partitioned waveform method for simple 1-D Earth models and found an excellent agreement between the two sets of synthetic seismograms.

Perturbations in the waveforms with respect to the reference 3-D model are assumed to be entirely due to perturbations in the wavenumbers, i.e.,

$$k_n(\omega, s) = k_n^{ref}(\omega, s)\big(1 + \delta \ln k_n(\omega, s)\big). \tag{7.14}$$

To first order, the perturbations in the wavenumbers can be related to changes in the local model parameters, $\delta \ln m_i(s, r)$ via sensitivity kernels $K_i(\omega, s, r)$,

$$\delta \ln k_n(\omega, s) = \int_0^a \sum_i K_{ni}(\omega, s, r) \delta \ln m_i(s, r) dr, \tag{7.15}$$

where $i = 1, 2, ..., 6$ represents different model parameters (e.g. ρ, V_P, V_S, ζ_S, ζ_P, and η), depending on the parameterization. In PWI, we make the simplifying assumption that the model perturbations can be represented by a path average that is expanded onto a small set of radial basis functions $h_j(r)$,

$$\overline{\delta \ln m_i}(r) = \frac{1}{\Delta} \int_\Delta \delta \ln m_i(s, r) ds = \sum_j \gamma_{ij} h_j(r), \tag{7.16}$$

where the γ_{ij} are the basis function coefficients and Δ is the epicentral distance. In this study we use triangular basis functions, with the first and last basis functions being half-triangles. With these assumptions, the path integral in (7.13) becomes

$$\int_\Delta k_n(\omega, s) ds = \overline{k_n^{ref}}(\omega)\Delta + \sum_i \sum_j \gamma_{ij} \overline{K_{nij}}(\omega), \tag{7.17}$$

where $\overline{k_n^{ref}}(\omega)$ is a path average wavenumber calculated through the reference 3-D model and $\overline{K_{nij}}(\omega)$ is a path average sensitivity kernel.

We solve for the γ_{ij} coefficients using a nonlinear waveform fitting algo-
rithm, with the details given in Witek et al. (2022) (in review). The data fitting
is generally split into two parts: (1) fundamental mode extraction and fitting,
and (2) full mode sum fitting. In (1), we perform phase-matched filtering
to extract the fundamental mode from the observed seismogram (Goforth &
Harrin, 1979; Harrin & Goforth, 1977). After a minimum fitting frequency
is determined, the extracted fundamental mode is subjected to a series of
Gaussian bandpass filters. We determine window boundaries for each fil-
tered waveform by finding where the envelope drops below one fourth of
the maximum value, and we refer to each filtered, windowed waveform as
a time-frequency window. In order to minimize the chances that we are fit-
ting unmodeled phases or effects such as scattering, we perform a series of
checks on each time-frequency window. We require that the minimum fitting
frequency permits at least three fundamental mode wavelengths between the
source and receiver to ensure the far-field approximation. The minimum fre-
quency also cannot permit more than 12 wavelengths to avoid cycle skips
(Lebedev et al., 2005). We avoid fitting waves with off-great-circle propa-
gation by checking the fundamental mode source radiation pattern and ex-
cluding traces that correspond to nodal directions. We also check that the
amplitude ratio between the synthetic and observed waveforms is less than
5.

After fitting the fundamental mode, we use the resulting path average
model as an initial model to fit the full synthetic waveform, which contains
all modes $n = 0, 1, 2, ..., 20$. Summing up to the 20th overtone ensures that
the S-wave and S-wave multiples can be sufficiently reconstructed, but we
note that this does not necessarily imply that all modes will be equally con-
strained. When fitting the full synthetic, we set an early time limit to be 10%
before the predicted S-wave arrival if the source-receiver distance is less than
$35°$. Otherwise, we use the predicted SS-wave arrival time. This is done in

order to prevent fitting body waves that bottom in the complex lower mantle, since we ignore the 2-D nature of the sensitivity kernels (Marquering & Snieder, 1995; Van der Lee & Nolet, 1997). We subject the full synthetic to the same Gaussian bandpass filters that were used for the fundamental fit, and after creating the time-frequency windows, we perform similar quality control checks.

3-D reference model

The tomography model is parameterized using the isotropic shear wave speed parameter $V_S^2 = \frac{1}{2}(V_{SH}^2 + V_{SV}^2)$ and the radial anisotropy parameter $\zeta_S = (V_{SH}^2 - V_{SV}^2)/2V_S^2$, but for plotting purposes we plot the widely used $\xi = \frac{V_{SH}^2}{V_{SV}^2}$. We couple variations in density and isotropic P-wave velocity to variations in isotropic S-wave velocity via the scaling relationships $\delta ln\rho/\delta lnV_S = 0.4$ (Anderson et al., 1988) and $\delta lnV_P/\delta lnV_S = 0.5$ (Robertson & Woodhouse, 1995). The sensitivity of the surface waves to other parameters, such as, e.g., to the η parameter and to azimuthal anisotropy are ignored.

The reference model is a 3-D locally radially anisotropic version of the 21 elastic moduli tensors described in the previous sections and used to calculate the synthetics, with the azimuthally anisotropic part set to zero and V_{SH} and V_{SV} set to the average values. The other parameters, i.e., V_P, η and ρ are kept unmodified.

Linear Inversion

After applying the automatic waveform fitting procedure to all ray paths in the dataset, we define a misfit equation as

$$S(\boldsymbol{\mu}) = (G\boldsymbol{\mu} - \boldsymbol{d})^T C_e^{-1} (G\boldsymbol{\mu} - \boldsymbol{d}) + \lambda_D^2 |I\boldsymbol{\mu}|^2 + \lambda_F^2 |F\boldsymbol{\mu}|^2, \qquad (7.18)$$

where $\boldsymbol{d}$ is a data vector containing all independent constraints ($\boldsymbol{\eta}$) and G is a linear constraints matrix created by projecting the eigenvectors of the Hessian from each waveform fit onto the 3-D model's basis functions whose coefficients are gathered in the vector $\boldsymbol{\mu}$. F represents the discrete horizontal gradient operator acting on $\boldsymbol{\mu}$, I is the identity matrix and C_e is a diagonal data covariance matrix. We also include model norm damping (λ_D) and horizontal gradient norm damping (flattening; λ_F). Optimal values are estimated by performing a trade-off curve (i.e., L-curve) analysis. The misfit equation is then optimized using up to 100 iterations of the LSQR algorithm of Paige and Saunders (1982).

7.3   Results

To test the ability of the automatic partitioned waveform inversion to recover shear-wave velocity structures and radial anisotropy, we conduct a series of synthetic inversion tests. We invert the SEM waveforms for V_S and for ξ. We compute V_P and ρ using a scaling factor of $\delta ln V_P / \delta ln V_S = 0.5$ and $\delta ln \rho / \delta ln V_S = 0.4$, taking the shear wave velocities from the starting model described in section 7.2.4.

We start by performing a first test, which we shall refer to as Test1, using seismic data from the ideal station distribution described in section 7.2.3 (Figure 7.4). The dataset consists of 11,992 waveforms from shallow (i.e. $\sim$10-20 km depth) and deep events (i.e., $\sim$100-600 km depth). Next, we perform other tests whereby we invert 869 waveforms computed using a station distribution (Figure 7.4) obtained by selecting stations resembling a more realistic seismic data coverage (e.g., such as the one observed in the Pacific ocean). From this group of tests with realistic data coverage we have selected what we called Test2 and Test3, which exhibit model norm and variance reduction

similar to Test1, respectively. Figure 7.6 presents the results from Test1. Figures 7.7 and 7.8 show the results of Test2 and Test3. In Table 7.2 we list the selected damping and smoothing factors for each test and the resulting model norm and variance reduction. Our "best" solutions for the visualization were selected by choosing regularization factors that balance the trade-off between the model norm and data misfit.

By comparing the results of Test1 in Figure 7.6(b-j,l-t) with the true model in the top panels (Figure 7.6a-k), we observe good similarities in both shear velocity and radial anisotropy structures. For example, the strongest low velocity anomaly associated with the ridge is well recovered at every latitude. The same is true for the fast anomaly associated with the slab down to ~150 km depth. On the contrary, as shown by the black contours representing +1% anomalies in $\delta ln V_S$, the retrieved V_S model does not correctly recover the fast anomaly at depth, i.e., below ~150-200 km. Similarly, the right panels of Figure 7.6 show the recovered radial anisotropy. By comparing the results (Figure 7.6l-t) with the true model (Figure 7.6k), we observe that the inversion recovers the negative radial anisotropy beneath the ridge and the positive radial anisotropy beneath the oceanic plate (i.e. from the ridge to the trench). The black contours, representing +2% anomalies in $\delta ln \xi$, highlight the efficiency of the inversion in recovering the age-dependent positive radial anisotropy region between the ridge and the trench.

Figures 7.7 and 7.8 show that using a more realistic station distribution strongly affects the inversion results. In Figure 7.7, which shows the results of Test2 with similar model norm to that of Test1 (see Table 7.2), moving along the latitude we observe several substantial differences between the input and output models both in shear wave velocity and in radial anisotropy. For example, the strong slow velocity anomaly beneath the ridge gradually varies from 10° to -10° of latitude (Figure 7.7b-j) and its typical conical shape appears rougher than in the true model (Figure 7.7a) or in Test1 (Figure 7.6b-j).

The thickness of the fast velocity anomaly varies with latitude as well, showing lateral changes that are not present in the true model. Similarly, radial anisotropy varies with decreasing latitude, but its large scale features such as the descending margin separating positive and negative ζ, the low values beneath the ridge and in correspondence of the slab, are still recovered.

Figure 7.8 shows the results of Test3, i.e., with similar variance reduction to Test1. We observe that at extreme latitudes (i.e. 10°, 7.5°, 5°, -5°, -7.5° and -10°, Figure 7.8(b-d, h-j)) the fast V_S anomaly in the back-arc region is not imaged, while the main fast V_S anomaly is confined in the top $\sim$70-100 km. Figure 7.8(l-t) shows the retrieved radial anisotropy and, in addition to the differences between the various latitudes, we observe that the predicted $\delta ln\zeta$ model is characterized by a flat positive radial anisotropy anomaly confined in the top 100 km depth, i.e., the inversion does not recover the depth-age dependency of $\delta ln\zeta$ that is present in the input model.

7.4   Discussion

We focus our discussion on the geodynamic interpretation of the models obtained from Test1 (Figure 7.6), Test2 (Figure 7.7) and Test3 (Figure 7.8), and how they differ from the true model.

First, we discuss the isotropic V_S anomaly patterns and then we interpret the variations in radial anisotropy in terms of upper mantle dynamics. By comparing the results obtained from the three tests considered, we also discuss how the ray density and the choice of damping and smoothing constraints influence the seismic tomographic results.

In all tests the recovered isotropic structures are characterized by two major slow and fast anomalies, which can be interpreted as upwelling astenospheric mantle at lithospheric depths and descending lithospheric slab at asthenospheric depths (Figure 7.6). The recovered low velocity zone allows to

Table 7.2: *Trade-off curves from PWI. In column the model norm, (vr) variance reduction, (λ_D) damping factor, (λ_{F1}) flattening factor for V_S, (λ_{F2}) flattening factor for ζ. In bold the regularization factors selected for the best result of Test1 (λ_D=0.1, λ_{F1}=0.2, and λ_{F2}=0.2, which has a model norm of ∼2.31 and vr=91%), Test2 with similar model norm (λ_D=0.1, λ_{F1}=0.2, and λ_{F2}=0.2, which has a model norm of ∼2.23 and vr=95%) and Test3 with similar variance reduction (λ_D=0.3, λ_{F1}=0.3, and λ_{F2}=0.39, which has a model norm of ∼1.45 and vr=90%).*

	norm	vr	λ_D	λ_{F1}	λ_{F2}
Ideal station distribution					
	6.94752	0.958463	0.0	0.0	0.0
	6.82162	0.958425	0.001	0.001	0.0013
	6.22312	0.958181	0.003	0.003	0.0039
	4.58705	0.954383	0.01	0.01	0.013
	3.38871	0.944508	0.03	0.03	0.039
	2.34178	0.918469	0.1	0.1	0.13
	1.41792	0.828163	0.3	0.3	0.39
	0.499744	0.474115	1.0	1.0	1.3
	0.0912407	0.108406	3.0	3.0	3.9
	2.25526	0.899904	0.1	0.3	0.39
Test1	**2.31078**	**0.910066**	**0.1**	**0.2**	**0.2**
Real station distribution					
	7.82907	0.996084	0.0	0.0	0.0
	7.65969	0.99603	0.001	0.001	0.0013
	6.93362	0.995794	0.003	0.003	0.0039
	4.87635	0.992112	0.01	0.01	0.013
	3.28788	0.981922	0.03	0.03	0.039
	2.22963	0.960109	0.1	0.1	0.13
Test3	**1.4459**	**0.900145**	**0.3**	**0.3**	**0.39**
	0.606954	0.616766	1.0	1.0	1.3
	0.133245	0.181018	3.0	3.0	3.9
Test2	**2.2383**	**0.952082**	**0.1**	**0.2**	**0.2**

clearly distinguish the position of the ridge, located at 80°E of longitude (Figure 7.6). Using the contour lines indicating the +1% of $\delta ln V_S$ as a reference, we observe however that, due to a degradation of the surface wave resolution power with increasing depth, the subducted portion of the oceanic lithosphere is imaged as a short slab hanging down to only ∼150 km of depth. In addition, the subducting slab and the relatively thin upper plate located on the eastern side of the trench appear much thicker (∼100 km) than in the input model owing to lateral and vertical smoothing. Thus, the retrieved

structure of the subduction zone appears to be more compatible with that of a collisional margin that experienced thickening and shallow slab breakoff.

Overall, the age-dependent gradual thickening of the lithosphere can be inferred from all isotropic V_S models, which is consistent with the imposed thermal structure based on the half space cooling model (Turcotte & Schubert, 2014). However, the LAB is much more discontinuous in models with a realistic station distribution (Test2 and Test3).

In an upper mantle dominated by A-type olivine textures, horizontally and vertically oriented fabrics result in, respectively, strongly positive ($V_{SV} < V_{SH}$) and weakly negative ($V_{SV} > V_{SH}$) radial anisotropy (Karato et al., 2008), which can be used to infer patterns of mantle flow. Small negative values of ξ are present in Test1 and Test2 beneath the ridge where the geodynamic model reproduces asthenospheric mantle upwelling. In contrast, both Test1 and Test2 do not exhibit negative anisotropy in correspondence of the relatively thin subducting material, which is likely due to the limited lateral resolution of the surface wave tomographic method. Test3 does not recover any substantial negative ξ at all. Hence, for certain inversion parameters, inferring vertical components of mantle flow from surface waves alone might not be always possible.

The age-dependent distribution of positive radial anisotropy resulting form the gradual thickening of the lithosphere as described by the half-space cooling model and the resulting deepening of the low-viscosity, highly anisotropic asthenospheric channel is recovered both in Test1 and Test2. In contrast, Test3 exhibits a different, age-independent structure, resembling that predicted by the plate cooling model (Parson & McKenzie, 1977) (Figure 7.8). Thus, in Test3 the age-independent character of the oceanic lithosphere is only evident from radial anisotropy profiles, while the V_S profiles tend to show a thickening of the oceanic lithosphere.

Results of Test3 are consistent with most existing V_S and radial anisotropy regional and global scale models (e.g., Beghein et al., 2014; Burgos et al., 2014; Debayle et al., 2016; Schaeffer et al., 2016), with the distribution of isotropic V_S follows the predictions of the half-space cooling model. In contrast, the radial anisotropy models do not show any significant age-depth dependence and tend to be characterized by an upper layer where $V_{SV} > V_{SH}$ and a lower layer where $V_{SV} < V_{SH}$, with a transition that occurs at the same depth of $\sim$60–80 km for all ages (Auer et al., 2014; Beghein et al., 2014; Burgos et al., 2014; Chang et al., 2015; French et al., 2013; Nettles & Dziewonski, 2008). A similar result was found by Beghein et al. (2019) by applying a Bayesian model space search approach to three published Pacific surface wave dispersion data sets. In these models the recovered radial anisotropy structures differ even in pattern and, and in contrast to those of isotropic V_S and azimuthal anisotropy, display no obvious age dependence. However, given the uncertainties, the authors concluded that radial anisotropy, azimuthal anisotropy and velocity models could actually reflect compatible, age-dependent, lithosphere-asthenosphere boundary (LAB) depth estimates as expected from the half-space cooling model.

The obtained distributions of radial anisotropy resembling either the half-space cooling model (Test1 and Test2) or the plate cooling model (Test3) clearly demonstrate how small changes in the inversion parameters (e.g., damping and smoothing factors) can cause large changes in the tomographic result, especially for models with a sparse, realistic distribution of receivers. In turn, this can have major implications for the interpretation of the models in terms of Earth's dynamics and cooling. The plate cooling model has been frequently invoked to explain the age-independent trend of surface heat flux and bathymetry observed for seafloor ages > 70-80 Myr. Mechanisms that would explain an age-independent thermal structure of the oceanic lithosphere are plate erosion by bottom heating or plate delamination by small

scale convection or by plume-lithosphere interaction (Parson & McKenzie, 1978; Stein & Stein, 1992). The success of the plate cooling model in explaining these surface observables owes, however, entirely to the use of an artificial boundary condition at the bottom, which comprises two free parameters, plate thickness and basal temperature (Korenaga et al., 2021). There is no such a boundary in the real mantle with a constant temperature, but these free parameters allow the plate model to be flexible enough to fit observations on older seafloor. More recently, Korenaga et al. (2021) proposed an updated version of the classic half-space cooling model. By incorporating the effects of incomplete viscous relaxation, P-T dependent physical parameters, radiogenic heating, and mainly secular cooling the authors were able to predict the thickening of the lithosphere together with the bathymetry and surface heat fluxes. The authors, however, do not provide an explanation for the age-independency of the radial anisotropy profiles in current tomography models.

Similar to Beghein et al. (2019), here we conclude that radial anisotropy models are likely poorly constrained and could be in fact consistent with the half-space cooling model, and that a more thorough investigation of the model parameters is warranted in seismic tomography studies. Differently from radial anisotropy models that display negative radial anisotropy in the upper 60-80 km of the oceanic lithosphere (Beghein et al., 2014; Burgos et al., 2014; Nettles & Dziewonski, 2008), our inversions show $V_{SH} > V_{SV}$ also at lithospheric depths. This could be ascribed to, for example, melt-assisted deformational processes occurring at the ridge yielding fabrics different from those modelled here (Hansen et al., 2016a; Holtzman et al., 2003; Kaminski, 2006), and/or to a different corner flow dynamics at the ridge (as an example, Hedjazian et al. (2017) obtained a weakly positive radial anisotropy within the lithosphere due to a more inclined fabrics than in our model). Recent

studies based on local ocean-bottom seismic arrays deployed in areas not affected by upwelling plumes found that radial anisotropy is actually positive ($\xi \geq 5\%$) in the shallow oceanic lithosphere down to at least 30 km below the seafloor (Russel et al., 2018). Thus, the negative ξ retrieved at lithospheric depths in plate- and global-scale surface wave models might be related to the fact that these surface-wave studies have not included the high-frequency data required to fully resolve anisotropy at the shallowest depths (Chang & Ferreira, 2017; Hansen et al., 2016a).

Finally, we note that at old ages most V_S profiles in tomographic models exhibit a deepening of the fast anomaly, which could be interpreted as a sudden and anomalous increase in lithospheric thickness (e.g., Debayle et al., 2016; Isse et al., 2019; Schaeffer & Lebedev, 2013). However, we suggest that this could be related to the effect of lateral smearing occurring in areas close to subduction zones and continental passive margins where the lithosphere is present at larger depths than predicted by the half-space cooling model. Data from oceanic plates too close to these margins should be then discarded when stacked in age-depended profiles.

7.5 Conclusions

In this study, we combined geodynamic simulations with seismological forward and inverse modelling to investigate which realistic upper mantle isotropic and anisotropic features can and cannot be resolved with classical tomography methods. We used the automatic partitioned waveform inversion (PWI) method of Witek et al. (2022) (in review) to perform seismic tomography inversions of $\sim$11,992 synthetic waveforms computed using the spectral element method for a realistic 3-D Earth model obtained from geodynamics simulations and fabrics calculations. The 3-D geodynamic model reproduces
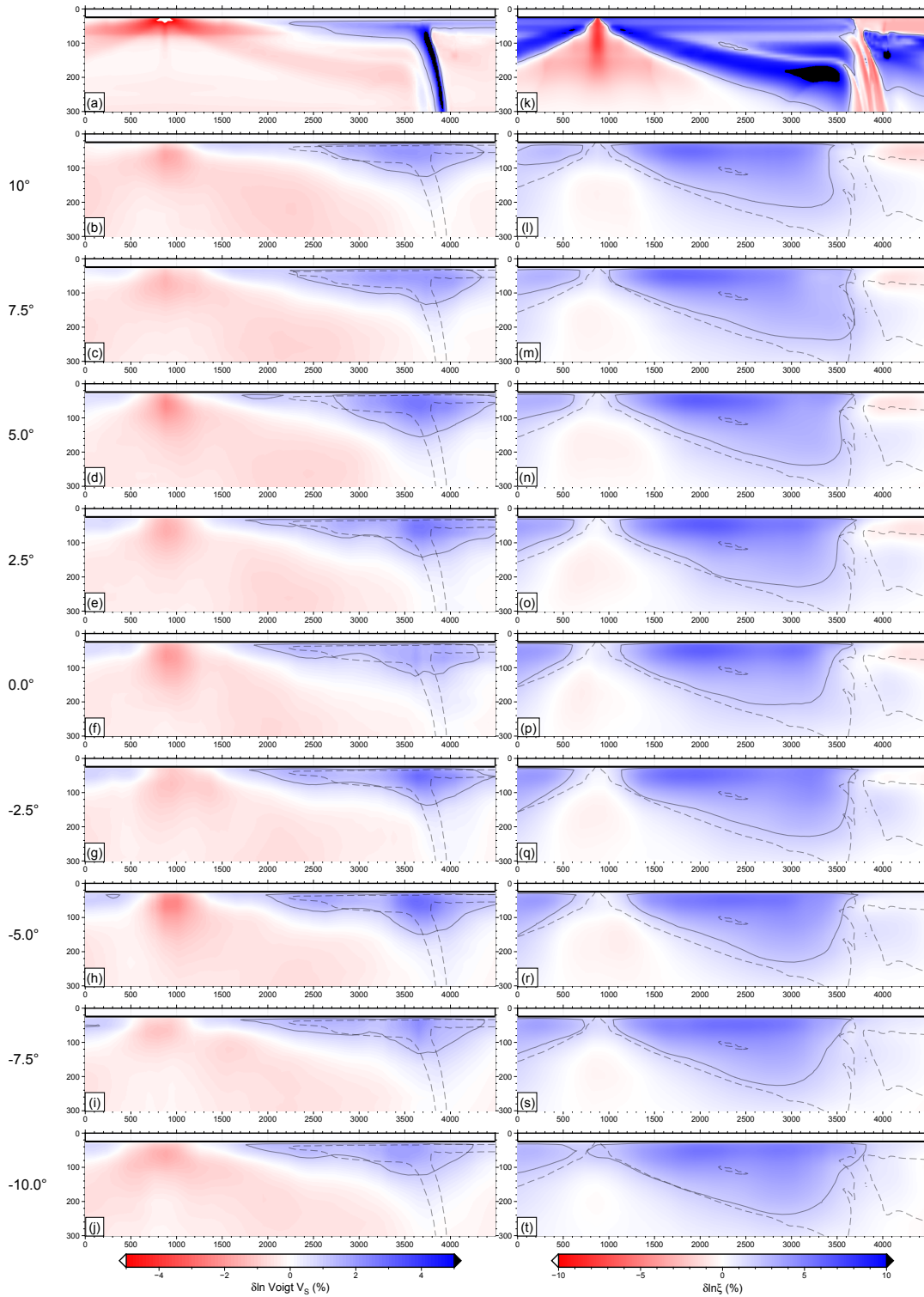
Figure 7.6: *Results of Test1. Top panels (a,k) are the true δlnV$_S$ and δlnξ models for reference. +1% δlnV$_S$ and +2% δlnξ contours outline the true slab geometry and radial anisotropy. (b-j) are the recovered δlnV$_S$ and (l-t) are the recovered δlnξ at different latitudes. The +1% δlnV$_S$ and +2% δlnξ contours are drawn in black on the left (b-j) and right (l-t) panels, respectively, for the true model (dashed line) and the obtained result (solid line).*
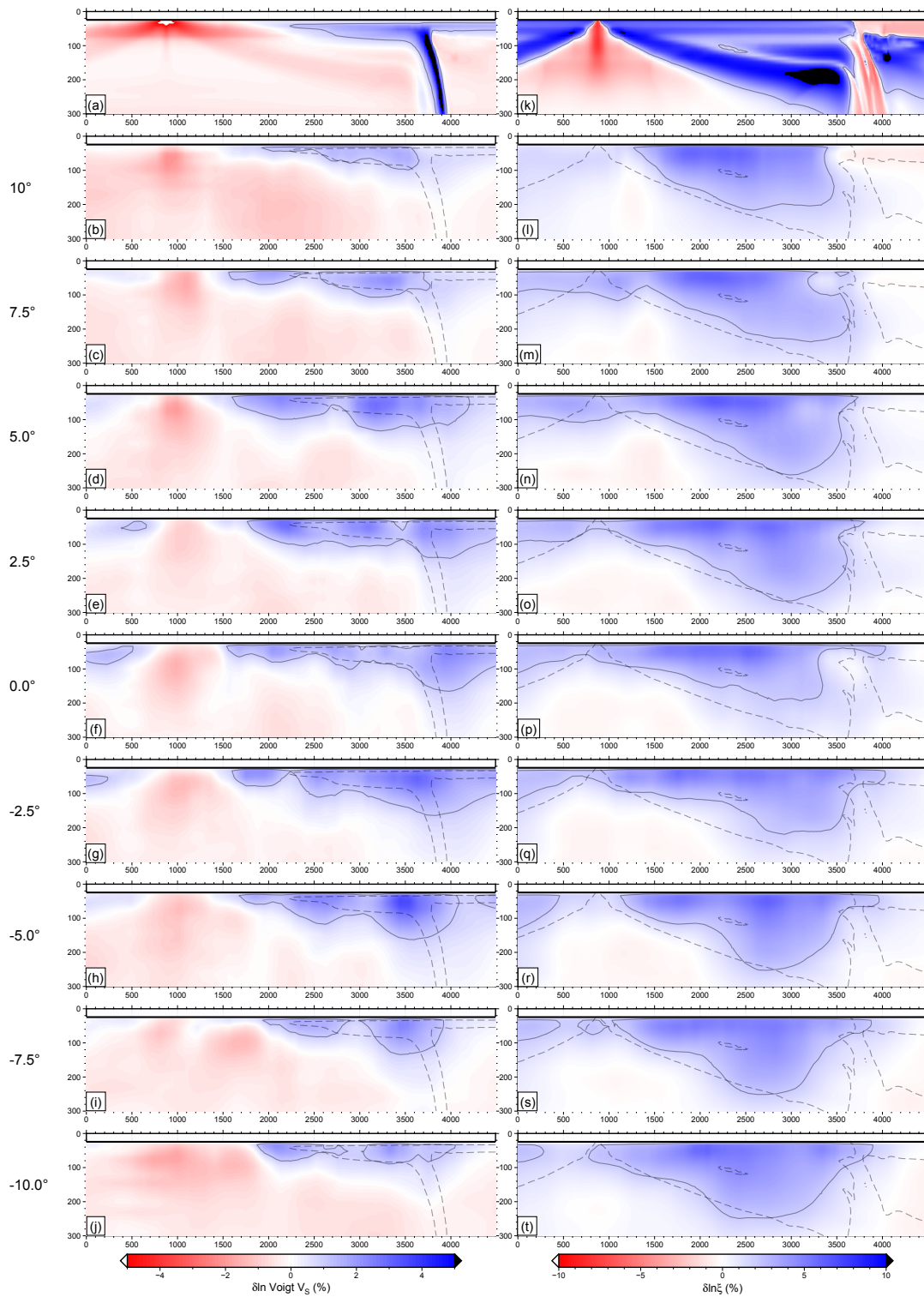
Figure 7.7: *Results of Test2 with similar model norm to Test1 showed in Figure 7.6. Velocity variations and radial anisotropy are plotted as in Figure 7.6*

a geological setting composed by an oceanic ridge, in the middle of the mod-
elling domain, and two subduction zones, to the western and eastern sides
of the domain. We tested ideal and more realistic seismic station coverages,
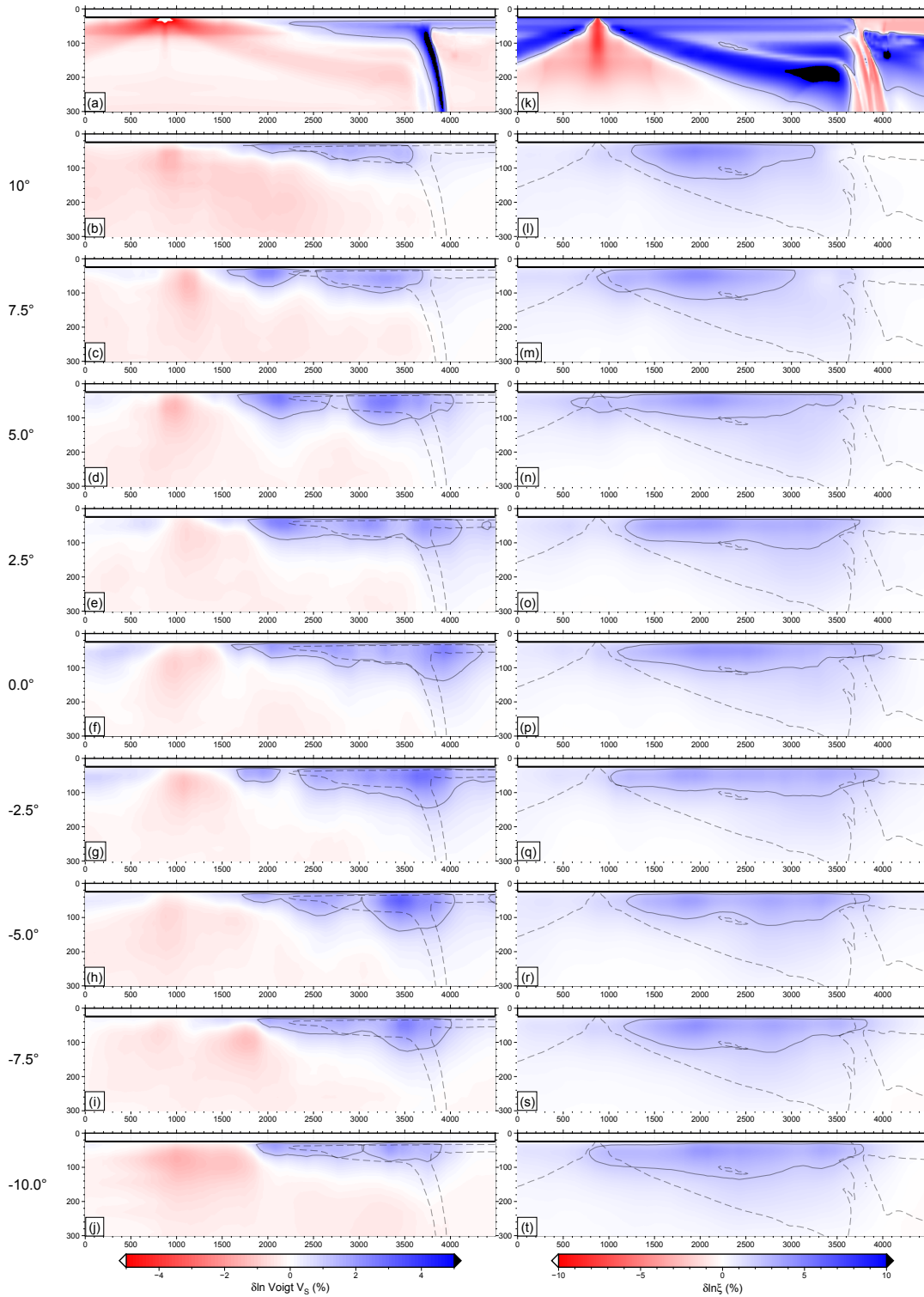
Figure 7.8: *Results of Test3 with similar variance reduction to Test1 showed in Figure 7.6. Velocity variations and radial anisotropy are plotted as in Figure 7.6*

which showed the limits and capabilities of the tomographic inversions.

The models of isotropic V_S and radial anisotropy that we obtained from the PWI inversions show that the tomographic result is strongly influenced

both by the ray density and the regularization, i.e., by the choice of the damping and smoothing factors. While changes in station coverage can cause some distortions in the retrieved isotropic and radially anisotropic structures, the large scale features can still be resolved by applying less regularization than in typical real tomography inversions. On the other hand, by applying the L-curve "corner" tradeoff criteria to select regularization, which is typically used in tomography inversions, causes substantial changes in the tomography result. For example, by changing regularization one can obtain anisotropic models similar to the half-space cooling model, showing age-dependent lithospheric structures, or, conversely, obtain results similar to the plate cooling model, characterized by flat and age-independent lithospheric structures. Moreover, in all cases, the retrieved subducted slabs can be strongly distorted, showing substantial artificial thickening and also loosing a clear fast velocity signature below ~ 100 km depth. Future work combining surface wave data with higher frequency body wave data should help resolve these issues. Moreover, efforts to continue enhancing seismic data coverage are essential, notably to cover the Earth's oceans, such as with large scale ocean bottom seismometer deployments (e.g., PacificArray, Rhum-rum experiment, UPFLOW)

Acknowledgments

Chapter 8

CONCLUSIONS

Due to the presence of intrinsically anisotropic crystals, such as olivine and pyroxene, that align along preferential direction when subjected to deformation, seismic anisotropy forms in the upper mantle. Several studies aimed at revealing seismic anisotropy distribution as it is essential to correctly investigate the Earth's internal structure and dynamics. However, most tomographic methods rely on the assumption of an isotropic Earth.

In this work we firstly have constrained numerical modelling parameters for estimating strain-induced seismic anisotropy. From our study, through a comparison with laboratory experiments, it emerged that the A-type I olivine fabric matches fabrics of pure olivine aggregates, while it tends to overestimate seismic anisotropy of harzburgitic or more fertile mantle compositions. When applied to a larger-scale geodynamic model, it results into trench-perpendicular SKS fast azimuths along the entire model. On the contrary, we observed that the AG-type olivine fabric better fits the multiphase aggregates laboratory experiments and when used in the larger-scale geodynamic model, it results into trench-parallel SKS splitting where a vertical flow is present, i.e. in proximity of the ridge and the trench. We note that the elastic response of the modeled geological scenario depends on the choice of the D-Rex parameters (i.e. M, λ and χ). For example, we observe that imposing a poorly efficient dynamic recrystallization together with same activities of [100](010) and [001](010) slip systems and a combination of 70% olivine

and 30% entstatite yields numerical results that better fit seismological observations.

By performing teleseismic P-wave travel time tomography, in Chapter 4 we presented model ani-NEWTON21, the first anisotropic tomography of the upper mantle of the Central Mediterranean. Comparing isotropic and anisotropic tomographic models, obtained using the same dataset and methodology, we observed that the primary effect of including anisotropic parameters in the inversion is to reduce the magnitude of low-velocity anomalies, highlighting how such features would contaminate purely isotropic images as artifacts. In the Central Mediterranean we identify three main segments of subducting lithosphere belonging to the (1) Eurasian, (2) Ionian, and (3) Adria plates, characterized by several slab windows and tears. Among the main slabs the Alpine appears composed by three main portions characterized by different dip angles: the western and eastern portions dive nearly vertical in the upper mantle, while the central portion dips steeply toward the southeast and tends to flatten at depth. Along the Tyrrhenian coast of the Italian peninsula, the Northern Apenninic and Calabrian slabs sink into the upper mantle and stagnate at the transition zone, separated by a wide, shallow slab window. On the eastern side of the Adria plate, model ani-NEWTON21 images the complex structure of the Dinaric and Hellenic slabs subducting north-eastward. The P-wave anisotropic patterns are interpreted as horizontal asthenospheric flows around the main isotropic bodies (e.g., in the Central-Eastern Alps and Calabrian slab where the fast azimuths orient trench-parallel) and vertical flows induced by the subductions (e.g., in the Tyrrhenian sea, in front of the Calabrian-Sicilian coast, where steeply dipping fabrics orient trench-perpendicular).

Using the tomographic methodology of VanderBeek and Faccenda (2021)

already applied in Chapter 4 on real data, in Chapter 5 we performed synthetic P-wave anisotropic tomography using the present-day elastic properties from the 3-D numerical model reproducing the geodynamic evolution of the Central-Western Mediterranean region over the last ~20-30 Myr. With the geodynamic model as target model, by performing different tests under different conditions (e.g., with different data errors, different receiver distributions, different regularization factors, etc), we observed that the reliability of the solution of a P-wave delay times tomography strongly depends on data quality and ray coverage. By performing isotropic and anisotropic inversions of the synthetic data and comparing them with the geodynamic model it emerged that (i) not including anisotropy distorts the tomographic image introducing false velocity anomalies and (ii) in the anisotropic tomography, although the recovered anisotropic patterns are consistent with the target model, an underestimation of their magnitude is observed.

The tomographic results of Chapter 6 show that teleseismic S-waves alone can constrain 3-D upper mantle isotropic structures and anisotropic patterns, however they also demonstrate that teleseismic S-waves are strikingly sensitive to anisotropy. As for P-waves, this sensitivity is documented by the appearance of imaging artifacts when working in isotropic assumption, significantly corrupting S-wave images of isotropic upper mantle velocities thus leading to erroneous inferences on subduction dynamics. Distortions of slab geometry (e.g., changes in dip and appearance of slab gaps) and low-velocity artifacts were observed to be dependent on the orientation in which S-wave delays are measured (e.g., radial or transverse). We investigated which direction is the best to reduce these artifacts and we found that when measured in the direction of maximum S-wave energy (i.e. polarization direction), these artifacts are still present but appear at a generally reduced magnitude.

In Chapter 7, by performing partitioned waveform inversion of shear

and surface waves propagating through a 3-D geodynamic model, we evaluated limits and capabilities of combining geodynamic and seismological techniques in recovering the main isotropic structures, such as slabs and mid-ocean ridge, and radial anisotropy. We tested the effect of using ideal or more realistic station coverage showing that this (i.e. the ray density) influences the tomographic result. In particular, the first order effect of using a poor ray density is the distortion of both the isotropic and anisotropic features that leads to wrong interpretation of upper mantle structure and dynamics. Lastly, showing different tomographic images obtained from tests with different damping and smoothing factors, we observed that the regularization parameters substantially change the tomography, producing V_S and radial anisotropy models that are consistent with those predicted by the half space cooling model, thus characterize by age-dependent thickening of the lithosphere, or predicted by the plate cooling model, characterized by flat and age-independent lithospheric structures.

The variability of the solutions that we have observed in the various chapters of this Thesis, which involved the use of different seismic imaging techniques performed in different conditions and with different types of datasets, shows us how difficult it is to constrain the results of a seismic tomography and therefore produce an unequivocally correct result. Therefore, the interpretation of the tomographic images should always take into account various factors, such as the type of data and seismic phase used which will directly influence the resolution and the sensitivity of the tomography (e.g., local or teleseismic events? P-, S- or surface-waves? Delay times or full waveforms?), the type of approximations and assumptions imposed to simplify the numerical problem (e.g., isotropy assumption?), the regularization to solve the ill-posed problem (i.e. the choice of damping and smoothing factors), the coverage of the seismic rays, the data error, the inversion method, etc. However, seismic tomography turns out to be the most powerful tool to investigate the

Earth's interior but in order to guarantee its correct realization it is necessary that the scientific community (i) considers seismic anisotropy in the inversion processes, (ii) guarantee a good and homogeneous distribution of receivers that does not only include land and finally (iii) improves the quality of the data by performing even more precise picking.

Future perspectives

Considering the success of the anisotropic seismic tomography of the Central Mediterranean presented in Chapter 4 using ISC-EHB bulletin delays, we expect better quality anisotropic models could be obtained using a rigorously quality controlled dataset of multi-frequency delay time measurements. Furthermore, the same methodology can be applied to generate an anisotropic model of the entire Mediterranean and European region in order to get a more complete view of the underlying and complex upper mantle dynamics.

To improve synthetic tests, such those performed in Chapter 5,6 and 7, and to make them more realistic, thus representative of real geological scenarios, we think that future studies should involve improved geodynamic models that account for compositional variations, presence of fluids/melt and lithospheric fossil fabrics that affect the seismic properties of natural tectonic settings.

Further developments of the study involving the partitioned inversion of S- and surface-waves addressed in Chapter 7 could be applied to a Pacific-like geodynamic context and include not only radial but also azimuthal anisotropy among the inversion parameters.

Considering that most of both real and synthetic tomographic models discussed in this Thesis or present in the literature are obtained inverting regional or teleseismic first P- and S-wave travel times (or delay times), we envisage that further research should involve the simultaneous use of later

seismic phases, i.e. not only P- or S-wave first data but also those generated by the sharp discontinuities present in the Earth's interior. Due to their intrinsic characteristic and their origin linked to the presence of these deep discontinuities, the later phases illuminate areas not illuminated by the first P and S data, thus leading to new findings on upper and lower mantle structure and dynamics.

Given the well known utility of P-waves and that of S-waves demonstrated with our synthetic tests (e.g., in Chapter 6) in constraining realistic upper mantle anisotropy, possible future improvements could aim at jointly invert P- and S-waves datasets. The use of both P and S phases together with an improved ray coverage obtained including teleseismic and local arrivals will allow for a new and more precise parametrisation of the model.

Finally, next studies will extend the current hexagonal symmetry (i.e. with 2 distinct anisotropy axes, 5 independent elastic coefficients) to orthorhombic (i.e. with 3 distinct anisotropy axes, 9 independent elastic coefficients) in order to ensure a more realistic simulation of the elastic response of the upper mantle and to better constrain the recent 3-D deformational history.

Bibliography

Aki, K. (1980). Quantitative seismology. *Theory and methods*, *1*, 557.

Aki, K., Christoffersson, A., & Husebye, E. S. (1977). Determination of the three-dimensional seismic structure of the lithosphere. *Journal of Geophysical Research*, *82*(2), 277–296.

Amato, A., Alessandrini, B., Cimini, G., Frepoli, A., & Selvaggi, G. (1993). Active and remnant subducted slabs beneath italy: Evidence from seismic tomography and seismicity. *Annals of Geophysics*, *36*(2).

Anderson, D. L. (1961a). Elastic wave propagation in layered anisotropic media. *Journal of Geophysical Research*, *66*(9), 2953–2963.

Anderson, D. L. (1965). Recent evidence concerning the structure and composition of the earth's mantle. *Physics and Chemistry of the Earth*, *6*, 1–131.

Anderson, D. L. (1989). *Theory of the earth*. Blackwell scientific publications.

Anderson, J. (1961b). Magnetic anisotropy in single-crystal nickel films. *Proceedings of the Physical Society (1958-1967)*, *78*(1), 25.

Anderson, O. L., Schreiber, E., Liebermann, R. C., & Soga, N. (1988). Some elastic constant data on minerals relevant to geophysics. *Elastic Properties and Equations of State*, *26*, 237–270.

Antolik, M., Gu, Y. J., Ekström, G., & Dziewonski, A. M. (2003). J362d28: A new joint model of compressional and shear velocity in the earth's mantle. *Geophysical Journal International*, *153*(2), 443–466.

Arab, M., Maherssi, C. E., Granjeon, D., Roure, F., Déverchère, J., Cuilhé, L., Hassaim, M., Mouchot, N., Doublet, S., & Khomsi, S. (2020). On the origin and consequences of crustal-scale extension between africa and sicily since late miocene: Insights from the kaboudia area, western pelagian sea. *Tectonophysics*, *795*, 228565.

Asamori, K., & Zhao, D. (2015). Teleseismic shear wave tomography of the japan subduction zone. *Geophysical Supplements to the Monthly Notices of the Royal Astronomical Society*, *203*(3), 1752–1772.

Aster, R. C., Borchers, B., & Thurber, C. H. (2018). *Parameter estimation and inverse problems*. Elsevier.

Auer, L., Boschi, L., Becker, T., Nissen-Meyer, T, & Giardini, D. (2014). Savani: A variable resolution whole-mantle model of anisotropic shear velocity variations based on multiple data sets. *Journal of Geophysical Research: Solid Earth*, *119*(4), 3006–3034.

Backus, G. E. (1965). Possible forms of seismic anisotropy of the uppermost mantle under oceans. *Journal of Geophysical Research*, *70*(14), 3429–3439.

Bai, Q., Mackwell, S., & Kohlstedt, D. (1991). High-temperature creep of olivine single crystals 1. mechanical results for buffered samples. *Journal of Geophysical Research: Solid Earth*, *96*(B2), 2441–2463.

Balling, P., Grützner, C., Tomljenović, B., Spakman, W., & Ustaszewski, K. (2021). Post-collisional mantle delamination in the dinarides implied from staircases of oligo-miocene uplifted marine terraces. *Scientific reports*, *11*(1), 1–11.

Barruol, G., Bonnin, M., Pedersen, H., Bokelmann, G. H., & Tiberi, C. (2011). Belt-parallel mantle flow beneath a halted continental collision: The western alps. *Earth and Planetary Science Letters*, *302*(3-4), 429–438.

Bauville, A., & Baumann, T. S. (2019). Geomio: An open-source matlab toolbox to create the initial configuration of 2-d/3-d thermo-mechanical simulations from 2-d vector drawings. *Geochemistry, Geophysics, Geosystems*, *20*(3), 1665–1675.

Becker, T. W., Lebedev, S, & Long, M. (2012). On the relationship between azimuthal anisotropy from shear wave splitting and surface wave tomography. *Journal of Geophysical Research: Solid Earth*, *117*(B1).

Becker, T. W. (2006). On the effect of temperature and strain-rate dependent viscosity on global mantle flow, net rotation, and plate-driving forces. *Geophysical Journal International*, *167*(2), 943–957.

Becker, T. W., & Boschi, L. (2002). A comparison of tomographic and geodynamic mantle models. *Geochemistry, Geophysics, Geosystems*, *3*(1).

Becker, T. W., Chevrot, S., Schulte-Pelkum, V., & Blackman, D. K. (2006a). Statistical properties of seismic anisotropy predicted by upper mantle geodynamic models. *Journal of Geophysical Research: Solid Earth*, *111*(B8).

Becker, T. W., Schulte-Pelkum, V., Blackman, D. K., Kellogg, J. B., & O'Connell, R. J. (2006b). Mantle flow under the western united states from shear wave splitting. *Earth and Planetary Science Letters*, *247*(3-4), 235–251.

Beghein, C., Yuan, K., Schmerr, N., & Xing, Z. (2014). Changes in seismic anisotropy shed light on the nature of the gutenberg discontinuity. *Science*, *343*, 1237—1240.

Beghein, C., & Trampert, J. (2004). Probability density functions for radial anisotropy from fundamental mode surface wave data and the neighbourhood algorithm. *Geophysical Journal International*, *157*(3), 1163–1174.

Beghein, C., Xing, Z., & Goes, S. (2019). Thermal nature and resolution of the lithosphere – asthenosphere boundary under the pacific from surface waves. *Geophysical Journal International*, *216*, 1441–1465.

Beller, S., & Chevrot, S. (2020). Probing depth and lateral variations of upper-mantle seismic anisotropy from full-waveform inversion of teleseismic body-waves. *Geophysical Journal International*, *222*(1), 352–387.

Bellman, R. (1958). On a routing problem. *Quarterly of applied mathematics*, *16*(1), 87–90.

Berenger, J.-P. (1994). A perfectly matched layer for the absorption of electromagnetic waves. *Journal of computational physics*, *114*(2), 185–200.

Bezada, M., Faccenda, M, & Toomey, D. (2016). Representing anisotropic subduction zones with isotropic velocity models: A characterization of the problem and some steps on a possible path forward. *Geochemistry, Geophysics, Geosystems*, *17*(8), 3164–3189.

Bezada, M., Humphreys, E., Toomey, D., Harnafi, M, Dávila, J., & Gallart, J. (2013). Evidence for slab rollback in westernmost mediterranean from improved upper mantle imaging. *Earth Planet. Sci. Lett*, *368*, 51–60.

Bijwaard, H., & Spakman, W. (1999). Tomographic evidence for a narrow whole mantle plume below iceland. *Earth and Planetary Science Letters*, *166*(3-4), 121–126.

Bijwaard, H., & Spakman, W. (2000). Non-linear global p-wave tomography by iterated linearized inversion. *Geophysical Journal International*, *141*(1), 71–82.

Bijwaard, H., Spakman, W., & Engdahl, E. R. (1998). Closing the gap between regional and global travel time tomography. *Journal of Geophysical Research: Solid Earth*, *103*(B12), 30055–30078.

Blackman, D. (2007). Use of mineral physics, with geodynamic modelling and seismology, to investigate flow in the earth's mantle. *Reports on Progress in Physics*, *70*(5), 659.

Blackman, D. K., & Kendall, J.-M. (1997). Sensitivity of teleseismic body waves to mineral texture and melt in the mantle beneath a mid–ocean ridge. *Philosophical Transactions of the Royal Society of London. Series A: Mathematical, Physical and Engineering Sciences*, *355*(1723), 217–231.

Blackman, D. K., & Kendall, J.-M. (2002). Seismic anisotropy in the upper mantle 2. predictions for current plate boundary flow models. *Geochemistry, Geophysics, Geosystems*, *3*(9), 1–of.

Blackman, D. K., Kendall, J.-M., Dawson, P. R., Wenk, H.-R., Boyce, D., & Morgan, J. P. (1996). Teleseismic imaging of subaxial flow at mid-ocean ridges: Traveltime effects of anisotropic mineral texture in the mantle. *Geophysical Journal International*, *127*(2), 415–426.

Bodmer, M., Toomey, D. R., Hooft, E. E., & Schmandt, B. (2018). Buoyant asthenosphere beneath cascadia influences megathrust segmentation. *Geophysical Research Letters*, *45*(14), 6954–6962.

Bodmer, M., Toomey, D. R., VanderBeek, B., Hooft, E., & Byrnes, J. S. (2020). Body wave tomography of the cascadia subduction zone and juan de fuca plate system: Identifying challenges and solutions for shore-crossing data. *Geochemistry, Geophysics, Geosystems*, *21*(12), e2020GC009316.

Bokelmann, G., Qorbani, E., & Bianchi, I. (2013). Seismic anisotropy and large-scale deformation of the eastern alps. *Earth and Planetary Science Letters*, *383*, 1–6.

Boneh, Y., Morales, L. F., Kaminski, E., & Skemer, P. (2015). Modeling olivine cpo evolution with complex deformation histories: Implications for the interpretation of seismic anisotropy in the mantle. *Geochemistry, Geophysics, Geosystems*, *16*(10), 3436–3455.

Boschi, L., & Dziewonski, A. M. (1999). High-and low-resolution images of the earth's mantle: Implications of different approaches to tomographic modeling. *Journal of Geophysical Research: Solid Earth*, *104*(B11), 25567–25594.

Boschi, L., & Dziewonski, A. M. (2000). Whole earth tomography from delay times of p, pcp, and pkp phases: Lateral heterogeneities in the outer core or radial anisotropy in the mantle? *Journal of Geophysical Research: Solid Earth*, *105*(B6), 13675–13696.

Bozdağ, E., Peter, D., Lefebvre, M., Komatitsch, D., Tromp, J., Hill, J., Podhorszki, N., & Pugmire, D. (2016). Global adjoint tomography: First-generation model. *Geophysical Journal International*, *207*(3), 1739–1766.

Brownlee, S. J., Schulte-Pelkum, V., Raju, A., Mahan, K., Condit, C., & Orlandini, O. F. (2017). Characteristics of deep crustal seismic anisotropy from a compilation of rock elasticity tensors and their expression in receiver functions. *Tectonics*, *36*(9), 1835–1857.

Brun, J.-P., Faccenna, C., Gueydan, F., Sokoutis, D., Philippon, M., Kydonakis, K., & Gorini, C. (2016). The two-stage aegean extension, from localized to distributed, a result of slab rollback acceleration. *Canadian journal of earth sciences*, *53*(11), 1142–1157.

Buland, R., & Chapman, C. (1983). The computation of seismic travel times. *Bulletin of the Seismological Society of America*, *73*(5), 1271–1302.

Bunge, H.-P., Hagelberg, C., & Travis, B. (2003). Mantle circulation models with variational data assimilation: Inferring past mantle flow and structure from plate motion histories and seismic tomography. *Geophysical Journal International*, *152*(2), 280–301.

Burgos, G., Montagner, J.-P., Capdeville, Y., Mocquet, A., & Drilleau, M. (2014). Oceanic lithosphere–asthenosphere boundary from surface wave dispersion data. *Journal of Geophysical Research: Solid Earth*, *119(2)*, 1079–1093.

Byrnes, J. S., Toomey, D. R., Hooft, E. E., Nábělek, J., & Braunmiller, J. (2017). Mantle dynamics beneath the discrete and diffuse plate boundaries of the j uan de f uca plate: Results from c ascadia i nitiative body wave tomography. *Geochemistry, Geophysics, Geosystems*, *18*(8), 2906–2929.

Calcagnile, G, & Panza, G. (1980). The main characteristics of the lithosphere-asthenosphere system in italy and surrounding regions. *Pure and Applied Geophysics*, *119*(4), 865–879.

Calò, M, Bodin, T., & Romanowicz, B. (2016). Layered structure in the upper mantle across north america from joint inversion of long and short period seismic data. *Earth and Planetary Science Letters*, *449*, 164–175.

Calò, M, Dorbath, C., Luzio, D, Rotolo, S. G., & D'anna, G. (2012). Seismic velocity structures of southern italy from tomographic imaging of the ionian slab and petrological inferences. *Geophysical Journal International*, *191*(2), 751–764.

Calò, M., Parisi, L., & Luzio, D. (2013). Lithospheric p-and s-wave velocity models of the sicilian area using wam tomography: Procedure and assessments. *Geophysical Journal International*, *195*(1), 625–649.

Cara, M, & Lévêque, J. (1987). Waveform inversion using secondary observables. *Geophysical Research Letters*, *14*(10), 1046–1049.

Carminati, E, Wortel, M., Spakman, W, & Sabadini, R. (1998). The role of slab detachment processes in the opening of the western–central mediterranean basins: Some geological and geophysical evidence. *Earth and Planetary Science Letters*, *160*(3-4), 651–665.

Carminati, E., Lustrino, M., & Doglioni, C. (2012). Geodynamic evolution of the central and western mediterranean: Tectonics vs. igneous petrology constraints. *Tectonophysics*, *579*, 173–192.

Carter, N. L., & Ave'Lallemant, H. G. (1970). High temperature flow of dunite and peridotite. *Geological Society of America Bulletin*, *81*(8), 2181–2202.

Chang, S.-J., & Ferreira, A. M. (2017). Improving global radial anisotropy tomography: The importance of simultaneously inverting for crustal and mantle structure. *Bulletin of the Seismological Society of America*, *107*(2), 624–638.

Chang, S.-J., & Ferreira, A. M. (2019). Inference on water content in the mantle transition zone near subducted slabs from anisotropy tomography. *Geochemistry, Geophysics, Geosystems*, *20*(2), 1189–1201.

Chang, S.-J., Ferreira, A. M., & Faccenda, M. (2016). Upper-and mid-mantle interaction between the samoan plume and the tonga–kermadec slabs. *Nature communications*, *7*(1), 1–9.

Chang, S.-J., Ferreira, A. M., Ritsema, J., van Heijst, H. J., & Woodhouse, J. H. (2014). Global radially anisotropic mantle structure from multiple datasets: A review, current challenges, and outlook. *Tectonophysics*, *617*, 1–19.

Chang, S.-J., Ferreira, A. M., Ritsema, J., van Heijst, H. J., & Woodhouse, J. H. (2015). Joint inversion for global isotropic and radially anisotropic mantle structure including crustal thickness perturbations. *Journal of Geophysical Research: Solid Earth*, *120*(6), 4278–4300.

Chen, M., & Tromp, J. (2007). Theoretical and numerical investigations of global and regional seismic wave propagation in weakly anisotropic earth models. *Geophysical Journal International*, *168*(3), 1130–1152.

Chertova, M., Spakman, W, Geenen, T, Van Den Berg, A., & Van Hinsbergen, D. (2014). Underpinning tectonic reconstructions of the western mediterranean region with dynamic slab evolution from 3-d numerical modeling. *Journal of Geophysical Research: Solid Earth*, *119*(7), 5876–5902.

Chevrot, S. (2000). Multichannel analysis of shear wave splitting. *Journal of Geophysical Research: Solid Earth*, *105*(B9), 21579–21590.

Chevrot, S. (2006). Finite-frequency vectorial tomography: A new method for high-resolution imaging of upper mantle anisotropy. *Geophysical Journal International*, *165*(2), 641–657.

Chevrot, S., Favier, N., & Komatitsch, D. (2004). Shear wave splitting in three-dimensional anisotropic media. *Geophysical Journal International*, *159*(2), 711–720.

Chevrot, S., & Van Der Hilst, R. D. (2003). On the effects of a dipping axis of symmetry on shear wave splitting measurements in a transversely isotropic medium. *Geophysical Journal International*, *152*(2), 497–505.

Christensen, D. H., & Abers, G. A. (2010). Seismic anisotropy under central alaska from sks splitting observations. *Journal of Geophysical Research: Solid Earth*, *115*(B4).

Civello, S., & Margheriti, L. (2004). Toroidal mantle flow around the calabrian slab (italy) from sks splitting. *Geophysical Research Letters*, *31*(10).

Coates, R., & Chapman, C. (1990). Quasi-shear wave coupling in weakly anisotropic 3-d media. *Geophysical Journal International*, *103*(2), 301–320.

Confal, J. M., Faccenda, M., Eken, T., & Taymaz, T. (2018). Numerical simulation of 3-d mantle flow evolution in subduction zone environments in relation to seismic anisotropy beneath the eastern mediterranean region. *Earth and Planetary Science Letters*, *497*, 50–61.

Connolly, J. A. (2005). Computation of phase equilibria by linear programming: A tool for geodynamic modeling and its application to subduction zone decarbonation. *Earth and Planetary Science Letters*, *236*(1-2), 524–541.

Crameri, F. (2018a). Geodynamic diagnostics, scientific visualisation and staglab 3.0. *Geoscientific Model Development*, *11*(6), 2541–2562.

Crameri, F. (2018b). Scientific colour-maps. *Zenodo. doi*, *10*.

Crampin, S. (1984). Effective anisotropic elastic constants for wave propagation through cracked solids. *Geophysical Journal International*, *76*(1), 135–145.

Crotwell, H. P., Owens, T. J., & Ritsema, J. (1999). The taup toolkit: Flexible seismic travel-time and ray-path utilities. *Seismological Research Letters*, *70*(2), 154–160.

Currie, C. A., Cassidy, J. F., Hyndman, R. D., & Bostock, M. G. (2004). Shear wave anisotropy beneath the cascadia subduction zone and western north american craton. *Geophysical Journal International*, *157*(1), 341–353.

Dahlen, F., & Tromp, J. (2021). *Theoretical global seismology*. Princeton university press.

Dalton, C. A., & Ekström, G. (2006). Global models of surface wave attenuation. *Journal of Geophysical Research: Solid Earth*, *111*(B5).

Debayle, E, Dubuffet, F., & Durand, S. (2016). An automatically updated s-wave model of the upper mantle and the depth extent of azimuthal anisotropy. *Geophysical Research Letters*, *43*, 674—682.

Debayle, E., & Ricard, Y. (2012). A global shear velocity model of the upper mantle from fundamental and higher rayleigh mode measurements. *Journal of Geophysical Research: Solid Earth*, *117*(B10).

Dewey, J., Helman, M., Knott, S., Turco, E, & Hutton, D. (1989). Kinematics of the western mediterranean. *Geological Society, London, Special Publications*, *45*(1), 265–283.

Díaz, J, Gil, A., & Gallart, J. (2013). Uppermost mantle seismic velocity and anisotropy in the euro-mediterranean region from pn and sn tomography. *Geophysical Journal International*, *192*(1), 310–325.

Dijkstra, E. W. et al. (1959). A note on two problems in connexion with graphs. *Numerische mathematik*, *1*(1), 269–271.

Durham, W., & Goetze, C. (1977). Plastic flow of oriented single crystals of olivine: 1. mechanical data. *Journal of geophysical Research*, *82*(36), 5737–5753.

Dziewonski, A. M., & Anderson, D. L. (1981). Preliminary reference earth model. *Physics of the earth and planetary interiors*, *25*(4), 297–356.

Dziewonski, A. M., Hager, B. H., & O'Connell, R. J. (1977). Large-scale heterogeneities in the lower mantle. *Journal of Geophysical Research*, *82*(2), 239–255.

Eberhart-Phillips, D., & Mark Henderson, C. (2004). Including anisotropy in 3-d velocity inversion and application to marlborough, new zealand. *Geophysical journal international*, *156*(2), 237–254.

El-Sharkawy, A., Meier, T., Lebedev, S., Behrmann, J. H., Hamada, M., Cristiano, L., Weidle, C., & Köhn, D. (2020). The slab puzzle of the alpine-mediterranean region: Insights from a new, high-resolution, shear wave velocity model of the upper mantle. *Geochemistry, Geophysics, Geosystems*, *21*(8), e2020GC008993.

Emry, E. L., Shen, Y., Nyblade, A. A., Flinders, A., & Bao, X. (2019). Upper mantle earth structure in africa from full-wave ambient noise tomography. *Geochemistry, Geophysics, Geosystems*, *20*(1), 120–147.

Escher, A., & Beaumont, C. (1997). Formation, burial and exhumation of basement nappes at crustal scale: A geometric model based on the western swiss-italian alps. *Journal of structural Geology*, *19*(7), 955–974.

Estève, C, Audet, P, Schaeffer, A., Schutt, D, Aster, R., & Cubley, J. (2020). The upper mantle structure of northwestern canada from teleseismic body wave tomography. *Journal of Geophysical Research: Solid Earth*, *125*(2), e2019JB018837.

Evans, B, & Goetze, C. (1979). The temperature variation of hardness of olivine and its implication for polycrystalline yield stress. *Journal Geophysical Research*, *84*, 5505–5524.

Faccenda, M, Minelli, G, & Gerya, T. (2009). Coupled and decoupled regimes of continental collision: Numerical modeling. *Earth and Planetary Science Letters*, *278*(3-4), 337–349.

Faccenda, M. (2014). Mid mantle seismic anisotropy around subduction zones. *Physics of the Earth and Planetary Interiors*, *227*, 1–19.

Faccenda, M., & Capitanio, F. A. (2012). Development of mantle seismic anisotropy during subduction-induced 3-d flow. *Geophysical Research Letters*, *39*(11).

Faccenda, M., & Capitanio, F. A. (2013). Seismic anisotropy around subduction zones: Insights from three-dimensional modeling of upper mantle deformation and sks splitting calculations. *Geochemistry, Geophysics, Geosystems*, *14*(1), 243–262.

Faccenda, M., Ferreira, A. M., Tisato, N., Lithgow-Bertelloni, C., Stixrude, L., & Pennacchioni, G. (2019). Extrinsic elastic anisotropy in a compositionally heterogeneous earth's mantle. *Journal of Geophysical Research: Solid Earth*, *124*(2), 1671–1687.

Faccenda, M., Gerya, T. V., & Chakraborty, S. (2008). Styles of post-subduction collisional orogeny: Influence of convergence velocity, crustal rheology and radiogenic heat production. *Lithos*, *103*(1-2), 257–287.

Faccenna, C., & Becker, T. W. (2010). Shaping mobile belts by small-scale convection. *Nature*, *465*(7298), 602–605.

Faccenna, C., Becker, T. W., Auer, L., Billi, A., Boschi, L., Brun, J. P., Capitanio, F. A., Funiciello, F., Horvàth, F., Jolivet, L., et al. (2014). Mantle dynamics in the mediterranean. *Reviews of Geophysics*, *52*(3), 283–332.

Faccenna, C., Becker, T. W., Lallemand, S., Lagabrielle, Y., Funiciello, F., & Piromallo, C. (2010). Subduction-triggered magmatic pulses: A new class of plumes? *Earth and Planetary Science Letters*, *299*(1-2), 54–68.

Faccenna, C., Funiciello, F., Civetta, L., D Antonio, M., Moroni, M., & Piromallo, C. (2007). Slab disruption, mantle circulation, and the opening of the tyrrhenian basins. *Special Papers-Geological Society of America*, *418*, 153.

Faccenna, C., Funiciello, F., Giardini, D., & Lucente, P. (2001). Episodic back-arc extension during restricted mantle convection in the central mediterranean. *Earth and Planetary Science Letters*, *187*(1-2), 105–116.

Faccenna, C., Piromallo, C., Crespo-Blanc, A., Jolivet, L., & Rossetti, F. (2004). Lateral slab deformation and the origin of the western mediterranean arcs. *Tectonics*, *23*(1).

Ferreira, A. M., Faccenda, M., Sturgeon, W., Chang, S.-J., & Schardong, L. (2019). Ubiquitous lower-mantle anisotropy beneath subduction zones. *Nature Geoscience*, *12*(4), 301–306.

Fisher, N. I. (1995). *Statistical analysis of circular data*. cambridge university press.

Flinn, E. (1965). Signal analysis using rectilinearity and direction of particle motion. *Proceedings of the IEEE*, *53*(12), 1874–1876.

Forsyth, D. W., Webb, S. C., Dorman, L. M., & Shen, Y. (1998). Phase velocities of rayleigh waves in the melt experiment on the east pacific rise. *Science*, *280*(5367), 1235–1238.

Fox, M., Herman, F., Willett, S. D., & Schmid, S. M. (2016). The exhumation history of the european alps inferred from linear inversion of thermochronometric data. *American Journal of Science*, *316*(6), 505–541.

French, S., Lekic, V., & Romanowicz, B. (2013). Waveform tomography reveals channeled flow at the base of the oceanic asthenosphere. *Science*, *342*(6155), 227–230.

Fuchs, K. (1997). *Upper mantle heterogeneities from active and passive seismology* (Vol. 17). Springer Science & Business Media.

Fukao, Y., To, A., & Obayashi, M. (2003). Whole mantle p wave tomography using p and pp-p data. *Journal of Geophysical Research: Solid Earth*, *108*(B1), ESE–8.

Geiss, E. A new compilation of crustal thickness data for the mediterranean area. In: *Annales geophysicae. series b. terrestrial and planetary physics*. *5*. (6). 1987, 623–630.

Gerya, T. (2019). *Introduction to numerical geodynamic modelling*. Cambridge University Press.

Gerya, T. V., & Yuen, D. A. (2003). Characteristics-based marker-in-cell method with conservative finite-differences schemes for modeling geological flows with strongly variable transport properties. *Physics of the Earth and Planetary Interiors*, *140*(4), 293–318.

Giacomuzzi, G, Chiarabba, C, & De Gori, P. (2011). Linking the alps and apennines subduction systems: New constraints revealed by high-resolution teleseismic tomography. *Earth and Planetary Science Letters*, *301*(3-4), 531–543.

Giacomuzzi, G, Civalleri, M, De Gori, P, & Chiarabba, C. (2012). A 3d vs model of the upper mantle beneath italy: Insight on the geodynamics of central mediterranean. *Earth and Planetary Science Letters*, *335*, 105–120.

Goes, S, Govers, R, Vacher, & P. (2000). Shallow mantle temperatures under europe from p and s wave tomography. *Journal of Geophysical Research: Solid Earth*, *105*(B5), 11153–11169.

Goes, S., & van der Lee, S. (2002). Thermal structure of the north american uppermost mantle inferred from seismic tomography. *Journal of Geophysical Research: Solid Earth*, *107*(B3), ETG–2.

Goforth, T., & Harrin, E. (1979). Phase-matched filters: Application to the study of Love waves. *Bulletin of the Seismological Society of America*, *69*(1), 27–44. https://doi.org/10.1785/BSSA0690010027

Granet, M, Stoll, G, Dorel, J, Achauer, U, Poupinet, G, & Fuchs, K. (1995a). Massif central (france): New constraints on the geodynamical evolution from teleseismic tomography. *Geophysical Journal International*, *121*(1), 33–48.

Granet, M., Wilson, M., & Achauer, U. (1995b). Imaging a mantle plume beneath the french massif central. *Earth and Planetary Science Letters*, *136*(3-4), 281–296.

Grésillaud, A, & Cara, M. (1996). Anisotropy and p-wave tomography: A new approach for inverting teleseismic data from a dense array of stations. *Geophysical Journal International*, *126*(1), 77–91.

Gueguen, E., Doglioni, C., & Fernandez, M. (1998). On the post-25 ma geodynamic evolution of the western mediterranean. *Tectonophysics*, *298*(1-3), 259–269.

Gutscher, M.-A., Malod, J, Rehault, J.-P., Contrucci, I, Klingelhoefer, F, Mendes-Victor, L, & Spakman, W. (2002). Evidence for active subduction beneath gibraltar. *Geology*, *30*(12), 1071–1074.

Hammond, W. C., & Toomey, D. R. (2003). Seismic velocity anisotropy and heterogeneity beneath the mantle electromagnetic and tomography experiment (melt) region of the east pacific rise from analysis of p and s body waves. *Journal of Geophysical Research: Solid Earth*, *108*(B4).

Hansen, L., Qi, C., & Warren, J. (2016a). Olivine anisotropy suggests gutenberg discontinuity is not the base of the lithosphere. *Proceedings of the National Academy of Science*, *113*(38), 10503–10506.

Hansen, L. N., Warren, J. M., Zimmerman, M. E., & Kohlstedt, D. L. (2016b). Viscous anisotropy of textured olivine aggregates, part 1: Measurement of the magnitude and evolution of anisotropy. *Earth and Planetary Science Letters*, *445*, 92–103.

Hansen, L. N., Zhao, Y.-H., Zimmerman, M. E., & Kohlstedt, D. L. (2014). Protracted fabric evolution in olivine: Implications for the relationship among strain, crystallographic fabric, and seismic anisotropy. *Earth and Planetary Science Letters*, *387*, 157–168.

Hanson, D. R., & Spetzler, H. A. (1994). Transient creep in natural and synthetic, iron-bearing olivine single crystals: Mechanical results and dislocation microstructures. *Tectonophysics*, *235*(4), 293–315.

Harrin, E., & Goforth, T. (1977). Phase-matched filters: Application to the study of Rayleigh waves. *Bulletin of the Seismological Society of America*, *67*(5), 1259–1275. https://doi.org/10.1785/BSSA0670051259

Hawley, W. B., Allen, R. M., & Richards, M. A. (2016). Tomography reveals buoyant asthenosphere accumulating beneath the juan de fuca plate. *Science*, *353*(6306), 1406–1408.

Hedjazian, N., Garel, F., Rhodri Davies, D., & Kaminski, E. (2017). Age-independent seismic anisotropy under oceanic plates explained by strain history in the asthenosphere. *Earth and Planetary Science Letters*, *460*, 135–142.

Hess, H. (1964). Seismic anisotropy of the uppermost mantle under oceans. *Nature*, *203*(4945), 629–631.

Hicks, S. P., Nippress, S. E., & Rietbrock, A. (2012). Sub-slab mantle anisotropy beneath south-central chile. *Earth and Planetary Science Letters*, *357*, 203–213.

Holt, A. F., Royden, L. H., Becker, T. W., & Faccenna, C. (2018). Slab interactions in 3-d subduction settings: The philippine sea plate region. *Earth and Planetary Science Letters*, *489*, 72–83.

Holt, A., Royden, L., & Becker, T. (2017). The dynamics of double slab subduction. *Geophysical Journal International*, *209*(1), 250–265.

Holtzman, B. K., Kohlstedt, D. L., Zimmerman, M. E., Heildelbach, F., Hiraga, T., & Hustoft, J. (2003). Olivine anisotropy suggests gutenberg discontinuity is not the base of the lithosphere. *Science*, *301*, 1227–1230.

Hu, J., Faccenda, M., & Liu, L. (2017). Subduction-controlled mantle flow and seismic anisotropy in south america. *Earth and Planetary Science Letters*, *470*, 13–24.

Hua, Y., Zhao, D., & Xu, Y. (2017). P wave anisotropic tomography of the alps. *Journal of Geophysical Research: Solid Earth*, *122*(6), 4509–4528.

Huang, Z., Zhao, D., & Wang, L. (2011a). Frequency-dependent shear-wave splitting and multilayer anisotropy in northeast japan. *Geophysical Research Letters*, *38*(8).

Huang, Z., Zhao, D., & Wang, L. (2011b). Shear wave anisotropy in the crust, mantle wedge, and subducting pacific slab under northeast japan. *Geochemistry, Geophysics, Geosystems*, *12*(1).

Ismaıl, W. B., & Mainprice, D. (1998). An olivine fabric database: An overview of upper mantle fabrics and seismic anisotropy. *Tectonophysics*, *296*(1-2), 145–157.

Isse, T., Kawakatsu, H., Yoshizawa, K., Takeo, A., Shiobara, H., Sugioka, H., Ito, A., Suetsugu, D., & Reymond, D. (2019). Surface wave tomography for the pacific ocean incorporating seafloor seismic observations and plate thermal evolution. *Earth and Planetary Science Letters*, *510*, 116–130.

Jagoutz, O., Royden, L., Holt, A. F., & Becker, T. W. (2015). Anomalously fast convergence of india and eurasia caused by double subduction. *Nature Geoscience*, *8*(6), 475–478.

Jin, Z., Bai, Q., & Kohlstedt, D. (1994). High-temperature creep of olivine crystals from four localities. *Physics of the Earth and Planetary Interiors*, *82*(1), 55–64.

Jolivet, L., Augier, R., Faccenna, C., Negro, F., Rimmele, G., Agard, P., Robin, C., Rossetti, F., & Crespo-Blanc, A. (2008). Subduction, convergence and the mode of backarc extension in the mediterranean region. *Bulletin de la Société Géologique de France*, *179*(6), 525–550.

Jolivet, L., Augier, R., Robin, C., Suc, J.-P., & Rouchy, J. M. (2006). Lithospheric-scale geodynamic context of the messinian salinity crisis. *Sedimentary geology*, *188*, 9–33.

Jolivet, L., Faccenna, C., & Piromallo, C. (2009). From mantle to crust: Stretching the mediterranean. *Earth and Planetary Science Letters*, *285*(1-2), 198–209.

Kaminski, E. (2006). Interpretation of seismic anisotropy in terms of mantle flow when melt is present. *Geophysical Research Letters*, *33(2)*, L02304.

Kaminski, E, & Ribe, N. (2001). A kinematic model for recrystallization and texture development in olivine polycrystals. *Earth and Planetary Science Letters*, *189*(3-4), 253–267.

Kaminski, E., & Ribe, N. M. (2002). Timescales for the evolution of seismic anisotropy in mantle flow. *Geochemistry, Geophysics, Geosystems*, *3*(8), 1–17.

Kaminski, E., Ribe, N. M., & Browaeys, J. T. (2004). D-rex, a program for calculation of seismic anisotropy due to crystal lattice preferred orientation in the convective upper mantle. *Geophysical Journal International*, *158*(2), 744–752.

Kárason, H., & van der Hilst, R. D. (2001). Tomographic imaging of the lowermost mantle with differential times of refracted and diffracted core phases (pkp, pdiff). *Journal of Geophysical Research: Solid Earth*, *106*(B4), 6569–6587.

Karato, S.-i. (2008). Deformation of earth materials. *An Introduction to the Rheology of Solid Earth*, *463*.

Karato, S.-i., Jung, H., Katayama, I., & Skemer, P. (2008). Geodynamic significance of seismic anisotropy of the upper mantle: New insights from laboratory studies. *Annu. Rev. Earth Planet. Sci.*, *36*, 59–95.

Karato, S.-i., & Wu, P. (1993). Rheology of the upper mantle: A synthesis. *Science*, *260*(5109), 771–778.

Kästle, E. D., El-Sharkawy, A, Boschi, L, Meier, T, Rosenberg, C, Bellahsen, N, Cristiano, L, & Weidle, C. (2018). Surface wave tomography of the alps using ambient-noise and earthquake phase velocity measurements. *Journal of Geophysical Research: Solid Earth*, *123*(2), 1770–1792.

Kästle, E. D., Molinari, I., Boschi, L., Kissling, E., & Group, A. W. (2022). Azimuthal anisotropy from eikonal tomography: Example from ambient-noise measurements in the alparray network. *Geophysical Journal International*, *229*(1), 151–170.

Kästle, E. D., Rosenberg, C., Boschi, L., Bellahsen, N., Meier, T., & El-Sharkawy, A. (2019). Slab break-offs in the alpine subduction zone. *Solid Earth Discussions*, 1–19.

Kästle, E. D., Rosenberg, C., Boschi, L., Bellahsen, N., Meier, T., & El-Sharkawy, A. (2020). Slab break-offs in the alpine subduction zone. *International Journal of Earth Sciences*, *109*(2), 587–603.

Katayama, I., & Karato, S.-i. (2008). Low-temperature, high-stress deformation of olivine under water-saturated conditions. *Physics of the Earth and Planetary Interiors*, *168*, 125–133.

Kawakatsu, H., & Yoshioka, S. (2011). Metastable olivine wedge and deep dry cold slab beneath southwest japan. *Earth and Planetary Science Letters*, *303*(1-2), 1–10.

Kendall, E., Ferreira, A. M., Chang, S.-J., Witek, M, & Peter, D. (2021). Constraints on the upper mantle structure beneath the pacific from 3-d anisotropic waveform modeling. *Journal of Geophysical Research: Solid Earth*, *126*(4), e2020JB020003.

Kendall, J.-M. (1994). Teleseismic arrivals at a mid-ocean ridge: Effects of mantle melt and anisotropy. *Geophysical Research Letters*, *21*(4), 301–304.

Kennett, B., & Engdahl, E. (1991). Traveltimes for global earthquake location and phase identification. *Geophysical Journal International*, *105*(2), 429–465.

Kennett, B. L., Engdahl, E., & Buland, R. (1995). Constraints on seismic velocities in the earth from traveltimes. *Geophysical Journal International*, *122*(1), 108–124.

Kern, H. (1993). P-and s-wave anisotropy and shear-wave splitting at pressure and temperature in possible mantle rocks and their relation to the rock fabric. *Physics of the Earth and Planetary Interiors*, *78*(3-4), 245–256.

Kim, Y.-W., Chang, S.-J., Witek, M., Ning, J., & Wen, J. (2021). S-velocity mantle structure of east asia from teleseismic traveltime tomography: Inferred mechanisms for the cenozoic intraplate volcanoes. *Journal of Geophysical Research: Solid Earth*, *126*(3), e2020JB020345.

Király, Á., Faccenna, C., & Funiciello, F. (2018). Subduction zones interaction around the adria microplate and the origin of the apenninic arc. *Tectonics*, *37*(10), 3941–3953.

Kohlstedt, D., & Goetze, C. (1974). Low-stress high-temperature creep in olivine single crystals. *Journal of Geophysical Research*, *79*(14), 2045–2051.

Komatitsch, D., & Tromp, J. (1999). Introduction to the spectral element method for three-dimensional seismic wave propagation. *Geophysical journal international*, *139*(3), 806–822.

Komatitsch, D., & Tromp, J. (2002). Spectral-element simulations of global seismic wave propagation—i. validation. *Geophysical Journal International*, *149*(2), 390–412.

Korenaga, T., Korenaga, J., Kawakatsu, H., & Yamano, M. (2021). A new reference model for the evolution of oceanic lithosphere in a cooling earth. *Journal of Geophysical Research: Solid Earth*, *126*(6), e2020JB021528.

Koulakov, I, Kaban, M., Tesauro, M., & Cloetingh, S. (2009). P-and s-velocity anomalies in the upper mantle beneath europe from tomographic inversion of isc data. *Geophysical Journal International*, *179*(1), 345–366.

Kuhlemann, J. (2007). Paleogeographic and paleotopographic evolution of the swiss and eastern alps since the oligocene. *Global and Planetary Change*, *58*(1-4), 224–236.

Kustowski, B, Ekström, G, & Dziewoński, A. (2008). Anisotropic shear-wave velocity structure of the earth's mantle: A global model. *Journal of Geophysical Research: Solid Earth*, *113*(B6).

Lai, H., & Garnero, E. J. (2020). Travel time and waveform measurements of global multi-bounce seismic waves using virtual station seismogram stacks. *Geochemistry, Geophysics, Geosystems*, *21*(1), e2019GC008679.

Lebedev, S., Nolet, G., Meier, T., & van der Hilst, R. D. (2005). Automated multimode inversion of surface and S waveforms. *Geophysical Journal International*, *162*, 951–964. https://doi.org/10.1111/j.1365-246X.2005.02708.x

Lebedev, S., Chevrot, S., & van der Hilst, R. D. (2002). Seismic evidence for olivine phase changes at the 410-and 660-kilometer discontinuities. *Science*, *296*(5571), 1300–1302.

Lebedev, S., & Nolet, G. (2003). Upper mantle beneath southeast asia from s velocity tomography. *Journal of Geophysical Research: Solid Earth*, *108*(B1).

Lebedev, S., & Van Der Hilst, R. D. (2008). Global upper-mantle tomography with the automated multimode inversion of surface and s-wave forms. *Geophysical Journal International*, *173*(2), 505–518.

Lei, J., & Zhao, D. (2006). Global p-wave tomography: On the effect of various mantle and core phases. *Physics of the Earth and Planetary Interiors*, *154*(1), 44–69.

Lévêque, J.-J., & Masson, F. (1999). From ach tomographic models to absolute velocity models. *Geophysical Journal International*, *137*(3), 621–629.

Lévêque, J.-J., Rivera, L., & Wittlinger, G. (1993). On the use of the checker-board test to assess the resolution of tomographic inversions. *Geophysical Journal International*, *115*(1), 313–318.

Li, C, van der Hilst, R., Engdahl, E., & Burdick, S. (2008). A new global model for 3-d variations of p-wave velocity in the earth's mantle. *Geochemistry, Geophysics, Geosystems*, *9*, Q05018.

Li, C., & Van Der Hilst, R. D. (2010). Structure of the upper mantle and transition zone beneath southeast asia from traveltime tomography. *Journal of Geophysical Research: Solid Earth*, *115*(B7).

Lippitsch, R., Kissling, E., & Ansorge, J. (2003). Upper mantle structure beneath the alpine orogen from high-resolution teleseismic tomography. *Journal of Geophysical Research: Solid Earth*, *108*(B8).

Liu, Q, & Gu, Y. (2012). Seismic imaging: From classical to adjoint tomography. *Tectonophysics*, *566*, 31–66.

Liu, X., & Zhao, D. (2016a). Backarc spreading and mantle wedge flow beneath the japan sea: Insight from rayleigh-wave anisotropic tomography. *Geophysical Journal International*, *207*(1), 357–373.

Liu, X., & Zhao, D. (2016b). P and s wave tomography of japan subduction zone from joint inversions of local and teleseismic travel times and surface-wave data. *Physics of the Earth and Planetary Interiors*, *252*, 1–22.

Liu, X., & Zhao, D. (2016c). Seismic velocity azimuthal anisotropy of the japan subduction zone: Constraints from p and s wave traveltimes. *Journal of Geophysical Research: Solid Earth*, *121*(7), 5086–5115.

Lloyd, S., & Van Der Lee, S. (2008). Influence of observed mantle anisotropy on isotropic tomographic models. *Geochemistry, Geophysics, Geosystems*, *9*(7).

Lo Bue, R., Faccenda, M., & Yang, J. (2021). The role of adria plate lithospheric structures on the recent dynamics of the central mediterranean region. *Journal of Geophysical Research: Solid Earth*, e2021JB022377. https://doi.org/https://doi.org/10.1029/2021JB022377

Lonergan, L., & White, N. (1997). Origin of the betic-rif mountain belt. *Tectonics*, *16*(3), 504–522.

Long, M. D. (2013). Constraints on subduction geodynamics from seismic anisotropy. *Reviews of Geophysics*, *51*(1), 76–112.

Long, M. D., & Becker, T. W. (2010). Mantle dynamics and seismic anisotropy. *Earth and Planetary Science Letters*, *297*(3-4), 341–354.

Long, M. D., & Silver, P. G. (2008). The subduction zone flow field from seismic anisotropy: A global view. *science*, *319*(5861), 315–318.

Long, M. D., & Silver, P. G. (2009a). Mantle flow in subduction systems: The subslab flow field and implications for mantle dynamics. *Journal of Geophysical Research: Solid Earth*, *114*(B10).

Long, M. D., & Silver, P. G. (2009b). Shear wave splitting and mantle anisotropy: Measurements, interpretations, and new directions. *Surveys in Geophysics*, *30*(4), 407–461.

Lucente, F. P., Chiarabba, C., Cimini, G. B., & Giardini, D. (1999). Tomographic constraints on the geodynamic evolution of the italian region. *Journal of Geophysical Research: Solid Earth*, *104*(B9), 20307–20327.

Lucente, F. P., Margheriti, L., Piromallo, C., & Barruol, G. (2006). Seismic anisotropy reveals the long route of the slab through the western-central mediterranean mantle. *Earth and Planetary Science Letters*, *241*(3-4), 517–529.

Lucente, F. P., & Speranza, F. (2001). Belt bending driven by lateral bending of subducting lithospheric slab: Geophysical evidences from the northern apennines (italy). *Tectonophysics*, *337*(1-2), 53–64.

Luth, S., Willingshofer, E., Sokoutis, D., & Cloetingh, S. (2013). Does subduction polarity changes below the alps? inferences from analogue modelling. *Tectonophysics*, *582*, 140–161.

Lyu, C., Pedersen, H. A., Paul, A., Zhao, L., & Solarino, S. (2017). Shear wave velocities in the upper mantle of the western alps: New constraints using array analysis of seismic surface waves. *Geophysical Journal International*, *210*(1), 321–331.

Magni, V., Faccenna, C., van Hunen, J., & Funiciello, F. (2014). How collision triggers backarc extension: Insight into mediterranean style of extension from 3-d numerical models. *Geology*, *42*(6), 511–514.

Maino, M., Decarlis, A., Felletti, F., & Seno, S. (2013). Tectono-sedimentary evolution of the tertiary piedmont basin (nw italy) within the oligo–miocene central mediterranean geodynamics. *Tectonics*, *32*(3), 593–619.

Mainprice, D. (2010). 16 seismic anisotropy of the deep earth from a mineral and rock physics perspective. *Treatise on Geophysics, Volume 2: Mineral Physics*, 437.

Mainprice, D., Hielscher, R., & Schaeben, H. (2011). Calculating anisotropic physical properties from texture data using the mtex open-source package. *Geological Society, London, Special Publications*, *360*(1), 175–192.

Malinverno, A., & Ryan, W. B. (1986). Extension in the tyrrhenian sea and shortening in the apennines as result of arc migration driven by sinking of the lithosphere. *Tectonics*, *5*(2), 227–245.

Marquering, H., & Snieder, R. (1995). Surface-wave mode coupling for efficient forward modelling and inversion of body-wave phases. *Geophysical Journal International*, *120*(1), 186–208. https://doi.org/10.1111/j.1365-246X.1995.tb05920.x

Masson, Y., & Romanowicz, B. (2017). Box tomography: Localized imaging of remote targets buried in an unknown medium, a step forward for understanding key structures in the deep earth. *Geophysical Journal International*, *211*(1), 141–163.

Masters, T. G., Johnson, S., Laske, G., & Bolton, H. (1996). A shear-velocity model of the mantle. *Philosophical Transactions of the Royal Society of London. Series A: Mathematical, Physical and Engineering Sciences*, *354*(1711), 1385–1411.

Mauffret, A, Frizon de Lamotte, D, Lallemant, S., Gorini, C., & Maillard, A. (2004). E–w opening of the algerian basin (western mediterranean). *Terra Nova*, *16*(5), 257–264.

McEvilly, T. (1964). Central us crust—upper mantle structure from love and rayleigh wave phase velocity inversion. *Bulletin of the Seismological Society of America*, *54*(6A), 1997–2015.

Menke, W. (2015). Equivalent heterogeneity analysis as a tool for understanding the resolving power of anisotropic travel-time tomography. *Bulletin of the Seismological Society of America*, *105*(2A), 719–733.

Menke, W., & Levin, V. (2003). The cross-convolution method for interpreting sks splitting observations, with application to one and two-layer anisotropic earth models. *Geophysical Journal International*, *154*(2), 379–392.

Miller, M., & Piana Agostinetti, N. (2012). Insights into the evolution of the italian lithospheric structure from s receiver function analysis. *Earth Science Planetary Letters*, *345-348*, 49–59.

Mishin, Y. A., Gerya, T. V., Burg, J.-P., & Connolly, J. A. (2008). Dynamics of double subduction: Numerical modeling. *Physics of the Earth and Planetary Interiors*, *171*(1-4), 280–295.

Mochizuki, E. (1995). Anisotropic tomography of p-wave traveltimes. *Geophysical Journal International*, *123*(1), 297–300.

Mohammadzaheri, A., Sigloch, K., Hosseini, K., & Mihalynuk, M. G. (2021). Subducted lithosphere under south america from multifrequency p wave tomography. *Journal of Geophysical Research: Solid Earth*, *126*(6), e2020JB020704.

Molinari, I., & Morelli, A. (2011). Epcrust: A reference crustal model for the european plate. *Geophysical Journal International*, *185*(1), 352–364.

Montagner, J.-P., & Nataf, H.-C. (1986). A simple method for inverting the azimuthal anisotropy of surface waves. *Journal of Geophysical Research: Solid Earth*, *91*(B1), 511–520.

Monteiller, V., Chevrot, S., Komatitsch, D., & Fuji, N. (2013). A hybrid method to compute short-period synthetic seismograms of teleseismic body waves in a 3-d regional model. *Geophysical Journal International*, *192*(1), 230–247.

Moser, T. (1991). Shortest path calculation of seismic rays. *Geophysics*, *56*(1), 59–67.

Moulik, P, & Ekström, G. (2014). An anisotropic shear velocity model of the earth's mantle using normal modes, body waves, surface waves and long-period waveforms. *Geophysical Journal International*, *199*(3), 1713–1738.

Müller, G. (1971). Approximate treatment of elastic body waves in media with spherical symmetry. *Geophysical Journal International*, *23*(4), 435–449.

Munzarová, H., Plomerová, J., & Kissling, E. (2018). Novel anisotropic teleseismic body-wave tomography code anitomo to illuminate heterogeneous anisotropic upper mantle: Part i—theory and inversion tuning with realistic synthetic data. *Geophysical Journal International*, *215*(1), 524–545.

Neri, G, Marotta, A., Orecchio, B., Presti, D, Totaro, C., Barzaghi, R., & Borghi, A. (2012). How lithospheric subduction changes along the calabrian arc in southern italy: Geophysical evidences. *International Journal of Earth Sciences*, *101*(7), 1949–1969.

Neri, G., Orecchio, B., Totaro, C., Falcone, G., & Presti, D. (2009). Subduction beneath southern italy close the ending: Results from seismic tomography. *Seismological Research Letters*, *80*(1), 63–70.

Nettles, M., & Dziewonski, A. (2008). Radially anisotropic shear velocity structure of the upper mantle globally and beneath north america. *Journal of Geophysical Research: Solid Earth*, *113*.

Nicolas, A., Boudier, F., & Boullier, A. (1973). Mechanisms of flow in naturally and experimentally deformed peridotites. *American Journal of Science*, *273*(10), 853–876.

Nicolas, A., & Christensen, N. I. (1987). Formation of anisotropy in upper mantle peridotites-a review. *Composition, structure and dynamics of the lithosphere-asthenosphere system*, *16*, 111–123.

Nishimura, C. E., & Forsyth, D. W. (1989). The anisotropic structure of the upper mantle in the pacific. *Geophysical Journal International*, *96*(2), 203–229.

Nissen-Meyer, T., van Driel, M., Stähler, S. C., Hosseini, K., Hempel, S., Auer, L., Colombi, A., & Fournier, A. (2014). Axisem: Broadband 3-d seismic wavefields in axisymmetric media. *Solid Earth*, *5*(1), 425–445.

Nocquet, J.-M., Sue, C., Walpersdorf, A, Tran, T, Lenôtre, N, Vernant, P, Cushing, M, Jouanne, F, Masson, F, Baize, S, et al. (2016). Present-day uplift of the western alps. *Scientific reports*, *6*(1), 1–6.

Nolet, G. (1990). Partitioned waveform inversion and two-dimensional structure under the network of autonomously recording seismographs. *Journal of Geophysical Research*, *95*(B6), 8499–8512. https://doi.org/10.1029/JB095iB06p08499

Obayashi, M., & Fukao, Y. (1997). P and pcp travel time tomography for the core-mantle boundary. *Journal of Geophysical Research: Solid Earth*, *102*(B8), 17825–17841.

Obayashi, M., Yoshimitsu, J., Nolet, G., Fukao, Y., Shiobara, H., Sugioka, H., Miyamachi, H., & Gao, Y. (2013). Finite frequency whole mantle p wave tomography: Improvement of subducted slab images. *Geophysical Research Letters*, *40*(21), 5652–5657.

Paffrath, M., Friederich, W., the AlpArray, & working group, A.-S. D. (2021). Imaging structure and geometry of slabs in the greater alpine area – a p-wave traveltime tomography using alparray seismic network data. *Solid Earth Discussions*, *2021*, 1–40. https://doi.org/10.5194/se-2021-58

Paige, C. C., & Saunders, M. A. (1982). Lsqr: An algorithm for sparse linear equations and sparse least squares. *ACM Transactions on Mathematical Software (TOMS)*, *8*(1), 43–71.

Panning, M., & Romanowicz, B. (2006). A three-dimensional radially anisotropic model of shear velocity in the whole mantle. *Geophysical Journal International*, *167*(1), 361–379.

Panning, M., Lekić, V, & Romanowicz, B. (2010). Importance of crustal corrections in the development of a new global model of radial anisotropy. *Journal of Geophysical Research: Solid Earth*, *115*(B12).

Panza, G., Pontevivo, A, Chimera, G, Raykova, R, & Aoudia, A. (2003). The lithosphere-asthenosphere: Italy and surroundings. *Episodes*, *26*(3), 169–174.

Park, J., & Levin, V. (2002). Seismic anisotropy: Tracing plate dynamics in the mantle. *Science*, *296*(5567), 485–489.

Parson, B., & McKenzie, D. (1977). An analysis of the variation of ocean floor bathymetry and heat flow with age. *Journal of Geophysical Research: Solid Earth*, *82(5)*, 803–827.

Parson, B., & McKenzie, D. (1978). Mantle convection and the thermal structure of the plates. *Journal of Geophysical Research: Solid Earth*, *83*, 4485–4496.

Patacca, E., Sartori, R, & Scandone, P. Tyrrhenian basin and apennines. kinematic evolution and related dynamic constraints. In: *Recent evolution and seismicity of the mediterranean region*. Springer, 1993, pp. 161–171.

Patankar, S. V. (2018). *Numerical heat transfer and fluid flow*. CRC press.

Paulatto, M., Annen, C., Henstock, T. J., Kiddle, E, Minshull, T. A., Sparks, R., & Voight, B. (2012). Magma chamber properties from integrated seismic tomography and thermal modeling at montserrat. *Geochemistry, Geophysics, Geosystems*, *13*(1).

Peccerillo. (2017). *Cenozoic volcanism in the tyrrhenian sea region*. Springer.

Peral, M., Ruh, J., Zlotnik, S., Funiciello, F., Fernàndez, M., Vergés, J., & Gerya, T. (2020). Analog and numerical experiments of double subduction systems with opposite polarity in adjacent segments. *Geochemistry, Geophysics, Geosystems*, *21*(6), e2020GC009035.

Piromallo, C., & Morelli, A. (1997). Imaging the mediterranean upper mantle by p-wave travel time tomography. *Annals of Geophysics*, *40*(4).

Piromallo, C., & Morelli, A. (2003). P wave tomography of the mantle under the alpine-mediterranean area. *Journal of Geophysical Research: Solid Earth*, *108*(B2).

Platt, J., & Vissers, R. (1989). Extensional collapse of thickened continental lithosphere: A working hypothesis for the alboran sea and gibraltar arc. *Geology*, *17*(6), 540–543.

Portner, D. E., Beck, S., Zandt, G., & Scire, A. (2017). The nature of subslab slow velocity anomalies beneath south america. *Geophysical Research Letters*, *44*(10), 4747–4755.

Portner, D. E., & Hayes, G. P. (2018). Incorporating teleseismic tomography data into models of upper mantle slab geometry. *Geophysical Journal International*, *215*(1), 325–332.

Pratt, R. G. (1999). Seismic waveform inversion in the frequency domain, part 1: Theory and verification in a physical scale model. *Geophysics*, *64*(3), 888–901.

Presti, D., Totaro, C., Neri, G., & Orecchio, B. (2019). New earthquake data in the calabrian subduction zone, italy, suggest revision of the presumed dynamics in the upper part of the subducting slab. *Seismological Research Letters*, *90*(5), 1994–2004.

Qorbani, E., Bokelmann, G., Kovács, I., Horváth, F., & Falus, G. (2016). Deformation in the asthenospheric mantle beneath the carpathian-pannonian region. *Journal of Geophysical Research: Solid Earth*, *121*(9), 6644–6657.

Raleigh, C., Kirby, S., Carter, N., & Lallemant, H. A. (1971). Slip and the clinoenstatite transformation as competing rate processes in enstatite. *Journal of Geophysical Research*, *76*(17), 4011–4022.

Ranalli, G. (1995). *Rheology of the earth*. Springer Science & Business Media.

Rappisi, F., & Faccenda, M. (2019). Geodynamic and seismological numerical modelling for seismic anisotropy studies. *AGUFM*, *2019*, DI21B–0038.

Rappisi, F., VanderBeek, B., Faccenda, M, Morelli, A, & Molinari, I. (2022). Slab geometry and upper mantle flow patterns in the central mediterranean from 3d anisotropic p-wave tomography. *Journal of Geophysical Research: Solid Earth*, e2021JB023488.

Rawlinson, N, Pilia, S, Young, M, Salmon, M, & Yang, Y. (2016). Crust and upper mantle structure beneath southeast australia from ambient noise and teleseismic tomography. *Tectonophysics*, *689*, 143–156.

Rawlinson, N, & Spakman, W. (2016). On the use of sensitivity tests in seismic tomography. *Geophysical Journal International*, *205*(2), 1221–1243.

Rawlinson, N., Fichtner, A., Sambridge, M., & Young, M. K. (2014). Seismic tomography and the assessment of uncertainty. *Advances in geophysics*, *55*, 1–76.

Rawlinson, N., Pozgay, S, & Fishwick, S. (2010). Seismic tomography: A window into deep earth. *Physics of the Earth and Planetary Interiors*, *178*(3-4), 101–135.

Reuber, G. S., & Simons, F. J. (2020). Multi-physics adjoint modeling of earth structure: Combining gravimetric, seismic, and geodynamic inversions. *GEM-International Journal on Geomathematics*, *11*(1), 1–38.

Ribe, N. M. (1989). Seismic anisotropy and mantle flow. *Journal of Geophysical Research: Solid Earth*, *94*(B4), 4213–4223.

Ribe, N. M., & Yu, Y. (1991). A theory for plastic deformation and textural evolution of olivine polycrystals. *Journal of Geophysical Research: Solid Earth*, *96*(B5), 8325–8335.

Ringwood, A. E. (1975). Composition and petrology of the earth's mantle. *MacGraw-Hill*, *618*.

Ritsema, J., Deuss, A., Van Heijst, H., & Woodhouse, J. (2011). S40rts: A degree-40 shear-velocity model for the mantle from new rayleigh wave dispersion, teleseismic traveltime and normal-mode splitting function measurements. *Geophysical Journal International*, *184*(3), 1223–1236.

Ritsema, J., Heijst, H. J. v., & Woodhouse, J. H. (1999). Complex shear wave velocity structure imaged beneath africa and iceland. *Science*, *286*(5446), 1925–1928.

Robertson, G., & Woodhouse, J. (1995). Evidence for proportionality of p and s heterogeneity in the lower mantle. *Geophysical Journal International*, *123*(1), 85–116.

Romagny, A., Jolivet, L., Menant, A., Bessière, E., Maillard, A., Canva, A., Gorini, C., & Augier, R. (2020). Detailed tectonic reconstructions of the western mediterranean region for the last 35 ma, insights on driving mechanisms. *BSGF-Earth Sciences Bulletin*, *191*(1), 37.

Romanowicz, B. (2003). Global mantle tomography: Progress status in the past 10 years. *Annual Review of Earth and Planetary Sciences*, *31*(1), 303–328.

Romanowicz, B. A. Seismic tomography of the earth's mantle (D. Alderton & S. A. Elias, Eds.; Second Edition). In: In *Encyclopedia of geology (second edition)* (D. Alderton & S. A. Elias, Eds.; Second Edition). Ed. by Alderton, D., & Elias, S. A. Second Edition. Oxford: Academic Press, 2021, pp. 587–609. ISBN: 978-0-08-102909-1. https://doi.org/https://doi.org/10.1016/B978-0-08-102908-4.00169-7.

Ronchi, C., Iacono, R., & Paolucci, P. S. (1996). The "cubed sphere": A new method for the solution of partial differential equations in spherical geometry. *Journal of computational physics*, *124*(1), 93–114.

Rosenbaum, G., Lister, G. S., & Duboz, C. (2002a). Relative motions of africa, iberia and europe during alpine orogeny. *Tectonophysics*, *359*(1-2), 117–129.

Rosenbaum, G., Lister, G. S., Duboz, C., et al. (2002b). Reconstruction of the tectonic evolution of the western mediterranean since the oligocene. *Journal of the Virtual Explorer*, *8*(January).

Ruan, Y., Lei, W., Modrak, R., Örsvuran, R., Bozdağ, E., & Tromp, J. (2019). Balancing unevenly distributed data in seismic tomography: A global adjoint tomography example. *Geophysical Journal International*, *219*(2), 1225–1236.

Rümpker, G., & Silver, P. G. (1998). Apparent shear-wave splitting parameters in the presence of vertically varying anisotropy. *Geophysical Journal International*, *135*(3), 790–800.

Russel, J., Gaherty, J., Lin, P.-Y., Lizarrardle, D., Collins, J., Hirth, G., & Evans, R. (2018). High-resolution constraints on pacific upper mantle petrofabric inferred from surface-wave anisotropy. *Journal of Geophysical Research: Solid Earth*, *124*, 631–657. https://doi.org/https://doi.org/10.1029/2018JB016598

Russell, J. B., Gaherty, J. B., Lin, P.-Y. P., Lizarralde, D., Collins, J. A., Hirth, G., & Evans, R. L. (2019). High-resolution constraints on pacific upper mantle petrofabric inferred from surface-wave anisotropy. *Journal of Geophysical Research: Solid Earth*, *124*(1), 631–657.

Ryan, W. B., Carbotte, S. M., Coplan, J. O., O'Hara, S., Melkonian, A., Arko, R., Weissel, R. A., Ferrini, V., Goodwillie, A., Nitsche, F., et al. (2009). Global multi-resolution topography synthesis. *Geochemistry, Geophysics, Geosystems*, *10*(3).

Sadourny, R. (1972). Conservative finite-difference approximations of the primitive equations on quasi-uniform spherical grids. *Monthly Weather Review*, *100*(2), 136–144.

Savage, M. (1999). Seismic anisotropy and mantle deformation: What have we learned from shear wave splitting? *Reviews of Geophysics*, *37*(1), 65–106.

Scarfì, L., Barberi, G., Barreca, G., Cannavò, F., Koulakov, I., & Patanè, D. (2018). Slab narrowing in the central mediterranean: The calabro-ionian subduction zone as imaged by high resolution seismic tomography. *Scientific reports*, *8*(1), 1–12.

Schaeffer, A., & Lebedev, S. (2013). Global shear speed structure of the upper mantle and transition zone. *Geophysical Journal International*, *194*(1), 417–449.

Schaeffer, A., & Lebedev, S. (2014). Imaging the north american continent using waveform inversion of global and usarray data. *Earth and Planetary Science Letters*, *402*, 26–41.

Schaeffer, A., Lebedev, S., & Becker, T. (2016). Azimuthal seismic anisotropy in the earth's upper mantle and the thickness of tectonic plates. *Geophysical Journal International*, *207*(1), 901–933.

Schmandt, B., & Humphreys, E. (2010). Seismic heterogeneity and small-scale convection in the southern california upper mantle. *Geochemistry, Geophysics, Geosystems*, *11*(5).

Selvaggi, G, & Chiarabba, C. (1995). Seismicity and p-wave velocity image of the southern tyrrhenian subduction zone. *Geophysical Journal International*, *121*(3), 818–826.

Sengupta, M. K., & Toksöz, M. N. (1976). Three dimensional model of seismic velocity variation in the earth's mantle. *Geophysical Research Letters*, *3*(2), 84–86.

Sieminski, A., Liu, Q., Trampert, J., & Tromp, J. (2007). Finite-frequency sensitivity of surface waves to anisotropy based upon adjoint methods. *Geophysical Journal International*, *168*(3), 1153–1174.

Sieminski, A., Paulssen, H., Trampert, J., & Tromp, J. (2008). Finite-frequency sks splitting: Measurement and sensitivity kernels. *Bulletin of the Seismological Society of America*, *98*(4), 1797–1810.

Silver, P. G. (1996). Seismic anisotropy beneath the continents: Probing the depths of geology. *Annual review of earth and planetary sciences*, *24*(1), 385–432.

Silver, P. G., & Chan, W. W. (1988). Implications for continental structure and evolution from seismic anisotropy. *Nature*, *335*(6185), 34–39.

Silver, P. G., & Chan, W. W. (1991). Shear wave splitting and subcontinental mantle deformation. *Journal of Geophysical Research: Solid Earth*, *96*(B10), 16429–16454.

Simmons, N., Myers, S., & Johannesson, G. (2011). Global-scale p wave tomography optimized for prediction of teleseismic and regional travel times for middle east events: 2. tomographic inversion. *Journal of Geophysical Research: Solid Earth*, *116*(B4).

Simmons, N. A., Forte, A. M., & Grand, S. P. (2006). Constraining mantle flow with seismic and geodynamic data: A joint approach. *Earth and Planetary Science Letters*, *246*(1-2), 109–124.

Simmons, N. A., Myers, S. C., Johannesson, G., & Matzel, E. (2012). Llnl-g3dv3: Global p wave tomography model for improved regional and teleseismic travel time prediction. *Journal of Geophysical Research: Solid Earth*, *117*(B10).

Skemer, P., & Hansen, L. N. (2016). Inferring upper-mantle flow from seismic anisotropy: An experimental perspective. *Tectonophysics*, *668*, 1–14.

Skemer, P., Katayama, I., Jiang, Z., & Karato, S.-i. (2005). The misorientation index: Development of a new method for calculating the strength of lattice-preferred orientation. *Tectonophysics*, *411*(1-4), 157–167.

Sobolev, S. V., Grésillaud, A., & Cara, M. (1999). How robust is isotropic delay time tomography for anisotropic mantle? *Geophysical research letters*, *26*(4), 509–512.

Song, T.-R. A., & Kawakatsu, H. (2012). Subduction of oceanic asthenosphere: Evidence from sub-slab seismic anisotropy. *Geophysical Research Letters*, *39*(17).

Song, W., Yu, Y., Shen, C., Lu, F., & Kong, F. (2019). Asthenospheric flow beneath the carpathian-pannonian region: Constraints from shear wave splitting analysis. *Earth and Planetary Science Letters*, *520*, 231–240.

Spakman, W, & Nolet, G. Imaging algorithms, accuracy and resolution in delay time tomography. In: *Mathematical geophysics*. Springer, 1988, pp. 155–187.

Spakman, W, Wortel, M., & Vlaar, N. (1988). The hellenic subduction zone: A tomographic image and its geodynamic implications. *Geophysical research letters*, *15*(1), 60–63.

Spakman, W. (1990). Tomographic images of the upper mantle below central europe and the mediterranean. *Terra Nova*, *2*(6), 542–553.

Spakman, W. (1991). Delay-time tomography of the upper mantle below europe, the mediterranean, and asia minor. *Geophysical Journal International*, *107*(2), 309–332.

Spakman, W., van der Lee, S., & van der Hilst, R. (1993). Travel-time tomography of the european-mediterranean mantle down to 1400 km. *Physics of the Earth and Planetary Interiors*, *79*(1-2), 3–74.

Spakman, W., & Wortel, R. A tomographic view on western mediterranean geodynamics. In: *The transmed atlas. the mediterranean region from crust to mantle*. Springer, 2004, pp. 31–52.

Stein, C., & Stein, S. (1992). A model for the global variation in oceanic depth and heat flow with lithospheric age. *Nature*, *359*, 123–129.

Sturgeon, W., Ferreira, A., Faccenda, M., Chang, S.-J., & Schardong, L. (2019). On the origin of radial anisotropy near subducted slabs in the midmantle. *Geochemistry, Geophysics, Geosystems*, *20*. https://doi.org/https://doi.org/10.1029/2019GC008462

Su, W.-j., & Dziewonski, A. M. (1997). Simultaneous inversion for 3-d variations in shear and bulk velocity in the mantle. *Physics of the Earth and Planetary Interiors*, *100*(1-4), 135–156.

Tarantola, A. (1986). A strategy for nonlinear elastic inversion of seismic reflection data. *Geophysics*, *51*(10), 1893–1903.

Tasaka, M., Zimmerman, M. E., Kohlstedt, D. L., Stünitz, H., & Heilbronner, R. (2017). Rheological weakening of olivine+ orthopyroxene aggregates due to phase mixing: Part 2. microstructural development. *Journal of Geophysical Research: Solid Earth*, *122*(10), 7597–7612.

Thomsen, L. (1986). Weak elastic anisotropy. *Geophysics*, *51*(10), 1954–1966.

Tommasi, A. (1998). Forward modeling of the development of seismic anisotropy in the upper mantle. *Earth and Planetary Science Letters*, *160*(1-2), 1–13.

Toomey, D. R., Solomon, S. C., & Purdy, G. (1994). Tomographic imaging of the shallow crustal structure of the east pacific rise at 9° 30 n. *Journal of Geophysical Research: Solid Earth*, *99*(B12), 24135–24157.

Toomey, D., & Foulger, G. (1989). Tomographic inversion of local earthquake data from the hengill-grensdalur central volcano complex, iceland. *Journal of Geophysical Research: Solid Earth*, *94*(B12), 17497–17510.

Tromp, J., Komatitsch, D., & Liu, Q. (2008). Spectral-element and adjoint methods in seismology. *Communications in Computational Physics*, *3*(1), 1–32.

Turcotte, D, & Schubert, G. (2014). Geodynamics, 160–228, 263–334, 425–463.

van Hinsbergen, D. J., Vissers, R. L., & Spakman, W. (2014). Origin and consequences of western mediterranean subduction, rollback, and slab segmentation. *Tectonics*, *33*(4), 393–419.

van Zelst, I., Crameri, F., Pusok, A. E., Glerum, A., Dannberg, J., & Thieulot, C. (2021). 101 geodynamic modelling: How to design, carry out, and interpret numerical studies. *Solid Earth Discuss.*, 1–80.

Van der Hilst, R. D., Widiyantoro, S., & Engdahl, E. (1997). Evidence for deep mantle circulation from global tomography. *Nature*, *386*(6625), 578–584.

Van der Lee, S, & Nolet, G. (1997). Upper mantle s velocity structure of north america. *Journal of Geophysical Research: Solid Earth*, *102*(B10), 22815–22838.

Van der Meer, D. G., Van Hinsbergen, D. J., & Spakman, W. (2018). Atlas of the underworld: Slab remnants in the mantle, their sinking history, and a new outlook on lower mantle viscosity. *Tectonophysics*, *723*, 309–448.

Van Hinsbergen, D. J., Torsvik, T. H., Schmid, S. M., Maţenco, L. C., Maffione, M., Vissers, R. L., Gürer, D., & Spakman, W. (2020). Orogenic architecture of the mediterranean

region and kinematic reconstruction of its tectonic evolution since the triassic. *Gond-wana Research*, *81*, 79–229.

VanDecar, J., & Crosson, R. (1990). Determination of teleseismic relative phase arrival times using multi-channel cross-correlation and least squares. *Bulletin of the Seismological Society of America*, *80*(1), 150–169.

VanderBeek, B. P., & Faccenda, M. (2021). Imaging upper mantle anisotropy with teleseismic p-wave delays: Insights from tomographic reconstructions of subduction simulations. *Geophysical Journal International*, *225*(3), 2097–2119.

Vignaroli, G., Faccenna, C., Jolivet, L., Piromallo, C., & Rossetti, F. (2008). Subduction polarity reversal at the junction between the western alps and the northern apennines, italy. *Tectonophysics*, *450*(1-4), 34–50.

Villagómez, D. R., Toomey, D. R., Geist, D. J., Hooft, E. E., & Solomon, S. C. (2014). Mantle flow and multistage melting beneath the galápagos hotspot revealed by seismic imaging. *Nature Geoscience*, *7*(2), 151–156.

Vinnik, L., Kind, R, Kosarev, G., & Makeyeva, L. (1989). Azimuthal anisotropy in the lithosphere from observations of long-period s-waves. *Geophysical Journal International*, *99*(3), 549–559.

Virieux, J., & Operto, S. (2009). An overview of full-waveform inversion in exploration geophysics. *Geophysics*, *74*(6), WCC1–WCC26.

Wang, J., Xiao, Z., Liu, C., Zhao, D., & Yao, Z. (2019). Deep learning for picking seismic arrival times. *Journal of Geophysical Research: Solid Earth*, *124*(7), 6612–6624.

Wang, J., & Zhao, D. (2008). P-wave anisotropic tomography beneath northeast japan. *Physics of the Earth and Planetary Interiors*, *170*(1-2), 115–133.

Wang, N., Montagner, J.-P., Fichtner, A., & Capdeville, Y. (2013). Intrinsic versus extrinsic seismic anisotropy: The radial anisotropy in reference earth models. *Geophysical Research Letters*, *40*(16), 4284–4288.

Wang, W., & Becker, T. W. (2019). Upper mantle seismic anisotropy as a constraint for mantle flow and continental dynamics of the north american plate. *Earth and Planetary Science Letters*, *514*, 143–155.

Wang, Z., & Zhao, D. (2021). 3d anisotropic structure of the japan subduction zone. *Science advances*, *7*(4), eabc9620.

Warren, J. M., Hirth, G., & Kelemen, P. B. (2008). Evolution of olivine lattice preferred orientation during simple shear in the mantle. *Earth and Planetary Science Letters*, *272*(3-4), 501–512.

Wei, W., Zhao, D., Wei, F., Bai, X., & Xu, J. (2019). Mantle dynamics of the eastern mediterranean and middle east: Constraints from p-wave anisotropic tomography. *Geochemistry, Geophysics, Geosystems*, *20*(10), 4505–4530.

Wenk, H. R. (2016). *Preferred orientation in deformed metal and rocks: An introduction to modern texture analysis*. Elsevier.

Wessel, P, Luis, J., Uieda, L, Scharroo, R, Wobbe, F, Smith, W., & Tian, D. (2019). The generic mapping tools version 6. *Geochemistry, Geophysics, Geosystems*, *20*(11), 5556–5564.

Wiens, D. A., Conder, J. A., & Faul, U. H. (2008). The seismic structure and dynamics of the mantle wedge. *Annu. Rev. Earth Planet. Sci.*, *36*, 421–455.

Witek, M, Chang, S.-J., Lim, D., Ning, S, & Ning, J. (2021). Radial anisotropy in east asia from multimode surface wave tomography. *Journal of Geophysical Research: Solid Earth*, *126*(7), e2020JB021201.

Witek, M, van der Lee, S, Kang, T.-S., Chang, S.-J., Ning, J, & Ning, S. (2018). S velocity model of east asia from a cluster analysis of localized dispersion. *Journal of Geophysical Research: Solid Earth*, *123*(11), 9712–9732.

Witek, M., Lee, S.-M., Chang, S.-J., & van der Lee, S. (2022). Automated partitioned waveform inversion for radially anisotropic structure. *Geophysical Journal International*, *20*, –.

Wortel, M., & Spakman, W. (2000). Subduction and slab detachment in the mediterranean-carpathian region. *Science*, *290*(5498), 1910–1917.

Wortel, R., Govers, R., & Spakman, W. Continental collision and the step-wise evolution of convergent plate boundaries: From structure to dynamics. In: *Subduction zone geodynamics*. Springer, 2009, pp. 47–59.

Wu, H., & Lees, J. M. (1999). Cartesian parametrization of anisotropic traveltime tomography. *Geophysical Journal International*, *137*(1), 64–80.

Wüstefeld, A., Bokelmann, G., Barruol, G., & Montagner, J.-P. (2009). Identifying global seismic anisotropy patterns by correlating shear-wave splitting and surface-wave data. *Physics of the Earth and Planetary Interiors*, *176*(3-4), 198–212.

Yang, J., & Faccenda, M. (2020). Intraplate volcanism originating from upwelling hydrous mantle transition zone. *Nature*, *569*, 88–91.

Young, M., Tkalčić, H, Bodin, T, & Sambridge, M. (2013). Global p wave tomography of earth's lowermost mantle from partition modeling. *Journal of Geophysical Research: Solid Earth*, *118*(10), 5467–5486.

Zhang, H, & Thurber, C. (2007). Estimating the model resolution matrix for large seismic tomography problems based on lanczos bidiagonalization with partial reorthogonalization. *Geophysical Journal International*, *170*(1), 337–345.

Zhang, H., Thurber, C., & Bedrosian, P. (2009). Joint inversion for vp, vs, and vp/vs at safod, parkfield, california. *Geochemistry, Geophysics, Geosystems*, *10*(11).

Zhang, S., & Karato, S.-i. (1995). Lattice preferred orientation of olivine aggregates deformed in simple shear. *Nature*, *375*(6534), 774–777.

Zhao, D., Hasegawa, A., & Horiuchi, S. (1992). Tomographic imaging of p and s wave velocity structure beneath northeastern japan. *Journal of Geophysical Research: Solid Earth*, *97*(B13), 19909–19928.

Zhao, D., & Hua, Y. (2021). Anisotropic tomography of the cascadia subduction zone. *Physics of the Earth and Planetary Interiors*, *318*, 106767.

Zhao, D., Wang, K., Rogers, G. C., & Peacock, S. M. (2001). Tomographic image of low p velocity anomalies above slab in northern cascadia subduction zone. *Earth, planets and space*, *53*(4), 285–293.

Zhao, L., Paul, A., Malusà, M. G., Xu, X., Zheng, T., Solarino, S., Guillot, S., Schwartz, S., Dumont, T., Salimbeni, S., et al. (2016). Continuity of the alpine slab unraveled by high-resolution p wave tomography. *Journal of Geophysical Research: Solid Earth*, *121*(12), 8720–8737.

Zhou, H.-w. (1996). A high-resolution p wave model for the top 1200 km of the mantle. *Journal of Geophysical Research: Solid Earth*, *101*(B12), 27791–27810.

Zhou, Q., Hu, J., Liu, L., Chaparro, T., Stegman, D. R., & Faccenda, M. (2018). Western us seismic anisotropy revealing complex mantle dynamics. *Earth and Planetary Science Letters*, *500*, 156–167.

Zhu, H., Bozdağ, E., Peter, D., & Tromp, J. (2012). Structure of the european upper mantle revealed by adjoint tomography. *Nature Geoscience*, *5*(7), 493–498.

Zhu, H., Komatitsch, D., & Tromp, J. (2017). Radial anisotropy of the north american upper mantle based on adjoint tomography with usarray. *Geophysical Journal International*, *211*(1), 349–377.

Zhu, H., & Tromp, J. (2013). Mapping tectonic deformation in the crust and upper mantle beneath europe and the north atlantic ocean. *Science*, *341*(6148), 871–875.

Acknowledgements

I would like to dedicate a few lines to all those who have been close to me in this path of personal and professional growth.

A heartfelt thanks to my supervisor Manuele Faccenda for his availability, patience and prompt response to all my requests. Thank you for believing in me and providing me with every material and tool useful for my training.

Thanks to my co-supervisor and friend Brandon Vanderbeek, for patiently putting up with and supporting me even outside working hours.

Thanks to Albert who, although in his own way, was the soul of our office and a great coffee break buddy.

Thanks to the moral and professional support of Rosalia. Thanks for stopping me from tearing the thesis into a thousand pieces!

Thanks to Barolo (not the wine!) for making returning home after hours in the office even better.

Thanks to all members of the NEWTON group, "the Newtonians", friends before colleagues.

Thanks to Ana Ferreira, Sung-Joon Chang and Michael Witek who helped me carry out my research from different parts of the world.

Thanks to the reviewers Maximiliano Bezada and Marco Calò for their constructive feedback and comments.

Finally, I thank all the staff of the Geosciences Department of the University of Padova who made me feel part of this team since my first day in Veneto.